الجمهورية الجزائرية الديمقراطية الشعبية
République Algérienne Démocratique Et Populaire
وزارة التعليم العالي والبحث العلمي
Ministère de L'Enseignement Supérieur et de La Recherche Scientifique
جامعة فرحات عباس- سطيف1
Université Ferhat Abbas - Sétif 1

THÈSE

Présentée à l'Institut d'Optique et de Mécanique de Précision pour l'obtention du Diplôme de

DOCTORAT 3ème Cycle LMD

Domaine : Sciences et Technologies
Filière : Optique et Mécanique de Précision
Spécialité : Mécanique Appliquée

Par

ARIANE Khalissa

THÈME

Contribution au développement des vitrocéramiques à propriétés mécaniques et biocides élevées

Soutenue, le 12/11/2020

Devant la commission d'examen formée de:

Président du Jury	BELKHIR Nabil	Professeur	UFA Sétif-1
Rapporteur	CHORFA Abdellah	Professeur	UFA Sétif-1
Co-Rapporteur	RUBIO Fausto	Directeur de recherche	ICV-CSIC Madrid
Examinateur	LAOUAMRI Hind	MCA	UFA Sétif-1
Examinateur	BOUDCHICHA Mohamed Redda	MCA	ENP Constantine
Invité	BOUZRARA Ferhat	Professeur	USMB Jijel

Wolfram HÖLAND and **George BEALL** state

“*Knowledge of the literature, good observation skills, and deductive reasoning were clearly evident in allowing the chance events to bear fruits***”**

Acknowledgements

Praises to **Allah** and peace be upon the beloved final Prophet Mohamed.

Coming to the end of these unforgettable years, lots of memories flash back into my mind where lots of people have played a major role and without them, this thesis would not have been possible.

First and foremost, I would like to thank my supervisor, Prof. **Abdellah CHORFA**, professor at Ferhat Abbas University-Setif, for his support, direction, regular intellectual discussions throughout the duration of this thesis.

I convey my sincere gratitude to my co-supervisor, Dr. **Fausto RUBIO ALONSO**, scientific researcher, head of Instituto de Cerámica y Vidrio (ICV-CSIC), for his sympathy, good humor, continuous asking and precious help since the first day I arrived to Madrid.

I would like also to express my gratitude to the president of the jury, Prof. **Nabil BELKHIR**, as well as to all the jury members, Prof. **Ferhat BOUZRARA**, Dr. **Mohamed Redda BOUDCHICHA**, and Dr. **Hind LAOUAMRI**, for accepting the task of evaluating my thesis work.

I would like to express my deepest gratitude to Dr. **Juan RUBIO ALONSO**, scientific researcher, head of Departamento Química Física Superficies y Procesos, Instituto de Cerámica y Vidrio (ICV-CSIC), whose valuable guidance has been the ones that helped me patch this project and make it full proof success, his suggestions and his instructions has served as the major contributor towards the completion of the project.

I would like to express my respect to Dr. **Aitana TAMAYO**, scientific researcher, Instituto de Cerámica y Vidrio (ICV-CSIC), for her constructive ideas, for all the explanations and the fruitful discussions.

In particular, I would like to express my gratitude to Prof. **Lakhdar SMATA**, Professor at Ferhat Abbas University-Setif, as teacher and previous mentor.

I would also to record my special appreciation to **John-Jairo Aguilera CORREA**, MSc, PhD, Departamento de Microbiología Clínica, Instituto de Investigación Sanitaria, Fundación Jiménez Díaz, Madrid, for the biological measurements.

I would like also to thank, Dr. **Miguel Angel Rodriguez BARBERO**, scientific researcher, Instituto de Cerámica y Vidrio (ICV-CSIC), for his disponibility and his help at the process of melting.

My kind respect goes to one of the most gentle person, Prof. **Mohamed HAMIDOUCHE**, Professor at Ferhat Abbas University, Setif, for all his help when he was the head of Emerging Materials Research Unit (URME-Setif).

Secondly, I extend my gratitude to the Institute of Optics and Precision Mechanics (IOMP-Sétif) for giving me this opportunity.

I gratefully acknowledge both the Ministry of Higher Education of Algeria and the Instituto de cerámica y vidrio (ICV-CSIC, Spain) for the internship, which made this research possible.

I would like to extend my appreciation to all members of the Instituto de Cerámica y Vidrio for their help and support in my work. It was nice to meet *David*, *Nilo*, *Sandra*, *Pablo*, *Monica* and *Paloma*.

Thanks to everyone who has participated either directly or indirectly in this accomplishment. In particular, *Assia*, *Hasna*, *Dalila*, *Tatevik* (Armenia), *Abdelaziz*, *Hossem*, *Hadjer*, *Meriem*, *Hocine*, *Ahlem* and *Imed* (Tunisia), *Mohamed* (Egypt), *Ikram* (Morocco), *Souhir*, *Nedjoua* and *Norelhouda* for the atmosphere of work, fraternity, support and joy that they have established.

Last, but not least, I would like to thank all my family members (siblings, nephews and nieces). Words can not express how grateful I am to my parents. Thank you for being there for me each time I needed your support. Your prayer for me was what sustained me thus far and hereafter. I would like to say a special thank you to my brother, *Bouzid*, who has always supported and encouraged me.

I gratefully thank to Allah for reasons too numerous to mention.

Table of contents

List of Figures

List of Tables

Nomenclature

A	Arrhenian pre-exponential factor
A_0	Frequency factor
a^*	Color from green (-) to red (+)
b^*	Color from blue (-) to yellow (+)
E	Young's modulus
E_c	Activation energy
E_{cab}	Activation energy (Augis and Bennet)
E_{ck}	Activation energy (Kissinger)
E_{cms}	Activation energy (Matusita and Sakka)
E_{co}	Activation energy (Ozawa)
E_g	Activation energy of glass transition
E_v	Optical band gap energy
F_I	Fragility index
$F_{I\text{-}0}$	Reference fragility
$F_{I\text{-}DTA}$	Fragility index calculated from the DTA measurements
$F_{I\text{-}vis}$	Fragility index calculated from viscosity measurements
h	Planck's constant
$h\nu$	Incident photon energy
H_v	Hardness (Vickers)
k	Boltzmann constant
K	Constant
K_H	Hruby parameter
L^*	Lightness from black (0) to white (100)

m	Growth morphology index
m	Machinability parameter
N	Number density of nuclei with a crystalline phase factor
n	Avrami exponent
n	index represent the nature of band transition
n_D	Refraction index
n_v	Number of atoms of the crystallizing component phase per unit volume of the liquid
P	Poise
R	Universal gas constant
r^*	Minimum size of a nucleus
S	Resistance to devitrification of a glass
T	Temperature
T_C	Crystallization temperature
T_g	Glass transition temperature
T_l	Liquidus temperature
T_m	Melting temperature
T_N	Nucleation temperature
T_{NC}	Nucleation/crystallization temperature
T_o	Onset of peak crystallization temperature
T_p	Exothermic peak temperature (from DTA curves)
T_{rg}	Reduced glass transition temperature
T_s	Softening temperature
t	Time
U	Growth rate

V	Volume per formula unit
v	DTA heating rate
V_m	Molar volume of the crystal phase
W^*	Thermodynamic
w_2	Criterion of Glass Forming Ability
x	Crystallized fraction volume
α	Absorption coefficient
β_2	Criterion of Glass Forming Ability
ΔG_D	Kinetic free energy
ΔT_o	Supercooled liquid region
Δw	Full-width
ΔG	Bulk free energy change per mole in crystallization
γ	Criterion of Glass Forming Ability
σ	Crystal-liquid interfacial free energy per unit area
θ	Contact angle

Abbreviations

ATR	Attenuated Total Reflectance
BG (s)	Base glass (es)
CIE	International Commission on Illumination
CFU	Colony forming units
CNT	Classical Nucleation Theory
CTE	Coefficient of Thermal Expansion
DTA	Differential Thermal Analysis
DSC	Differential Scanning Calorimetry
E. coli	Escherichia coli
EDS	Energy Dispersion Spectroscopy
FE-SEM	Field Emission Scanning Electron Microscopy
FTIR	Fourier Transform Infrared Spectroscopy
GC (s)	Glass ceramic (s)
GFA	Glass forming ability
GS	Glass stability
HF	Hydrofluoric acid
HSM	Hot-Stage Microscopy
ICDD	International Centre for Diffraction Data
JCPDS	Joint Committee on Powder Diffraction Standards
JMAK	Johnson-Mehl-Avrami-Kolmogorov relation
KBr	Potassium Bromide powder
LMAS	Lithium Magnesium Aluminosilicate
MAS	Magnesium Aluminosilicate

NC	Nucleation/Crystallization
Pk	Exothermic peak
Pt	Platinum
SiC	Silicon carbide
SS	Saline solution
TA	Thermal analysis
XRD	X-ray Diffraction
XRF	X-ray Fluorescence

General Introduction

General introduction

Modern science and technology constantly require new materials with special properties to achieve magnificent innovations. This development centers on the improvement of scientific and technological fabrication and working procedures. That means rendering them economically more favorable, and better in quality. In this context, the development of materials with the excellent mechanical, optical and ability to inhibit bacterial growth has been of great interest in recent years due to their potential use in everyday products. In this sense, glasses and glass ceramics (GCs) are interesting alternatives due to their high chemical durability, structural possibility, forming ability, hardness and transparency. They can be used as worktops, surface of implants, touch screens, bathroom and kitchen surfaces, pharmaceutical and cosmetic bottles etc. [1–4].

Among the different glass ceramic (GC) systems, the most commercially successful is the $Li_2O–Al_2O_3–SiO_2$, Lithium-aluminosilicate (LAS) system, and the $MgO–Al_2O_3–SiO_2$, Magnesium-aluminosilicate (MAS) system. The LAS system is of particular importance from a technological viewpoint. Over the past three decades, much attention has been paid to the crystal phases and properties of this material due to their excellent thermo-physical properties [5–7]. Otherwise, MAS system was also attracted great attention owing to its good mechanical properties [8,9]. However, it still has many disadvantages, such as high cost of machining and high melting temperature, which limit its development. The addition of MgO to the LAS system, forming a $Li_2O–MgO–Al_2O_3–SiO_2$ (LMAS) system which helps to decrease the crystallization temperature and, lower the batch material cost [10], had been rarely studied [11,12]. In addition, since the nucleation and crystallization of these systems are complicated, the progress in developing these kinds of glass ceramics has been rather slow. Different nucleating agents are normally employed being TiO_2, ZrO_2, F and P_2O_5 the most frequently used to increase the crystalline phases in GC systems. It is well known that additions of P_2O_5 to certain silicate glass compositions promote volume nucleation and GC formation and markedly increases the crystal nucleation rate [13]. In addition, the presence of fluorine in the base glass (BG) enhances phase separation, reduces the crystallizing temperature, refines the microstructure and improves the physical and mechanical properties of the GCs [14,15]. The fluorine content variation has a significant influence on the crystallization kinetics as well as crystal morphology [16]. Crystallization is accomplished by subjecting appropriate glasses to a carefully regulated heat-treatment schedules resulting

in the nucleation and growth of crystal phases within the glass [17]. The variety of crystalline phases in LMAS and MAS materials leads to a wide variation in thermal and mechanical properties. Beside the latter properties, glass and glass ceramic materials are also a special class of biocide materials developed with keen interest due to the extended duration of their bactericide action. One method of developing biocide properties in these materials consists of incorporating metallic ions capable of eliminating bacteria (bactericide elements) into the glass structure. Among those metallic ions, antibacterial property of silver ions (Ag) were known since ancient times [18] and can be gained to the glasses either by doping Ag ions to the glass network (their biocidal action is then much longer lasting, since they are released progressively as the glass dissolves) or coating metal oxides to the glass surface (their effect is then limited in time, since they may be progressively washed-out) [19].

Pointing out the need for further research in the strategies to treat contamination, this work is focused on the development of an antibacterial glass ceramic that could be used for medical and kitchenware applications. This study was carried out with an effort to show that LMAS and MAS glass ceramics can be new candidate materials for biological applications besides their excellent thermo-physical, optical and mechanical properties. Through the single stage heat treatment of these materials, so as to guarantee the maximum nucleation of the base glass and to limit growth of nuclei, we expect to simultaneously obtain high transmittance for these glass ceramics. We have selected silver to obtain biocide coatings, a simple and low-cost method to obtain silver dispersed nanoparticles attached to the surface of base glass and glass ceramic. The biocide activity of the coatings was studied against Escherichia coli (Gram-negative bacteria).

The main objectives of this research are:

i. To elaborate glass ceramics in the MAS and LMAS systems by controlled crystallization

ii. To study the effect of heat-treatment on the crystallization of both systems

iii. To study the nucleation and crystallization mechanism of glass ceramics through kinetic characterization

iv. To study the effect of nucleating agents (P_2O_5 and F) on the crystallization kinetics and mechanical properties of both glass ceramics

v. To study the optical and mechanical properties of the produced MAS and LMAS glass ceramics

vi. To study the biocide activity of these glass ceramics after silver coating

vii. To compare the different properties of the base glasses (BGs) with those of the corresponding glass ceramics

The dissertation contents are divided into five sections based on the outcomes of the experimental results and discussions from this study, including an introduction section, three chapters and a conclusion section in comparison of the results obtained for both glass ceramic systems.

A brief description of each chapter is presented here.

Chapter I presents relevant literature with a focus on MAS and LMAS glass ceramic materials. The study on the kinetics of a glass by non-isothermal method was explained. In addition, the fabrication techniques (nucleation and crystal growth) and the different properties and application of glass ceramics were also reviewed.

Chapter II presents the details of the fabrication works used, encompasses preparation of base glasses and the corresponding glass ceramics. The experimental techniques used, including characterization of base glasses and glass ceramics as well as thermal, structural and microstructural measurements as determined by means of differential thermal analysis (DTA), Hot-stage microscopy (HSM), dilatometrie, X-ray diffraction (XRD), Field emission scanning electronic microscopy (FE-SEM), Raman and Fourier-Transform Infrared (FTIR) spectroscopies, are also presented here. The measurements of optical, mechanical and biological properties of base glasses and the corresponding glass ceramics of both systems were also performed.

Chapter III presents the different results obtained from the different characterization methods of LMAS and MAS base glasses and the corresponding glass ceramic and their discussion. The influence of the chemical composition, nucleating agents (P_2O_5 and F) and heat-treatments on the characteristics of the obtained glass ceramics are also reported and discussed. The obtained optical, mechanical and physical properties and their relationship with structural changes are also discussed. The crystallization kinetics of both systems are studied. Moreover, a comparison of the different properties of the base glasses with those of the corresponding glass ceramics is reported.

Chapter I:

Glass ceramic

Chaptre I: Glass ceramic

I.1 Introduction

The literature survey in this chapter presents an overview of the processing of glass ceramics. The relationships between the properties of glass ceramics and their constitutions are also covered, with particular focus on glass ceramics of $MgO–Al_2O_3–SiO_2$ (MAS) and $LiO_2–MgO–Al_2O_3–SiO_2$ (LMAS) systems. This chapter also provides a comprehensive review on the history of glass ceramic materials with the emphasis on the relationships between thermo-mechanical properties, phases and microstructure.

I.2 Historical

Glass ceramics are polycrystalline solids prepared by the controlled crystallization of glasses. Crystallization is accomplished by subjecting suitable glasses to a carefully regulated heat-treatment schedules which result in the nucleation and growth of crystal phases within the glass [6].

If the French chemist Réaumur [20] in the 18th century was the first to be interested in the crystallization of glasses in order to make porcelain, it is the American Stanley Donald Stookey [21] who accidentally discovered glass ceramic in 1953. Stookey at the time was not primarily interested in ceramics. He was preoccupied in precipitating silver particles in glass in order to achieve a permanent photographic image. He was studying as host glasses lithium silicate compositions. The story is that the young researcher at Corning Glass Works, meant to anneal a piece of glass sample (a lithium silicate) in order to precipitate silver particles (meant to form a permanent photographic image) in a furnace at 600 °C. He accidentally overheated the glass to about 900 °C due to a programming error of the furnace. Surprisingly, he observed a white material that had not changed in shape. He immediately recognized it as a ceramic, evidently produced without distortion from the original glass article. A second serendipitous event then occurred. He dropped the sample accidentally, and it sounded more like metal than glass. He then realized that the ceramic he had produced had unusual strength [22,23]. In a further research effort he found that similar results may be obtained by using special additives, so-called *nucleating agents*, instead of the photo-nucleation process [24,25].

Stookey recalled that lithium alumino-silicate crystals had been reported with very low thermal expansion characteristics. He soon found that silver or other colloidal metals are not

effective in nucleation of these alumino-silicate crystals. He, therefore, tried adding titania as a nucleating agent in alumino-silicate glasses and discovered it to be amazingly effective. Strong and thermal shock-resistant glass ceramics were then developed commercially within a year or two of this work with well-known products, such as rocket nose cones and Corning Ware cookware resulting [21]. More recently, glass ceramic processing has been greatly extended to include non-silicates and even non-oxide compositions, and to include the preparation of the precursor glasses by sol-gel technique, chemical vapor deposition, and other means of production of the base glasses are possible [26].

Numerous researchers have investigated the crystallization of glasses, and many functional glass ceramics have been developed commercially so far [27,28]. One strong motivation for the development of glass ceramics is to improve mechanical properties of base glasses, e.g., improvements of hardness and fracture toughness of glasses due to the design and control of the microstructure of glass ceramics. Another attractive motivation is to develop new optical, electrical, and magnetic active glass related materials through the crystallization of glasses. For example, various glass ceramics exhibiting second harmonic generation (SHG) and ferro-electricity have been developed so far [29–32]. Although the development of glass ceramics is complicated and time consuming, the wide spectrum of their chemical synthesis is useful for achieving different properties [23].

I.3 Definition

Glass ceramic materials are fine grained polycrystalline solid containing residual glass phase. The precursor glass is melted, quenched and shaped, then is thermally converted into a composite material with a crystalline phase dispersed within a glass matrix [33]. Glass ceramics always contain a residual glassy phase and one or more embedded crystalline phases, with widely varying crystallinity ranging from 0.5 % to 99.5 %, most frequently 30–70 %. The new crystals produced in this way grow directly in the glass phase, and at the same time slowly change the composition of the remaining glass.

The main advantages of glass ceramics are that, in principle they can be produced by any glass forming technique, their nano- or micro-structure can be designed for a given application, they have zero or very low porosity, and the desired properties can be combined, including very low thermal expansion coefficient with transparency in the visible wavelength range, for instance, for cooking ware, or very high strength and toughness with translucency, biocompatibility chemical durability, and relatively low hardness, for instance, for dental

applications [6,23,34]. For all these reasons, glass ceramics have found numerous applications, from domestic products to high-tech areas, such as large telescopic mirrors, substrates of hard disks, and bones substitutions.

I.4 Factors of design of glass ceramics

According to W. Höland and G.H. Beall [35] « Microstructure is of equal importance to composition ». In the design of glass ceramics, the two most important factors are composition and microstructure. This feature is the key to most mechanical and optical properties, and it can promote or diminish the characteristics of key crystals in glass ceramics [36]. The development of a glass ceramic generally takes place in three stages [37]:

i) choice of the composition of the base glass to obtain the desired crystalline phase;

ii) synthesis of the parent glass by a melting process (+ possible quenching) and then shaping (mold);

iii) Crystallization of the glass, the heat-treatment will be chosen according to the mechanism of crystallization engaged and the desired microstructure.

I.4.1 Composition of parent glasses

The bulk chemical composition controls the ability to form a glass and determines its degree of workability. It also determines whether internal or surface nucleation can be achieved. The choice of composition may be limited by the desired glass forming process, which requires a glass of specific stability towards devitrification, as indicated by its liquidus-viscosity relationship [6].

I.4.2 Preparation of parent glass

Glasses are made by heating together a mixture of raw materials at a sufficiently high temperature to permit the material to react with one another and to encourage the escape of gas bubbles from the melt; this latter is referred to as refining the glass. The refining stage is followed by cooling the glass to its working temperature. The simplest shaping operation available to the glass maker is that of casting. During the shaping of glass, internal stresses are produced due to the presence of temperature gradient within the glass during cooling, and these stresses must be removed by annealing or they make result in fracture of the glass. The stresses

are relaxed due to viscous flow and the glass is then cooled at a sufficiently slow rate to prevent the establishment of large temperature gradients within it.

I.4.3 Crystallization

The heat-treatment process is a critical stage in the production of a glass ceramic and must be carefully controlled to ensure that the desired types and proportions of crystals are formed. The term crystallization actually refers to a combination of two processes: *nucleation* and *crystal growth* [38]. Nucleation and crystallization can be described as the thermal and kinetic processes which allows the formation from a structurally disordered phase, a stable solid phase with a regular ordered geometry [39].

Microstructure, which includes the geometric arrangement of the crystalline phases and the distribution of the residual glass, can be made to complement or take advantage of the properties of particular phases. Complete transparency in polycrystalline silicate ceramics depends on a microstructure with particles well below the wavelength of light, and thus far this has only been achieved in highly efficiently nucleated glass ceramics [6]. Microstructure plays a key role in determining the ultimate properties of glass ceramic materials. A wide variety of microstructural configurations can result from tailoring both composition and thermal treatment. Either surface nucleation/crystallization or internal nucleation or a combination of both can be used to design a glass ceramic with the desired properties [36].

Most types of microstructures that form in glass ceramics cannot be produced in any other material. The glass phases may themselves demonstrate different structures. Furthermore, they may be arranged in the microstructure in different morphological ways. Crystal phases possess an even wider variety of characteristics. They may demonstrate special morphologies related to their particular structures, as well as considerable differences in appearance depending on their mode of growth.

I.5 The glass ceramic process

The glass may be partially devitrified, either by heat-treatment or by irradiation with a pulsed femtosecond laser [40–42], or by the joint use of a UV laser and heat-treatment [43]. The most common method, which is also the one we will use, is devitrification by heat-treatment. The glass ceramic process comprises the preparation of a homogeneous glass, the shaping of the glass to produce the required articles and, finally, the application of a controlled heat-treatment process to convert the glass into microcrystalline glass ceramic.

I.5.1 The heat-treatment process

Two processes cause a phase separation in glassy systems:

i) The nucleation / crystal growth process;

ii) The process of spinodal decomposition.

Size, dispersion state, chemical composition, and morphology (i.e., droplet type or spinodal type) of phase separated regions vary with the chemical composition of base glasses and heat-treatment conditions, and thus a deep understanding of phase separation in a given glass is required for the design and control of the crystallization of glasses [44,45].

I.5.1.1 Nucleation / crystal growth process

The scientific basis for the crystallization of undercooled liquids were established by Tamman [46], whose investigations showed the existence of two mechanisms involved in "devitrification", namely (Figure I-1): i) Nucleation of embryos, germes, and nucleus and, ii) Growth of crystals over the former particles.

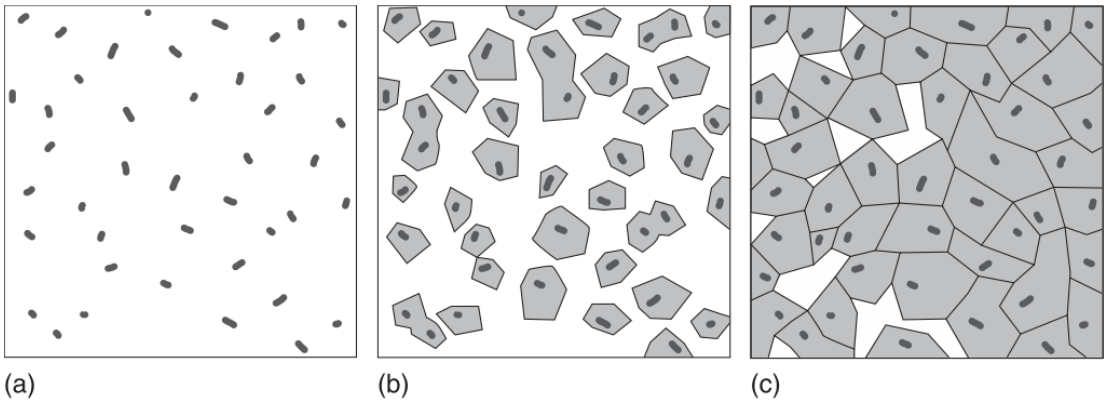

Figure I-1 *From glass to glass ceramic: (a) Nuclei formation, (b) crystal growth on nuclei, and (c) glass ceramic microstructure* [23]

However, the general theories on nucleation and crystallization in glasses were established between 1960 and 1980 due to the importance for controlling these phenomena in the production of the glass ceramic materials [17,47]. Thus, a nondesirable defect in glasses has been transformed in a powerful mechanism to obtain ceramic materials with technologically useful properties by using the glass processing and the careful stages of the nucleation and crystallization carried out from the original glass.

Nucleation generally takes place at a temperature slightly higher than the glass transition temperature (T_g), followed by crystal growth at a higher temperature depending on the composition. These two steps can take place separately or an overlap between them might occur. The crystallization process can be controlled in terms of the dependence of the nucleation and growth rates on temperature.

a) Nucleation

Nucleation is a decisive factor for controlled crystallization. If no nuclei are present, crystal growth cannot occur and the material will form a glass. Even if some nuclei are present, but no growth has occurred, the extremely small size and low volume fraction of the nuclei prevents their detection, so that the solid is, for all practical purposes, still a glass [38]. However, crystallization can be understood simply by using Classical Nucleation Theory (CNT) which allows a physical approach to understand easily the main processes. Gibbs published in 1876 a seminal paper on the thermodynamic description of equilibrium between phases [48]. The kinetics aspect of the transformations was still very poorly understood until Arrhenius formulated the notion of activation energy in 1889. Further, CNT was developed by Volmer and Weber [49] in 1926, then modified in 1935 by Becker and Döring [50] whose gave the theory the current form. The CNT theory is based on two hypotheses [37]:

i) It is considered that a nucleus, regardless of its size, can be considered with the macroscopic entity. This means the same properties (including thermodynamic), the same structure, the same composition and the same density;

ii) The nuclei formed are of spherical shape with a radius r and, a flat-type interface, to minimize the surface energy.

The nucleation of crystalline phases in glasses can take place following two types of mechanisms, namely [39,51]:

i) Homogeneous nucleation, when the nuclei are originated from their own melt composition, generally having the same chemical composition as the precipitated crystalline phase.

ii) Heterogeneous nucleation, when the crystals are nucleated over particles or interfaces foreign to the melt, such as impurities or interfaces (melt-air, melt-crucible walls, etc.

Homogeneous nucleation corresponds to the transformation of a nuclei from a metastable state (glass) to a more stable state (crystal), favored by the lower volume free energy of the crystal state compared to that of the liquid state (Figure I-2a). However, heterogeneous nucleation leads to a reduction in the surface energy (Figure I-2b). The model for heterogeneous nucleation is an adaptation of the CNT through two types of changes. The first amendment is geometrical: nuclei that grow on substrate have no longer the form of complete spheres but are treated as spherical caps. A complete wet surface by the supercooled liquid promotes nucleation.

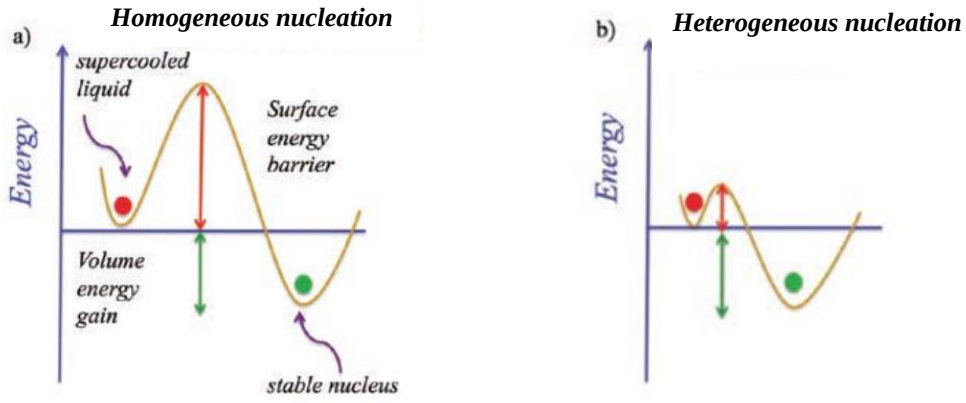

Figure I-2 *Energy diagram comparing: a) the homogeneous nucleation and b) the heterogeneous nucleation which is favored by a low surface energy barrier* [37]

According to CNT theory, the rate of homogeneous steady state crystal nucleation (*I*) in a one-component supercooled liquid is related to absolute temperature *T* by the well-known expression:

$$I = A \exp[-W^* + \Delta G_D/kT] \quad \text{(I.1)}$$

where *W** and ΔG_D are the thermodynamic and kinetic free energy barriers to nucleation respectively and *k* the Boltzmann constant. The pre-exponential factor *A* may be expressed as

$$A = 2n_v V^{1/3}(kT/h)(\sigma/kT)^{1/2} \quad \text{(I.2)}$$

where n_v is the number of atoms of the crystallizing component phase per unit volume of the liquid, *V* the volume per formula unit, σ the crystal-liquid interfacial free energy per unit area and *h* Planck's constant.

The thermodynamic barrier *W** required for a spherical nucleus with critical radius r^* to cross the energy barrier is given by:

$$W^* = 16\pi\sigma^3 V_m^2 / 3\Delta G^2 \quad \text{(I.3)}$$

$$r^* = -2\sigma V_m / \Delta G \quad \text{(I.4)}$$

where ΔG is the bulk free energy change per mole in crystallization, V_m the molar volume of the crystal phase and r^* is the minimum size that a nucleus must reach to be stable and able to grow to give a crystal.

On the other hand, heterogeneous nucleation is due to the fact that the driving force for forming the nuclei starting from the nucleation sites is higher than that of the parent glass. This introduces the term of contact angle θ between the substrate (or catalyst) and the melt. Therefore, the wettability is defined by the contact angle θ between the nucleus and the surface for heterogeneous nucleation ($\theta = 0$ for a perfect contact; $\theta = \pi$ for contact reduced to a point with the flat substrate) [52]. For low contact angle, surface energy will be lower and the nucleation rate will therefore be greater (Figure I-3) [37]. For heterogeneous nucleation:

i) The heterogeneous nucleation rate is always smaller than the homogeneous nucleation rate;

ii) The same critical radius r^* exists for both homogeneous and heterogeneous nucleation processes;

iii) The contact angle (θ) plays a major role in the determination of heterogeneous nucleation rate.

The CNT theory exhibits limitations due to disagreements between its predictions and real experimental data for certain systems. However, up to date, there is still no comprehensive theory for describing the whole crystallization process.

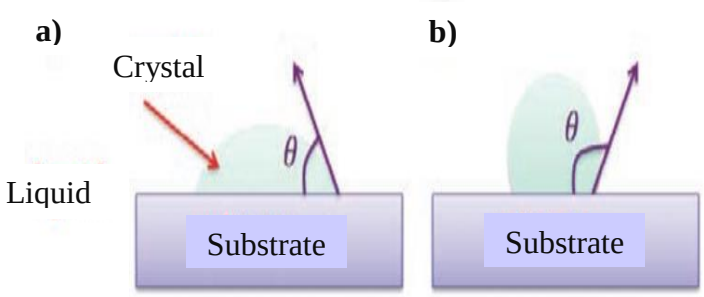

Figure I-3 *Growth of a nucleus (crystal) on a surface favoring heterogeneous nucleation (substrate): a) low values of θ promote nucleation and b) large values of θ limit nucleation*

b) Nucleating agents

Some glass compositions are self-nucleating, but, more commonly, certain components known as nucleating agents are added to the batch to promote phase separation and internal nucleation. The nucleating agents melt homogeneously into the glass but promote very fine scale phase separation on reheating [28]. The addition of nucleating agents facilitates heterogeneous nucleation. These agents are introduced in the melts in small quantities, creating discontinuities in the glassy lattice. Stookey developed a wide range of glass compositions which contained titanium dioxide as the nucleating agent. The use of metallic phosphates to promote the controlled crystallization of glasses was discovered by McMillan and co-workers in Great Britain [17]. Nucleating agents can be classified as shown in Table I-1.

The addition of metallic (Au, Ag, Pt, Pd, etc. in ionic form) or non-metallic nucleating agents (TiO_2, ZrO_2, P_2O_5, Ta_2O_5, WO_3, fluorides, etc.) can favor a volume crystallization process [53,54] with a large nucleation rate. In this case, a controlled crystalline growth will make it possible to obtain numerous crystals with a limited size leading to diverse optical and mechanical applications. The amounts of nucleating agents required are variable from one system to another. They are typically of the order of 2.0 to 8.0 mol% in the case of oxides and less than 1 mol% in the case of colloids. These additions make it possible to obtain a high nucleation rate (up to more than 10^6 μm^{-3}) which, coupled with controlled crystal growth, may lead to improved or innovative optical and mechanical properties [37].

Table I-1 *Classification of nucleating agents* [39]

Metallic colloids	- Colloids formed into the glass: Cu - Introduced colloids: Pt, Ag
Oxides	- By valence changes: TiO_2, MoO_3, V_2O_5 - By charge decompensation in the glassy lattice: P_2O_5
halides	F^-
Glass in glass phase separation	

c) Crystal growth

Nucleation is followed by one or more high temperature treatments to promote crystallization of the primary phase or phases and development of the desired microstructure. The growth process continues until neighboring crystals impinge, creating a highly crystalline body with a small amount of residual glass, or until the residual glass is depleted in the crystal forming components. Certain glass ceramics are specifically designed to possess a microstructure of uniformly dispersed, nonimpinging crystals in a matrix of continuous residual glass [28]. Nucleation and crystal growth depend on temperature and can display a greater or lesser overlap in temperature.

d) Two-step crystallization process

This method is applied when the curves of nucleation and growth rates, as a function of temperature, have a limited overlap (as shown in Figure I-4). The crystallization heat-treatment comprises two steps:

- The first corresponds to the nucleation step and is carried out around T_N, corresponding to the maximum nucleation rate (generally T_N is slightly greater than T_g), where T_N is the nucleating temperature and, T_g is the glass transition temperature.
- The second consists of a phase of crystalline growth and is carried out at a higher temperature, around T_C, which corresponds to the maximum of the crystalline growth rate, where T_C is the crystallization temperature.

This two-step process is preferred when strong crystallization is desired (large and large crystals) [29].

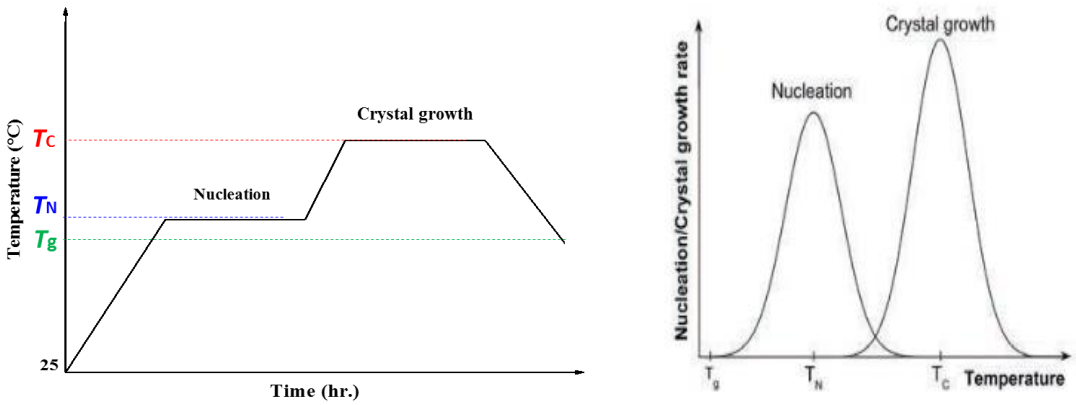

Figure I-4 *Glass crystallization process in two-steps: (left) heat-treatment cycle, and (right) nucleation and crystal growth rate in dependence on temperature*

e) Single-step heat-treatment

The one-step crystallization process is a simplification of the previous two-step process. If it is desired to generate a maximum of nano-crystals, the crystalline growth step is then strongly restricted, or even deleted. It is particularly adapted when the curves of nucleation and growth rates as a function of temperature have a large overlap (as shown in Figure I-5). In this case, the nucleation and the growth are carried out at one and the same temperature step. This T_{NC} temperature corresponds to the optimal nucleation / crystal growth rate).

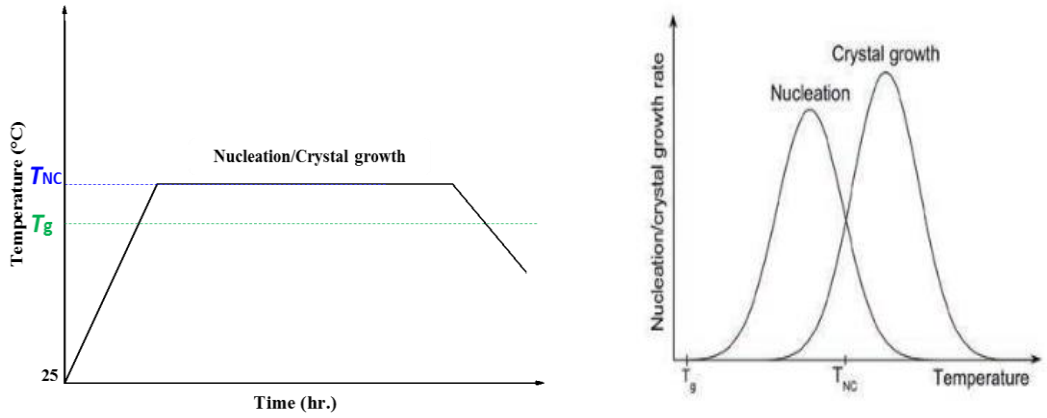

Figure I-5 *Glass crystallization process in one-step: (left) heat-treatment cycle, and (right) nucleation and crystal growth rate in dependence on temperature*

I.5.1.2 Spinodal decomposition:

The morphology developed by spinodal decomposition will be quite different from that due to nucleation and growth. The spinodal decomposition produces a composite material with a second phase separated as a highly connected sponge structure in contrast with the classical nucleated glass in which are embedded small spherical crystallites. The most important parameter affecting the morphology of phase separation is the composition of the liquid. Both phases will gradually and continually change in composition until they reach the compositions of the equilibrium liquids. Most importantly, both phases will have a high degree of connectivity, so that continuous pathways through the material exist for each phase [38,55,56]. The crystallized portion generally represents more than 70% of the total volume of the material. The resulting microstructure consists of a uniform dispersion of small interconnected coherent particles as in a spongy structure [56], the region beneath the spinodal boundary is sometimes referred to as the interconnected region [38].

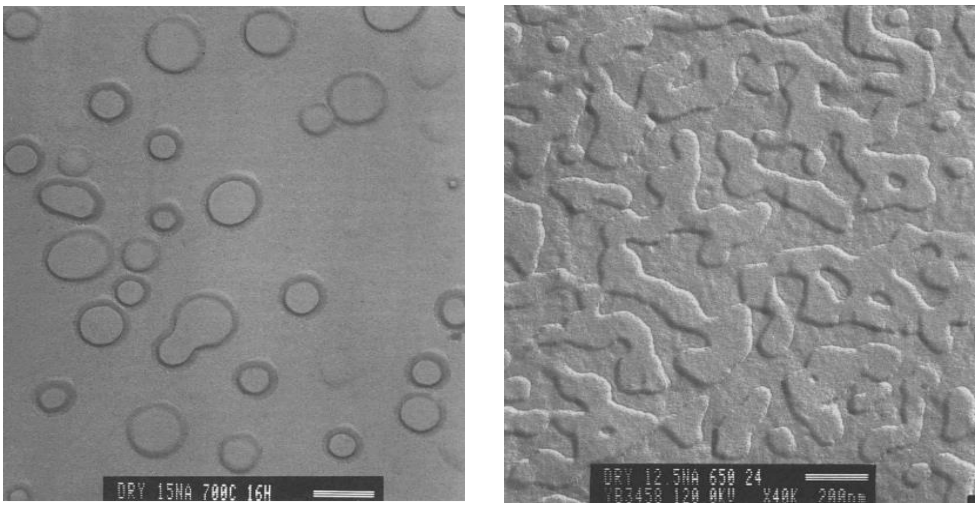

Figure I-6 *Representation of the morphology of a glass ceramic resulting from: (left) nucleation/growth process or (right) spinodal decomposition* [38]

The two processes of devitrification of glass are distinct and lead to glass ceramic of different morphology, which is illustrated in Figure I.6. Similarly, the choice of a suitable nominal composition [9,28] or modified by the addition of a demixing initiator (fluoride, phosphate, etc. [6,57–59]) can generate a bimodal phase separation with the presence of nodules. This demixing can be of nucleation/growth type (demixing in the form of spheres) or of spinodal type (entanglement of domains). During crystallization, the size of the crystals will then be at most equal to the size of the demixed zones. The size of the nodules being dependent on the composition of the glass and the conditions of synthesis, there again the morphology and the size of the crystals are controllable. During crystallization, the size of the crystals will then be at most equal to the size of the demixed zones. The size of the domains being dependent on the composition of the glass and the conditions of synthesis.

I.6 Transformation kinetics

The kinetics of crystal nucleation and growth are of crucial importance in determining the glass forming abilities (GFA) of melts. They also determine the glass forming systems which are suitable to be converted into glass ceramics by controlled heat-treatment.

I.6.1 Structural relaxation

Structural relaxation is a general phenomenon occurring when a glass is maintained at a temperature below its glass transition temperature (T_g). The fragility index (F_I) was firstly proposed by Angell [60] in order to characterize the structural relaxation. Glass forming liquids that exhibit an approximately Arrhenius temperature dependence of the viscosity are defined as

strong-glass formers and those, which exhibit a non-Arrhenius behavior are declared fragile-glass former [61]. The index, F_I, is considered a kinetic property since it is related to the variation of the glass viscosity near T_g so the determination of F_I must be ideally performed through viscosity measurements. Nevertheless, these type of measurements are in general extremely difficult when the inorganic glasses present strong crystallization tendencies or high melting temperatures [62]. An elegant approach to overcome this issue is the employment of indirect methods based in differential thermal analyses [63–65]. Among these methods, probably the most used one is the Kissinger method that can be expressed as in equation [64]:

$$ln\left(\frac{T_g^2}{v}\right) = \frac{E_g}{RT_g} + Constant \quad \text{(I.5)}$$

where E_g is the activation energy of glass transition which takes into account the molecular motion and rearrangement of atoms around T_g.

The F_I index calculated from the DTA measurements ($F_{I\text{-}DTA}$) can be expressed as a function of both E_g and T_g according to [66,67]:

$$F_{I-DTA} = \frac{E_g}{R\,T_g\,ln10} \quad \text{(I.6)}$$

The reported values of F_I varies widely within the range comprised between F_I = 14.97 for *strong glasses* and F_I = 200 for *fragile glasses* [68]. Nevertheless, the use of equation (I.5) together with the DTA data instead of using the viscosity measurements could lead in some errors in the determination of the correct F_I values. However, Zheng *et al.* [69] demonstrated that the differences between the T_g values as obtained by either one or the other technique are completely equivalents just by taking into account that the T_g data obtained by DTA can be used if the following equation is employed:

$$F_{I-vis} = 1.289\,(F_{I-DTA} - F_{I-0}) + F_{I-0} \quad \text{(I.7)}$$

where $F_{I\text{-}vis}$ is the correct fragility ($F_I = F_{I\text{-}vis}$) determined from viscosity measurements and $F_{I\text{-}0}$ is the reference fragility corresponding to a pefect strong glass which exhibits an Arrhenius behaviour ($F_{I\text{-}0}$ =14.97).

I.6.2 Glass Forming Ability and Glass Stability

Glass formation requires prevention of formation of the equilibrium crystalline phase when the melt is cooled below the freezing temperature. This involves either complete suppression of the formation of the crystal nuclei or suppression of growth of the tiny crystalline phase that has formed. The ability of a melt to form a glassy phase on solidification has been termed the glass-forming ability (GFA). GFA, as related to the ease of devitrification, is very crucial for understanding the underlying mechanism of amorphization. A very large number of parameters have been proposed to explain the formation and thermal stability of glasses, since the first attempt by Turnbull [70] in 1969, to reflect the relative GFA among bulk metallic glasses. It indicates the urgent need of a reliable parameter to estimate the GFA.

The continued efforts in this direction, in the recent past, has led to an agreement that a good GFA criterion should consider the two major aspect of glass formation, namely the stability of the liquid phase and its resistance to crystallization. The stability of liquid, which is in turn related mainly to the short-range chemical and structural ordering of atoms in the molten state and the thermodynamic stability of the liquid, may be measured at two conditions: equilibrium state and metastable state. The other aspect, the resistance to crystallization, as namely glass stability (GS), is primarily determined by the relative thermodynamic and kinetic stability (determined by nucleation and growth of crystalline phase) of the solid amorphous phase as compared to crystalline phases [60]. This indicates that if a supercooled liquid phase can be stabilized and precipitation of the competing crystalline phases is suppressed, the possibility of formation of glass is increased. Therefore, both of these aspects of amorphization need to be taken into account as far as the GFA is concerned [71,72]. A list of various GFA and GS criteria, based on characteristic temperatures include liquidus temperature (T_l), glass transition temperature (T_g), the onset of crystallization temperature (T_o), the crystallization temperature (T_p) and the melting temperature (T_m), has been given in Table I.2.

It was concluded that a single parameter cannot satisfactorily explain the GFA of a system. Different parameters were able to give a strong correlation for different systems. All of these parameters should be giving similar results, but they do not. The majority of the parameters have relevance and validity only in some cases [73]. So, the GFA parameters, usually measured with a differential thermal analysis (DTA) or a differential scanning calorimetry (DSC), still remain room for further investigations.

Table I-2 *Summary of the quantitative criteria proposed to evaluate the GFA and the GS*

Parameter	***Equation***	***Reference***	***Numbering***
Reduced glass transition temperature	$T_{rg} = T_g/T_m$	[70]	(I.8)
Supercooled liquid region	$\Delta T_{og} = T_o - T_g$	[74]	(I.9)
α	$\alpha = \frac{T_o}{T_l} = \frac{\Delta T_{og}}{T_l} + \frac{T_g}{T_l}$	[75]	(I.10)
β_2	$\beta_2 = \frac{T_o T_g}{(T_l - T_o)^2}$	[76]	(I.11)
γ	$\gamma = \frac{T_o}{T_g + T_l}$	[77]	(I.12)
γ_m	$\gamma_m = \frac{2T_o - T_g}{T_l}$	[78]	(I.13)
ω_2	$w_2 = \frac{T_g}{2T_o - T_g} - \frac{T_g}{T_l}$	[79]	(I.14)
β	$\beta = \frac{T_o}{T_g} + \frac{T_g}{T_l}$	[75]	(I.15)
δ	$\delta = \frac{T_o}{T_l - T_g}$	[80]	(I.16)
ξ	$\xi = \frac{\Delta T_{og}}{T_o} + \frac{T_g}{T_l}$	[81]	(I.17)
φ	$\varphi = T_{rg}(\frac{\Delta T_{og}}{T_g})^{0.143}$	[82]	(I.18)
Hrubÿ parameter	$K_H = \frac{T_o - T_g}{T_m - T_o}$	[83]	(I.19)
S	$S = \frac{(T_p - T_o)(T_o - T_g)}{T_g}$	[84]	(I.20)

I.6.3 Crystallization Kinetic and Mechanisms

Crystallization kinetic parameters, providing the crystallization mechanism of a glass [85], include the activation energy of crystallization E_c, the crystal growth index n (the Avrami exponent) and the morphology index m (which depends on the dimensionality of the crystal growth). The activation energy E_c reflects the sensitivity of a glass to temperature variation and thus affects the controllability of a crystallization process, and the n and m reflect the crystallization mechanism.

The standard theory of transformation kinetics via nucleation and crystal growth is developed by Johnson and Mehl and Avrami and Kolmogorov [86–88]. Therefore, this theory is called the JMAK theory. JMAK transformation kinetics describes the extent to which a material is transformed during a certain phase transformation, as a function of temperature and time. The JMAK equation is universal and applicable to glass ceramics [37].

$$x = 1 - exp(-(At)^n) \tag{I.21}$$

with

$$A = A_0\, exp(-\frac{E_c}{RT_p}) \tag{I.22}$$

Where x is the volume fraction crystallized, n depends on both the growth mechanism and the dimensionality of the crystal, A is the Arrhenian pre-exponential factor depending on the temperature, t is the time, A_0 is the frequency factor, R is the gas constant and, T_p is the crystallization temperature.

The different kinetic analyses are based on non-isothermal experiments such as those carried out by DTA. The Kissinger [64,89] equation is widely applied to calculate the crystallization activation energy E_{ck} which can be obtained from the heating rate dependence of the crystallization peak temperature according to the equation:

$$ln\left(\frac{v}{T_p^2}\right) = \frac{-E_{ck}}{R\,T_p} + constant \tag{I.23}$$

where v is the DTA heating rate.

In a similar manner, Ozawa [90,91] proposed a modified form of the Kissinger's equation. According to Ozawa model, the change of $\ln(1/T_p^2)$ with v is negligibly small compared to the change of $\ln(v)$ and therefore, the Kissinger's equation must be written as:

$$ln(v) = -1.0516\ \frac{E_{co}}{RT_p} + constant \quad \text{(I.24)}$$

where E_{co} is the activation energy for crystallization from the Ozawa method.

Another method that may be used for determining the activation energy and crystallization parameters, is that of Augis and Bennett [92,93]. They have proposed the following equation:

$$ln\left(\frac{v}{T_p - T_o}\right) = \frac{-E_{cab}}{R.T_p} + constant \quad \text{(I.25)}$$

where E_{cab} is the activation energy for crystallization from the Augis and Bennett method and, T_o is the onset temperature. The differences between T_p and T_o are taken into account [94].

When the E_{cab} is known, the Augis and Bennett method also leads to the determination of the Avrami parameter *n*:

$$n = \frac{2.5\ R\ T_p^2}{\Delta w\ E_{cab}} \quad \text{(I.26)}$$

where Δw is the full-width of the exothermic peak (Pk) at half-maximum intensity. As evident in equation (I.26), higher Δw values result in smaller *n* values, and *vice versa.*

Matusita and Sakka [95] have stated that equation (I.23) is valid only if crystal growth occurs on a fixed number of nuclei and have suggested a modified form of the Kissinger equation as:

$$ln\left(\frac{v^n}{T_p^2}\right) = -m\frac{E_{cms}}{R.T_p} + constant \quad \text{(I.27)}$$

where E_{cms} is the activation energy for crystallization from the Matusita–Sakka method. As it can be observed, this equation takes into consideration the two parameters, *n* and *m* that characterize the crystallization growth mechanism and the activation energy.

Furthermore, Xu *et al.* [96] have demonstrated that for most oxide-glass systems that E_c and E_{ck} are related by the equation:

$$E_c = \frac{n}{m}\ E_{ck} \quad \text{(I.28)}$$

Table I-3 *Determination of the activation energies for crystallization: values for numerical parameters n and m; after Matusita et al.* [95,97,98]

Crystallization mechanism	***n***	***m***
Bulk crystallization with a constant number of nuclei (i.e. the number of nuclei is independent of the heating rate)		
Three-dimensional growth of crystals	3	3
Two-dimensional growth of crystals	2	2
One-dimensional growth of crystals	1	1
Bulk crystallization with an increasing number of nuclei (i.e. the number nuclei is inversely proportional to the heating rate)		
Three-dimensional growth of crystals	4	3
Two-dimensional growth of crystals	3	2
One-dimensional growth of crystals	2	1
Surface crystallization	1	1

For $m = n$, when crystallization occurs on a fixed number of nuclei, $E_{ck} = E_c$. Thus, for crystal growth that occurs on a fixed number of nuclei, the analysis of DTA data by the Kissinger model, equation (I.23) yields the correct value of E_c. When the number of nuclei changes during the DTA measurements, we have the option to use equation (I.21) or we can determine E_{ck} from equation (I.23) and then multiply this term by n/m to obtain the correct activation energy. The parameter m is related to n through the crystallization mechanism process and, can take on various values as summarized in Table I.3.

I.7 Glass compositions for glass ceramic production

Depending upon chemical composition, a large number of glasses with different chemical and physical properties can be prepared. The purpose of this section is to discuss practical examples of glass ceramics derived from LMAS and MAS systems.

I.7.1 Glass ceramics derived from the $MgO–Al_2O_3–SiO_2$ system

Magnesium aluminum silicate glass ceramic belongs to technologically important materials. They are known for their excellent microwave properties [99,100], good mechanical properties [101–105], e.g., Young's moduli [101], hardness [101,102,106] mechanical strengths [102,107] and good thermal properties like thermal shock resistance, thermal stability [108] and lower thermal expansion coefficient [105]. It has high transparency [109,110] and good chemical stability [111]. Hence, glass ceramics in this system offer a large variety of novel fields of application, e.g. for electronic packaging devices [103,112], as millimeter-wave dielectrics [113,114] or as hard disk substrates [115], for armor application [116]. It is used in the production of proto-type components, used in medicines for the axles of mechanisms providing energy for implanted cardio-stimulators and are also used in the production of welding jets or as holders for welded components [117,118]. MAS glasses seem to be a very promising laser host material with respect to high power applications [119].

The distinctive properties of glass ceramic systems arise from the formation of a major crystalline phase, tailored by the choice of the composition of the base glass as well as by the crystallization procedure [120]. This gives the material designer many options to meet the requirements of a product idea. The preparation of these materials is of special importance. The development of MAS glass ceramics has been carried out by following two approaches: sintering route [121], and glass route [122]. In the first approach, controlled crystallization is carried out on a pre-shaped compacted sample through surface nucleation. On the other hand, in glass route we first prepare glassy material in desired shapes and sizes and then carry out the controlled crystallization by following special heating schedule through a process of bulk nucleation.

The effects of chemical composition, especially the addition of nucleating agents, such as TiO_2, ZrO_2, CeO_2, La_2O_3, Y_2O_3, P_2O_5 and the alkali oxides on the structure and properties of glass ceramics, have been widely investigated by many researchers [103,109,123–127]. In many glass ceramics system, more than one kind of nucleating agents are used to obtain optimum microstructure and properties. As to MAS glass ceramics, the most important nucleating agents are TiO_2 [125] and ZrO_2 [126,127], or a combination of both [128].

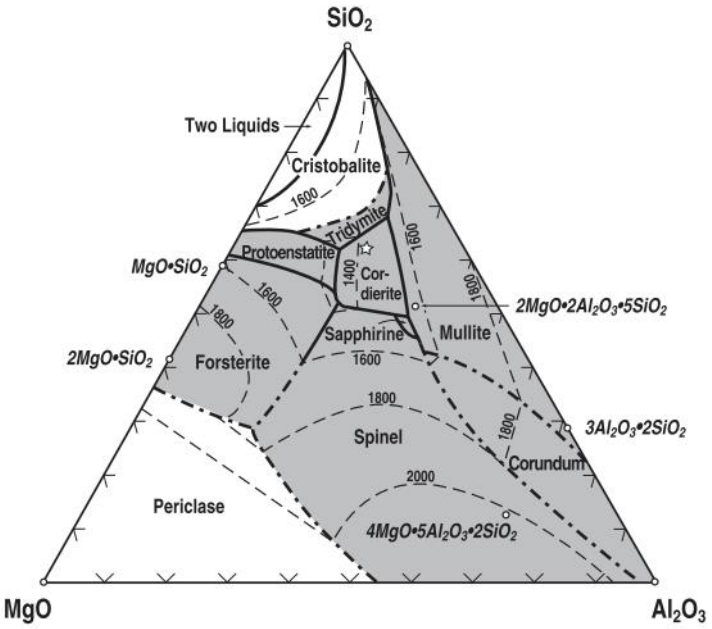

Figure I-7 *SiO_2–Al_2O_3–MgO phase diagram indicating the parent glass composition of Corning cordierite glass ceramic* [23]

The ternary phase diagram in Figure I-7 shows the composition of the three basic components, SiO_2, Al_2O_3, and MgO of the bulk glass. During the crystallization process, crystal phases such as cordierite ($2MgO–2Al_2O_3–5SiO_2$), cristobalite (SiO_2), forsterite ($2MgO–SiO_2$), mullite ($3Al_2O_3–2SiO_2$), spinel ($MgO–Al_2O_3$), and enstatite ($MgO–SiO_2$) can be produced in some materials [129], and which depend on the percentage of MgO or Al_2O_3 during the preparation of those glass ceramics. A small amount of residual glass matrix lies between the crystal phases.

The precipitation of crystal phases depend on the cooling regime and the initial composition of the base glass. In addition, due to the high concentrations of SiO_2 and Al_2O_3, the MAS glasses present high melting temperatures and viscosities, which make them difficult to prepare [110,130]. Some fluxes, like alkali oxides, have been introduced to reduce the melting temperature. At the same time, it also brought some unexpected effects, such as loss of transparency and large thermal expansion coefficient. However, a high content of MgO lowers the temperature of crystallization [131]. Moreover, crystal growth was markedly affected by small changes in composition and, as a consequence the mechanical properties of the material were also affected.

Glass ceramics with a primary crystal phase of cordierite, $Mg_2Al_4Si_5O_{18}$, are of great commercial importance. The first glass ceramics of this type were developed at the Corning

Glass Works [6,21]. Subsequently, further glass ceramics of this basic type were developed. Cordierite glass ceramics are distinguished for their special properties such as high mechanical strength, low dielectric constant, low thermal expansion coefficient, good thermal stability, and thermal shock resistance [132]. However, enstatite is found in three structural polymorphs: orthorhombic forms protoenstatite and orthoenstatite, and the monoclinic form clinoenstatite. G. H. Beall [133] successfully developed glass ceramics featuring an enstatite $MgSiO_3$, primary crystal phase in the ternary SiO_2–Al_2O_3–MgO system with small amounts of Al_2O_3. This crystal phase demonstrated very interesting properties during the cooling of the glass ceramics, such as high flexural strength and high fracture toughness. Moreover, nanocrystalline and transparent glass ceramics with the orthosilicate forsterite (Mg_2SiO_4) as the major crystalline phase were developed by [134]. More particularly, the glass ceramic have a small crystal size to make the glass ceramic material optically transparent and were doped with chrome (Cr). In order to achieve a fine grained glass ceramic based on forsterite, it was deemed necessary to produce a glass displaying amorphous phase separation where one of the phases is highly enriched in MgO. In addition, MAS glass ceramics containing spinel and quartz solid solution, have good mechanical properties, high transparency and good chemical stability [110,111,135].

I.7.2 Glass ceramics derived from the Li_2O–MgO–Al_2O_3–SiO_2 system

Ternary Li_2O–Al_2O_3–SiO_2 system is widely applied in glass ceramic production due to their low coefficient of thermal expansion (CTE), good dielectric properties, excellent thermal shock resistance and high transparency [7,136,137]. MAS system was also attracted great attention owing to its good mechanical properties. However, it still has many disadvantages, such as high cost and high melting temperature, which limit its development. However, during last years, more complex systems like Li_2O–MgO–Al_2O_3–SiO_2 and CaO–MgO–Al_2O_3–SiO_2 (CMAS) are gaining scientific and technological interest. In contrast with it, LMAS system has a relatively low expansion coefficient, lower melting temperature and lower material cost due to the Mg^{2+} doping [9,138]. Different oxides like Na_2O, K_2O, CaO, B_2O_3 and ZnO can form part of the LMAS system thus rendering different properties.

At the same time, different nucleating agents are normally employed being TiO_2, ZrO_2, F and P_2O_5 the most frequently used to increase the crystalline phases in this LMAS and other glass ceramic systems. The crystallization of some glasses in LMAS system has been studied as a function of the thermal treatment temperature without and with TiO_2 additions used as nucleating agent. Prior to crystallization there exists a wide development of phase separation.

The main crystalline phases precipitated in LMAS glasses were β-spodumene and μ-cordierite [39]. Shennawai *et al.* [139] have studied the effect of nucleating agent like TiO_2 and ZrO_2 on the nature of the crystalline phases developed in LMAS glass matrix. TiO_2 and ZrO_2 were found to decrease the expansion coefficient of the investigated glasses. However, the use of a mixture of the TiO_2, ZrO_2 and F nucleating agents in the same glass ceramic has demonstrated to present a synergistic effect on the crystallization mechanism of spodumene-willemite-diopside glasses [140]. In the work of El-Shennawi *et al.* [141], the crystallization behaviour of some LMAS glasses with and without the nucleation catalysts TiO_2 and ZrO_2 was investigated. The study indicated that the parent glass composition, nucleating agents used, and the crystallization parameters, determine the crystalline phase constitution and microstructures of the resultant materials; leading in some cases to ultra-fine glass ceramic microstructures. In addition, doping B_2O_3 or P_2O_5 in the LMAS system can promote phase separation and crystallization of glasses. With the B_2O_3 or P_2O_5 addition, the size of spherical phase separation droplet increased and the crystallization temperature of LMAS glass ceramics decreased [142]. The mainly crystalline phase were β-quartz solid solution (s.s) ($Li_2Al_2Si_3O_{10}$), lithium silicate (Li_2SiO_3) and forsterite (Mg_2SiO_4). Besides, adding B_2O_3 or P_2O_5 in LMAS system increased the thermal expansion coefficient.

Recently, LMAS glass ceramics was used as the interlayer to join SiC coated carbon/carbon (C/C) composites and LAS glass ceramics [143,144]. Carbon/carbon (C/C) composites are applied successfully in aeronautic and astronautic fields as the ideal high temperature structure materials for their excellent mechanical properties at high temperature. Joining of these two materials is a possible way to benefit from the functional features given by LAS glass ceramics as well as the favorable mechanical properties given by C/C composites [145]. Results show that both the Mg content and microhardness decreased gradually from the SiC side to the LAS glass ceramics side in the gradient LMAS interlayer. The thermal expansion coefficient of LMAS glass ceramics increased with the increase of Mg content. The gradient LMAS interlayer could effectively improve the distribution of process-induced thermal stress in the joint, relieve the mismatch of CTE between SiC transition layer and LAS glass ceramics and increase the bonding strength of the joint [145].

Due to the complexity in the study of the crystallization mechanisms attributed to the use of these complex nucleating agents in the LMAS system, they have been rarely studied and in

the few reports found in the literature, such agents are used in very low concentrations [146,147].

I.8 Properties and applications

Glass ceramics have been shown to feature favorable thermal, chemical, biological, and dielectric properties, generally superior to metals and organic polymers in these areas. Moreover, glass ceramics also demonstrate considerable advantages over inorganic materials, such as glasses and ceramics. This wide range of applications reflects the variety of properties that can be obtained with glass ceramics playing on the composition of the base glass, the nature of the crystallizing phases and the material microstructure. Glass ceramic products display generally a combination of several specific properties difficult to obtain with a glass or a ceramic. Such properties are, for example, a high thermal resistance associated to a zero thermal expansion (case of glass ceramic cooktops) or a good mechanical strength associated with translucency (case of the glass ceramics used for dental restoration).

I.8.1 Thermal Properties

A particular advantage in the production of glass ceramics is that products demonstrating almost zero shrinkage can be produced. These specific materials are produced on a large scale for industrial, technological, and domestic applications (e.g., kitchenware).

Materials with a wide range of thermal expansion coefficient can be obtained (-4 to 12×10^{-6} K^{-1}). In particular, it is possible to obtain materials with zero or negative expansion. This is the case when crystalline phases with negative thermal expansion are precipitated. The thermal expansion of the material is the weighted average of the expansion of the different crystalline phases and of the residual glass [148]. Stookey developed the first strong and thermal shock resistant white alumino-silicate glass ceramic called Pyroceram (Corning Glass Works, USA). This material was the first to be marketed for use as household crockery; it was also called Corning Ware cookware in 1959 [23,34]. Its zero thermal expansion coefficient made this material interesting for other applications, too. Whether subjected to different high temperatures over various lengths of time or rapid and repeated switching on and off of the cooking temperature, the shape and size of the cooking surface remain unchanged.

I.8.2 Optical Properties

Since glass ceramics are non-porous and usually contain a glass phase, they demonstrate a high level of translucency and in some cases even high transparency. Furthermore, it is also possible to produce very opaque glass ceramics, depending on the type of crystal and the microstructure of the material. Glass ceramics can be produced in virtually every color. Fluorescence, both visible and infrared, and opalescence in glass ceramics are also important optical characteristics.

Numerous studies have been devoted to the development of glass ceramics for optics and even photonics. These materials have applications in the fields of communications and solar energy. Highly transparent glass ceramics are distinguished from parent glass by better mechanical performance and in active optics, particularly due to the segregation of optical dopants in crystallites [149,150]. The preservation of the transparency in the visible range during crystallization conventionally requires a homogeneous distribution of nanometric crystals (much smaller than the incident light wavelength, typically < 50 nm) within the glass ceramic or the refractive index of the crystals has to be equal to that of the residual glass. It then requires a strong nucleation in volume uniformly distributed in the material followed by a limited crystal growth. These transparent materials can present a high crystalline fraction (exceeding, for example, more than 80% in volume). This requires the precipitation of a very large number of nuclei [151,152].

I.8.3 Biological Properties

Among the applications in the development of glasses and glass ceramics in biology, the production of biocidal materials, that is to say able of limiting the proliferation of viruses, bacteria and fungi on their surface, or even of eliminating them, will be maintained. Classically, glasses can be used as carriers for nanoparticles with well-known bactericidal properties, such as copper or silver nanoparticles [153]. These nanoparticles are either supported on the surface of the glass (their effect is then limited in time, since they may be progressively washed-out), or included inside hydro-soluble glass [19,154] (their biocidal action is then much longer lasting, since they are released progressively as the glass). Porous glass ceramics in the $Li_{1+x}Al_xTi_{2-x}(PO_4)_3$ system with a silver concentration gradient (crystalline phase $AgTi_2(PO_4)_3$ on the surface, and $LiTi_2(PO_4)_3$:Al in volume) have been also prepared, and show interesting bacteriostatic properties [155]. These glass ceramics, either intrinsically biocidal or carriers of

biocidal nanoparticles, may be used as particles, coatings on the surfaces to be treated (surface of implants, or also glazes on tiles in hospitals, etc). Their potential applications are numerous. But, apart from a few exceptions [156], the properties of glass ceramics potentially arising from these systems remain mostly unexplored, which opens a potentially wide field of studies.

I.8.4 Mechanical Properties

Glass ceramics can be produced as machinable materials represents an additional advantage [157,158]. In other words, by first processing the glass melt, a primary shape is given to the material. Next, the glass ceramic is provided with a relatively simple final shape by drilling, milling, grinding, or sawing. Furthermore, the surface characteristics of glass ceramics, for example, roughness, polishability, luster, or abrasion behavior, can also be controlled. In addition, its toughness and hardness are superior to those of glass, because crack propagation, which is very fast in a fragile material such as glass, will be stopped or deflected by crystallites [159].

Depending on the microstructure of the material, very variable mechanical properties can be observed. Glass ceramics therefore have better mechanical properties than glasses. Examples of their applications include:

- Glass ceramics based on canasite (a chain silicate of formula $K_2Na_4Ca_5Si_{12}O_{30}F_4$) or lithium disilicate ($Li_2Si_2O_5$) have a microstructure consisting of an entanglement of needle-like crystals which leads to exceptional tensile strengths and tenacity [23,133,159].
- Glass ceramics of $Ca_5(PO_4)3F$ from SiO_2–Al_2O_3–P_2O_5–CaO–CaF_2 system and which are used as bone prostheses and for dental reconstructions, have been studied for their biocompatibility and good mechanical properties [160,161];
- Glass ceramics based on SiO_2–Al_2O_3–CaO–ZrO_2–TiO_2 are studied for the storage of radioactive waste, due to their good mechanical resistance [162]. These glass ceramics have a crystallized phase of composition $CaZrTi_2O_7$ (zirconolite), which incorporates very well some radioactive ions such as minor actinides (Np, Am, Cm).

Chapter II:

Experimental procedures and characterization techniques

Chaptre II: Experimental procedures and characterization techniques

II.1 Purpose of work

The main purpose of this research was to synthesis glass ceramics which possess excellent mechanical properties and high biocide. Our aim was also to investigate the possible role of P_2O_5 in the $Li_2O–MgO–Al_2O_3–SiO_2$ and $MgO–Al_2O_3–SiO_2$ glass ceramic systems in order to achieve the improvement of excellent mechanical, optical and biological properties. In this chapter, the different experimental techniques used throughout the thesis work are detailed. These mainly include base glasses and the corresponding glass ceramics synthesis procedures, their thermal characterization, using differential thermal analysis (DTA) and hot-stage microscopy (HSM) and their structural characterization, using Field emission scanning electron microscopy (FE-SEM), X-ray powder diffraction (XRD), Raman spectroscopy and Fourier Transform Infrared spectroscopy (FTIR). In addition, mechanical properties, using dilatometry, micro-indentation, and flexion, have been described. Moreover, crystallization kinetics have been determined. In this study, a paint mixture (silver salt, clays, water and Arabic rubber) has been prepared and applied on the glass ceramic surface in order to investigate the effect of silver ions on the ion release ability and antibacterial activity of the obtained glass ceramics.

II.2 Preparation of glass ceramic samples

II.2.1 Glass ceramics derived from LMAS system

The starting raw materials were SiO_2 (purity > 99%), Al_2O_3 (purity > 99%), TiO_2 (purity 99.9%), P_2O_5 (purity > 98%), cryolite (Na_3AlF_6), $MgCO_3$, Na_2CO_3, Li_2CO_3 and zirconium silicate ($ZrSiO_4$, purity 99 %). The detailed nominal compositions of these glass ceramics are given in Table II-1. Base glass batches of 100 g with desired compositions were in the form of fine powders that were well mixed using a mixer (TURBULA-system Schatz).The mixer is a three dimensional shaker/mixer for fast and homogeneous mixing of powder substances for 1 h. The different batches were prepared with similar compositions (SiO_2, Al_2O_3, F, etc.) and increasing P_2O_5 concentration (1.0–3.0 mol%) and, an additional base glass was prepared without P_2O_5 in order to analyze the effect of this nucleating agent in the crystallization mechanism. The obtained base glasses have been labelled in accordance with their respective P_2O_5 contents (mol%), i.e.,GP1–GP3.

Table II-1 *Nominal compositions (mol%) of the LMAS glass ceramics*

	SiO_2	Al_2O_3	Li_2O	MgO	TiO_2	F	Na_2O	ZrO_2	P_2O_5
GP0	54.92	5.09	10.01	15.06	5.00	6.28	1.47	2.17	/
GP1	53.93	5.06	10.01	15.04	5.02	6.26	1.47	2.19	1.02
GP2	52.99	5.07	10.00	15.07	5.05	6.25	1.45	2.17	1.95
GP3	52.78	4.95	09.58	15.01	4.98	6.26	1.41	2.09	2.94

II.2.2 Glass ceramics derived from MAS system

The samples of Magnesium aluminum silicate (MAS) glass ceramic with different P_2O_5 content were prepared by mixing SiO_2 (purity 100%), Al_2O_3 (purity > 99%), $MgCO_3$, MgF_2, P_2O_5 (purity>98%), K_2CO_3 and H_3BO_3. The glass ceramic sample without P_2O_5 content (MP0) was prepared as a reference sample. The concentration of P_2O_5 was varied from 1.0, 2.0 and 3.0 mol% for MP1, MP2 and MP3 samples, respectively. The detailed nominal compositions of these glass ceramics are given in Table II-2.

Table II-2 *Nominal compositions (mol%) of the MAS glass ceramics*

	SiO_2	Al_2O_3	K_2O	MgO	B_2O_3	MgF_2	P_2O_5
MP0	40.08	8.73	5.56	22.08	1.50	22.04	/
MP1	38.35	8.84	5.63	22.37	1.52	22.33	0.95
MP2	36.77	8.95	5.70	22.63	1.54	22.59	1.82
MP3	35.15	9.05	5.76	22.90	1.56	22.86	2.72

II.2.3 Elaboration of base glasses

After mixing the different batches, they were calcined in a platinum crucible at 900 °C for 3 h (10 °C/min). For MAS glass ceramic system, MgF_2 was added to the calcined charge then mixed again for 1 h. The melting of the last charge was carried out in a Platinum (Pt) crucible at about 1600 °C in an electrically heating furnace (10 °C/min) and held for 2 h for complete homogenization. The molten charge was poured in a preheated copper molds and so formed glasses (Figure II-1). The photographs of as-prepared samples are as shown in Figure

II-2. To ensure a good homogeneity, the obtained BGs were ground and melted once again for two additional hours.

a) Furnace for melting *b) Poured onto pre-heated copper molds*

Figure II-1 *Elaboration of base glasses*

Figure II-2 *Photographs of the obtained base glasses (left: GP0 and right: MP3)*

The as-prepared glasses were annealed immediately at 550 °C for 4 h and then were slowly cooled (2 °C/min) to room temperature in a programmed manner in the aim to eliminate thermal residual stresses, since the outer surface cooled at a faster rate than the inner surface (Figure II-3). The annealed glasses were observed through a strain viewer (light polarizer) to detect the presence and location of stresses and any flaws or imperfections that may have caused premature failure. It may be mentioned that annealing is one of the important steps. If it is not carried out properly, the cracks are developed on glassy parts, which would further increase during crystallization.

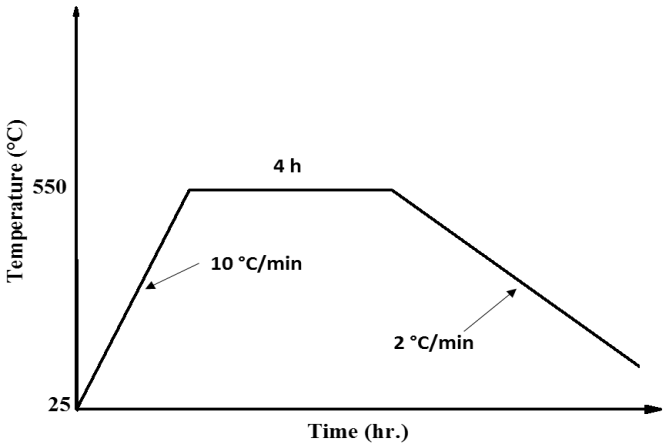

Figure II-3 *Annealing process*

As-prepared glasses (LMAS and MAS) were ground using an agate mortar and sieved through a 50 mesh to obtain glass powder for those analysis that need such particle size for being carried out.

II.2.4 Fabrication of samples

The annealed glass blocks were cut into pieces to about 2 mm thickness with a cutting machine (Buehler, IsoMet 4000, unear precision saw). The homogeneously samples (20×20×2 mm^3) were polished using polisher machine (Buehler-Beta, Grinder/Polisher) in preparation for characterization. All samples were first grounded with 320 grit silicon carbide (SiC) abrasive paper to ensure flatness. Samples were then polished gradually using carbide abrasive paper for 6–8 minutes at the following intervals: 600 grit SiC, 1200 grit SiC, 2500 grit SiC, 4000 grit SiC and finally 3µ diamond disk. Samples were then rinsed with ultrasonic waves using ultrasonic cleaning instrument (FALC, HK7200). Figure II-4 shows the resulted polished LMAS samples.

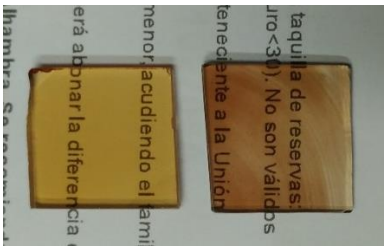

Figure II-4 *The obtained polished samples (GP1: left and GP2: right)*

II.2.5 Synthesis of glass ceramics

Heat-treatment of samples was carried out according to the thermal analysis results. In order to promote nucleus formation in the glass structure it is useful to choose a temperature higher than the transition temperature (T_g) as the nucleation temperature. It is well known that nucleation is usually held a period of time at a temperature corresponded to viscosity of 10^{11} to 10^{12} P, according to the preliminary estimate, the optimum nucleation temperature lies between T_g and T_g+50 °C [17]. Therefore, in order to obtain glass ceramic samples containing microcrystals and also in the aim to keep transparency of the glass, the obtained samples are subjected to a controlled crystallization in one stage nucleation/crystallization (NC). In present investigation, (T_g+ 50 °C) was chosen as the NC temperature of the glass for the time of 3 hours, using a programmable resistance-heating furnace. Figure II-5 shows the thermal protocol for the elaboration of glass ceramic. Glass ceramic samples were heat treated 3 h at T_{NC} with a heating rate of 10 °C/min. The obtained GCs were referred to as GP0GC–GP3GC for LMAS system and MP0GC–MP3GC for MAS system.

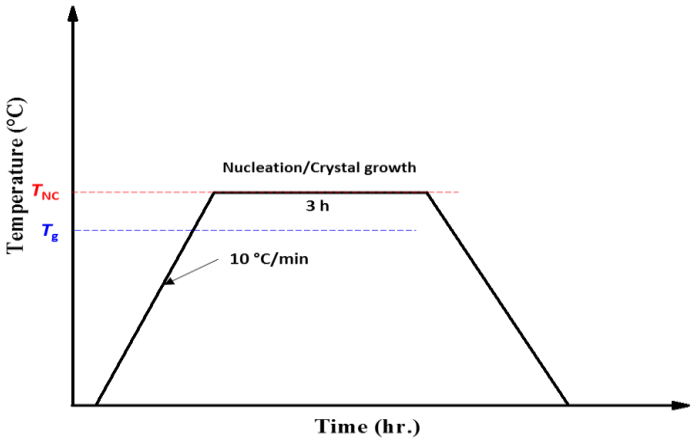

Figure II-5 *Synthesis of glass ceramics*

II.2.6 Silver stain coating

Silver stain coating was obtained following the traditional techniques described in [163]. In order to study the biocide activity, we have used $AgNO_3$ as Ag salt, arabic rubber as agglomerate and a commercial clay (Kaolin).

Prepared slurries contained 16 wt% of $AgNO_3$ (Merck, analytical grade), 48 wt% of a commercial clay and 36 wt% of a mixture of arabic rubber and water (Henkel). All the slurries were obtained by mixing the different components during 20 min under vigorous stirring. After

that, medieval glass substrates were painted on only one side. They were dried at room temperature for 2 h then heat treated at 500 °C for different time 2, 4 and 8 h. A heating rate cycle of 2 °C/min for heating and 1 °C/min for cooling was used. Finally, GC painted substrates were washed with distilled water then rinsed with ultrasonic waves to remove any residual slurry. The painted GCs were referred to as GP0Ag2–GP0Ag8 for LMAS system and MP0Ag2–MP0Ag8 for MAS system, in accordance with the heat-treatment time used for the silver stain coating. Figure II-6 shows photographs of the sample GP1 after different treatment.

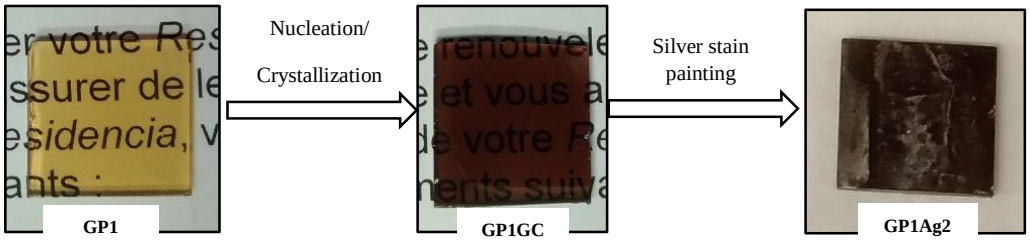

Figure II-6 *Photographs of the sample GP1 after different treatments*

II.3 Analysis

II.3.1 Chemical composition analysis

The chemical compositions of the obtained glasses were determined using an X-ray fluorescence instrument with the analysis curve IQ^+ (XRF, Philips, Magic Pro, USA). A weight of 20 mg of powdered specimen was used.

II.3.2 Thermal Analysis

II.3.2.1 Dilatometric measurements

Dilatometric measurements (Netzsch instrument) were performed using a heating rate of 5 °C/min and specimens with dimensions 5×5×10 mm^3 to investigate the thermal expansion coefficient (TEC) of the base glass and the glass ceramic specimens over the temperature range of 30–1200 °C using silica as probe in an inert (Ar) atmosphere. LMAS and MAS glass ceramic samples have been treated 4 h at the temperature of the main peak of crystallization extracted from DTA curves.

II.3.2.2 Hot-Stage Microscopy

The sintering behavior of the glass powders was investigated by hot-stage microscopy (HSM). An EM201 (Leica) instrument equipped with a CCD camera (Sony) was used from

room temperature to 1300 °C with a heating rate of 10 °C/min under flowing air. The HSM software calculates the percentage of decrease in height, width and area of the sample images. The digital photographs were automatically recorded and analyzed with an image analysis system during heating. A very small specimen (2 mm diameter and 3 mm height) made up of powder material was used to minimize the effects of temperature gradients inside the sample. Hot-stage microscopy is also a suitable technique for studying the behavior of glass viscosity in relation to temperature. The temperatures corresponding to the characteristic viscosity points such as first shrinkage (T_{FS}), maximum shrinkage (T_{MS}), softening (T_S), ball (T_B), half ball (T_{HB}), and flow (T_F) were obtained from the photographs taken during the HSM experiments following Scholze's definition [164–166]. The latter temperatures correspond to glass viscosities of $10^{9.1}$, $10^{7.8}$, $10^{6.3}$, $10^{5.4}$, $10^{4.1}$ and $10^{3.4}$ P, respectively.

II.3.2.3 Differential thermal analysis

Thermal analysis measurements were performed on an appropriate instrument (DTA, TA Instruments, SDT Q600, USA). For all measurement, a weight of 20 mg powdered specimen was placed in a Pt crucible and heated from 25 to 1300 °C at a heating rate of 10 °C/min in the air atmosphere.

a) Transformation kinetics

The study of crystallization kinetic of the considered samples was performed under non-isothermal measurements, using a differential thermal analysis (DTA, TA Instruments, SDT Q600, USA). Typically, 20 mg of each glass sample powder (< 50 μm) was heated from 25 to 1300 °C at different heating rates (2, 5, 10 and 20 °C/min) in air atmosphere. The different glasses were crushed and sieved to different particle sizes (50–100, 100–200, 200–500 and 500–1000 μm) and analyzed at 10 °C/min to estimate the dimensionality growth mechanism at each particle size. In all cases, a Pt crucible was used.

The DTA curves have been used to determine the crystallization mechanisms, include the activation energy of crystallization E_c, the Avrami exponent n and the morphology index m through analysis of the exothermic peaks at different heating rates. The glass transition (T_g), crystallization (T_p) and melting (T_m) temperatures were determined from the DTA curves. The glass forming abilities of melts, the glass stability and the structural relaxation were calculated using the different temperatures extracted from the DTA curves.

II.3.3 Microstructural analysis

II.3.3.1 X-ray diffraction

To study the microstructure development of glass ceramics, heat-treatment of LMAS glass powders was carried out at 650, 700, 750, 800 and 840 °C for 1 h and, of MAS glass powders at 700, 750, 800, 850, 900 and 950 °C for 1 h. The crystalline phases formed at different temperature were detected by X-ray diffraction (XRD, D8 Advance, Bruker Corp., Germany) at room temperature. Data were recorded in 2θ range of 10–70 °. The developed phases were identified by JCPDS numbers (Joint Committee on Powder Diffraction Standards), ICDD-PDF database (International Centre for Diffraction Data).

II.3.3.2 Field Emission Scanning Electron Microscopy

The morphology of the crystalline phases developed after heat-treatment was examined by field emission scanning electron microscopy (FE-SEM, Hitachi 4700, Japan). Fractured surfaces were etched with a 5 % hydrofluoric acid (HF) solution for 15 s for both glass ceramic systems samples, then rinsed with distilled water and then with alcohol until removed all HF. Next, they were placed in an ultrasonic bath at room temperature for 15 minutes and finally were dried at 50 °C. This etching procedure was necessary to partially remove the glassy phase, thereby enhancing the image contrast between the crystalline and glassy phases under FE-SEM. After that, the samples were gold-coated, using gold sputter instrument (EMSCOPE SC500), to increase the conductivity of the surfaces and prevent charge build-up by the electrons, before been observed in the FE-SEM. The layer deposited nearly evenly coats the surface of the specimen, faithfully reflecting the surface morphology. The FE-SEM was operating at 20 kV with backscattered electrons. The sample surface is scanned with an electron beam, while a monitor displays the information that interests us on the basis of the detectors available.

II.3.4 Structural analysis

II.3.4.1 Raman spectroscopy

Room temperature Raman spectra were recorded using a Raman spectrometer (Renishaw, UK) with a 50 mW internal Argon laser source at an excitation wavelength of 514 nm. All measurements were made in a back scattering geometry, using a 50× microscope objective lens. The spectra were averaged over 50 scans.

II.3.4.2 Fourier Transform Infrared Spectroscopy and Attenuated Total Reflectance

The structure of the glass samples was studied using Fourier Transform Infrared (FTIR) spectroscopy. The FTIR absorption spectra were recorded with a Perkin Elmer spectrometer (FTIR system, spectrum BX). Potassium bromide (KBr) pellets were used to record the FTIR spectra of the glass samples. Powders, being examined by Infrared Spectroscopy, in transmission mode, are generally prepared by grinding with KBr powder. The latter must be of spectroscopic grade purity, and be spectroscopically dry. The powder sample, approx 1.8 mg, and KBr, approx. 300 mg, must be grounded to reduce the particle size until crystallites can no longer be seen and it becomes somewhat "pasty" and sticks to the agate mortar. The mixture is then pressed, using a hydraulic press, into a disk. The spectrum quality is affected by the quality of the disk. The flatness of the baseline is dependent on the particle size and dispersion of the sample in the KBr powder. The spectra were recorded in a wave number range of 400−4000 cm^{-1}.

During Attenuated Total Reflectance (ATR) analysis, the sample is kept in contact with a diamond crystal allowing total internal reflection. An infrared ray arrives at the diamond crystal where the material under study has been placed. The internal reflection of the ray in the crystal gives rise to an evanescent wave which, at each reflection, continues beyond the surface of the crystal and penetrates the sample over about 1 μm. The penetration depth depends on the wavelength, the angle of incidence of the beam on the crystal, and the nature of the crystal. Spectra are thus obtained (curves of absorbance vs. wavenumber) that have absorption peaks characteristic of the functions present at the glass sample surface. The spectra were recorded in the wavenumber range of 600−4000 cm^{-1}.

II.3.5 Mechanical analysis

II.3.5.1 Hardness

In this study, nano-indentation was used to test mechanical properties, including the hardness (H_v) and the elastic modulus (E) in the glass ceramic material. Two components (30 wt.% resin and 12 wt.% hardener) were well mixed and stirred for a couple of minutes without introducing too many air bubbles. Then, the mixture has been left to rest for 2 minutes and poured carefully over the specimens with a standard diameter. Most specimens are small coupons of about 10 mm size. The indentation will be performed on the top surface of the

specimen. This requires a grinding/polishing procedure that will yield a smooth and flat surface. After that, the well-polished specimens were subjected to a diamond pyramid indenter (Vickers) under an optimum load of 500 mN for glass ceramic and base glass samples. The holding time after an indent was 10 s. Data were obtained using at least 10 indentations on each specimen and the average of this was used to calculate the hardness and the Young's modulus. The error reported being the standard deviation in the measurements.

II.3.5.2 Bending test

Three-point bending tests were performed for the determination of modulus of rupture (σ). A span length of 12 mm and a crosshead speed of 0.5 mm/min were used for all tests in a universal test machine (MicroTest, .EM1/50/FR). Flexural strength (three-point bending) of the glass ceramics was measured with parallelepiped samples (20×10×2 mm^3) in an ambient atmosphere. All samples were rinsed with ultrasonic waves using ultrasonic cleaning instrument (FALC, HK7200) before the test.

II.3.6 Optical analysis

II.3.6.1 Transparency

The optical transmission and reflection spectra were recorded by using a spectrometer UV-Visible (UV-Vis, Perkin Elmer Lambda 950) in the wavelength range of 100−1000 nm at room temperature.

II.3.6.2 Color parameters

From the obtained transmission and reflection spectra, color parameters have been calculated using the International Commission on Illumination (usually abbreviated CIE for its French name, commission internationale de l'éclairage) according to illuminant C (CIE 1931, corresponding to the spectral distribution of medium solar light for cloudy sky) and Observer 10 ° [163]. CIELAB color space (also known as CIE $L^*a^*b^*$ or sometimes abbreviated as simply "Lab" color space) expresses color as three values: L^*, a^* and b^*. In most cases of colorimetric study, we are looking for a more significant color gap than the color itself. The L^* coordinate is a measure of the lightness-darkness of the specimen. The greater the L^*, the lighter the specimen. The a^* coordinate is a measure of the chroma along the red/green axis. A positive a^* relates to the amount of redness, and a negative a^* relates to the greenness of a specimen. The b^* coordinate is a measure of the chroma along the yellow/blue axis. That is, a positive b^*

relates to the amount of yellowness; a negative b^* relates to the amount of blueness of the specimen. To decrease the possible deviations of the color values, the measurement of each specimen was repeated 3 times and averaged. The same operator made all measurements.

II.3.6.3 Refractive index

The refractive indexes (n_D) of the base glasses and glass ceramics were measured with an Abbe refractometer (ATAGO, model DR-A1) with a spectral line of sodium (589.3 nm). By very simple operation that needs only to set the boundary line of refraction at the cross hairs, the refractometer directly indicates a measured value of refractive index. Ten measurements were made on each sample and averaged at the ambient temperature of 22±02 °C.

II.3.7 Bacterial analysis

The antibacterial activity of samples was performed using Escherichia coli (*E. coli*) ATCC 25922 (Ec 25922), as gram negative bacteria. All the strains were kept frozen at –80 °C until the experiments were performed. The bacterial adhesion experiments on doped glass ceramic specimens were performed following the protocol adapted from previous studies [167,168]. The test was used to quantify the bacteria adhesion on the surfaces through the count of bacteria colonies forming units (CFU). Each sample was washed and vortexed for 15 s at 3000 rpm in pure distilled water (B. Braun, Melsungen, Germany) before this experiment was performed. Bacteria were inoculated in tryptic soy broth (bioMérieux, Marcy-l'Étoile, France) at 37 °C for 24 h. After culture, bacteria were centrifuged at 3500 rpm for 10 min at 22 °C. Supernatant was discarded, and the pellet was washed three times with sterile 0.9 % NaCl saline solution (SS) (B. Braun, Melsungen, Germany). Bacteria were then suspended and diluted in SS, reaching 108 CFU/ml bacterial solution, and 5 ml of this solution was incubated onto doped GC specimens in a sterile non-treated six-well plate (Thermo Fisher Scientific, MA, USA) at 37 °C for 90 min in order to allow adhesion in a static model. These experimental conditions allowed detection of a better bacterium/GC interaction. After incubation, samples were washed three times with SS to remove unattached bacteria, as described in the literature [169]. Finally, samples were then stained for 2 min with a Live/Dead Bac Light bacterial viability kit (Thermo Fisher Scientific, MA, USA) and rinsed with sterile water.

Different photographs (×40 magnification) were taken with a DM 2000 fluorescence microscope (Leica Microsystems, Wetzlar, Germany) for some samples. All photographs were taken using the same microscopy conditions (290- to 450-ms exposure time, 10.1× optical gain,

1.25 saturation level, and gamma of 10.00). The percentage of the total surface with adhered bacteria as well as the percentages of dead and live bacteria were calculated and analyzed by using ImageJ software (National Institutes of Health, Bethesda, MD, USA).

At the end of the growing period, cells were removed by centrifugation and the release of silver to the fermentation broth was determined by inductively coupled plasma (ICP).

Chapter III:
Results and discussion

Chaptre III: Results and discussion

III.1 Chapter preamble

In this chapter, the results obtained from the chemical, structural, optical, mechanical and biological testing of LMAS and MAS base glasses and the corresponding glass ceramic are presented and discussed. The influence of the chemical composition of the base glasses, the effect of a single nucleating agent (F) and double nucleating agents (P_2O_5 and F) and heat-treatments on the characteristics of the obtained glass ceramics are also reported and discussed. The crystallization kinetics of these systems are explained.

III.2 LMAS glass ceramic

III.2.1 Chemical analysis results

For all the investigated compositions, melting at 1600 °C for 2 h was sufficient to obtain bubble-free, homogeneous glasses. The experimental chemical concentrations of these glasses analyzed by XRF are given in Table III-1. In fact, during the fusion process of the glass mixture in the platinum crucible at 1600 °C, Fluoride loss can occur which will change the proportions of components given in Table II-1. It is known that fluoride losses occur during melting of silicate glasses [170], which is attributed to the high temperatures involved in the glass fabrication process. It should be noted that high temperature (~1600 °C) was needed for homogenization of the molten glass and even was required to obtain enough viscosity to cast it. In addition, the high Al_2O_3 content and the absence of F in GP2 sample is attributed to the use of an Aluminum crucible during the melting procedure, and then, their effect on the crystallization of LMAS glass ceramic was studied. Moreover, negligible changes were observed in the chemical composition of the base glasses after melting the glass batch.

Table III-1 *Chemical compositions (mol%) of the obtained LMAS base glasses (Al/Li =Al_2O_3/Li_2O and Si/Al = SiO_2/Al_2O_3)*

	Li_2O	MgO	Al_2O_3	SiO_2	CaO	Na_2O	TiO_2	ZrO_2	F	P_2O_5	Al/Li	Si/Al
GP0	10.95	15.16	05.32	58.21	0.34	1.51	5.40	2.20	0.86	0.00	0.48	10.94
GP1	11.28	15.00	05.31	57.41	0.33	1.82	5.37	2.13	0.49	0.81	0.47	10.81
GP3	11.91	14.71	05.20	55.42	0.34	1.52	5.15	2.07	0.51	3.12	0.44	10.65
GP2	09.28	13.40	16.38	50.56	0.30	1.39	4.79	1.98	0.00	1.87	1.76	03.08

III.2.2 Differential thermal analysis results

Figure III-1 shows the DTA thermograms of the obtained base glasses where different exothermic peak temperatures corresponding to the formation of several crystalline phases can be observed.

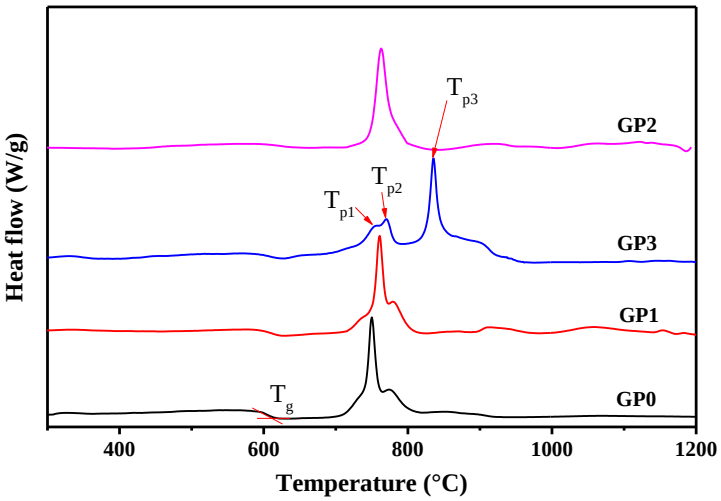

Figure III-1 *DTA curves of the LMAS specimens at the heating rate of 10 °C/min*

It is noticed that all the DTA curves exhibit similar trends with a small endothermic signal around 600 °C corresponding to the glass transition temperature, T_g. DTA curve of the GP2 sample has only one exothermic peak in the same temperature range, although the asymmetry toward high temperatures indicates the presence of a crystallization peak of low intensity. There were three exothermic peaks for the GP3 glass. The main exothermic peak was detected at 837 °C and two weak exothermic peaks at 756 and 771 °C. Adding P_2O_5 to the basic glass did not change the endothermic peak greatly; however, it increased the main exothermic peak temperature from 750 to 837 °C (Table III-2).

Table III-2 *crystallization peak temperatures and transition temperature (°C) of the obtained LMAS specimens from the DTA curves*

	T_g	T_{p1}	T_{p2}	T_{p3}
GP0	615	733	750	774
GP1	624	736	760	780
GP3	625	756	771	837
GP2	628	764	787	/

In contrast, for the samples GP2 with high Al_2O_3 concentration, the main exothermic peak appears between two smaller ones but, in the sample of high P_2O_5 concentration, such main peak changes and appears as at the high temperature one. These results show the effect of P_2O_5 as a crystallization promoter.

III.2.2.1 Transformation kinetics

a) Structural relaxation

The calculation of the E_g values from equation (I.5) is carried out by fitting the data shown in Figure III-2 to a straight line. Table III-3 collects the E_g, $F_{I\text{-}DTA}$ and $F_{I\text{-}vis}$ values obtained for the LMAS glasses studied in this work and calculated for the 5 °C/min heating rate. E_g values are in the range of silicate glasses with an Al_2O_3 molar concentrations varying between 0 and 20 % [69]. From the calculated E_g values, the $F_{I\text{-}DTA}$ and $F_{I\text{-}vis}$ indexes are obtained by using equation (I.6) and equation (I.7).

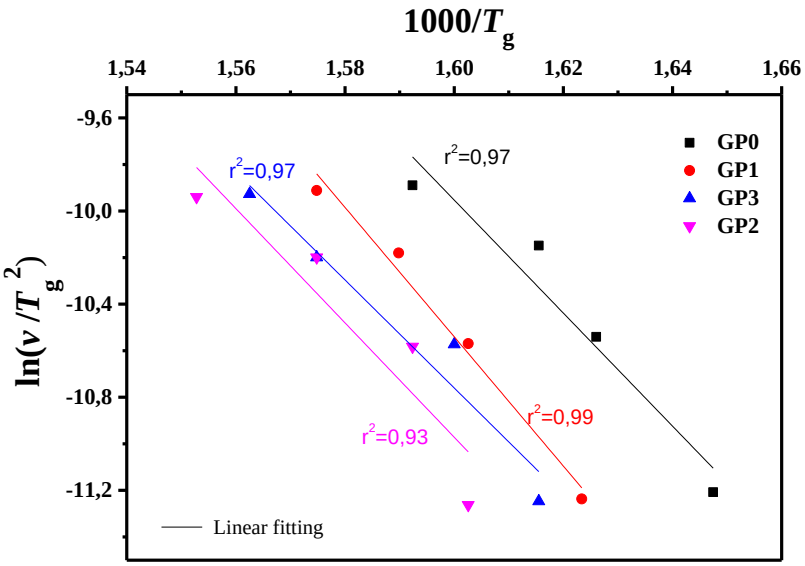

Figure III-2 *ln (v/T_g^2) vs. $1000/T_g$ plots of viscous flow in the different glasses transition range*

As observed in Table III-3, the F_I values of the studied BGs are higher than the values reported for vitreous silica which is close to 19 [62,171]. The higher values of the E_g yield to the higher values of F_I. The obtained glasses can be considered as *strong glasses* since all F_I values are higher than the silica glass (F_I = 19).

Table III-3 *Fragility indexes*

	E_g (kJ.mol^{-1})	$F_{I\text{-}DTA}$	$F_{I\text{-}vis}$
GP0	426	25.03	27.94
GP1	483	28.10	31.89
GP3	403	23.33	25.75
GP2	424	24.48	26.23

It is also observed that E_g and F_I increase only with the addition of a small amount of P_2O_5 (1.0 mol%) to the glass composition but if more P_2O_5 is added the inverse will happen. Variations of E_g and F_I can be explained on the basis of structural changes due to the introduction of phosphorus atoms. Although P_2O_5 generally acts as a nucleation agent to induce crystallization in aluminosilicate glasses containing Li, Mg, etc., it is also known that such effect strongly depends upon the *Al/Li* ratio [172]. For *Al/Li* < 0.2, P_2O_5 acts as a nucleating agent leading to an easy bulk crystallization and therefore the glass tends to be fragile whereas, if *Al/Li* > 0.7 P_2O_5 acts as a glass structure stabilizer improving the rigidity of the glass network, i.e. leading to a stronger glass [172]. According to the chemical compositions provided in Table III-1 and results of Table III-3, the studied glasses containing F present *Al/Li* ratios between 0.2 and 0.7 but they can be considered as strong glasses because their F_I values are closer to 19 than to 200. However, these results present some discrepancies because of the random variation with the P_2O_2 and Al_2O_3 content in the glasses. In order to discern these variations, the glass stability parameters are then further considered.

b) Glass Forming Ability and Glass Stability

Table III-4 collects the ω_2, β, K_H and *S* values obtained for the LMAS glasses studied in this work. The results recorded in Table III-4 show that the addition of P_2O_5 to the LMAS base glasses leads to an increase in β, K_H and a decrease in ω_2, which is translated to an increase in the GFA and GS of the glasses. The absence of F and the existence of higher Al_2O_3 content in the GP2 glass confers to this glass the major stability. It is also noticed that the *S* values do not follow any trend like the other three parameters so we cannot extract any correlation or conclusion. This problem may arise because the *S* parameter takes into account both the T_p values and the corresponding difference between T_p and T_o, and the studied glasses present several crystallization peaks so, it is difficult to analyze.

Table III-4 *GS and GFA parameters (calculated as an average for the four heating rates)*

	ω_2	β_2	K_H	S
GP0	0.27	3.14	0.12	3.46
GP1	0.27	3.26	0.12	2.98
GP3	0.25	3.95	0.14	4.42
GP2	0.21	4.07	0.21	2.65

c) Crystallization kinetic and mechanism

Crystallization peak temperatures have been determined by a deconvolution procedure, assuming that every peak presents a mixed Gaussian–Lorentzian (50 %–50 %) shape because this was the better fitting obtained. From these fitting peak positions (temperatures, T_p), full–widths (Δw) and intensities of the peaks were obtained.

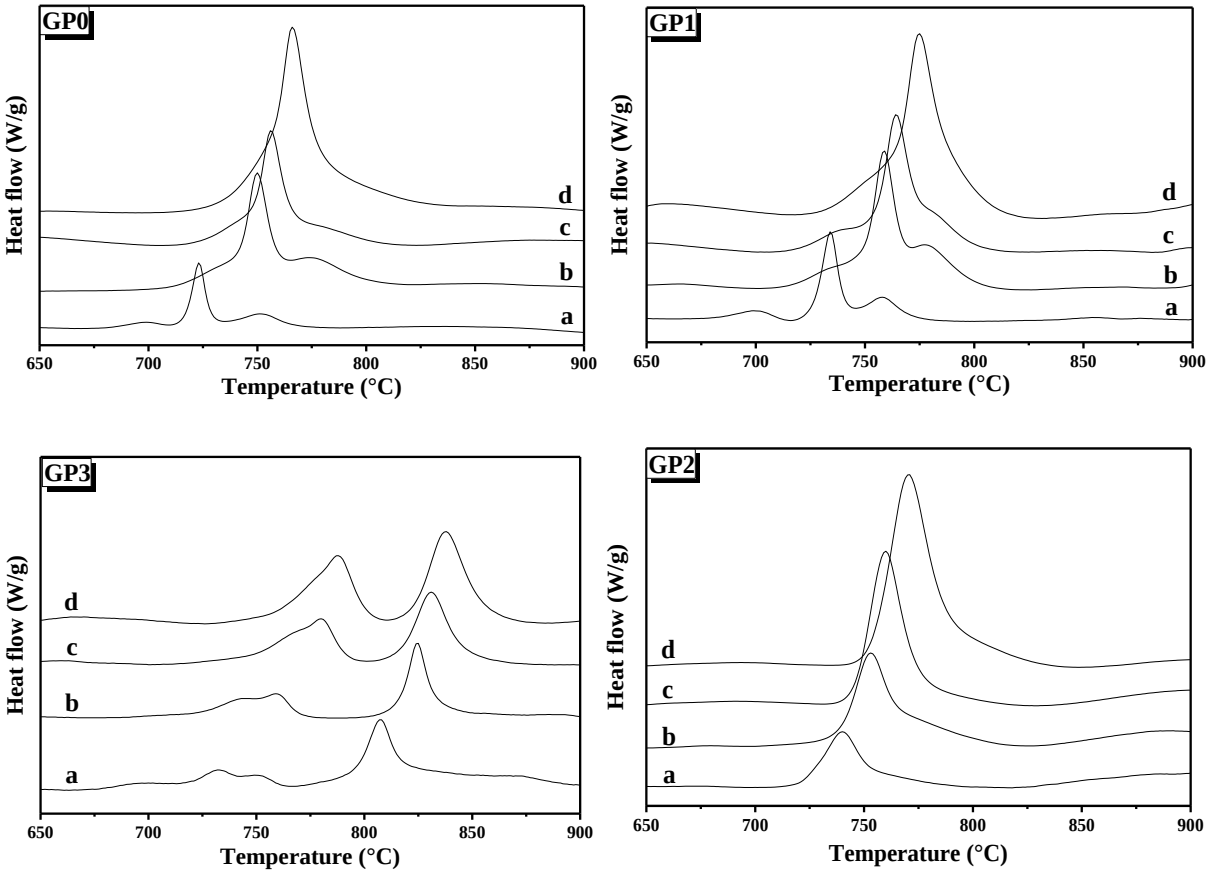

Figure III-3 *DTA curves of the LMAS glasses at different heating rates: (a) 5, (b) 10, (c) 15 and (d) 20 °C/min*

Table III-5 *Characteristic temperatures (°C) from the DTA Curves*

Sample	*Heating rate (°C/min)*	T_g	T_{p1}	T_{p2}	T_{p3}
GP0	05	607	697	723	751
	10	615	733	750	777
	15	619	741	756	780
	20	628	752	766	789
GP1	05	616	699	734	758
	10	624	735	759	778
	15	629	737	764	782
	20	635	754	775	789
GP3	05	619	733	751	808
	10	625	746	760	825
	15	635	771	781	832
	20	640	781	789	838
GP2	05	624	740	763	/
	10	628	753	778	
	15	635	760	788	
	20	644	770	794	

Figure III-3 shows the DTA curves of each glass heated at different rates, where the crystallization peaks can be well observed. The temperatures of glass transition and crystallization peaks values are presented and collected in Table III-5.

Data of Table III-5 show that T_g and T_p are increasing as P_2O_5 increases. These results are consistent with several works that have shown that additing P_2O_5 [173,174] or both F and P_2O_5 [175] to some MAS and LAS glasses increase both T_g and T_p. In the literature, it is also described that if the concentration of Li_2O is higher than that of MgO, the addition of P_2O_5 or F lead to a decrease of T_g and T_p [15,57,146].

According to Table III-1, the *Al/Li* ratio influences T_g and T_p in the sense that if this ratio is less or close to 0.2, the P_2O_5 acts as a nucleation promoter leading to a decrease of T_g and T_p; but if the ratio is higher than 0.7 then P_2O_5 acts as glass stabilizer increasing these characteristic temperatures [176]. Results of Table III-1 and Table III-5 show that $Al/Li \geq 0.2$ for all the studied glasses and the effect of the addition of P_2O_5 induce a stabilization of the glass network.

Kissinger plots for the different studied LMAS BGs at different heating rates using the temperature of the main peak are shown in Figure III-4. Figure III-5 shows the plot of ln(v) *vs.* $1000/T_p$. Figure III-6 shows the plot $\ln(v/(T_p-T_o))$ *vs.* $1000/T_p$ from which the E_{cab} has been obtained. In addition, the value of E_{co} can be obtained from the slope of the equation (1.24) and Figure III-7 shows the plot $\ln(v^n/T_p^2)$ *vs.* $1000/T_p$. The different plots for each sample of the different studied LMAS specimens are shown in appendix A.

The DTA curves present two or three peaks at different heating rates. Therefore, the E_c, n and m values have been determined for each peak of the studied glasses. The differences in the E_c values determined by different methods may be attributed to the different approximations that have been adopted while arriving at the final values from them, but, in most cases, the results are very close and the discussion of the crystallization kinetics can be carried out by taking average values of each parameter. The values of E_c for crystallization calculated by different methods and the values of Avrami exponent n and the m parameter are given in Table III-6 and Table III-7, respectively.

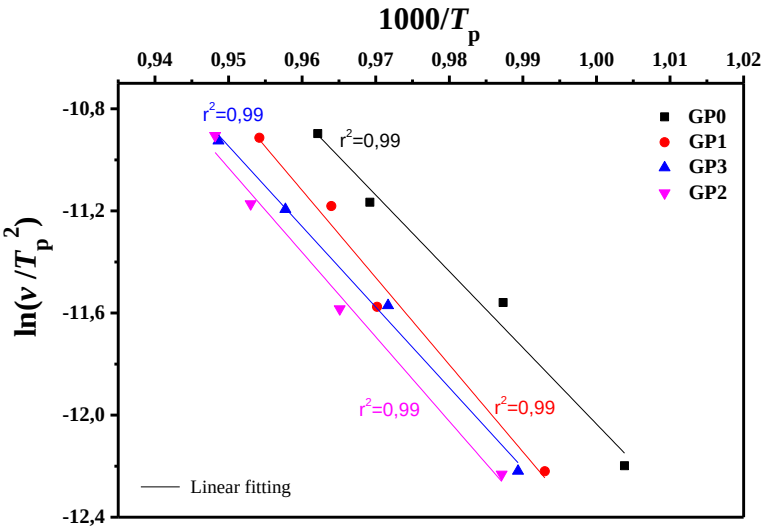

Figure III-4 *Kissinger plot: $\ln(v/T_p^2)$ vs. $1000/T_p$*

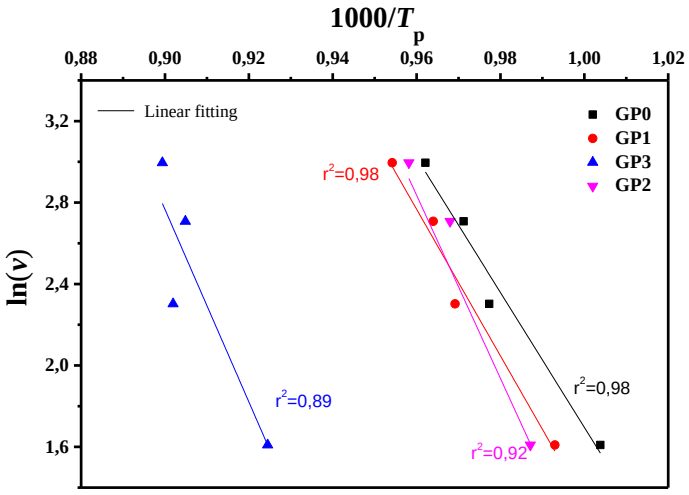

Figure III-5 *Ozawa plot:ln(v) vs. 1000/T_p*

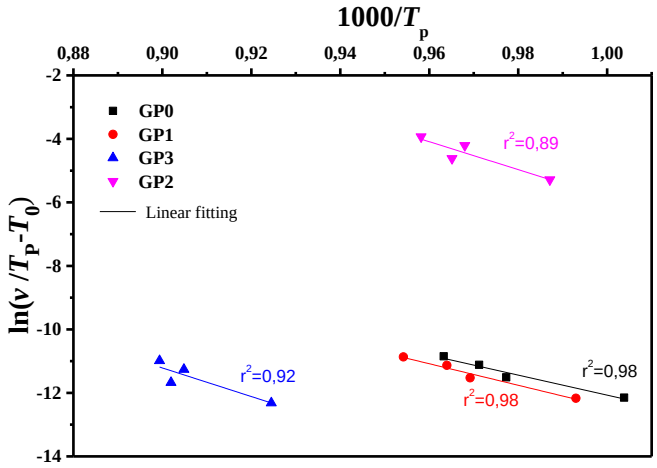

Figure III-6 *Augis & Bennett plot: ln(v/(T_p-T_0)) vs. 1000/T_p*

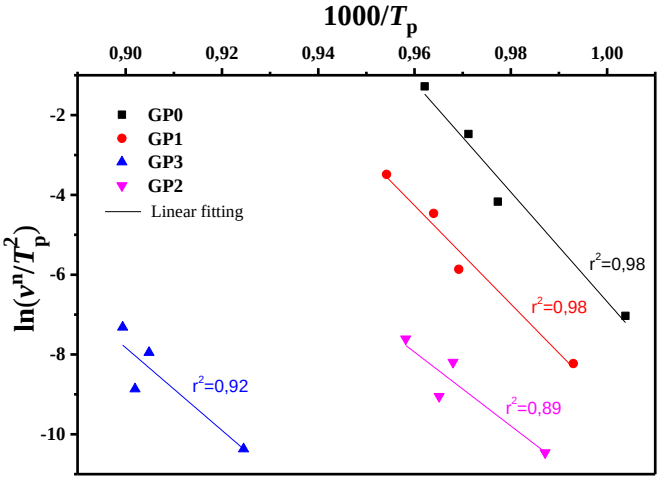

Figure III-7 *Matusita & Sakka plot: ln (v^n /T_p^2) vs. 1000/T_p*

Table III-6 *Activation energies (kJ/mol) of each exothermic peak for the studied LMAS spicemens*

	GP0			**GP1**			**GP3**			**GP2**	
	Pk1	***Pk2***	***Pk3***	***Pk1***	***Pk2***	***Pk3***	***Pk1***	***Pk2***	***Pk3***	***Pk1***	***Pk2***
Kissinger	190	258	303	192	282	379	239	313	375	352	386
Ozawa	196	262	305	198	285	377	244	314	374	356	358
Augis & Bennett	199	252	316	204	284	388	256	332	395	374	381
Matusita & Sakka	195	285	422	180	342	336	221	319	431	378	342

The activation energies of Table III-6 are in the range of 200–400 kJ/mol as correspond to LAS and MAS glass ceramic materials [177]. It is clear that for the glass with 5 mol% of Al_2O_3, E_c values increase with T_p indicating that it is necessary a higher temperatures to induce crystal growth. However, in the glass with 16 mol% of Al_2O_3 and although the two crystallization peaks appear at temperatures close to the low temperature peaks of the other glasses with lower Al_2O_3 concentration, the E_c values for such two crystallization peaks are very close the one of the high temperature peak of low Al_2O_3 glasses, and this result is due to the effect of Al_2O_3 limiting the mobility of the crystal forming cations [178]. The effect of P_2O_5 on the crystallization kinetics of LAS and MAS glasses has been extensively studied [146,178,179]. P_2O_5 is considered as a crystallization promoter due to its nucleating role. However, it has recently shown that such role depends on the composition of the BG, if K_2O and Al_2O_3 are replaced by P_2O_5, the activation energy for the crystallization decreases [178].

The parameters, *n* and *m* in this study are considered to be $n = m$, as is obvious from Table III-7. Therefore, in accordance to Donald [180] Matusita and Sakka [95], the crystallization mechanism is mainly of bulk type with a constant number of nuclei, although the specific values depends on the amount of F, P_2O_5 and Al_2O_3 in the BGs. It is observed that BGs containing F present a different behavior than those without it as shown in GP2 sample. For the F containing BGs, the addition of P_2O_5 leads to a decrease of the *n* and *m* values for the first and second peaks, while for the third peak *n* and *m* increase. This result indicates that the incorporation of P_2O_5 leads to a homogeneous crystallization mechanism for the three peaks and mainly with two and three dimensional growth of crystals. On the other hand, for the GP2 glass without F the *n* and *m* values correspond to bulk crystallization with two and one dimensional growth of crystals.

Table III-7 *n and m parameters for the studied samples (n and m calculated from equation (I.26) and equation (I.27), respectively)*

	GP0			**GP1**			**GP3**			**GP2**	
	Pk1	***Pk2***	***Pk3***	***Pk1***	***Pk2***	***Pk3***	***Pk1***	***Pk2***	***Pk3***	***Pk1***	***Pk2***
n	2.9	4.2	1.4	2.7	3.5	1.7	1.8	2.9	2.2	2,1	0,9
m	2.9	4.5	1.3	2.6	3.6	1.7	1.7	2.9	2.2	2.0	0.8

According to the results of Table III-7, the crystallization mechanism could be considered as a bulk one but when the amount of P_2O_5 increases it tends to be surface type. It would be necessary to add a concentration of ~5.0 mol% of P_2O_5 for a real surface crystallization of these type of glass ceramic (as shown in Figure III-8).

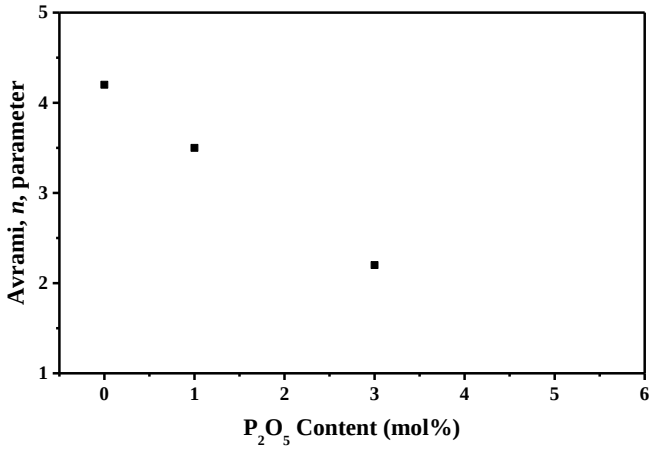

Figure III-8 *The plot of the Avrami, n, parameter vs. P_2O_5 content*

In order to confirm the dimensionality growth mechanism, Ray and Day [181] proposed a simple and rapid method to identify and distinguish surface from bulk crystallization. This method consists on analyzing the T_p and $T_p^2/\Delta w$ as a function of the particle size. Because as particle size increases the surface to volume ratio decreases, if surface crystallization is the dominant mechanism, then T_p and $T_p^2/\Delta w$ will decrease and, on the contrary, for bulk crystallization they will increase. DTA plots for BG samples GP0, GP1, GP3 and GP2 of different particle size (50–100, 100–200, 200–500 and 500–1000 µm) are shown in Figure III-9. In all the BGs, it is observed the same crystallization peaks, but, in the case of the GP0 and GP3 BGs, a new peak appears at temperatures of 760 and 820 °C, respectively. The kinetic mechanism of this new peak was not subjected to the analysis described above but it is clear

that it increases in intensity with the particle size indicating that the crystallization mechanisms is of bulk type. The rest of the crystallization peaks for these and other samples have been analyzed by the method described by Ray and Day [181].

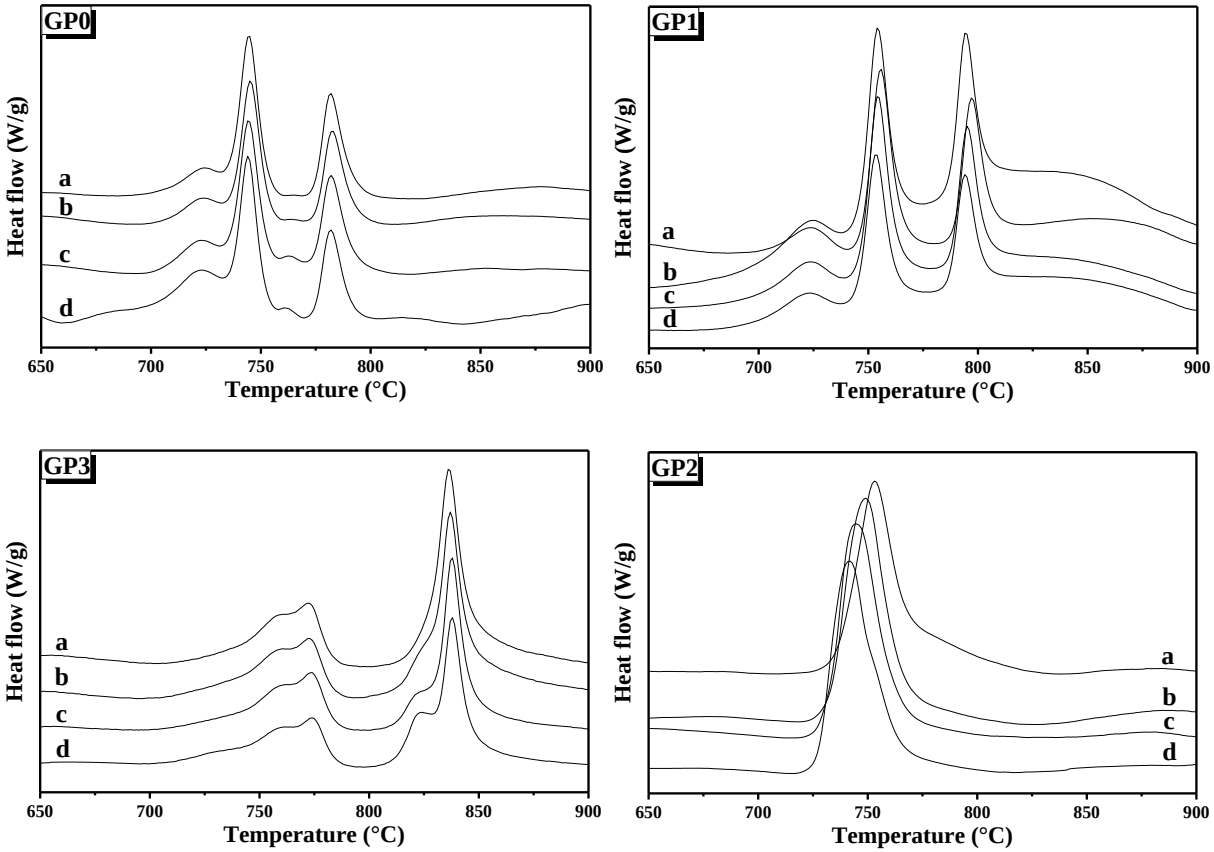

Figure III-9 *DTA plots of the studied samples for different particle sizes: (a) 50–100, (b) 100–200, (c) 200–500 and (d) 500–1000 µm*

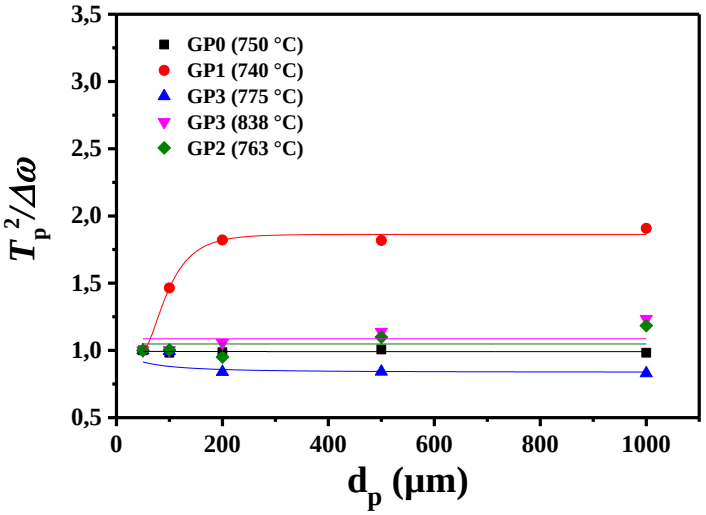

Figure III-10 *Plots of $T_p^2/\Delta w$ vs. average of particle size (d_p) for the main crystallization peak of each sample*

Figure III-10 presents the evolution of the $T_p^2/\Delta w$ for the main representative peaks of each glass. It is observed that the evolution of $T_p^2/\Delta w$ with the particle size varies from one glass to another and, in the case of the GP3 that presents two main peaks both give different evolution. In this GP3 glass while the peak at 775 °C shows a decrease $T_p^2/\Delta w$ with the particle size, the one at 838 °C shows an increase. In general it could be said that the evolution of $T_p^2/\Delta w$ with the particle size is an appropriate method for obtaining a conclusion about the crystallization mechanism or for distinguishing between surface and bulk crystallization types. This result has just been described by Marques *et al.* [182] when analyzing the crystallization of lithium disilicate glasses.

III.2.3 Identification of crystalline phases

The XRD patterns of different specimens GP0, GP1, GP3 and GP2 treated in the range 650–840 °C are shown in Figure III-11, Figure III-12, Figure III-13 and Figure III-14, respectively. GP0 and GP1 base glass samples present the amorphous characteristics of the glassy state. Moreover, there is no crystalline material detected in the sample GP0 or GP1 heated at 650 °C for 1 h, suggesting no precipitation of crystalline phase in those specimens. In addition, diffraction peaks start to emerge against the amorphous background after heating at 700 °C.

For the GP0 specimen, hexagonal lithium aluminum silicate ($Li_xAl_xSi_{1-x}O_2$, JCPDS No. 00-040-0073) was the main crystal at 700 and 750 °C for a certain period of time though the content was little. A similar lithium aluminum silicate phase was reported by Xingzhong *et al.* [147] in glasses containing 18 Al_2O_3–68 SiO_2–4 Li_2O (mol%) with different nucleating agents at a heating at temperatures between 790 and of 830 °C and by Ananthanarayan *et al.* [137] in glasses of 14 Al_2O_3–72 SiO_2–14 Li_2O (mol%) with 1.1 (mol%) P_2O_5 as nucleating agent at temperatures comprised between 600 to 925 °C. However, a large amount of β-spodumene ($LiAlSi_2O_6$, JCPDS No. 00-035-0797) have been precipitated and became the main crystal at higher temperatures 800 and 840 °C. The formation of β-spodumene has been reported in numerous works in a wide range of compositions and for multiple nucleating agents. When TiO_2 is used, β-spodumene appears at temperatures as high as 820 °C [183] but the addition of P_2O_5 seems to delay the formation this phase, as occurs in our materials [184]. In another study [185], by adding 8.0 wt% of MgF_2, a phase separation in the base glass occurs and leads to the formation of a primary crystal phase of MgF_2, which in turn promotes the formation of spherical β-spodumene crystals.

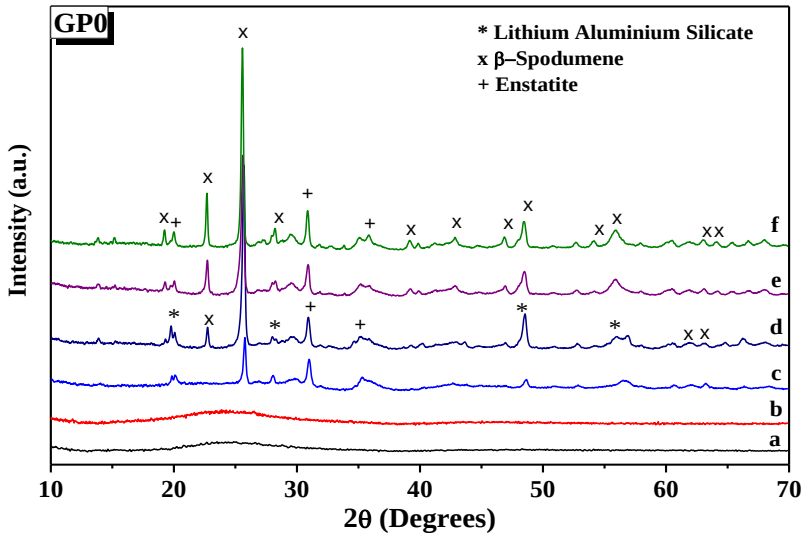

Figure III-11 *XRD patterns of GP0 specimen treated at: (a) BG, (b) 650, (c) 700, (d) 750, (e) 800 and (f) 840 °C*

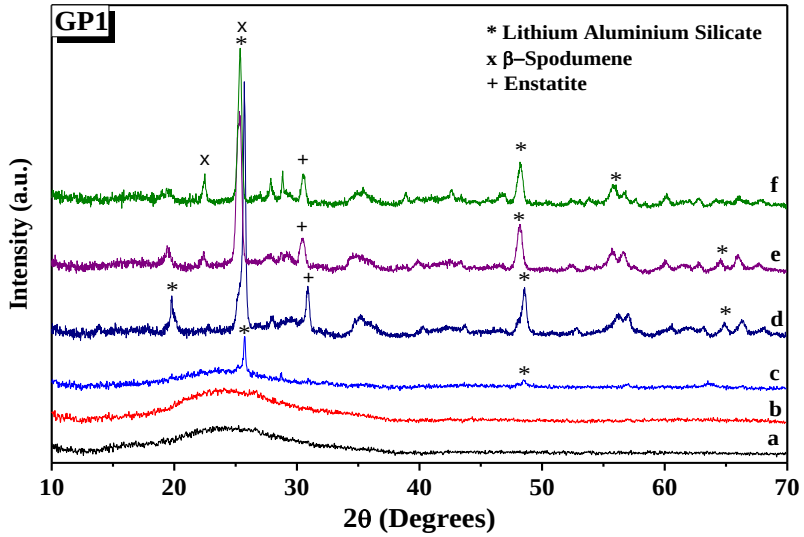

Figure III-12 *XRD patterns of GP1 specimen treated at: (a) BG, (b) 650, (c) 700, (d) 750, (e) 800 and (f) 840 °C*

Interestingly, GP2 and GP3 samples show the characteristic diffraction peaks in the BGs, which could be attributed to an impurity of pseudo phases already formed during melt quenching, but their intensities are quite weak. These pseudo phases were identified as Magnesium Aluminum Zirconium Oxide ($Mg_5Al_{2.4}Zr_{1.7}O_{12}$, JCPDS No. 00-034-1495) and Titanium Oxide (Ti_2O_3, JCPDS No. 00-010-0063).

The main peak was identified as the stable lithium aluminum silicate phase at 700 °C for GP1 and GP3. After further heating, at 750–840 °C, this peak increase and become a mixture

of different crystalline phases like the lithium aluminum silicate and β-spodumene, with the increasing of the heating temperature indicating the growth up of the crystallized particles. Moreover, the Enstatite ($MgSiO_3$, JCPDS No. 00-022-0714) and the β-spodumene were precipitated at 750 °C and 800 °C, respectively, in GP1 and GP3 samples. Compared the different XRD diffractograms of the same sample treated at different temperatures, very small 2θ-displacements were found at 26–27 °, which might be attributed to the additions of P_2O_5 in the glass ceramic, as well as a possible residual stress effect in the specimens [186].

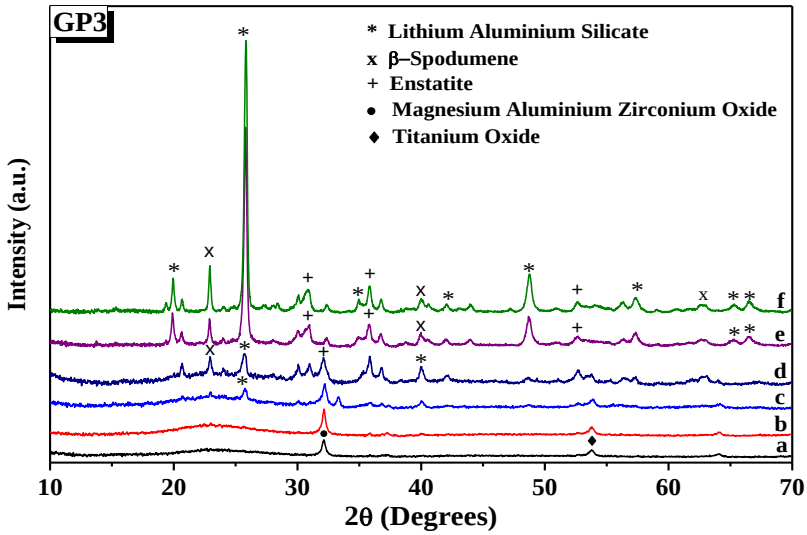

Figure III-13 *XRD patterns of GP3 specimen treated at: (a) BG, (b) 650, (c) 700, (d) 750, (e) 800 and (f) 840 °C*

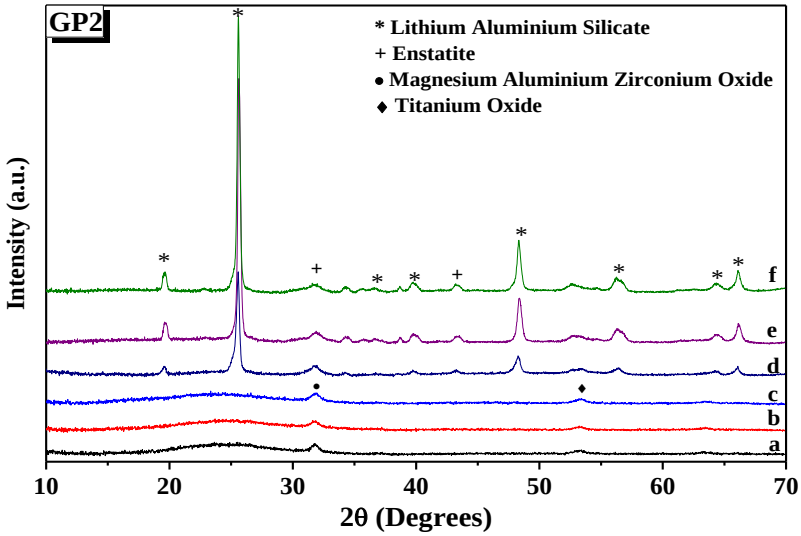

Figure III-14 *XRD patterns of GP2 specimen treated at: (a) BG, (b) 650, (c) 700, (d) 750, (e) 800 and (f) 840 °C*

For the GP2 glass ceramic with high Al_2O_3 content and without F as nucleating agent, lithium aluminum silicate is the main crystalline phase with a very small amount of β-spodumene was found. The latter results indicate that F is necessary for the crystallization of β-spodumene. Guo *et al.* [187] have shown that a small fluorine concentration in a glass improves the crystallization of β-spodumene and decreases the crystallization temperature about 110 °C lower than that containing no-fluorine, being this crystallization even more promoted in the presence of both P_2O_5 and fluorine [188].

In all cases and under identical experimental conditions, the intensity of the major diffraction peaks, $Li_xAl_xSi_{1-x}O_2$, increases with the increase of P_2O_5 concentration which indicates the influence of this nucleating agent in the crystallization reactions. The intensity of lithium aluminum silicate diffraction peaks tend to increase also with increasing heat-treatment temperature for the sample nucleated with P_2O_5. As it is observed from Figures III-12 and III-13, the β-spodumene peaks present lower intensities as the P_2O_5 concentration increased.

In accordance to these data, and from the results presented in Table III-1, Table III-2 and Figure III-1, three exothermic crystallization peaks were found in the thermograms of the glasses with F which is in line with the three crystalline phases appearing in the XRD of Figure III-11, Figure III-12, Figure III-13 and Figure III-14. But in the specimen GP2, just two peaks were found in the thermogram and just two crystalline phases emerged in the XRD diffractograms. Thus, it must be assumed that each peak corresponds to a given crystalline phase. The above commented results imply that fluorine and P_2O_5 are nucleating agents that favor the formation of β-spodumene while P_2O_5 mainly favors the formation of the lithium aluminum silicate phase.

III.2.4 Microstructure development

Figure III-15 shows the morphologies of the MLAS glasses treated at 750 °C for 1h, which were etched in a 5 % HF solution for 15 s. It is observed, from the presence of some crystals with a globular shape, assigned to the $Li_xAl_xSi_{1-x}O_2$ crystals. Crystal size was estimated using the Scherrer equation [189]. The crystal sizes are about 31, 30 and 29 nm for GP0, GP1 and GP3 glass ceramic specimens, respectively.

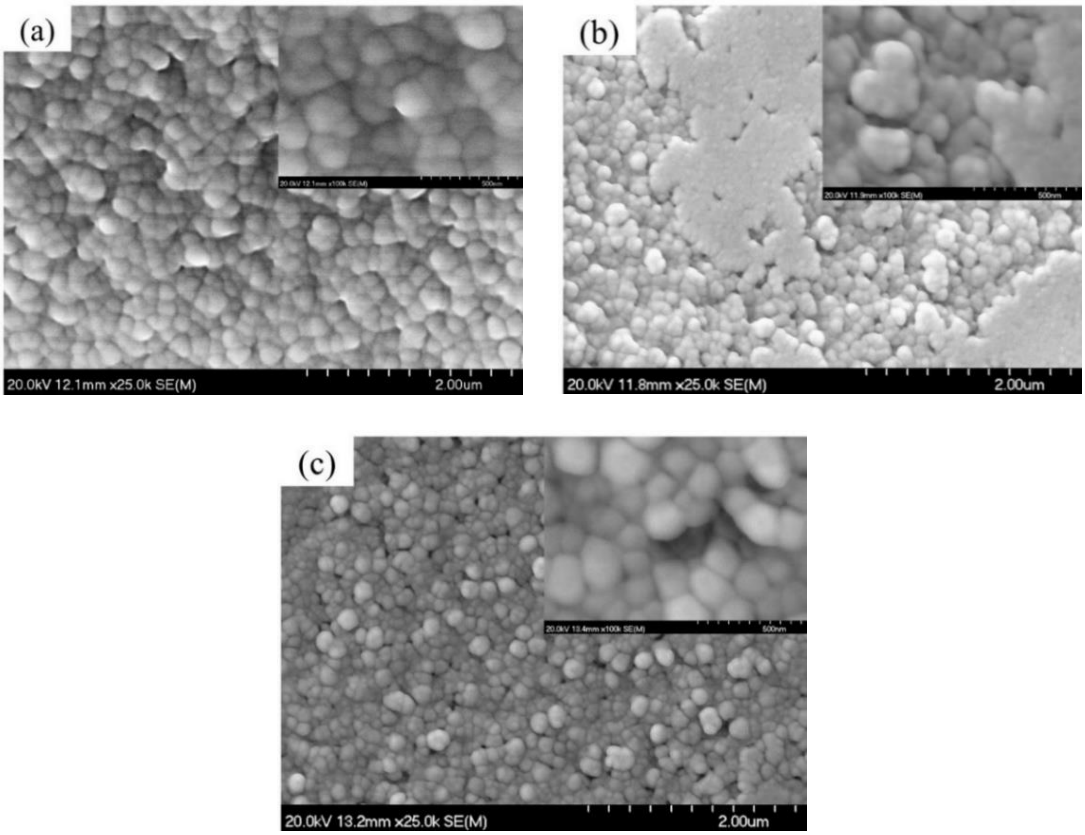

Figure III-15 *FE-SEM micrographs of (a) GP0, (b) GP1 and (c) GP3 specimens treated at 750 °C for 1h. Insets: Micrographs of the same samples in higher magnification*

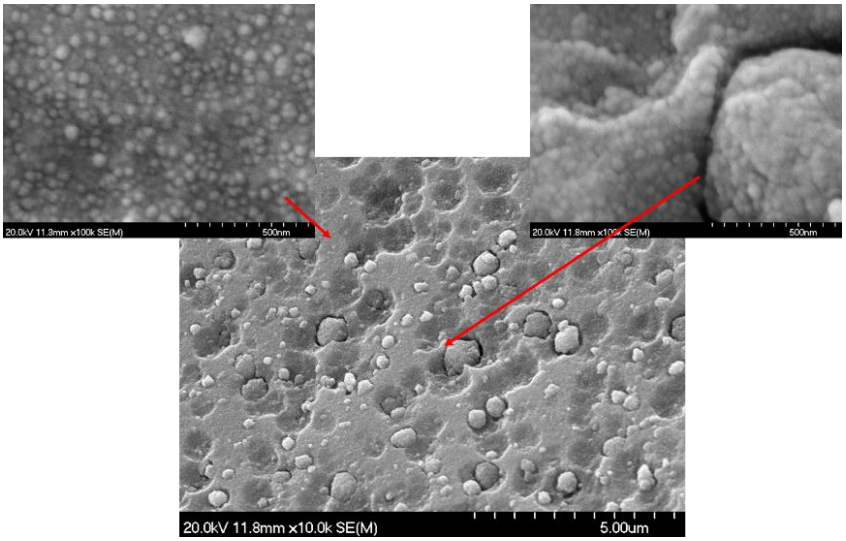

Figure III-16 *FE-SEM micrographs of GP2 treated at 750 °C for 1 h*

In the sample GP2, aggregated large particles with range of sizes 200–400 nm were precipitated uniformly (Figure III-16). The large particles were composed of fine particles with average size of 24 nm according to the Scherrer equation.

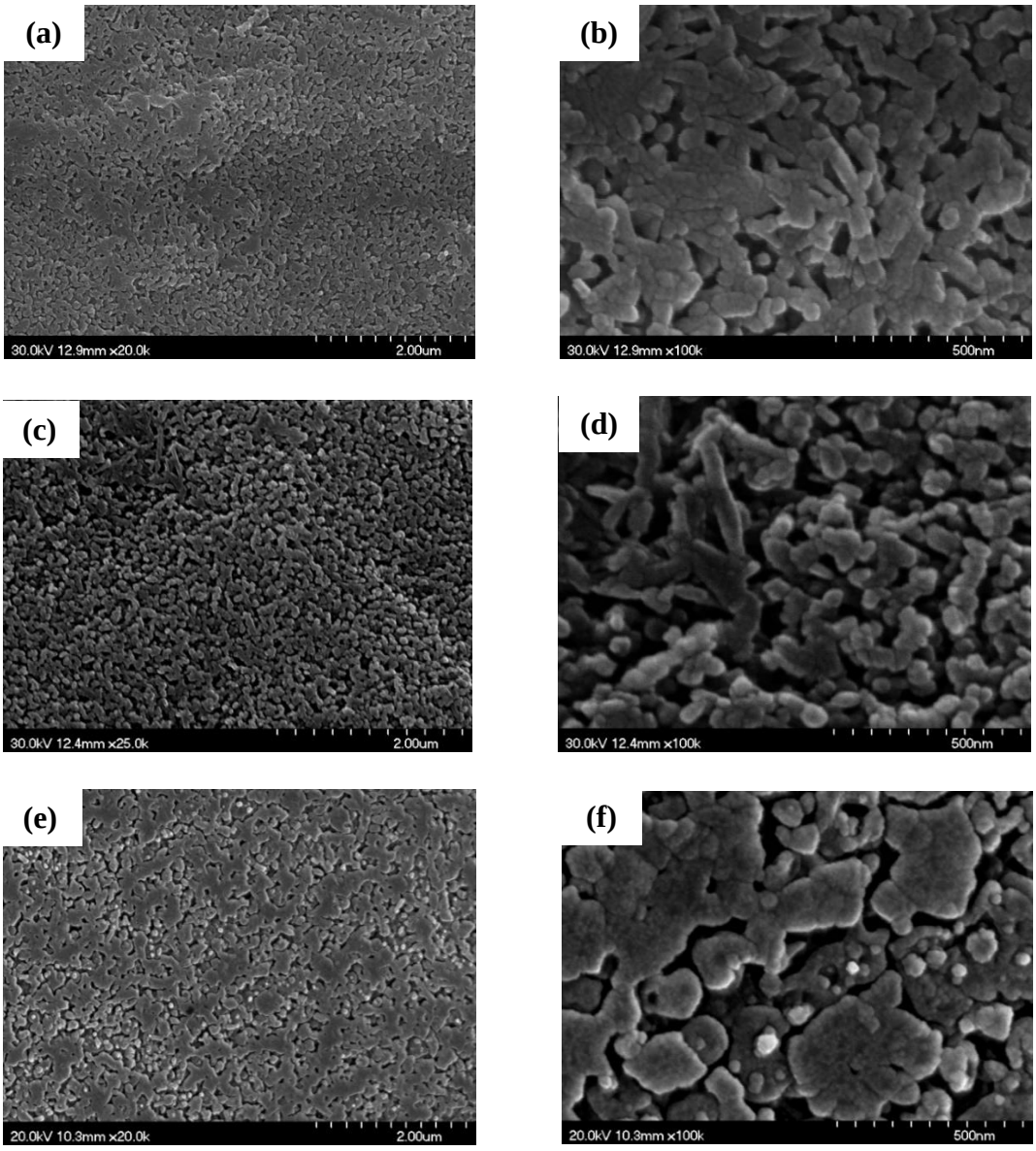

Figure III-17 *FE-SEM micrographs in different magnifications of (a, b) GP0, (c, d) GP1 and (e, f) GP3 samples treated at 755, 760 and 837 °C for 4 h, respectively*

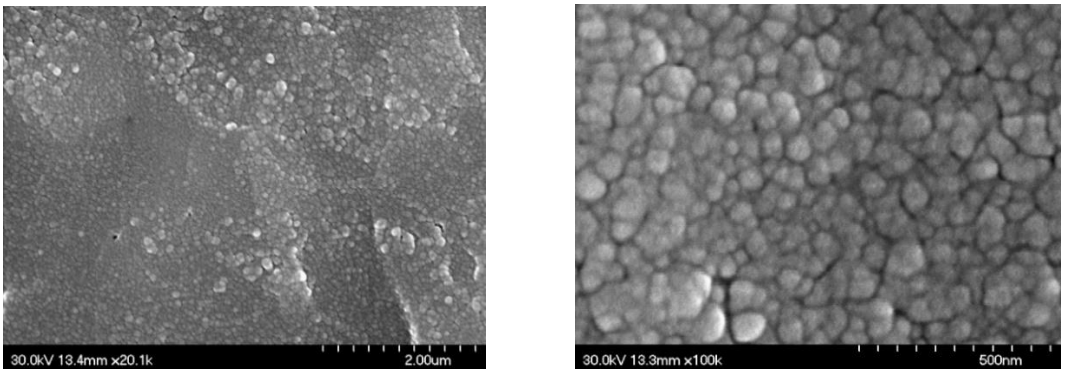

Figure III-18 *FE-SEM micrographs in different magnifications of the GP2 sample treated at 764 °C for 4 h*

After annealing LMAS specimens at the temperature of crystallization from DTA curves for 4 h, two continuous phases were observed in GP0, GP1 and GP3 (as observed in Figure III-17). It is clearly observed that, when the Al_2O_3 is maintained constant in the composition, all the glasses presented the same microstructure independently of the P_2O_5 content. For the GP0, GP1 and GP3 the crystals present a wide variety of crystal shapes with tubular, granular and plate-like microstructures, while for the GP2 the crystals are mainly globular or spherical-shaped crystals (as remarked in Figure III-18). The plate-like crystals of the GC with different P_2O_5 concentration are interlocked while the globular crystals are independent one to other.

It can seen from FE-SEM that the crystal grain size inside the glass ceramic sample is gradually increased with increasing P_2O_5 content. the crystals initially appear as a relatively dispersed single particle state, and slowly develop into larger-sized particles in which the crystal particles are in contact with each other and are tightly bonded. The distribution of these tiny crystals is relatively uniforme and distributed in the interior of the glass [190]. This is a spinodal phase separation. Due to the existence of P_2O_5, phosphate group will be consequentially separated from the silicate glass, leading to a phase separation, which plays a role in the nucleation and the microstructure formation of the glass ceramic [17,191,192]. On the other hand, separation of droplet was observed in the GP2 glass ceramic (as observed in Figure III-18), this might be a binodal phase separation [193]. These results may indicate that the binodal phase separation appeared in the glass ceramic having higher *Al*/*Li* value and free of fluoride, while the spinodal phase separation appeared in the glass ceramic having fluoride in the composition.

The introduction of both P_2O_5 and/or F^- promotes the crystallization of LMAS glass by increasing the crystallization temperature, the amount of nuclei, the grain size, crystal shape and crystallinity [194]. In previous work [146], it is reported that the coexistence of F^- and P_2O_5 affects the crystallization of LAS glass by "the mix-alkali" function. Complex nucleating agents can improve the crystallization of LAS glass by P_2O_5-inducing the phase separation and F^--modifying the glass structure.

III.2.5 Thermal characterization

III.2.5.1 Dilatometric results

It is generally agreed that properties, such as the coefficient of thermal expansion, depend on the nature and volume of the precipitated phases, as well as the heat-treatment process [35]. Properties of the crystalline phases are also affected by the structure, type and composition of the phases developed during crystallization process and by the developing of residual glassy matrix. The amount of the different crystalline phases is greatly important for optimizing the properties of glasses, which influences the thermo-mechanical properties of the GCs [195]. The effect of annealing temperature on the thermal expansion was determined by dilatometry. LMAS samples have been treated 4 h at the main crystallization temperature for each composition (750, 760, 837 and 764 °C for GP0, GP1, GP3 and GP2, respectively). The curves of dL/L_0 (%) *vs.* T (°C) were plotted as shown in Figure III-19. In the low-temperature region, between 300 and 500 °C, all the curves show a linear behaviour from where the TEC has been calculated. Above 500 °C, an inflexion region is remarked and followed by a new linear part until reaching its maximum which corresponds to the dilatometric softening point (T_{DS}). Glass transition temperature was estimated from the intersection of the two linear parts. Table III-8 presents the values T_g, T_{DS} and TEC for all the investigated LMAS BGs and GCs.

The thermal expansion coefficients of the investigated BGs are ranged from 7.35×10^{-6} $°C^{-1}$ to 9.47×10^{-6} $°C^{-1}$. The addition of P_2O_5 to the glass composition led to an increase of T_g, T_{DS} and TEC. However, when Al_2O_3 amount is increased, the opposite behaviour was observed, with an increase in the two characteristic temperatures and a decrease in TEC. In phosphate-bearing glasses, it is expected that a decrease of the polymerization degree of the glassy phase would produce a decrease in the T_g value and an increase of the TEC [196]. The observed increase in of both the T_g and TEC with the phosphate content has been already observed by some other authors in devitrified glasses and attributed this behaviour to a phase separation and the obtaining of a composite TEC [197]. In the absence of a phase separation, the most plausible explanation for the observed behaviour is the decrease of the bond strength further enhanced by the formation of CaF^+ structural units that provide a minor crosslinking degree in the glass network [197,198].

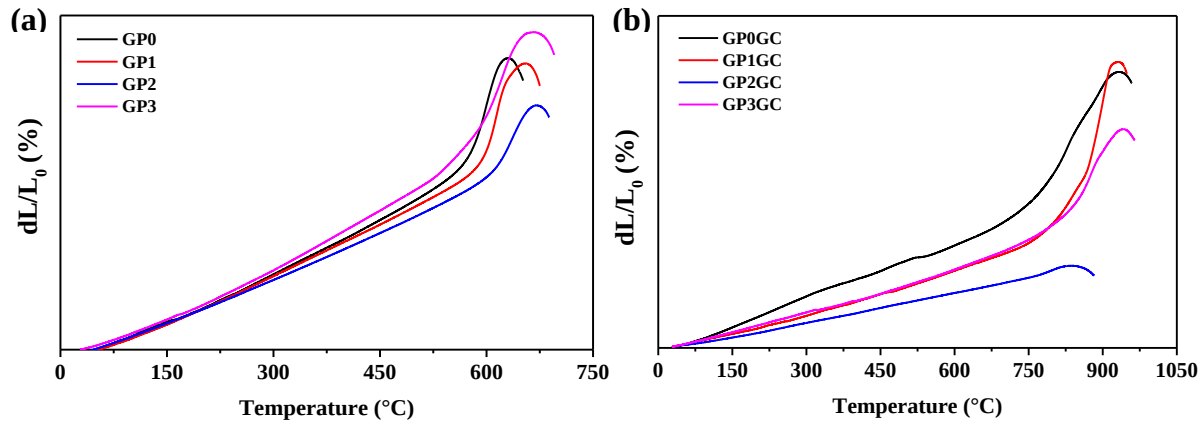

Figure III-19 *Dilatometric curves of LMAS samples: (a) BGs and (b) GCs*

The TEC curves shown in Figure III-19b are typical of glass ceramic materials where crystalline phases are embedded in a glass phase and thus, we can observe that T_g and T_{DS} temperatures falls beyond the corresponding temperatures in their parent glasses (Figure III-19a). The thermal expansion coefficient of our LMAS samples were found to vary from 7.12×10^{-6} °C^{-1} for GP0GC and 4.25×10^{-6} °C^{-1} for GP2GC. The GP0GC presents two changes in the slope at about 350 °C and 525 °C. These changes indicate the presence of several crystal phases. The first one can be assigned to a phase transition of α to β-cristobalite while the second one is indicative of a combination of α- to β-quartz transformation and γ- to β-lithium aluminosilicates [199]. The presence of quartz has not been detected by XRD, we might assume its presence in a very slow amount.

Table III-8 *TEC, T_g, T_{DS} of LMAS specimens*

		GP0	GP1	GP3	GP2
T_g (°C)	***BG***	572	593	601	578
	GC	747	846	815	733
T_{DS} (°C)	***BG***	637	651	668	672
	GC	934	858	942	835
TEC (α~300–500 °C) **±0.1 ×10^{-6} °C^{-1}**	***BG***	8.63	8.13	9.47	7.35
	GC	7.12	5.89	5.51	4.25

By comparing the values collected in Table III-8, the addition of P_2O_5 reduces the thermal expansion of the GC in a great manner with respect to the parent glass, and this reduction is more noticed by increasing Al_2O_3. T_g and T_{DS} increases in the LMAS GC. The observed results can be explained in terms of the crystalline phases detected in each LMAS GC material. Nevertheless, it must be taken into account that not only crystalline phases affect TEC but also the presence of the residual glass phase and its composition also influences in the structure of this residual glass [200].

The TEC values for the LMAS GC materials obtained in this work fits quite well with the bibliographic values [201–205]. In general, the higher glass phase content in the GC material the higher TEC [204,205]. Besides, the type of crystals also influences in TEC values, thus authors which studied β-spodumene-virgilite GC, lithium silicate-lithium disilicate-quartz GC, lithium-magnesium-silicate-cristobalite GC and lithium-aluminosilicate-magnesium calcium silicate with ZrO_2 reported values comprised between 4.0–5.2 × 10^{-6} °C^{-1}, 9.95–14.68 × 10^{-6} °C^{-1}, 8.5 × 10^{-6} °C^{-1} and 2.2–2.7 × 10^{-6} °C^{-1}, respectively [204]. For a LAS GC, the addition of P_2O_5 between 0 to 10 % leads to an increase in TEC from 4.0 to 5.1 × 10^{-6} °C^{-1} [206]. The results of Table III-8 show that the TEC of the LMAS GC decreases from 7.12 to 5.51 × 10^{-6} °C^{-1} a result that must indicate that the crystallinity of the LMAS GC increases with P_2O_5 addition and therefore the concentration of the residual glass phase decreases but by increasing the Al_2O_3 concentration TEC decreases [203].

III.2.5.2 Hot-stage microscopy results

Using both HSM and dilatometry is a simple and fast method for determining the evolution of base glasses. Decrease in the area and height of the samples as a function of the temperature is observed from the HSM photomicrographs (as shown in appendix C). Figure III-20 shows the variation of relative area (A/A_0) of LMAS samples as a function of the temperature during HSM experiments. The presence of two stages during the shrinkage process indicates the formation of crystalline phases during heating which reduce or avoid the shrinkage process until they were formed. The shrinkage process appeared in the temperature range 600–1100 °C, however the crystallization temperatures extracted from DTA curves were in the range of 700–850 °C only after the first stage. The addition of either P_2O_5 or Al_2O_3 to LMAS glass composition increase the beginning of shrinkage temperature while the end of shrinkage is only influenced by the high Al_2O_3 amount.

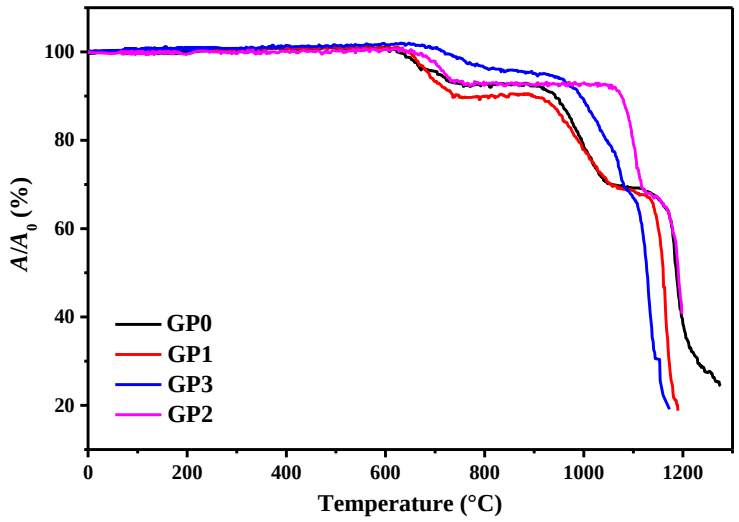

Figure III-20 *Variation in relative area (A/A_0: A_0 is the initial area at room temperature, A is the area at defined temperature) during the HSM experiments*

Table III-9 collects the temperatures corresponding to the fixed viscosities points extracted from [166] at which T_{FS}, T_{MS}, T_S, T_B, T_{HB} and T_F take place for the different glasses obtained by HSM measurements, and T_g obtained by dilatometry. T_{FS} values show a decreasing tendency with increasing content of P_2O_5, while it increases with the increase of Al_2O_3 amount since the high Al_2O_3 content lowers the sintering of particles. Thus, the formation of crystalline phases occurs in a shorter temperature range when the content of P_2O_5 increases.

Table III-9 *Experimental temperatures of the fixed viscosities points during the HSM experiment*

Characteristic points	**Temperatures (°C)**				***η* (P)**
	GP0	**GP1**	**GP3**	**GP2**	
Transition	572	593	601	578	$10^{12.3}$
First shrinkage	625	650	725	655	$10^{9.1}$
Maximum shrinkage	1050	1050	1050	1117	$10^{7.8}$
Softening	1157	1134	1064	1137	$10^{6.3}$
Ball	1170	1150	1115	1180	$10^{5.4}$
Half ball	1200	1161	1126	1190	$10^{4.1}$
Flow	1276	1190	1173	1198	$10^{3.4}$

Figure III-21 shows the logarithm of viscosity (η) versus temperature. All the different GCs present similar viscosity variations with temperature. For the GP0 sample, the faster decrease variation of η with temperature occurs in the 600–800 °C temperature range whereas; the GP3 sample needs 725 °C to achieve the same η of $10^{9.1}$. Moreover, the viscosity presents a slight decrease in temperature range of 800–1050 °C. The T_{MS} of the sample GP2 increased about 67 °C, this effect may be due to the high value of *Al*/*Li* in the composition producing an increase in the viscosity.

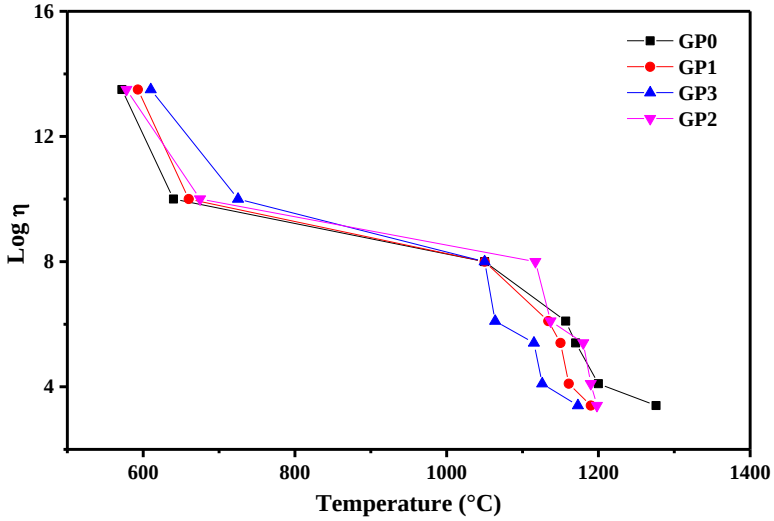

Figure III-21 *Viscosity curves of LMAS glasses obtained from HSM measurements*

The glasses prepared by Toplis and Dingweel [207] with Na/(Na + Al) < 0.6 showed that the addition of P to a glass gives an increase in the viscosity until a concentration of P_2O_5 about 7.0 mol%. As occurs in our materials, all the glasses containing equivalent amounts of Al_2O_3 present T_g values very close to each other but a small increase with the P_2O_5 concentration was determined. Besides, these glasses with similar Al_2O_3 concentration also show a temperature corresponding to the beginning of the shrinkage very close however, the glass labeled GP2, that contains a high quantity of Al_2O_3, shifts the T_{FS} to the high temperature. The presence of Al_2O_3 thus slows down particle sintering. For temperatures higher than 1050 °C, a rapid decrease variation of the viscosity with temperature occurs for all the GCs samples. As it has been clear, a viscosity value of $10^{3.4}$ for the GP0 sample is achieved at about 1276 °C, whereas GP3 needs just 1173 °C to achieve a similar viscosity. The results presented here demonstrate that the addition of 3.0 mol% P_2O_5, will affect a decrease of the T_F and the T_S about 103 and 93 °C, respectively. Also, it indicates that the P_2O_5 decreases the viscosity of glass melts, which is in good agreement with the other works [206].

III.2.6 Sructural analysis

III.2.6.1 Raman results

To understand the changes in the LMAS glass ceramic properties with the addition of P_2O_5, Raman spectra of all the glass ceramic samples treated at different temperatures were measured. Figure III-22 shows Raman spectra of BGs and glasses heat treated in the range 650–840 °C for 1 h. Similarly to the aluminosilicate materials, the Raman spectrum of GP0 and GP1 reference glasses consists of a strong band in the range of 1100–850 cm^{-1} and a shoulder in the range of 850–700 cm^{-1}. The presence of broad bands corresponds to a disordered phase [208]. Glass modifiers ions such as alkaline or alkaline-earth oxides induce the breakage of the Si–O–Si bonds leading to a decrease in the 460 cm^{-1} band and an increase of the 1100 cm^{-1} band [209]. The low intensity of the 500–200 cm^{-1} region indicates a large amount of broken $Si–O^-$ units because of the alkaline ions used in the glass composition (Li^+ and Na^+). At the same time the incorporation of high field-strength cations (Al^{3+}, Zr^{4+}, Ti^{4+}) leads to a redshift of the 1100 cm^{-1} band indicating that these cations are forming part of a three-dimensional network in a four-fold coordination, probably acting as network formers [210,211]. The variation of the T–O–T angle (where T represents tetrahedrally coordinated network-forming cations such as Si, Al, Zr and/or Ti) in the glass is the responsible of the disorder and the corresponding broadening of the Raman bands. Moreover, the presence of Li^+ in the glasses causes an increase in the intensity of the bands in the 1200–900 cm^{-1} spectral region due to the formation of non-bridging oxygens (NBO) in the silicate network [208,209].

Similarly, as occurred in the XRD patterns, the Raman spectra of the GP0 and GP1 glasses heat treated at 650 °C are similar to those of the base ones, despite the treatment temperature is above T_g. By increasing the temperature to 700 °C the Raman bands becomes broader and some small bands also appear. Motion of Si and O atoms in Si–O–Si bonds is shown in the spectra at 800 cm^{-1} and the band tends to decrease with the depolymerization of the network i.e. with the formation of NBO (i.e. Si–O bonds) [208].

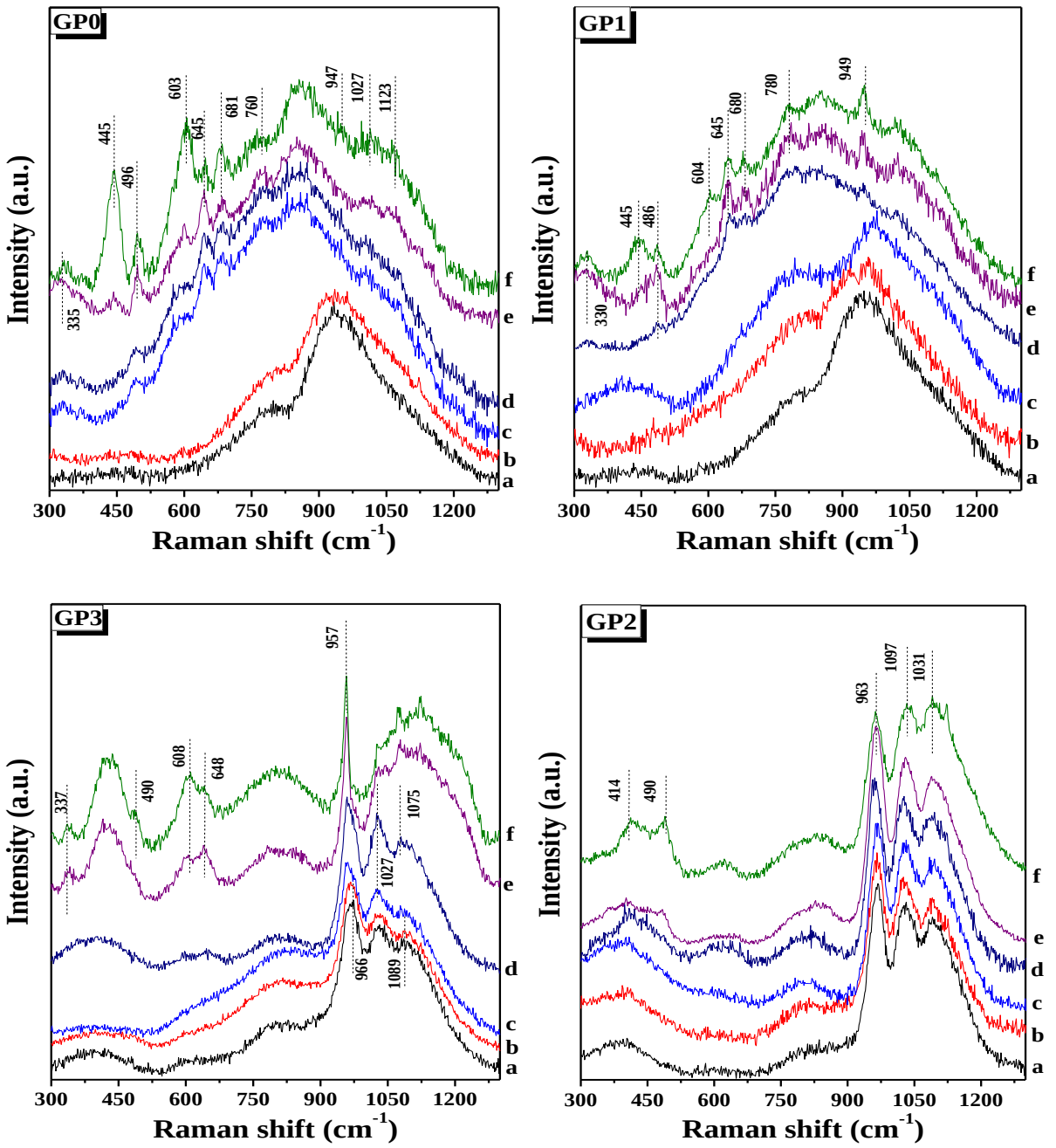

Figure III-22 *Raman spectra of different samples treated at: (a) BG, (b) 650, (c) 700, (d) 750, (e) 800 and (f) 840 °C*

In Figure III-22, we observe an increase in the band at 800 cm^{-1} due to the formation of new Si–O–Si, Si–O–Al, Si–O–Zr or Si–O–Ti bonds in new crystalline phases. When silicate glasses are treated above their T_g, the spectral region 1200–1000 cm^{-1} increase in intensity and width forming an unique band as it is observed for the glasses treated at 800 and 840 °C [212]. The broadening of the above mentioned bands is clearer in GP1 glass than in GP0, indicating that the addition of low P_2O_5 concentrations to the LMAS composition leads to a delay the formation of crystalline phases, as previously observed by XRD [184]. At 840 °C these glasses

present well defined Raman bands located at 440, 500, 610, 650 and 685 and 950 cm^{-1} while those at 260, 340, 780 and 850 cm^{-1} are broad. All of these peaks must be assigned to the formation of different polymorphs of spodumene such as γ, β and α types [211] but their low intensities suggest that the obtained GC materials still present an important glass phase that is not totally crystallized. In the spectra, the band at 500 cm^{-1} is attributed to β-spodumene [211] and the bands at 650 and 680 cm^{-1} also can be assigned to pyroxene minerals such as enstatite ($MgSiO_3$) [213]. The broad band around 1360 cm^{-1} appearing in the GP1 treated at 650 °C could be assigned to the P–O stretching vibration [214] and is the only band that could be attributed to the P–O bands because of its overlapping with Si–O–Si [215]. The asymmetric and symmetric stretching of P–O–P would appear at 620 and 1260 cm^{-1}, respectively whereas the symmetric stretching of a non-bridging oxygen at 1170 cm^{-1}. The characteristic symmetric stretching of the orthophosphate groups is normally found around 960 cm^{-1} [216]. The Li–O and Na–O vibrational modes are also difficult to detect because of the disorder at the Li and Na sites [217].

The incorporation of more than 3 mol% of P_2O_5 in GP3 produces important changes in the Raman spectra. Three broad and low intensity bands appear at 800, 600 and 400 cm^{-1} and another three high intensity and broad bands at 1100, 1030 and 970 cm^{-1} are attributed to P–O bonds [214]. In the low-frequency region the three bands be assigned to the presence of P_2O_5 in the glass structure by forming T–O–P bonds (were T = Si, Al, Zr or Ti) [214]. The presence of Si–O–Si and Si–O–M (M = Al, Mg, Zr and Ti) can influence the intensity of these bands [209,218]. Near 970 cm^{-1}, P_2O_5-bearing glasses such as $Na_2O–P_2O_5–SiO_2$ glasses present a Raman band assigned to the symmetric stretching vibration of P–O and P–O–Si tetrahedral bonds [219], while in orthophosphate and pyrophosphate glasses this band is split in two at 957 cm^{-1} and 1010 cm^{-1} [220]. Zirconium phosphates [221] and aluminous glasses [222] also present the split band but it tends to convert to a single band the P_2O_5 concentration increases indicating that at this Raman shift it can be present the P atoms in different environments (Si, Al, Zr, Ti). Upon heat treatment, XRD diffractograms showed small crystallization peaks at 750 °C. Raman spectroscopy does not detect any structural change suggesting that the samples contain a high quantity of glass phase. By increasing the temperature to 800 and 840 °C, the GP3GC present several bands at 640, 600, 430, 340 and 300 cm^{-1} previously assigned to different γ, β and α spodumene polymorphs [211] and enstatite [213]. The sharp peak at 957 cm^{-1} involves PO_4^{3-} ions and can be assigned to γ-Li_3PO_4 [223]. The broadband between 1270 and 1000 cm^{-1}

indicates that a glass network has been formed as it occurred in the GP0 and GP1 glasses. In the GP3 glass this band is not present because of the higher concentration of P_2O_5 [212].

The three main peaks at 1100, 1030 and 970 cm^{-1} are maintained in GP2 glass and involve the participation of Al^{3+} cations in the glass or glass ceramic structures forming Si–O(Al) silicate tetrahedral [222]. Because of the relatively low concentration of P=O bonds, it is quite difficult to distinguish these structures on the tail at the right of the 1100 cm^{-1} band.

III.2.6.2 FTIR results

The FTIR absorption spectra of the BG and GC specimens containing phosphorus (1.0–3.0 mol%) are shown in Figure III-23. The spectra are shown in the range of 1400–400 cm^{-1}, which is characteristic of the studied materials. It can be seen from Figure III-23, the intensity and width of the vibration band are changed with the increase of the temperature of heat-treatment and the vibration peaks become sharper. This indicates that the heat-treatment led to glass crystallization, which induced new absorption bands when the ordered crystalline array structure formed in the amorphous glass structure. The FTIR spectra of the different BGs consist of a wide and intense absorption band positioned at 1250–820 cm^{-1}, a medium band at 600–400 cm^{-1} and a weak broad band at 780–720 cm^{-1}. The latter band indicates the characteristic vibration of Al–O covalent bond in AlO_4 tetrahedron [224]. The band in the region 1250–820 cm^{-1} are mainly attributed to vibrations related to Si–O and Al–O stretching in the SiO_4 and AlO_4 tetrahedra [225], and could be attributed also to vibrations related to P–O and P–O–Si stretching in PO_4 tetrahedra [226]. In this spectral region and, specifically between 1000–850 cm^{-1}, the vibration of the Si–O- bands also appears, i.e. the NBO formed by the alkaline ions (Li^+ and Na^+) present in these glasses and this fact leads to an increase of the intensity and broadness of the left-part of this intense band [227]. The Si–O and P–O stretching vibrations appear as a non-symmetric band which starts at about 660 cm^{-1} and presents a maximum at 790 cm^{-1} which is independent of the P_2O_5 amount but shifts to 725 cm^{-1} for the GP2. In this later glass, the presence of Si–O–Al bonds leads to a decrease of this band, moreover, the shoulder close to 790 cm^{-1} suggest the coexistence of Si–O bonds. Near 470 cm^{-1}, all the glasses present the bending vibrations of O–Si–O and Si–O–Si bonds. It can be observed that for the GP3 glass, the latter band presents a shoulder 580 cm^{-1} due to the high concentration of P_2O_5 in this glass it might be assigned to O–P–O and P–O–Si bonds [215].

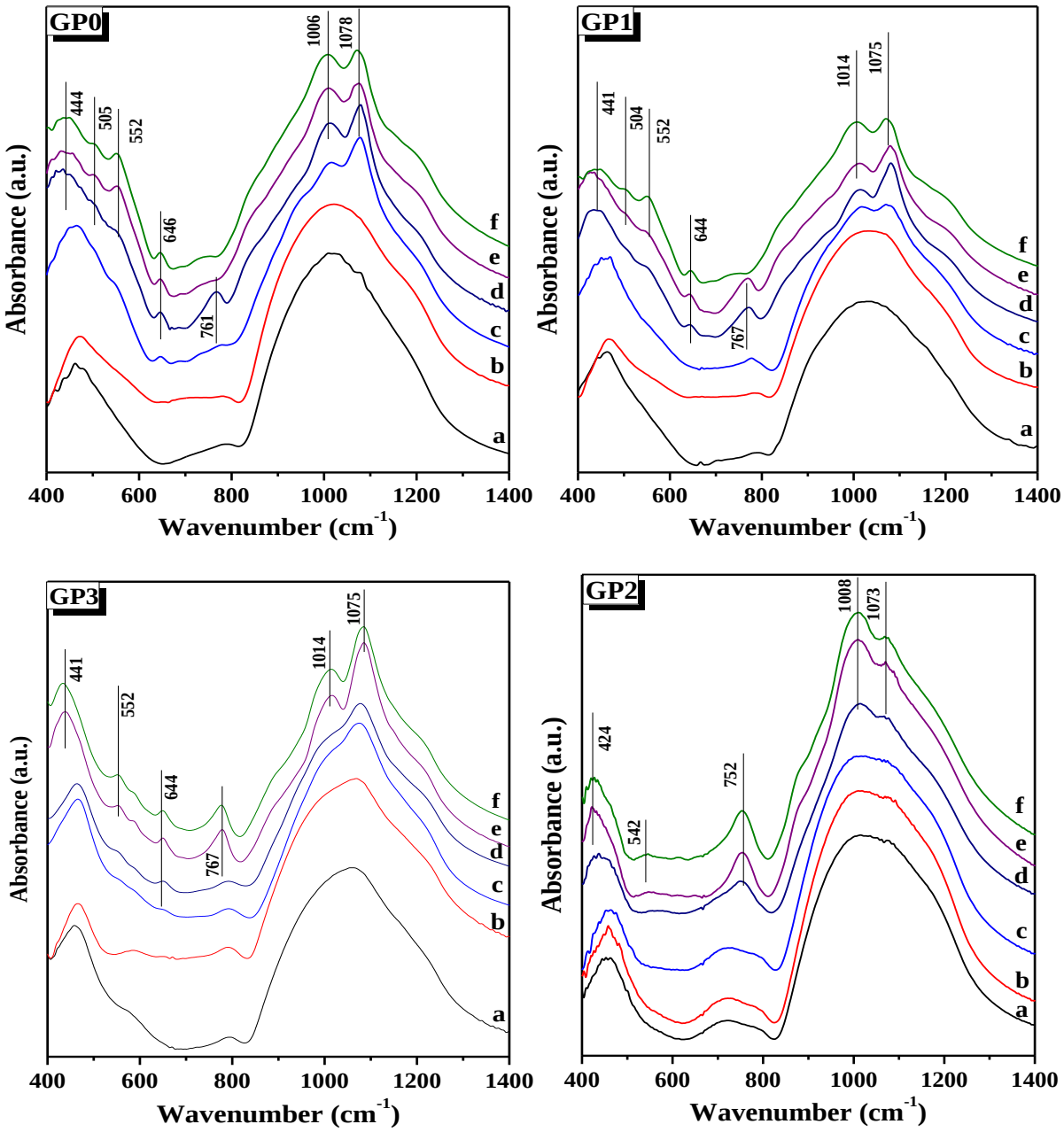

Figure III-23 *FTIR spectra of different LMAS specimens treated for 1 h at: (a) BG, (b) 650, (c) 700, (d) 750, (e) 800 and (f) 840 °C*

Compared with BGs, the infrared spectra of heated glasses show some different characteristics, the intensity and width of the vibration band are changed with the increase of the temperature of heat-treatment and some vibration peaks become sharper. This indicates that the heat-treatment led to glass crystallization, which induced new absorption bands when the ordered crystalline array structure formed in the amorphous glass structure. All spectra present the same features at similar heating temperatures although the only difference can be observed from the effect of P_2O_5 and Al_2O_3. It can be seen that absorption bands at 440 cm^{-1} and 765 cm^{-1} shift to the low-wavenumber segment, as mentioned in the literatures [190,228].

The band centered on 1000 cm^{-1} presents now several peaks. At 1080 cm^{-1}, the GP0GC presents a maximum which shifts to 1090 cm^{-1} in GP3GC because of the symmetric stretching of Si–O–Si bonds. This band decreases in intensity when the Al_2O_3 amount increases. By increasing the temperature of the treatment, the peak appearing at about 1017 cm^{-1} shifts to lower wavenumber. This band is assigned to the formation of lithium aluminosilicates and β-spodumene [229]. It should be noticed also that this is the most intense band in the spectra of the GP2GC. Close to 1210 cm^{-1} for the GP0GC and GP1GC and to 1220 cm^{-1} for the GP3GC a shoulder attributed to the anti-symmetric stretching of Si–O–Si bonds [209] indicates the release of some SiO_2 during the formation of β-spodumene. A shoulder located at 920, 930 and 960 cm^{-1} for the glasses containing 0.0, 1.0 and 3.0 mol% of P_2O_5, respectively, and at 900 cm^{-1} for the glass with high Al_2O_3 tends to the disappearance as the temperature increases. On its side, a new band appear at 850 cm^{-1} for low P_2O_5 content and 880 cm^{-1} for high P_2O_5 content which is attributed to the presence of this oxide. These shoulders could be associated to AlO_6 octahedral with NBO as well to the formation of new Si–O–Zr and Si–O–Ti bonds because the SiO_2 release after β-spodumene crystallization. Between 740 and 780 cm^{-1}, it appears the Al–O covalent bond in AlO_4 tetrahedron in aluminosilicates [179]. This band increases in intensity with both the P_2O_5 and Al_2O_3 concentrations in the glass and behaves similarly as the one located at 1010 cm^{-1} indicating that both correspond to the same crystal phase. The peak at 680 cm^{-1} is associated to the one at 560 cm^{-1} and can also be assigned to the vibrations of silicon-oxygen rings in $Na(Si_2O_5)$ phases [230]. In addition, the presence of two new peaks at 506 cm^{-1} and 560 cm^{-1} at low P_2O_5 concentration and assigned to AlO_6 octahedral [231] indicates that the amount of this oxide influences the formation of crystalline phases such as lithium aluminosilicate or β-spodumene [184]. For P_2O_5 concentrations lower that 1.0 mol% the formation of β-spodumene is favored, while for higher P_2O_5 concentrations the lithium aluminosilicate is the main crystalline phase formed as it was observed by XRD and Raman.

III.2.7 Mechanical properties

III.2.7.1 Hardness

Earlier investigation reported that the mechanical properties of glass ceramics specimens were highly dependent on the developed crystalline phase assemblages and microstructures [232]. The hardness of GC is related to both crystalline and residual glassy phases. The changes of the crystalline phases with temperature certainly affect the physical properties of the glass ceramics. Table III-10 shows the microhardness values and elastic modulus of BG and GC

specimens. The microhardness values of the BG samples are between 7.34 and 9.88 GPa. The mean values of Young's modulus of BG are in the range from 52.83 to 109.67 GPa. The largest H_v and the largest Young's modulus value were observed for GP2, being 9.88 and 109.67 GPa, respectively. The hardness value for glass ceramic specimens in this study decreases in the presence of fluoride content and as reported in earlier research [233], whereas no correlation with the P_2O_5 and the H_v value of the glasses has been found.

Table III-10 *Microhardness and Young's modulus values of BG and GC samples (the errors are standard deviation from mean)*

	(*Gpa*)	**GP0**	**GP1**	**GP3**	**GP2**
BG	H_v	07.52 ± 0.41	08.39 ± 0.25	07.34 ± 0.16	09.88 ± 0.27
	E	52.83 ± 2.13	77.46 ± 2.42	58.48 ± 1.16	109.67 ± 3.60
GC	H_v	11.43 ± 0.21	11.45 ± 0.28	11.13 ± 0.27	09.59 ± 0.23
	E	118.82 ± 1.43	118.02 ± 2.90	111.14 ± 2.78	107.62 ± 1.67

GCs possess higher H_v and E than BGs (GP0, GP1 & GP3), they are nearly equal for all samples, and thus the GC network becomes more rigid than in the BG. In contrast, GP2GC exhibit now the lowest value of H_v and E; of 9.59 and 107.63 GPa, respectively. In addition, GP2BG possess higher H_v and E than its corresponding GC. The slight differences encountered in the prepared LMAS GC may outcome from their difference microstructures and the crystalline phases present (Figure III.17) [233]. Large crystal size and intertwined structures lead to high H_v values than globular microstructure of lower crystal size and independent of each other. Therefore, the GP0, GP1 and GP3 GCs with high interlocking crystallinity lead to higher microhardness than the GP2GC which presents non-interlocking crystallinity, i.e. the interlocking between crystals leads to a more rigid structure that corresponds to higher H_v values.

The same behavior as the one encountered in the H_v values is found in the case of E values. In general, for glass materials with a continuous microstructure, the elastic modulus is related to the chemical composition and their corresponding atomic bonding energy, packing density, network dimensionality and network topology (chains, rings, etc.) [234]. However, in the case of GC materials, the elastic modulus mostly depends on the microstructure and type of crystalline phases [233]. The globular structure of GP2GC causes the decrease of the E value

whereas the GC presenting a platelet-like crystallinity present higher *E* values. The delay in the formation of crystalline phases at the highest P_2O_5 concentration may be the responsible of the observed lower *E* value.

III.2.7.2 Machinability

The machinability parameters were evaluated by the indentation method. Baik *et al.* [118,235] introduced (μ_1) the cutting energy at quasi-static state and (*m*) the machinability parameter as,

$$\mu_1 = H_v^{2.25} \quad \text{(III.1)}$$

$$m = 0.643 - 0.122\, H_v \quad \text{(III.2)}$$

Table III-11 shows cutting energy (μ_1) and machinability parameter (*m*) of the respective BG and GC specimens, which were calculated from equation (III.1) and equation (III.2), respectively. According to Tables III-10 and -11, specimen has the lowest H_v value and it has the highest machinability parameter of (–0.252) with lower cutting energy of 88.71 J.mm^{-3}, indicating that GP3BG has better machinability than other samples. Hence, 3.0 mol% P_2O_5 BG has better machinable characteristics. After heat-treatment, specimen (GP2) has the lowest H_v and the highest *m* (-0.527) with lower μ_1 (161.92 J.mm^{-3}) was used, indicating that GP2 glass ceramic has now better machinability compared to other samples. The hardness value of the specimen of GP2GC is low among three examined specimens (GP0GC, GP1GC and GP3GC). From the comparative study of variation of fluorine in glass ceramics, it is revealed that the free-fluorine and high Al_2O_3 content glass ceramic is easy to machine compared to the different studied LMAS samples.

Table III-11 *The machining parameters of the investigated LMAS specimens*

		GP0	**GP1**	**GP3**	**GP2**
BG	***m***	-0.275	-0.381	-0.252	-0.562
	μ_1 (J.mm^{-3})	93.730	120.035	88.712	173.123
GC	***m***	-0,751	-0,755	-0,715	-0,527
	μ_1 (J.mm^{-3})	240,296	241,585	226,406	161,918

III.2.7.3 Flexural strength

Figure III-24 represents the plot of the means of the measured flexural strength as a function of the P_2O_5 concentration for the four examined LMAS samples. The values of σ are between 127 and 194 MPa, and in the range of the literature [5,236]. The flexural strength reaches the maximum value of 194 MPa for the free-P_2O_5 sample. From the XRD analyses reported above, GP0 crystallized mainly on β-spodumene; while the addition of P_2O_5 delays its formation. It is noticed from the graph in Figure III-24 that the flexural strength is sensitive to a small addition of P_2O_5, because it decreases from 194 MPa in GP0 (free-P_2O_5 sample) to 127 MPa in GP1. It is found before that the flexural strength of LAS glass ceramics which based mainly on the crystallization of β-spodumene is in the range of 100–250 MPa [185]. In addition, σ reaches a value of 147 MPa in GP2 (free-fluorine sample) lower than GP0 (with fluorine). Holland et al. [237] reported that fluorine-containing LAS glass ceramics are much stronger than glass ceramics of similar compositions but contain no fluorine.

In the GP3 sample, high-strength (190 MPa) tubular and plate-like crystals can precipitate in the glass ceramics, while in GP2 glass ceramics the shapes of the crystals are usually typically spherical, yielding a strength of 147 MPa. The flexural strength determined in this study is significantly influenced by crystallinity and crystal shape.

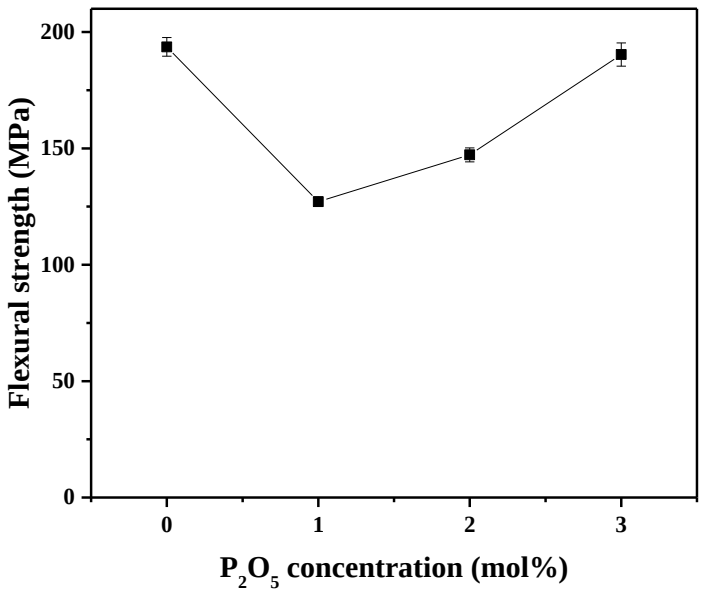

Figure III-24 *Flexural strength as a function of P_2O_5 concentration*

III.2.8 Optical properties

III.2.8.1 Transparency

The photographs of the polished samples are shown in Figure III-25. For all the investigated LMAS glasses, the colors were mainly golden yellowish for low P_2O_5 concentration to brownish for the high P_2O_5 one. However, the color's distribution in GP3 glass sample is uniform, it is blended between brown and light blue. The obtained blue color is very similar to the one found by Taruta *et al.* in lithium-mica GC having almost the same composition [193].

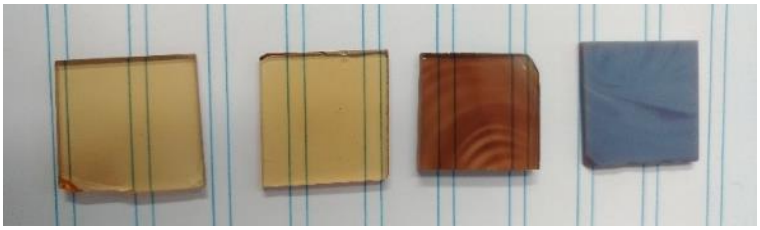

Figure III-25 *Photographs showing the appearance of BGs: GP0, GP1, GP2 and GP3 from left to right, respectively*

The transparency of the glass ceramic samples decreased with the increase of P_2O_5 concentration. The glass ceramic color is more pronounced and more brownish after crystallization. The origin of the darker coloration of LMAS glass ceramics in comparison with parent glasses may be linked to both structural and microstructural evolutions inducing for instance changes in the position of the d–d absorption and charge transfer bands and to light scattering by the small crystals formed inside the glass [28]. Generally, (ZrO_2,TiO_2)-doped LAS glass ceramics present a yellowish-brown coloration whose intensity increases with the crystallization rate and that is partly due to coloring elements like titanium. When the glass is heat-treated, various phenomena occur and the color darkens [238].

III.2.8.2 UV-Vis transmission spectra

Transmittance measurements (200–1100 nm) in the ultraviolet to near infrared (NIR) range were performed. UV-Vis transmittance spectra of BGs and GCs are presented in Figure III-26. Both the two transmittance curves GP0 and GP1 are of the same characteristics. GP0, GP1 and GP2 remain an approximately flat line in the NIR range with high transmittance 85, 80 and ~90 %, respectively.

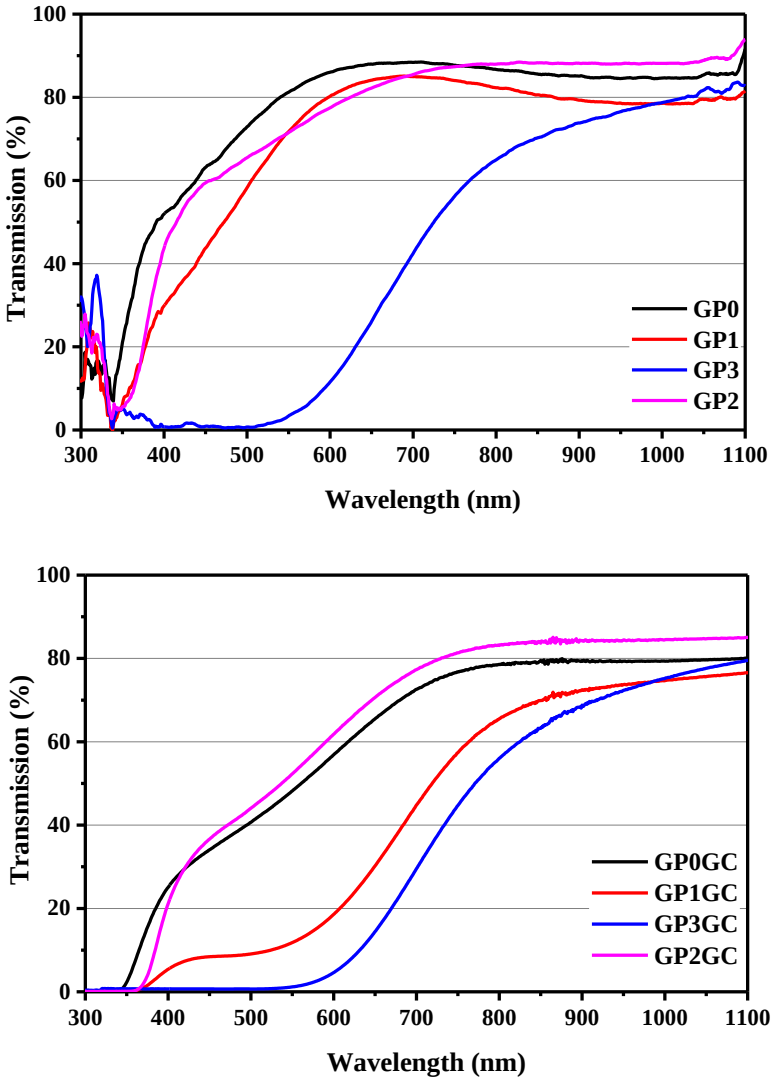

Figure III-26 *UV-Vis spectra of LMAS samples*

The optical cutoff of (GP0, GP1 and GP2) in the visible is in the region between 330–340 nm, while it is 500 nm for GP3, which explains the colors observed. However, the color's distribution in GP3 glass sample is uniform. The decrease of *Si/Al* molar ratio in glasses caused an increase of the opacity [239].

As shown in Figure III-26, the cutoff shifts toward longer wavelengths after crystallization and the transmittance of the samples decreases. The decrease of transparency in the visible range is due to the formation of large crystals. The crystal size is a crucial influencing factor on the light transmittance, the scattering effect of light will be enhanced, which results in the reduction of light transmittance. It had been found that in LAS glass ceramics, the finer grain means that the higher optical transparency can be obtained [5,10,240]. As it can be seen from Figure III-26, the behavior of GP0GC and GP2GC spectral curves is similar. In contrast,

the transmittance at the blue region of GP1GC diminishes to ~10 % and causes an increase in color intensity which makes the GP1GC glass ceramic sample looking brown. The transmittance at ultraviolet spectra are at the low side, and absorption phenomena is observed. The ultraviolet absorption is associated with the number of BO, and absorption limit move to the long wavelength in the case of less BO [241].

III.2.8.3 Optical band gap energy

Optical band gap energy (E_v) of each sample was calculated from Tauc's plot using data obtained from UV-Visible spectroscopy. The relation between absorption coefficient (α) and incident photon energy (hv) was used as proposed by Mott and Davis [242]:

$$\alpha = K\frac{(hv-E_v)^n}{hv} \qquad \text{(III.3)}$$

Where K is a constant, and n is the index, whose value depends on the type of the transition taking place that as 2, 3, 1/2 and 3/2 representing indirect allowed, indirect forbidden, direct allowed and direct forbidden transitions, respectively. In this work, direct allowed transitions (n=1/2) is valid based on Tauc relations [243]. Therefore, $(\alpha hv)^2$ was plotted against the photon energy (hv). The linear portions of the obtained curves were extrapolated to have an intercept on the X-axis. The intercept of the obtained line divided by slope, is equal to energy band gap of optical transitions, as shown in Figure III-27. The values obtained for E_v are shown in Table III-11 for the studied samples.

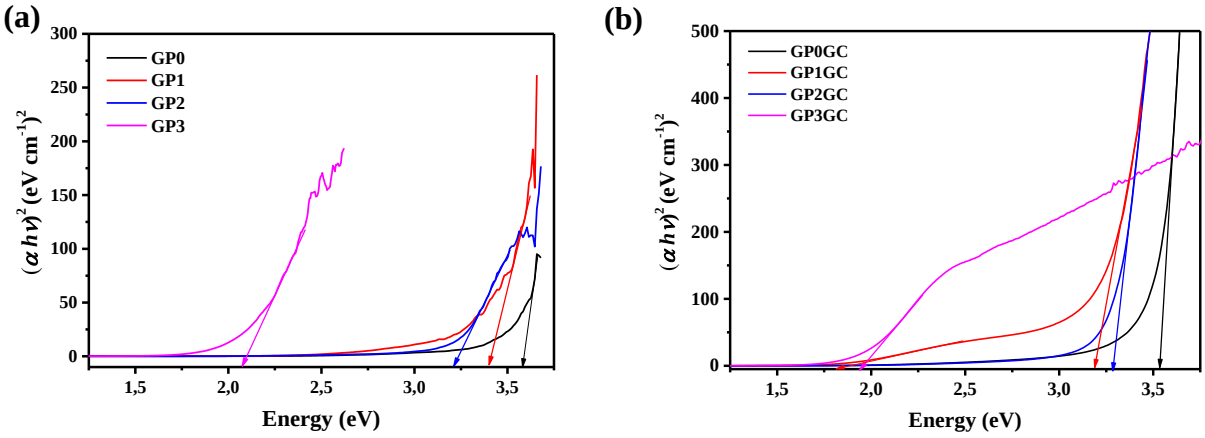

Figure III-27 *Schematic of band gap calculation using the Tauc plot for the studied samples: (a) BGs and (b) GCs*

For the BGs, the energy gap decreases strongly with increasing P_2O_5 content. The decreasing E_v causes the absorption at ultraviolet shifting to longer wavelength (as shown in

Figure III-26a). However, the E_v increases after crystallization in GP2GC (Figure III-26b); higher amount of Al_2O_3 in the presence of P_2O_5, but decreases with increasing P_2O_5 content in the presence of lower amount of Al_2O_3 (GP0GC, GP1GC & GP3GC) [244]. Al ions in the silicate network act as network former replacing the non-bridging oxygens (Si–O) by the bridging oxygens (Si–O–Al) and replacing the O–Si–O links by O–Al–O links, this replacement makes a shift in the main band increasing the energy gap [38]. Therefore, there are two opposite factors which have an effect on E_v in the sample GP2GC, the addition of P_2O_5 makes a strong decrease and the high amount of Al_2O_3 causes an increase. The decrease of E_v (GP0GC, GP1GC & GP3GC) can be associated with the increase of the amount of the non-bridging oxygens then the system has made it easier for the electrons to move through the materials [245].

Table III-12 *Optical band gap E_v of the LMAS samples*

		GP0	***GP1***	***GP2***	***GP3***
E_v (eV)	***BG***	3.58	3.40	3.20	2.06
	GC	3.53	3.18	3.28	1.93

III.2.8.4 Color parameters

From the transmittance and reflectance visible spectra of BGs and GCs, chromatic coordinates have been calculated. The values are given in the Table III-12.

The color analysis results indicate that the highest brightness and the lowest development of color are in GP0 sample. With the increase of P_2O_5, from GP0 to GP3, the L^* value decreases while the values of a^* and b^* parameters shift towards higher a^* and b^* indicating the appearance of the red/yellow color in the GP3 sample. The color's distribution in GP2 and GP3 samples is uniform, appearance of yellow/brown in GP2 and of brown/grey in GP3.

After heat-treatment process, the brightness value L^* decreases reaching a minimum value of $L^* = 19.1$ for the GP3GC sample which presented an amber color. However, GP2GC sample with high Al_2O_3 content, it has been noted a slight decrease of the color parameters.

Table III-13 *Chromatic coordinates of different BG and GC samples*

	L*	***a****	***b****
GP0	87.0	01.7	17.0
GP1	87.0	01.0	23.0
GP3	28.0	30.0	39.0
GP2	80.5	03.5	16.0
GP0GC	78.3	04.5	16.3
GP1GC	48.4	14.2	15.3
GP3GC	19.1	29.5	27.5
GP2GC	77.7	05.2	19.8

III.2.8.5 Refractive index

To achieve the purpose of transparency of glass ceramics, the either of two conditions should be realized: (*i*) the crystallites size are much smaller than the wavelength of light, or (*ii*) where the difference of refractive index between particles and surrounding medium are very small. The prepared BGs show low refractive index (in the range 1.5737–1.5882). It is clear that the GCs possess lower refractive index than their BGs, and it decreases as the P_2O_5 content increase (GP1GC and GP3GC), as is shown in Table III-14. The difference of n_D between the GCs and the BGs is very small, and their difference is only ~0.0002. The precipitated crystals have lower refractive index than that of the BGs, thus it is valid that the refractive index decreases for the formation of crystals. What is more, the continuous variation in glass and crystal compositions during crystallization causes a tiny change of the refractive index, which endows the GCs with high transparency.

Table III-14 *Values of refractive index of LMAS specimens*

		GP0	**GP1**	**GP3**	**GP2**
n_D	***BG***	1.5882	1.5843	1.5737	1.5863
	GC	1.5878	1.5825	1.5724	1.5861

III.2.9 Characterization of silver stained glass ceramics

III.2.9.1 FTIR-ATR results

The painted glass ceramic's structural properties were assessed using FTIR-ATR spectroscopy. The IR spectra of painted glasses are shown in Figure III-28.

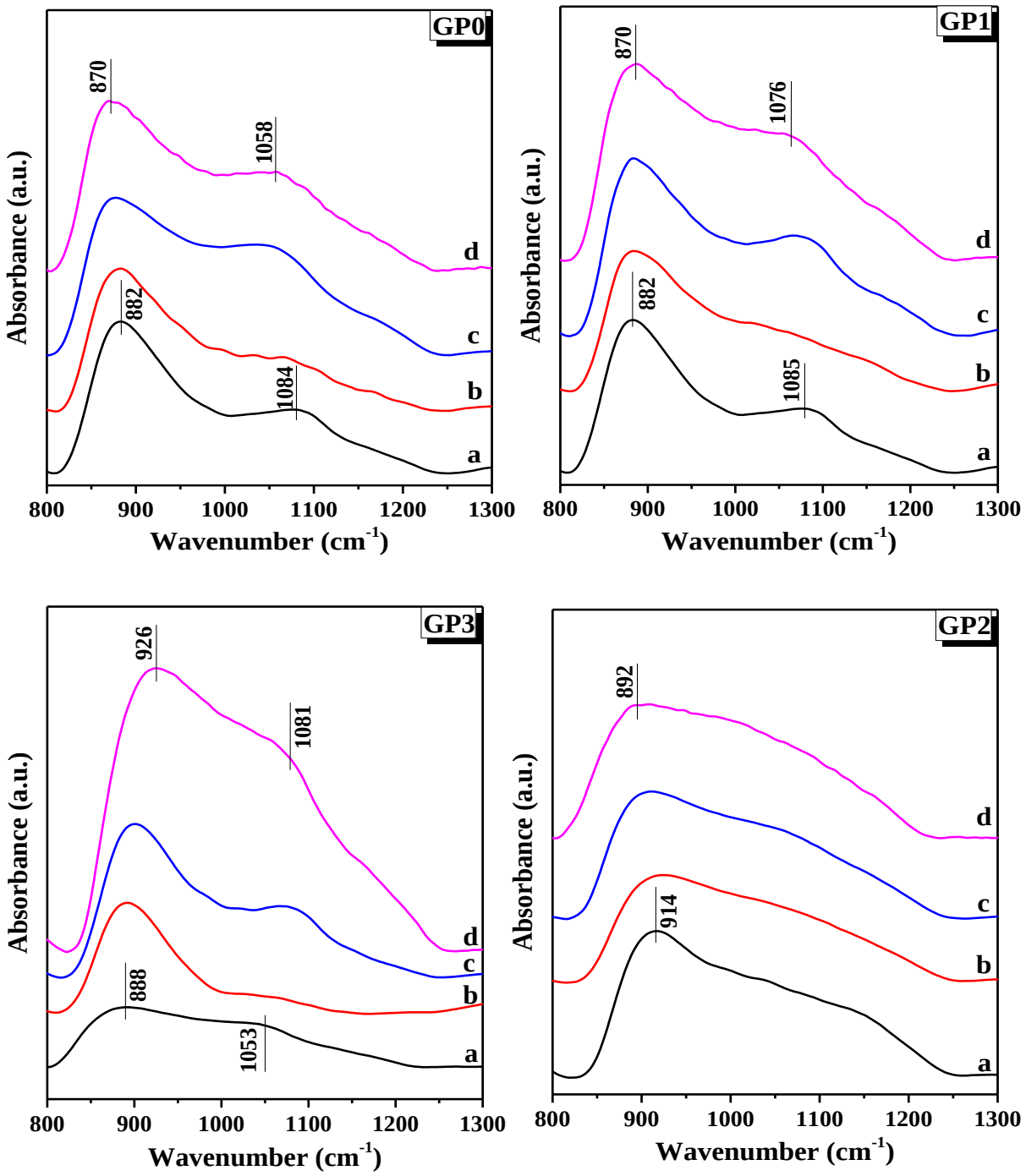

Figure III-28 *FTIR-ATR spectra of painted LMAS specimens: (a) GC 'reference', (b) 2h, (c) 4h and (d) 8h*

The spectra (GP0, GP1 & GP3) exhibit two absorption bands located around 1000−810 cm^{-1}, 1130−1000 cm^{-1} and one shoulder at 1240−1140 cm^{-1}. Compared with the reference sample, the absorption bands of the FTIR-ATR spectra of painted GCs (GP0GC, GP1GC & GP2GC) shift to the low-wavenumber segment with the increase of heating time. The shift of all the bands toward lower wavenumber indicates a weakening of the chemical bonds in the network when Ag is added in the network, due to a network depolymerization [246]. In contrast, with an increase of heating time, all bands are found to shift to higher wavenumber in GP3, which indicate increasing polymerization degree.

The increase in the intensity of the shoulder at 1090 cm^{-1} along with the shift of the optical band gap indicates an increasing number of non-bridging terminal oxygens [246].

III.2.9.2 UV-Vis transmission spectra

After heat-treatment of painted glass ceramics, it was observed an evident color variation in function of the materials used for the paste composition. It was obtained surface colored GCs from beige to brown. Figure III-29 shows UV-Vis transmission spectra of silver painted glass ceramics as well as the spectrum for the unpainted glass ceramic substrate.

As it can be seen from Figure III-29 that the behavior of painted GC materials spectral curves is similar to that of the unprepared GC. The optical cutoff of (GP0, GP1 and GP2) in the visible is in the region between 330−350 nm, while it is in the region between 500−580 nm for GP3. The transmittance of the painted samples decreases after silver stain. The transmittance of GP0Ag2, GP1Ag2, GP2Ag2 and GP3Ag2 diminished to 15, 20, 15 and 40 %, respectively, and causes an increase in color intensity.

For those painted GCs, the UV-Vis spectra presented an absorption band centered at ~560 nm for GP0GC then shifted to ~500 nm for GP3GC by the increase of P_2O_5. This band is might due to the formation and aggregation of metallic silver particles inside the GC structure. It is observed from the different transmittance spectra that the band intensity depends on the heating time of the painted GCs. The increase of treatment time caused the growth of cluster sizes and also the increase in the cluster volume fraction [247]. The later band is more apparent on GP1GC and GP3GC samples, showing that the formation of silver nanoparticles is more important in the structure of these GCs, which explains the intense staining of GP3GC (higher *Si/Al*) glass ceramic compared to GP2GC (lower *Si/Al*) one.

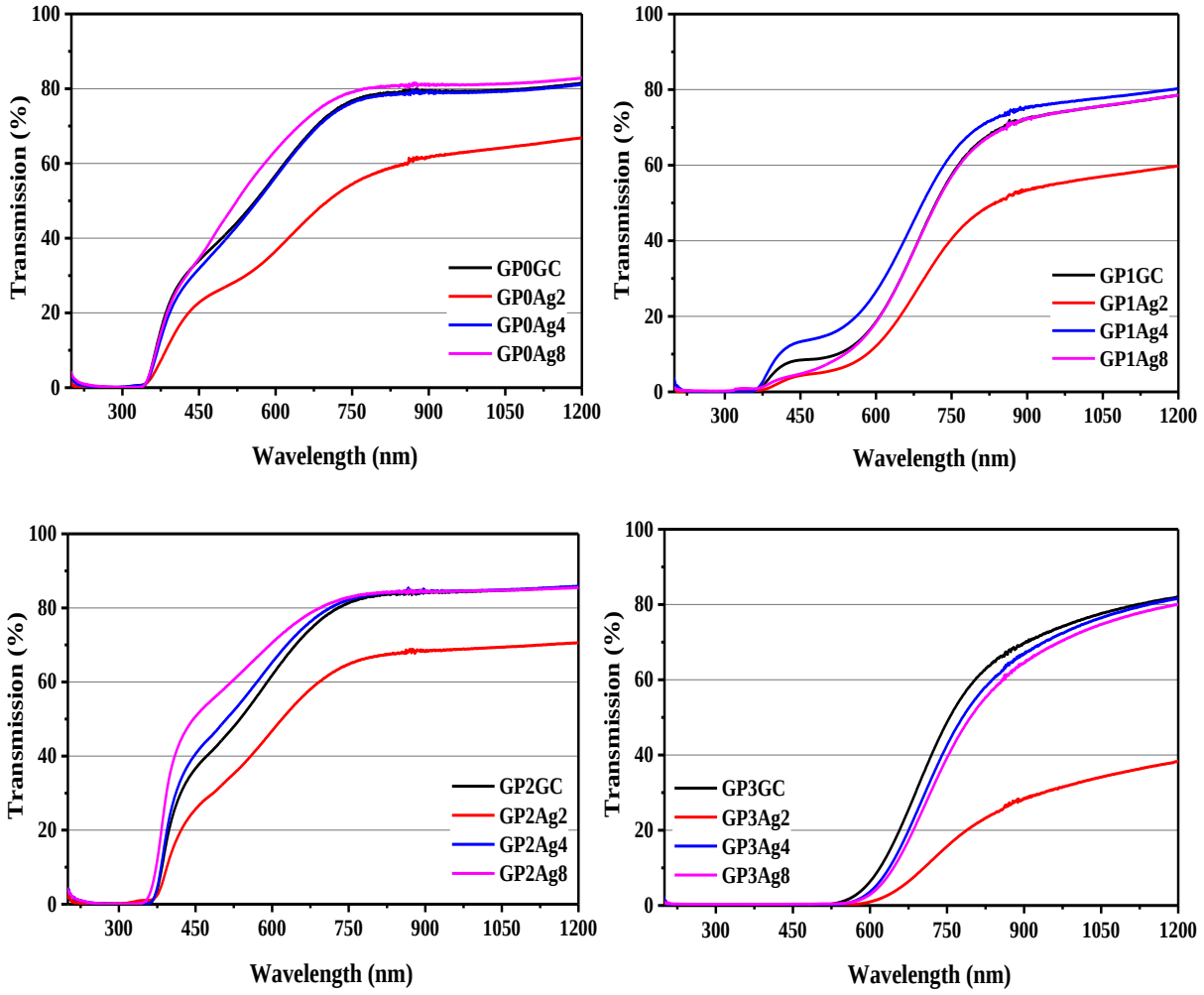

Figure III-29 *UV-Vis spectra of painted LMAS glass ceramics*

III.2.9.3 Optical band gap energy

The optical band gap, E_v, of the painted samples have been estimated by drawing Tauc plots of $(\alpha hv)^2$ *vs.* energy as shown in Figure III-30. The values obtained for E_v are shown in Table III-15 for the studied samples.

It is clear from the Table III-15 that the optical band gap showed a decrease on heating up to a period of 2 h. For further increase in heating time, these values started increasing. The decrease in optical band gap energy on heating up to a period of 2 h may be explained on the basis of the fact that the heating for a short time forms charge transfer complexes (CTCs) in the host lattice.

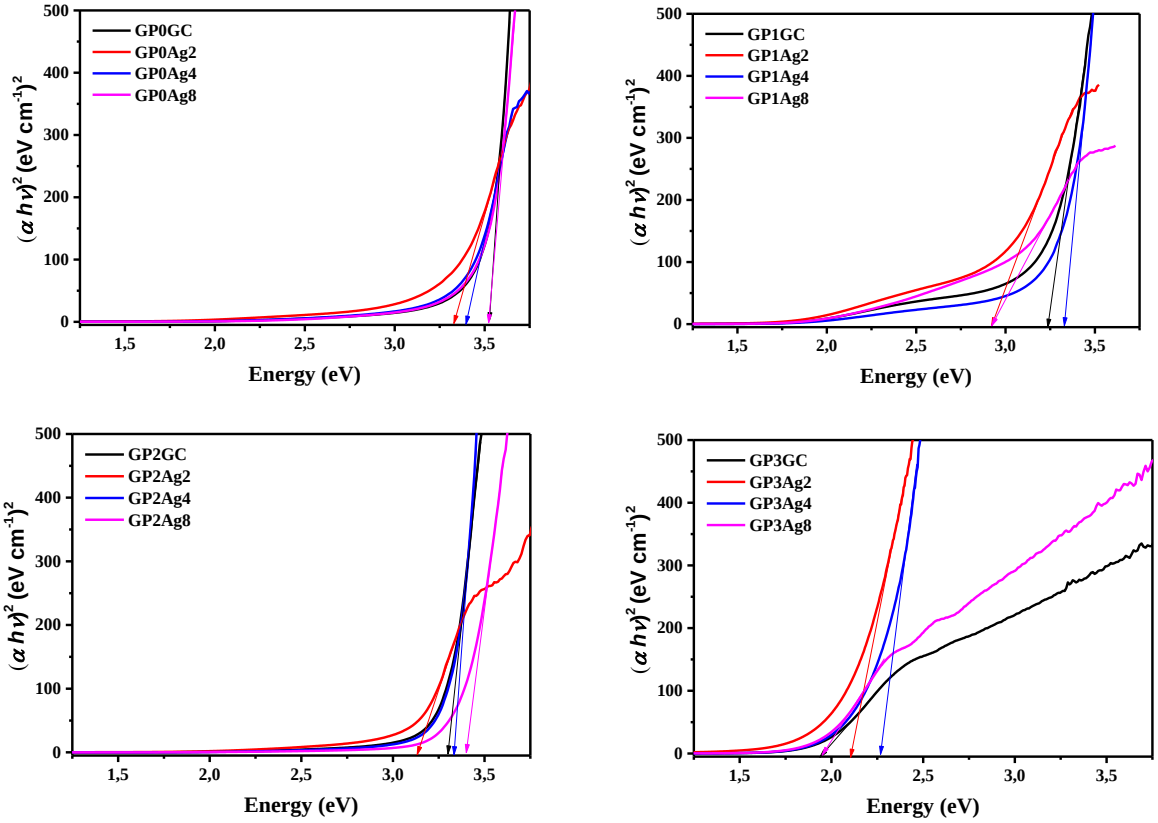

Figure III-30 *Schematic of band gap calculation using the Tauc plot for the studied samples*

When the heating time increases further, it leads to segregation of the $AgNO_3$ in the host matrix. These molecular aggregates impede the motion of charge carriers resulting in increased optical band gap energy [248].

Table III-15 *The optical band gap E_v of the studied LMAS samples*

		GC	*Ag2*	*Ag4*	*Ag8*
***Ev* (eV)**	**GP0**	3.53	3.32	3.39	3.53
	GP1	3.18	2.91	3.32	2.91
	GP3	1.93	2.10	2.26	1.93
	GP2	3.28	3.13	3.33	3.39

III.2.10 Bacterial analysis

The number of viable colonies of the bacterial cells were counted and colony forming units (CFU) were calculated for each sets. The reduction in colony number between the control and test samples were determined and the results are expressed as the logarithm reduction. Log reduction in bacterial count were calculated using the following equation [3]:

$$Log\ reduction = Log\ CFU\ at\ 90min_{controlsample} - \log CFU\ at\ 90min_{testsample} \quad \text{(III.4)}$$

Based on the results gathered from the antibacterial test (Figure III-31a), painted LMAS samples were found to exhibit a high antibacterial activity (>4 log within 90 min contact time) against *E. coli*. In addition to this, the painted glass ceramics treated for 8 h have an excellent biocide activity (>8 log after 90 min), which indicate that they are a powerful tool versus contamination. These results showed a CFU reduction of 99.999 % for all case (>5 log reduction). This means that the presence of silver nanoparticles attached to the glass ceramic surfaces confers it a very high biocide property against Gram-negative bacteria like *E. coli* ATCC 25922.

Painted glass ceramics significantly reduced the adherence of the *E. coli* strain within 90 min (Figure III-31b). Adhesion of the *E. coli* bacterial strain is shown in the Figure III-32. The bacterial viability of *E. coli* decreased significantly on the sample GP3Ag2.

The concentration of silver ions in solution was about four times those in the bacteria (Figure III-31c). The painted glass ceramic samples release silver ions in the bacterial cells, which enhance their bactericidal activity. The presence of silver ions in the solution, at about ~3 µg of silver, reduces the number of colonies of *E. coli*, achieving a logarithm reduction higher than 8 in the sample GP2Ag8, which means a completely safe disinfection. The silver nanoparticles show an efficient antimicrobial property due to their extremely large surface area, which provides better contact with the microorganisms. In previous work [249], it has been proven that in the case of *E. coli*, the lixiviation of ~1 µg/cm^2 of silver led to a strong biocide activity that reduced cell numbers by almost 6 logarithms. The painted glass ceramic samples release silver nanoparticles and silver ions and interact with the cell and some of them also penetrate into the cells causing its death, which enhance their bactericidal activity [250–252].

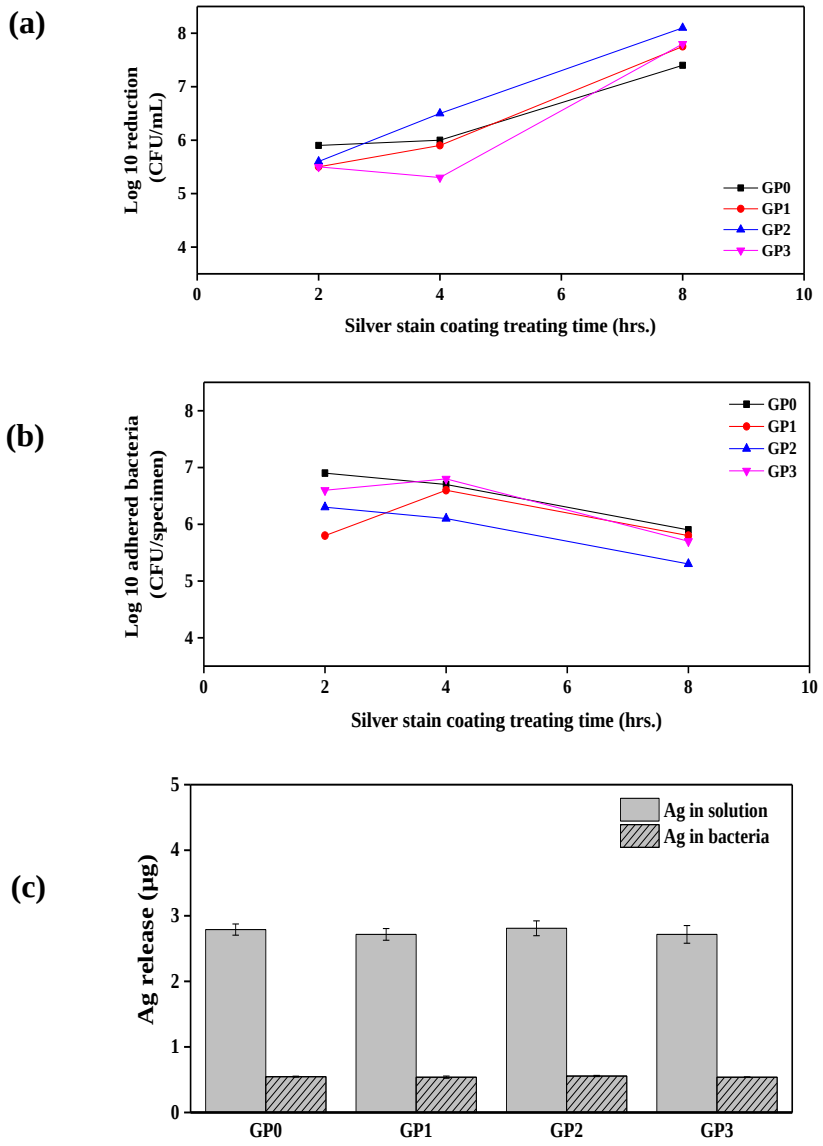

Figure III-31 *Antibacterial efficacy corresponding to different painted LMAS GCs: (a) logarithm of reductions of E. coli after 90 min, (b) logarithm of adhered bacteria and (c) means of Ag release*

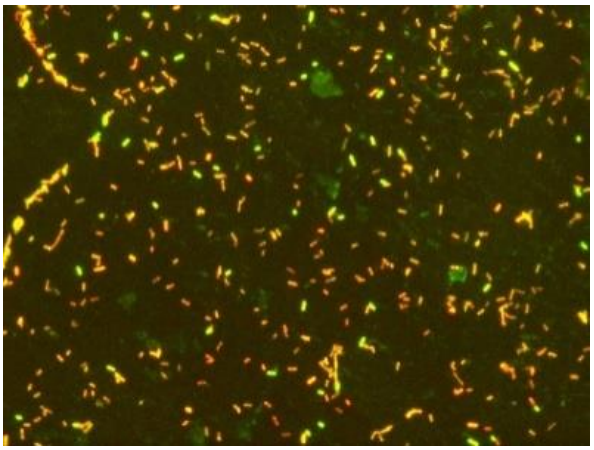

Figure III-32 *Adhered bacteria on the sample GP3Ag2, stained using a Live/Dead BacLight kit. Green indicates viable bacteria, and red indicates dead bacteria (Magnification, ×400; Ec 25922)*

The obtained antibacterial results clearly show that this glass ceramic free-P_2O_5 not only is effective to decrease the growth of bacteria but also to inhibit adhesion. P_2O_5 has not a significant influence on the biocide property, while the longer times (painted GCs treating time) are required to obtain good biocide results.

III.3 MAS glass ceramic

III.3.1 Chemical analysis results

A total weight loss 22 % was obtained after calcination. All elaborated glass compositions were suitable for easy casting after melting for 2 h at 1600 °C, resulting in homogeneous and transparent bubble free glasses. The XRF analysis results of elaborated samples are collected in Table III-16. Negligible changes were observed in the chemical composition of the as-prepared glasses after melting the different batches.

Table III-16 *Chemical compositions (mol%) of the obtained MAS base glasses*

	K_2O	MgO	Al_2O_3	SiO_2	B_2O_3	F	P_2O_5
MP0	5.13	33.80	8.52	40.02	1.40	11.14	0.00
MP1	4.78	33.50	9.71	40.36	1.37	9.48	0.79
MP2	4.76	34.07	8.63	39.93	1.29	9.74	1.58
MP3	4.80	33.69	8.38	39.65	1.30	9.83	2.35

III.3.2 Differential thermal analysis results

Figure III-33 shows the DTA thermograms of the obtained MAS base glasses. The endothermic peak indicates the glass transition temperature. The T_g values were determined to be approximately at 660, 667, 659 and 651 °C for MP0, MP1, MP2 and MP3, respectively. This suggests that the introduction of 1.0 mol% P_2O_5 made the glass transition temperature become higher. A further increase in the content of P_2O_5 (2.0–3.0 mol%) caused a marked decrease of these temperature, since P_2O_5 lowers the glass transition. This may associated with a lower glass viscosity. Series of exothermic reactions were observed over a temperature range of 700–1300 °C. This finding indicates that more than one phase crystallized in this system. The characteristic peaks temperatures, which were measured via DTA curves are given in Table III-17. The addition of 1.0 mol% P_2O_5 content in the composition led to an increasing crystallization temperature but a decreasing intensity of the main crystallization peak. With

addition of 2.0 mol% P_2O_5, the two crystallization peaks tend to merge into a single one, however, the asymmetry toward high temperatures indicates the presence of a crystallization peak of very low intensity.

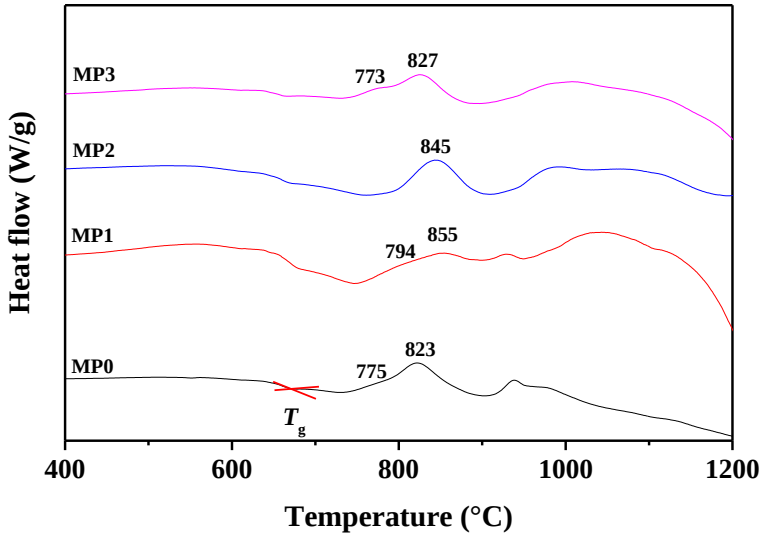

Figure III-33 *DTA curves of the MAS specimens at the heating rate of 10 °C/min*

With further increase of P_2O_5 content in compositions MP3, the crystallization peak tend to split into two crystallization peaks. Nevertheless, the introduction of P_2O_5 increases T_p and delays crystallization according to Tulyaganov and Marques researches [253,254], while broadens the crystallization peak according to Zheng *et al.* [175]. Harper and McMillan [255] observed that the phase separation prior to crystallization in the $Li_2O–SiO_2$ system with 1.0 and 2.0 mol% P_2O_5. It indicates that the complex nucleation agent consisting of fluorine and P_2O_5 will improve the crystallization of MAS glass ceramic, compared with only a single nucleation agent (F).

Table III-17 *Crystallization peak temperatures and transition temperature (°C) of the obtained MAS specimens from the DTA curves*

	T_g	T_{p1}	T_{p2}
MP0	660	775	823
MP1	667	794	855
MP2	659	780	845
MP3	651	773	826

III.3.2.1 Transformation Kinetics

a) Structural relaxation

By applying Kissinger's relation equation (I.5) on the glass transition process, it is possible to determine the activation energy E_g. The calculation of the E_g values is carried out by fitting the data shown in Figure III-34 to a straight line. The slopes of straight lines give the values for E_g. From the calculated E_g values, the $F_{I\text{-}DTA}$ and $F_{I\text{-}vis}$ indexes are obtained by using equation (I.6) and equation (I.7). Table III-18 collects the E_g, $F_{I\text{-}DTA}$ and $F_{I\text{-}vis}$ values obtained for the MAS GCs studied in this work and calculated for the 10 °C/min heating rate.

E_g values changed from 405 to 560 kJ.mol^{-1} by adding and increasing P_2O_5, and decreased to 444 when adding 3.0 mol% P_2O_5. The higher values of the E_g give the higher values of F_I. The reported values of F_I varies widely within the range comprised between F_I = 14.97 for *strong glasses* and $F_I \approx 200$ for *fragile glasses* [68]. F_I values of the studied MAS glass ceramics are higher than the values reported for vitreous silica which is close to 19 [62,171]. The values of glass fragility index indicate that the glass is formed from a kinetically stable liquid. The obtained MAS GCs can be considered as *strong glasses*.

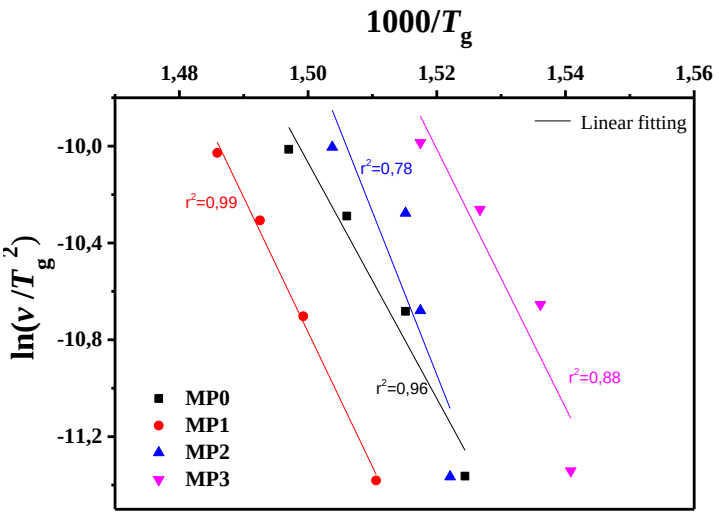

Figure III-34 *ln (ν/T_g^2) vs. 1000/T_g plots and activation energies of viscous flow in the different GCs transition range*

From Table III-18, it is observed that E_g and F_I increase only with the addition of a small amount of P_2O_5 (1.0 and 2.0 mol%) to the glass ceramic composition but if 3.0 mol% of P_2O_5 is added E_g and F_I decrease. Variations of E_g and F_I can be explained on the basis of structural changes due to the introduction of phosphorus atoms. It could be attributed to the creation of non bridging oxygen NBO in which leads less energy for breaking the bonds in the glass.

Table III-18 *Fragility indexes*

	E_g (kJ.mol^{-1})	$F_{I\text{-}DTA}$	$F_{I\text{-}vis}$
MP0	405.16	32.06	37.01
MP1	462.30	36.20	42.34
MP2	559.50	44.34	52.84
MP3	444.14	35.63	41.61

b) Glass Forming Ability and Glass Stability

Table III-19 collects some of GS and GFA parameters obtained for the studied GCs in this section. Thermal stability approach, *S*, suggests that there is a strong correlation between the glass stability and exotherm width. According to this approach more stable glasses exhibit broader exotherms [84]. The *S* parameter which reflects the resistance to crystallization was found to increase up with addition of 1.0 mol% P_2O_5 and then showed a decrease with further increase of P_2O_5 content.

An evaluation of the thermal stability of each glass was also achieved by measuring its working range [108]. A large ΔT_{og} value may indicate that the supercooled liquid can exist in a wide temperature range without crystallization and has a high resistance to the nucleation and growth of crystalline phases [73]. While all the investigated GCs exhibit a ΔT_{og} larger than ≈55 °C, a maximum can be seen for MP3 (≈99 °C). In our case, the addition of high amount of P_2O_5 increases the glass stability. When P_2O_5 content < 3.0 mol%, ΔT_{og} is lower (lower GS). Since crystallization is actually a competitive process with respect to glass formation, a large ΔT_{og} in MP3 would lead to a high GFA.

Table III-19 *GS and GFA parameters (calculated as an average for the four heating rates)*

	ω_2	β	K_H	S	γ_m	β_2	δ	ΔT_{og}	T_{rg}
MP0	0.30	1.64	0.12	09.02	0.65	2.07	1.31	55	0.579
MP1	0.28	1.66	0.16	13.12	0.67	2.17	1.37	83	0.526
MP2	0.22	1.69	0.20	13.10	0.71	2.72	1.44	91	0.546
MP3	0.21	1.70	0.19	11.60	0.72	2.76	1.45	99	0.521

It has been demonstrated that glasses that display only surface crystallization have a T_{rg} higher than approximately 0.58–0.60, whereas glasses with T_{rg} < 0.58 exhibit volume crystallization [256–258]. The P_2O_5 content in the glass ceramic composition has a considerable effect on the value of T_{rg}. An increase in P_2O_5 content leads to a change in the crystallization process of these GCs, from a mechanism of surface crystallization that is predominant in the free-P_2O_5 GC (the value of T_{rg} is near to 0.58) to a prevailing volume crystallization in MP1, MP2 and MP3 GCs. T_{rg} is related to the critical cooling rate [259], thus, the higher the value of T_{rg}, the lower is the required critical cooling rate to prevent crystallization from the melt during cooling. In this work, MP3 composition generates a melt with a higher tendency to crystallize during cooling.

K_H parameters demonstrate the tendency for devitrification during the heating process, i.e., the higher the value of this parameter, the more difficult it is to obtain a crystallized material [260,261]. It was observed that the addition of 2.0 and 3.0 mol% of P_2O_5 in this system provided stability to glass.

The addition of P_2O_5 to the MAS glass ceramic leads to an increase in β, β_2, γ_m, δ and a decrease in ω_2, which is translated to an increase in the GFA and GS of this glass ceramic. However, the most stable glass composition was found as MP3.

c) Crystallization Kinetic and Mechanism

Figure III-35 shows the typical DTA curves of MAS glass ceramic samples measured at different heating rates (5, 10, 15 and 20 °C/min), while Table III-20 presents the values of the thermal parameters obtained for these glass ceramic. Peak positions (temperatures), T_p, full-widths (Δw) and intensities of the peaks were obtained from a deconvolution procedure of different DTA curves assuming that every peak presents a mixed Gaussian–Lorentzian (50 %–50 %) shape.

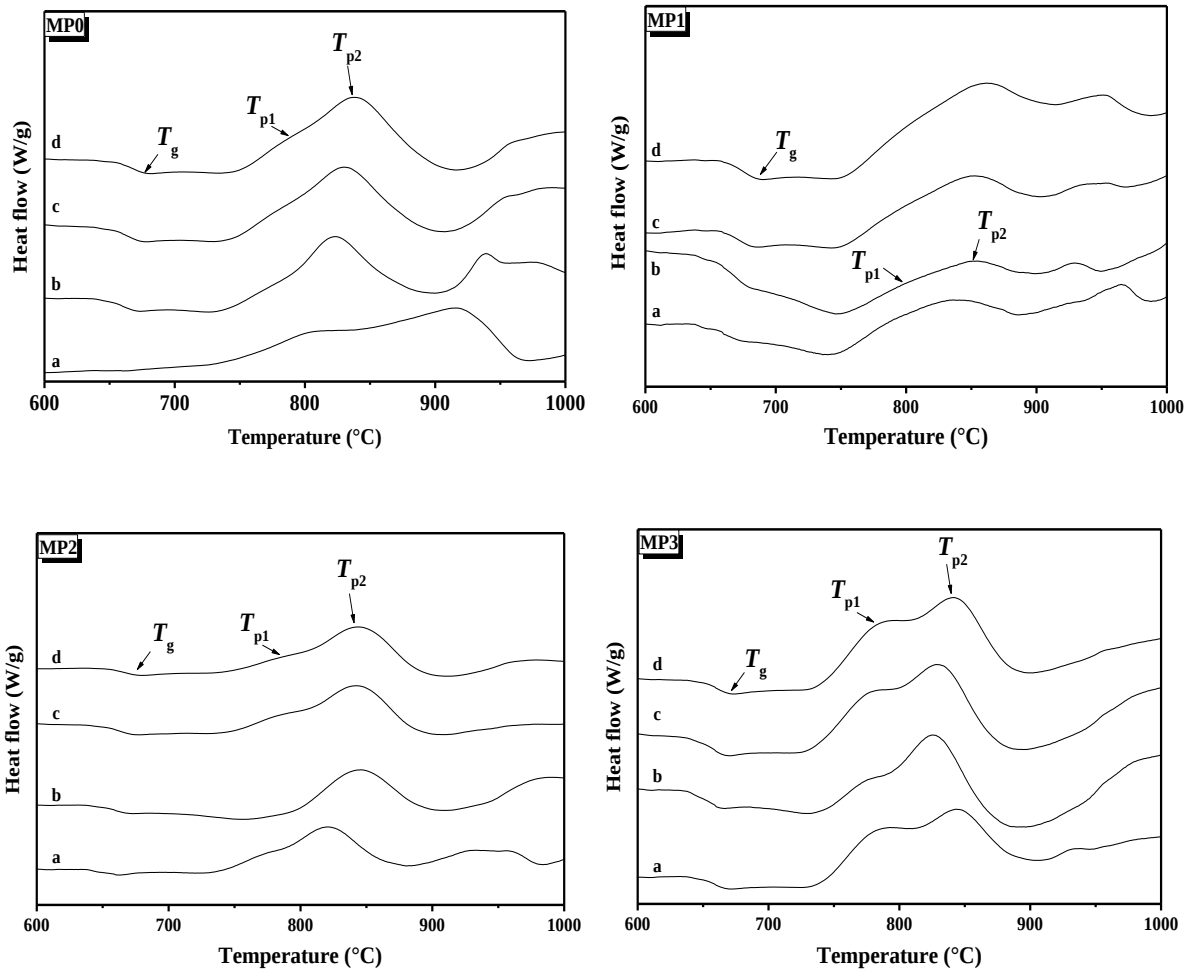

Figure III-35 *DTA curves of the MAS BGs at different heating rates: (a) 5, (b) 10, (c) 15 and (d) 20 °C/min*

All curves generally exhibit one endothermic peak and two exothermic peaks corresponding to the glass transition temperature and crystallization temperatures, respectively. Glass transition temperatures were determined between 649 and 673 °C, shifted to higher temperature with the increase of heating rate.

Han *et al.* [122] have reported that T_g is between 795 and 805 °C in MAS glass ceramic system nucleated by P_2O_5, ZrO_2 and TiO_2, higher values compared to our results. The crystallization peaks shifted generally to higher temperature with the increase of heating rate from 5 to 20 °C/min.

Table III-20 *Characteristic temperatures (°C) from the DTA Curves*

Sample	*Heating rate (°C/min)*	T_g	T_{p1}	T_{p2}
MP0	05	656	752.86	807.20
	10	660	775.20	823.32
	15	664	782.81	830.09
	20	668	789.28	839.40
MP1	05	662	767.42	835.59
	10	667	794.25	855.42
	15	670	793.00	854.24
	20	673	799.00	862.77
MP2	05	657	773.31	822.05
	10	659	780.01	844.85
	15	660	786.52	844.21
	20	665	788.00	844.74
MP3	05	649	786.25	846.32
	10	651	773.20	826.26
	15	655	779.57	831.90
	20	659	787.16	843.75

The variation of crystallization peak (main crystallization peak) with different DTA heating rates can be used to calculate activation energy for crystallization and to determine the crystallization mechanism. Kissinger plots for the different studied MAS glass ceramics at different heating rates are shown in Figure III-36. Figure III-37 shows ln(v) *vs.* 1000/T_p plot, which the E_{co} has been obtained. Figure III-38 shows the plot ln(v/(T_p-T_o)) *vs.* 1000/T_p from which the E_{cab} has been obtained. In addition, the value of E_{cms} can be obtained from the slope of the equation (I.27) and Figure III-39 shows the plot ln(v^n/T_p^2) *vs.* 1000/T_p. The different plots for each sample of the different studied MAS specimens are shown in appendix D.

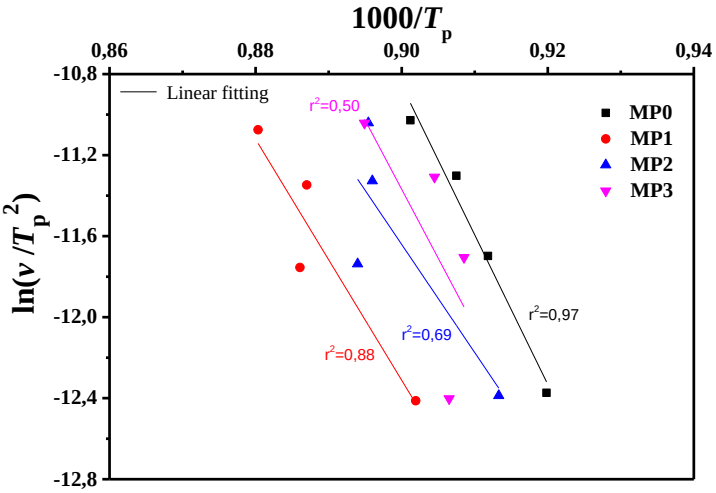

Figure III-36 *Kissinger plot: ($ln(v/T_p^2)$) vs. $1000/T_p$*

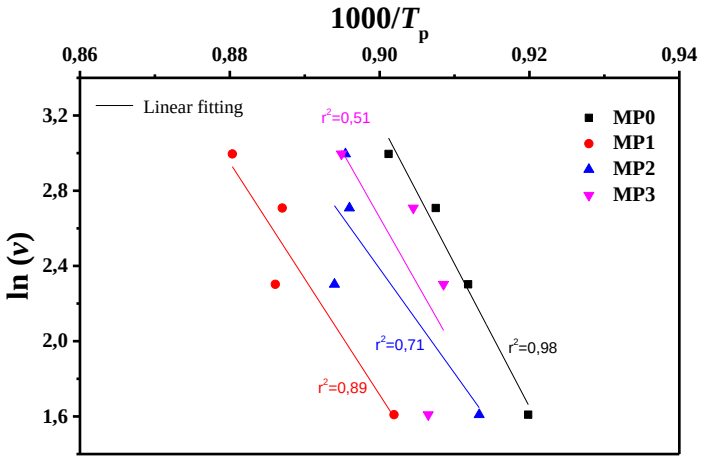

Figure III-37 *Ozawa plot: $ln(v)$ vs. $1000/T_p$*

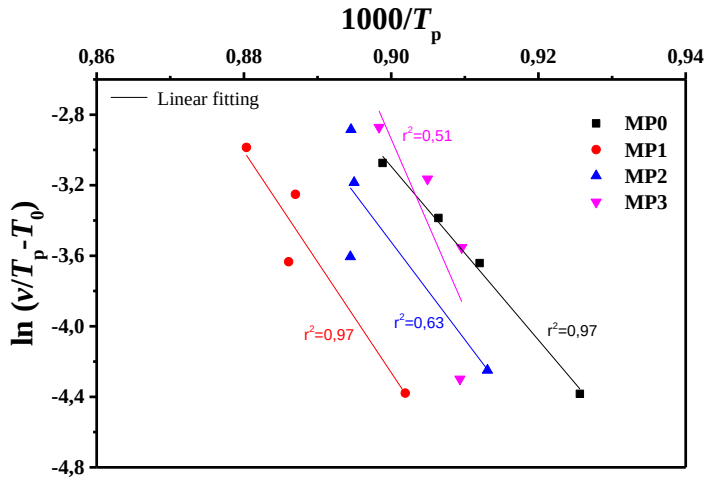

Figure III-38 *Augis and Bennett plot: $ln(v/(T_p-T_0))$ vs. $1000/T_p$*

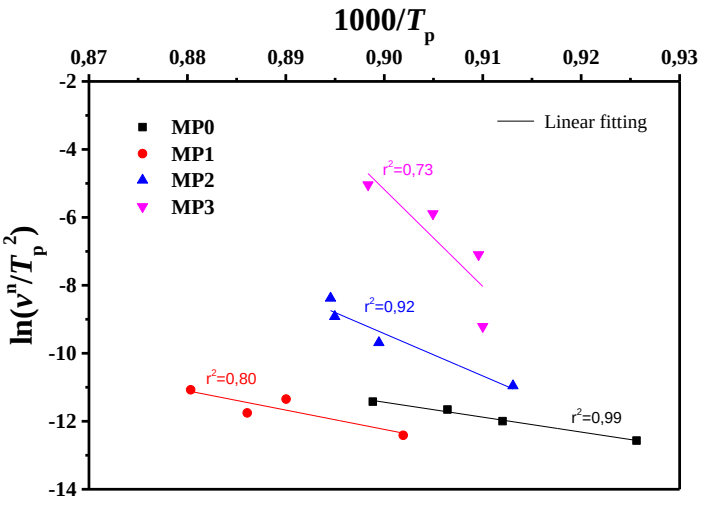

Figure III-39 *Matusita and Sakka plot: ln (v^n /T_p^2) vs. 1000/T_p*

The DTA curves present two peaks at different heating rates. However, the E_c, *n* and *m* values have been determined for both exothermic peaks of the studied GCs. The substantial differences in the E_c values determined by different methods may be attributed to the different approximations used for these models, but, in most cases, the results are very close. The values of E_c for crystallization calculated by different methods and the values of Avrami exponent *n* and the *m* parameter are given in Table III-21.

Table III-21 *Activation energies (kJ.mol^{-1}), n and m parameters of each exothermic peak for the studied MAS specimens (n and m calculated from equation (I.26) and equation (I.27), respectively)*

		E_{ck}	E_{co}	E_{cab}	E_{cms}	*n*	*m*
MP0	***Pk1***	322.39	323.06	329.74	346.22	1.07	1.05
	Pk2	422.07	418.68	409.52	403.85	0.87	0.89
MP1	***Pk1***	343,72	343,54	360,40	361,83	1.12	0.95
	Pk2	494,46	487,92	521,47	485.82	1.93	1.86
MP2	***Pk1***	285.81	288.44	314.59	291.88	1.02	0.94
	Pk2	457.85	452.88	460.34	439.45	1.89	1.92
MP3	***Pk1***	141.27	117.70	215.27	177.16	1.29	0.82
	Pk2	225.04	232.42	267.10	231.63	1.82	1.73

The activation energies are in the range of 200–500 kJ/mol as correspond to MAS glass ceramic materials [8,262,263]. The activation energy corresponding to the main exothermic peak (Pk2) of different MAS glass ceramics obviously increases with addition of 1.0 mol% P_2O_5, then decreases with the respective increasing of P_2O_5. Wherein, the E_c with 3.0 mol% P_2O_5 becomes the lowest, and reaches ~225 kJ/mol, which is far lower than the one with 1.0 mol% P_2O_5 (~500 kJ/mol). It is well known that low E_c value indicates high ability of crystallization. In addition, multiple nucleating agents in our system (both F and P_2O_5) may effectively lower the crystallization activation energy (more than 1.0 mol% of P_2O_5) compared with single one (F in MP0), which also could promote crystallization at lower temperatures. In other studies, the E_c for a MAS glass ceramic is reported to be 296 kJ/mol [8] with complex nucleating agents (P_2O_5, ZrO_2 and TiO_2) and 473 kJ/mol [262] with TiO_2 as a single nucleating agent.

Using activation energy value, the Avrami constant corresponding to the crystallization mechanism was determined. The values of *m* in this work are approximately equal to the values of *n*, the nuclei formed in the previous heat-treatment before the thermal analysis run are dominant (crystallization occurs on a fixed number of nuclei). Surface crystallization occurred in free-P_2O_5 sample (n=m=1). It is reported that glasses with a P_2O_5 content of 0.0 and 0.5 mol% showed a surface crystallization [264]. In other systems, however, the addition of trace amounts of P_2O_5 is required to transform the system to bulk crystallization e.g. the LAS and LMAS systems [265,266]. In our study, the incorporation of P_2O_5 suppresses the surface crystallization and promoted bulk crystallization. The crystallization index *m* is related to the dimensionality of the crystal growth, m=1 indicates one-dimensional growth (surface crystallization), and m=2 implies two-dimensional growth (bulk crystallization). From Table III-21, the *n* and *m* values indicate that the incorporation of P_2O_5 leads to a homogeneous crystallization mechanism for the two peaks and mainly with one- and two-dimensional growth of crystals.

III.3.3 Identification of crystalline phases

X-ray diffraction patterns of different MAS samples, as shown in Figure III-40, Figure III-41, Figure III-42 and Figure III-43, revealed important information on the phase development of the samples powder of BGs and of glasses treated at various temperatures 700, 750, 800, 850, 900 and 950 °C.

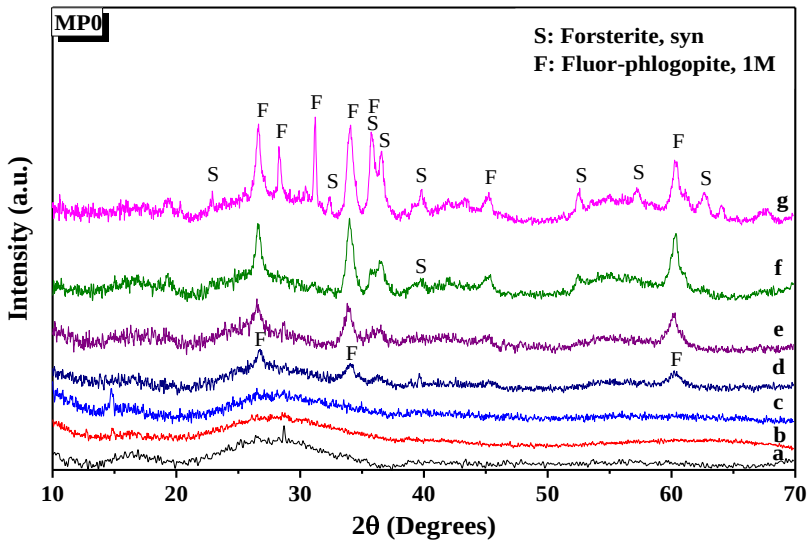

Figure III-40 *X-ray diffraction patterns of MP0 treated at: (a) BG, (b) 700, (c) 750, (d) 800, (e) 850, (f) 900 and (g) 950 °C*

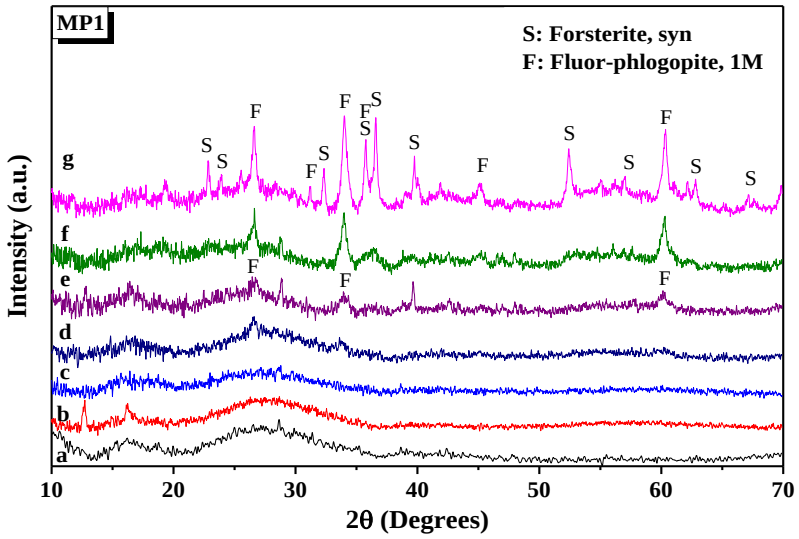

Figure III-41 *X-ray diffraction patterns of MP1 treated at: (a) BG, (b) 700, (c) 750, (d) 800, (e) 850, (f) 900 and (g) 950 °C*

Based on the obtained results it can be stated that the BGs are fully amorphous materials, as evidenced by the lack of clear reflections on diffractograms and occurrence of two broad halos around 17 ° and 28 °. In previous study, they found that if glass shows two broad halos in the XRD patterns, it indicates the presence of phase separation in the present glass [267].

When the MP0 glass was treated at 800 °C for 1 h, some weak diffraction peaks are observed on scattered spectrum of the sample, which indicates that the sample mainly includes glass phase and a small amount of crystal phase. According to JCPDS cards, the latter only

contained a kind of crystal phase, namely fluor-phlogopite (1M, KMg_3 (Si_3AlO_{10}) F_2, JCPDS No. 00-010-0494). Additionally, forsterite (Mg_2SiO_4, JCPDS No. 00-004-0769) crystalline phases are formed at the temperature of 900 °C. The fraction of the amorphous phase decreases during the higher temperature heating treatments. It is clearly seen from Figure III-40 that the diffraction intensity and width of fluor-phlogopite increases with the increase of the crystallization temperature into 950 °C. This means that sample MP0 contained more fluor-phlogopite crystals than forsterite. In MP1 treated at 800 °C, beside the amorphous phase (raised background) there is a range of reflexes which demonstrates the presence of crystalline phases. The performed analysis concluded that there was fluor-phlogopite crystal when heated at 800 °C and forsterite at 950 °C (Figure III-41). According to Figure III-42, fluor-phlogopite appeared when MP2 sample heated at 850 °C. At 900 °C, forsterite evidently appeared. The fluor-phlogopite appeared in MP3 sample heated at 750 °C though the peaks in the XRD pattern were small. As the heating temperature was increased, forsterite appeared at 800 °C while the peaks of fluor-phlogopite nearly do not change. However, much larger and stronger peaks of forsterite appeared at 950 °C, therefore forsterite turned into the master phase in MP3 sample (Figure III-43). Treatment at higher temperature showed an increase in the crystallinity but with relative decrease in fluorinated phase's contents as reported in [268]. P_2O_5 (3.0 mol%) additions induce forsterite crystallization as predominant phase.

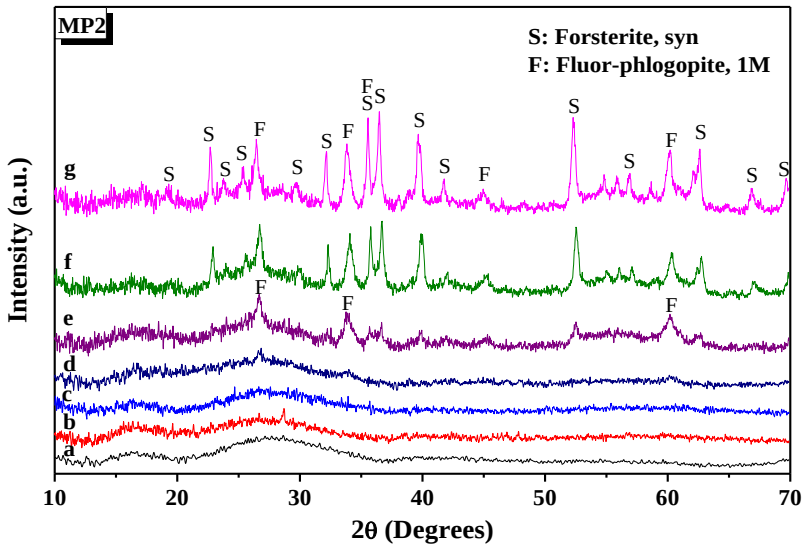

Figure III-42 *X-ray diffraction patterns of MP2 treated at: (a) BG, (b) 700, (c) 750, (d) 800, (e) 850, (f) 900 and (g) 950 °C*

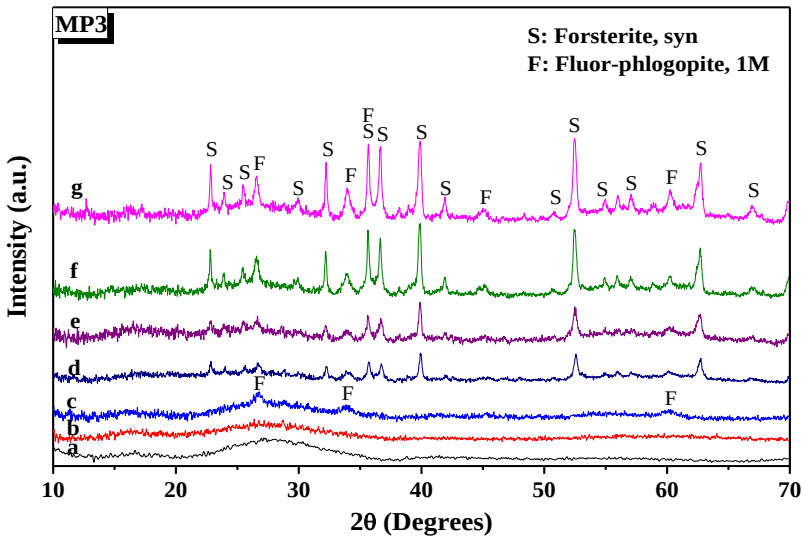

Figure III-43 *X-ray diffraction patterns of MP3 treated at: (a) BG, (b) 700, (c) 750, (d) 800, (e) 850, (f) 900 and (g) 950 °C*

As a result, the addition of P_2O_5 induces the forsterite and fluor-phlogopite formation, with predominance of the forsterite particularly at high temperatures. It is believed that the MgF_2 has an important effect on the formation of phlogopite phase. The fluorine loss at glass composition can be resulted in magnesium and silicon rich phase corresponds to forsterite formation which has been reported before [269]. The Mg_2SiO_4 becomes gradually the major crystalline phase, which indicates the influence of these nucleating agent in the crystallization reactions.

III.3.4 Microstructure development

Figures III-44 illustrates such micro-phase separations in a surrounding glass matrix (a penetration structure). All phases shown in the latter micrograph are amorphous. Each phase has a different chemical composition and is enriched of one or more chemical components compared to the surrounding phase. Such a phase separation causes the inner energy to decrease and enhances the degree of ordering inside the glass and therefore the thermodynamic stability of the system [270]. The size of the phase-separated region increases with the increase of P_2O_5 content.

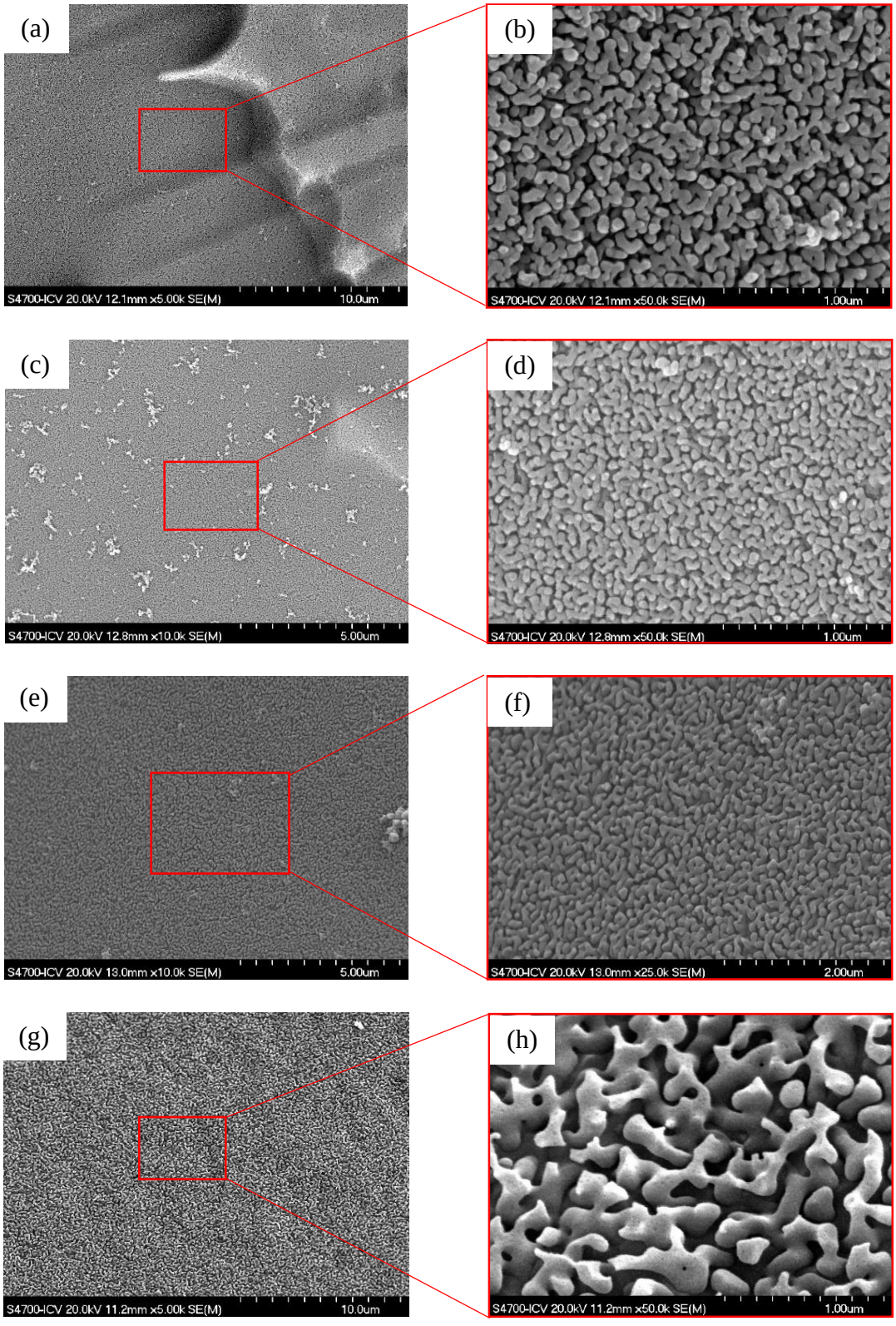

Figure III-44 *FE-SEM micrographs in different magnification of the MAS BGs: (a, b) MP0, (c, d) MP1, (e, f) MP2 and (g, h) MP3*

Figure III-45 shows the micrographs of MP0 heated sample, presented in different magnifications. In the glass ceramics, crystals are surrounded by an amorphous phase. MP0 showed that surface crystallization of *dendritic-like* growths were formed.

Figure III-46, Figure III-47 and Figure III-48 show the microstructure of MP1, MP2 and MP3 heated samples in different magnifications, respectively. All the samples are displaying unusual microstructures. Two different regions were observed: a *flower-like* crystals structure with almost circular shape and a matrix in which they were immersed. It can be seen also that P_2O_5 had a strong influence on the microstructure and morphology of MAS glass ceramic studied in this work. The addition of small amount of P_2O_5 to MAS glass ceramic changed the microstructure from a *dendritic-like* (MP0) to a *flower-like* crystals (MP1, MP2 and MP3). The difference in these two morphologies lies in the respective crystallization mechanisms. This finding is in accordance with the results in Table III-21. By increasing P_2O_5 content, the average diameter of the *flower-like* crystals increased, from 22 µm in MP1, ~26 µm in MP2 to 47 µm in MP3.

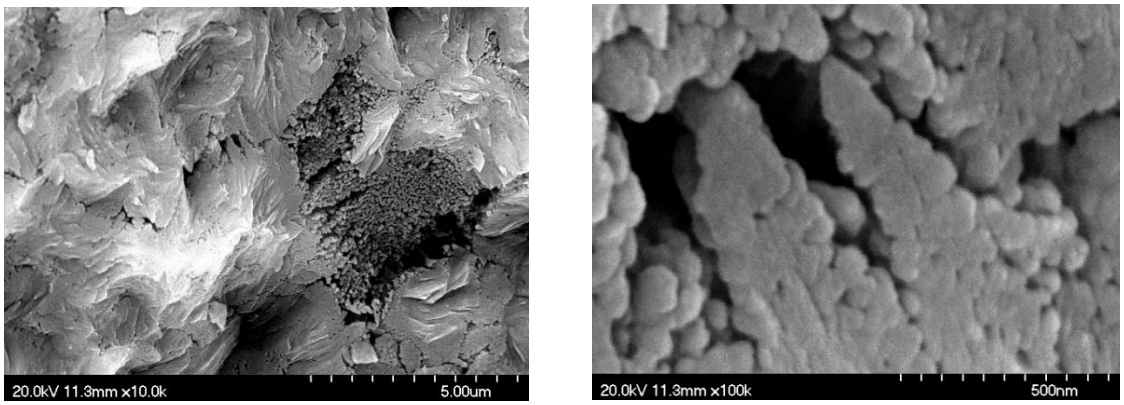

Figure III-45 *FE-SEM micrographs in different magnifications of the MP0 specimen heated at 956 °C for 4h*

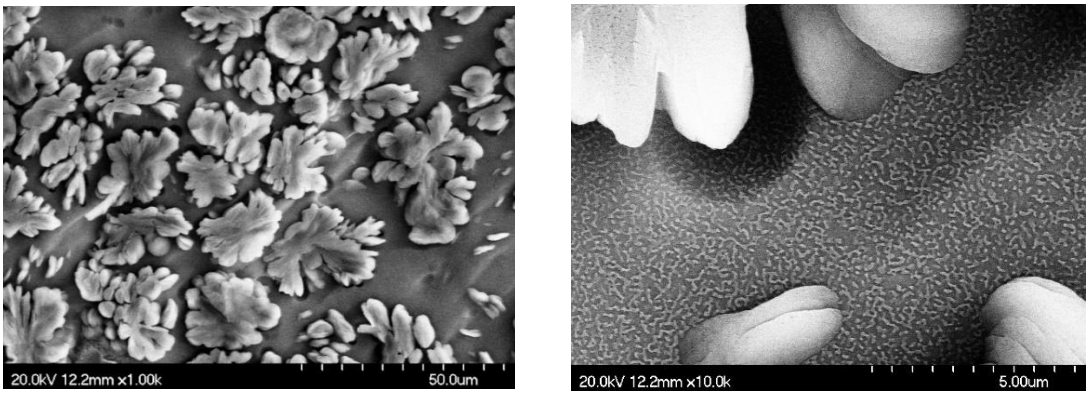

Figure III-46 *FE-SEM micrographs in different magnifications of the MP1 specimen heated at 850 °C for 4h*

The *flower-like* crystals were composed of some crystals with a globular shape. Crystal size was estimated using the Scherrer equation. With the increase of P_2O_5 content, the average size of globular particles increase from 16, 23 to 24 nm for the heated samples MP1, MP2 and MP3, respectively.

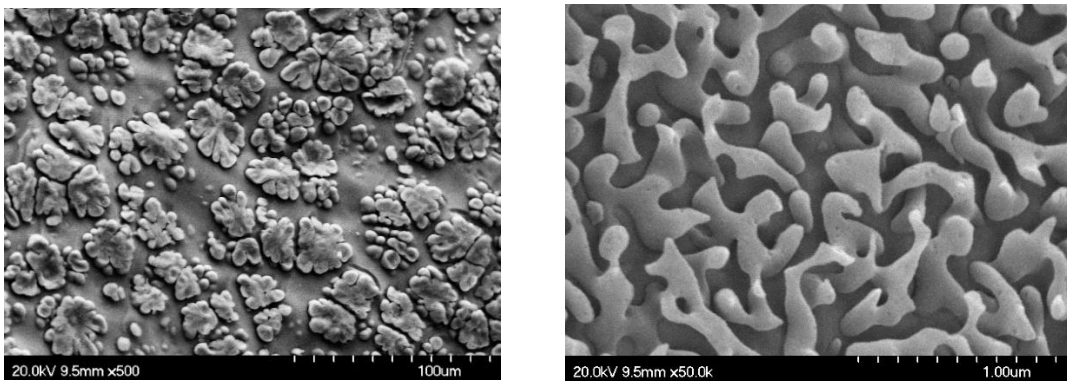

Figure III-47 *FE-SEM micrographs in different magnifications of the MP2 specimen heated at 830 °C for 4h*

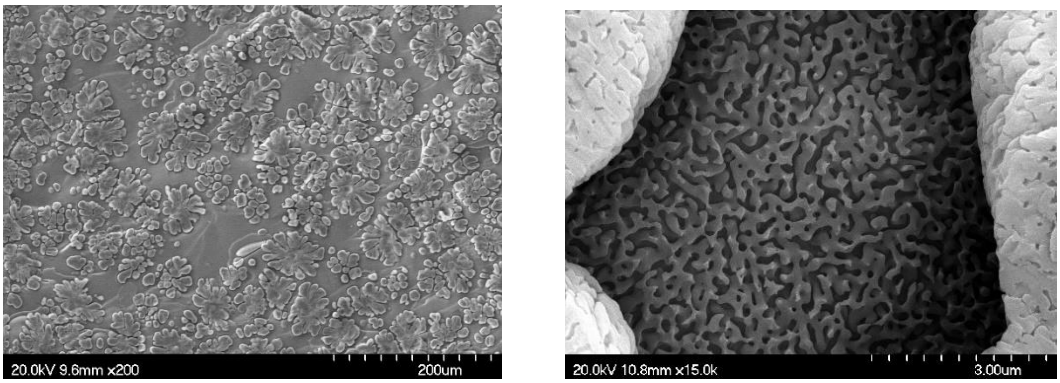

Figure III-48 *FE-SEM micrographs in different magnifications of the MP3 specimen heated at 823 °C for 4h*

III.3.5 Thermal characterization

III.3.5.1 Dilatometric results

Figure III-49 shows the thermal expansion behavior of the glass and the glass ceramics prepared at different treatment temperature. MAS samples have been treated 4 h at the main crystallization temperature for each composition. It is known that the heat-treatment schedule determines the proportions and nature of the resulting crystalline phases, and thus markedly affects the thermal expansion coefficient of the resultant glass ceramic material.

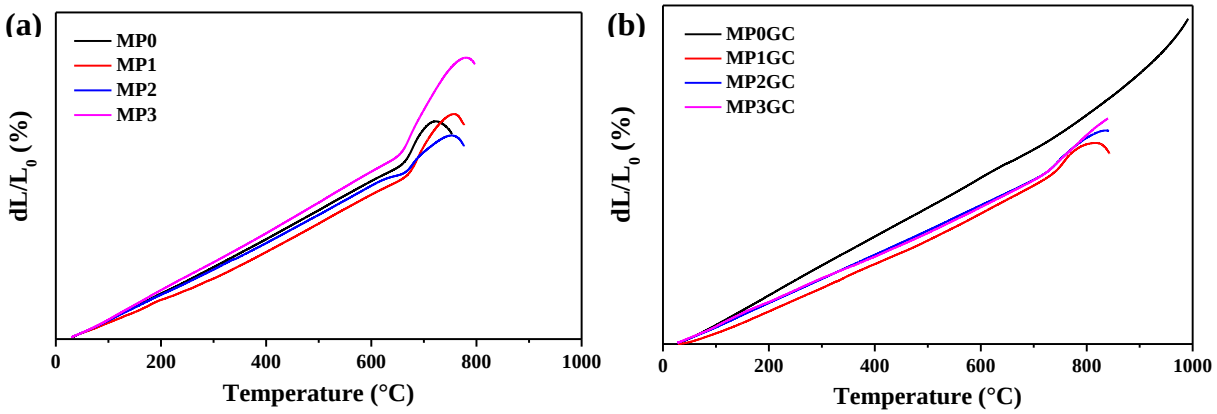

Figure III-49 *Dilatometric curves of MAS samples: (a) BGs and (b) GCs*

The TEC, T_g and T_{DS} of MAS base glasses vary in a somewhat complex manner as evident from Table III-22. After adding P_2O_5, the T_g increases while the T_{DS} decreases in value compared to the free-P_2O_5 sample. The TEC of the investigated MAS base glasses are ranged from 8.38×10^{-6} °C^{-1} to 9.16×10^{-6} °C^{-1} in the 300–500 °C range. There is a slow decrease when 1.0 or 2.0 mol% P_2O_5 was added, and then it rises sharply and attains a value 9.16×10^{-6} °C^{-1} after adding 3.0 mol% P_2O_5. T_g and T_{DS} increase after heat-treatment process compared to base glasses. The free-P_2O_5 GC sample (MP0GC) have the highest value of T_g and T_{DS}, 881 and 990 °C, respectively. In addition, the α-value decreases from a value of about 10.21×10^{-6} °C^{-1} (MP0GC) to a value of 7.98×10^{-6} °C^{-1} (MP3GC) in 300–500 °C range. These results could been associated with the crystallization behaviours from the XRD analysis. This is thought to be due to a higher percentage of forsterite phases formed by increasing content of the nucleating agent P_2O_5.

Table III-22 *TEC, T_g, T_{DS} of MAS specimens*

		MP0	MP1	MP2	MP3
T_g (°C)	*BG*	659	652	631	644
	GC	881	713	705	696
T_{DS} (°C)	*BG*	722	756	752	780
	GC	990	824	835	839
TEC (α~300–500 °C) **±0.1×10^{-6} °C^{-1}**	*BG*	08.71	08.47	08.38	09.16
	GC	10.21	08.31	08.55	07.98

The TEC of the MAS glass ceramics was also practically influenced by the concentration of nucleant used which had a significant effect on the resulting crystalline phases. The presence of fluorine in glass specimen increased the TEC values (11.14 mol% of fluorine in MP0), as found in previous work [233]. In previous glass ceramic works, the measured thermal expansion coefficient was 9.2×10^{-6} °C^{-1} for fluor-phlogopite [271], and 8.5×10^{-6} °C^{-1} for forsterite [139]. In the present investigation, marked changes in the thermal expansion occurred depending on the type of both the major and minor crystalline phases formed. Table III-22 shows that the thermal expansion coefficient decreased with formation of forsterite (MP1GC, MP2GC & MP3GC) which has a lower thermal expansion coefficient and increased under the dominance of the fluor-phlogopite (MP0GC).

III.3.5.2 Hot-stage microscopy results

By using the HSM characteristic temperatures (T_{FS}, T_{MS}, T_S, T_{HB}, and T_F) and those found by DTA analysis (T_g), the relative viscosity behavior of MAS specimens has been obtained. Figure III-50 presents variation in the relative area with respect to temperature as obtained from HSM for all the investigated MAS glasses.

The four glass samples present a reduction of the sample area (A/A_0) in the temperature region 750–800 °C, and a high one in the region 1250–1350 °C. This is due to the formation of the crystalline phases around 800 °C (as shown in Table III-17). In the temperature range (800–900 °C), the formation of crystalline phases avoid the sintering of glass particles, which are mainly transformed to crystals. Then, those crystals melt and transform to liquidus, which was indicated by the high decrease of the A/A_0 area in the region 1250–1350 °C.

Table III-23 summarizes the values of the temperatures corresponding to the characteristic viscosity points obtained from the photographs taken during the HSM experiment. Figure III-51 shows the logarithm of viscosity (η) as a function of temperature. In general, T_{FS} values show an increasing tendency with increasing content of P_2O_5 then it decreases at MP3 (3.0 mol% P_2O_5). The viscosity decreases very slowly in the wide temperature region (700–1200 °C), where the formed crystalline phases are stable.

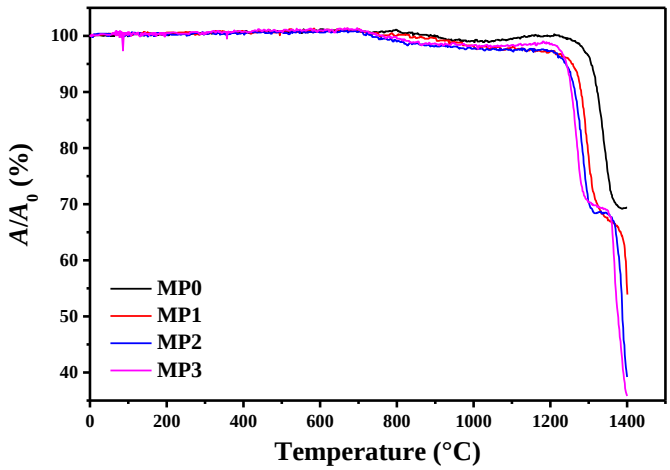

Figure III-50 *Variation in relative area (A/A_0: A_0 is the initial area at room temperature, A is the area at defined temperature) during the HSM experiments*

As it has been mentioned, Figure III-51 shows that MAS glasses present similar η variations with temperature except in the 1200–1400 °C range. For the MP3 glass an η value of $10^{7.8}$ P is achieved at about 1220 °C, whereas MP2 needs 1315 °C to achieve a similar viscosity. The above results have shown that P_2O_5 (1.0–2.0 mol%) influences several temperatures such as, maximum shrinkage, softening, ball, etc., and decreased the high-temperature viscosity of glass, while the viscosity increases when the content of P_2O_5 is more than (2.0 mol%). Xiao *et al.* also found that the viscosity of $Li_2O–Al_2O_3–SiO_2–P_2O_5$ glass decreased consistently as the P_2O_5 content increased [272]. The content of P_2O_5 has an obvious influence on the viscosity.

Table III-23 *Experimental temperatures of the fixed viscosities points during the HSM experiment*

Characteristic points	**Temperatures (°C)**				***η* (P)**
	MP0	**MP1**	**MP2**	**MP3**	
Transition	660	667	659	651	$10^{12.3}$
First shrinkage	705	710	720	700	$10^{9.1}$
Maximum shrinkage	1270	1280	1315	1220	$10^{7.8}$
Softening	1290	1295	1374	1275	$10^{6.3}$
Ball	1351	1380	1379	1350	$10^{5.4}$
Half ball	1391	1399	1387	1371	$10^{4.1}$
Flow	>1400 °C	>1400 °C	1398	1391	$10^{3.4}$

The flow temperature of MP0, MP1, MP2 and MP3 are >1400 °C, >1400 °C, 1398 °C and 1391 °C, respectively. It can be seen that, when the content of P_2O_5 increased to 3.0 mol%, the melting temperature of MAS glass decreased (Figure III-50). The main reason is P_2O_5 possess much lower melting point than those of Al_2O_3 and SiO_2, and introducing P_2O_5 lowered the eutectic point of the glass system [272].

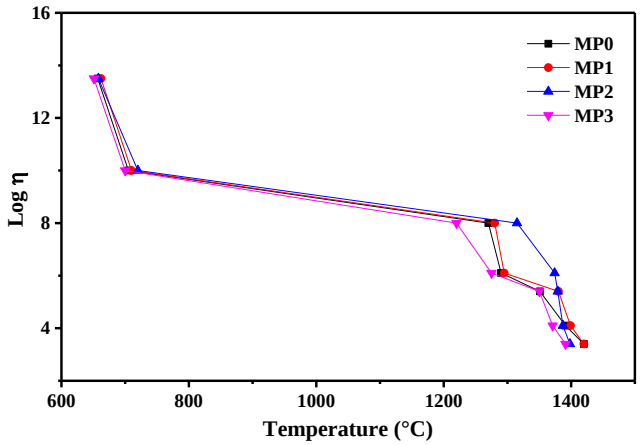

Figure III-51 *Viscosity curves of MAS glasses obtained from HSM measurements*

III.3.6 Structural analysis

III.3.6.1 Raman results

Raman spectra of all the glass ceramic samples treated at different temperatures were measured. Figure III-52 shows Raman spectra of base glass and glass samples heat treated 750–950 °C for 1 h. The Raman spectrum of MP0 base glass and MP0 treated at 700 °C consists of a broad band in the range of 1200–800 cm^{-1}. At 700 °C of heating, the Raman spectrum of MP0 consists of a wide broad band and a weak band in the range of 800–650 and 1200–800 cm^{-1}, respectively. After heat-treatment at 800 °C, absorption band at 683 cm^{-1} attributable to the fluor-phlogopite crystal appear. With further annealing 850–950 °C, the intensity of the peak at 683 cm^{-1} increase in intensity and broad while the band with maxima at 1034 cm^{-1} become sharper and two new weak bands to the appears at 276 and 320 cm^{-1}. Raman frequencies at 282, 326, 684, and 1034 cm^{-1} listed by Mckeown *et al.* [273] for phlogopite correspond with our observed bands at 276, 320, 683 and 1034 cm^{-1} for fluor-phlogopite.

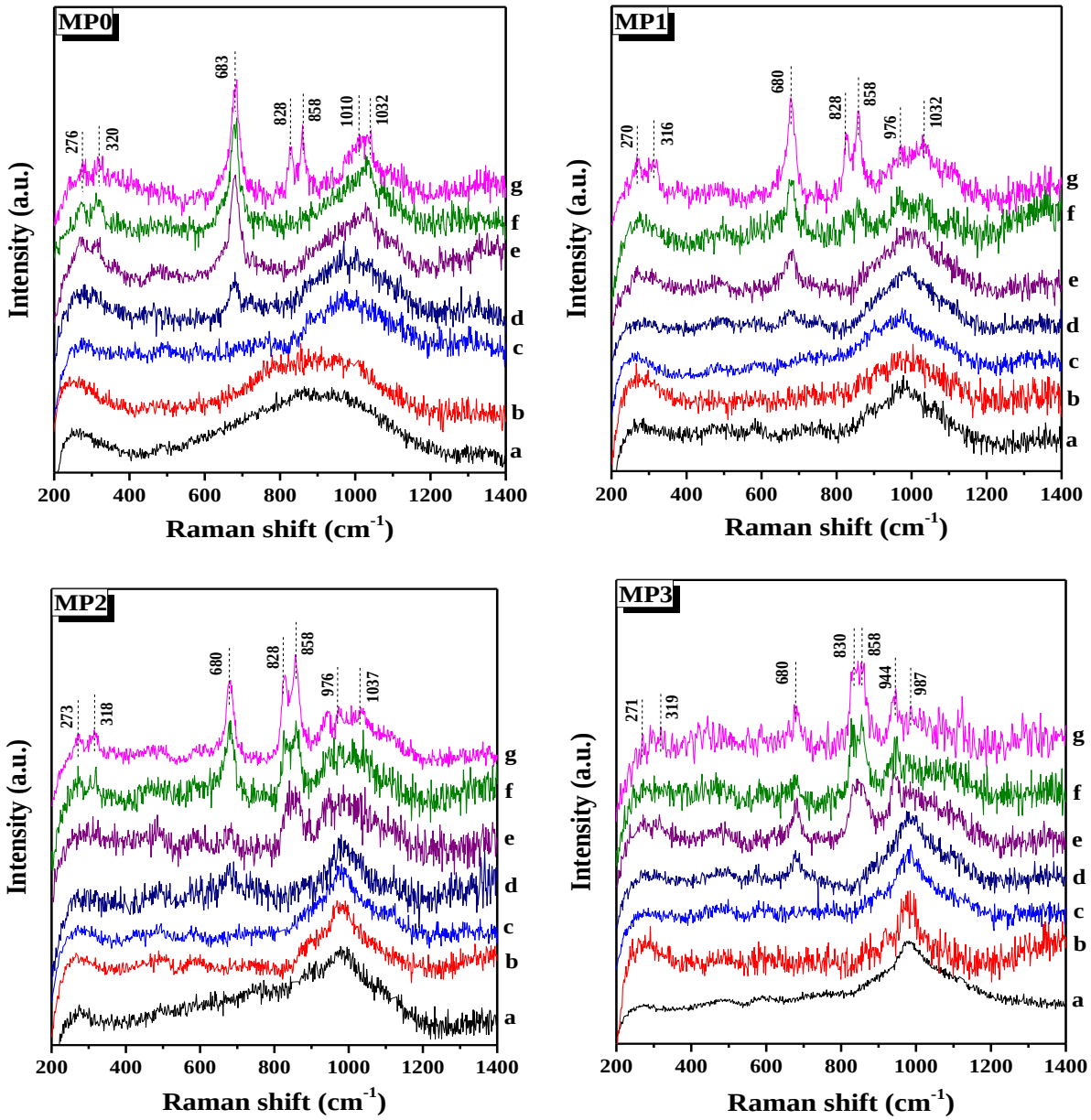

Figure III-52 *Raman spectra of different MAS samples treated at: (a) BG, (b) 700, (c) 750, (d) 800, (e) 850, (f) 900, and (g) 950 °C*

The transformation of the MP0 glass to a glass-ceramic leads to a narrowing of the Raman spectra mainly in the 1200–900 cm^{-1} range and a slight increase of the band at about 550 cm^{-1}. In addition, new two medium-intensity peaks at 832 and 858 cm^{-1} appear after heat-treatment at 950 °C, which are attributed to forsterite crystal. The Raman spectra of the forsterite crystals have a characteristic set of two bands, near 858 cm^{-1} which correspond to Si–O asymmetric stretching band $(Si–O)_{a\text{-}str}$ and ~832 cm^{-1} which correspond to Si–O symmetric stretching band $(Si–O)_{s\text{-}str}$. The two strongest Raman bands at 832 and 858 cm^{-1} in forsterite may be the mixtures of symmetric stretching and asymmetric stretching or asymmetric stretching for the 832 cm^{-1}

band and symmetric stretching or symmetric deformation for the 856 cm^{-1} band. The peak 322 cm^{-1} correspond to rotation of SiO_4 [274–276].

Fluor-phlogopite appears after heat treatment at 800 °C in MP1 and MP2 then increase in intensity with increasing heating temperature. forsterite appears at 900 °C in MP1 and at 850 °C in MP2 and MP3. In addition, forsterite become the main crystal in MP3. It is clear from (Figure III.52) that upon increasing of P_2O_5 content, the amount of fluor-phlogopite crystal decreases in the MAS glass ceramic while forsterite crystal increases.

III.3.6.2 FTIR results

FTIR test were carried out on the BGs and glasses treated at different temperatures (750–950 °C) to study the change in the structure of the glass. The room temperature FTIR absorbance spectra of different samples are presented in Figure III-53. The spectra are shown in the range of 400–1400 cm^{-1}, which is characteristic of the studied materials.

The spectra of BGs exhibit four broad absorbance bands in the region of 1400–400 cm^{-1}. The high full width at half maximum of the bands confirms a high percentage of the amorphous phase of the tested materials. The most intense bands lie in the 1400–800 cm^{-1} region, the next between 500 and 400 cm^{-1}, then between 650 and 500 cm^{-1}, while the least intensive lies between 800 and 650 cm^{-1}. The broad and intense band in the 1400–800 cm^{-1} region is assigned to the asymmetric stretching vibration of bridges Si–O-(Si) and Si–O-(Al), bonds associated with the tetrahedrons [SiO_4] and [AlO_4]. This range of wavenumbers depends on the number of NBOs, which form a tetrahedron [239,277]. Mg^{2+} and K^+ ions act as network modifiers, inducing NBOs, and lie in interspaces of the glass network. Al^{3+}, as a network former, can substitute Si^{4+} to form [AlO_4] tetrahedron [278,279]. As the molar ratio of $Al_2O_3/(MgO+K_2O)$ is less than 0.5, [AlO_4] tetrahedron is easy to form in the investigated glasses. According to the literature, bands in the region of 800–650 cm^{-1} come from stretching vibration of Al–O bond in [AlO_4] tetrahedron and/or symmetrical stretching vibrations of Si–O–(Si,Al) and vibrations related to presence of silico-oxygen and alumino-silico-oxygen rings [280,281]. The band near 560 cm^{-1} could be attributed to either stretching vibration of [MgO_4] [282] or to the bending vibration of the Al–O bond in [AlO_6] [283]. Also, the band near 450 cm^{-1} could be assigned to bending vibration of O–Si–O linkages and Si–O–Si-bending vibration modes of [SiO_4] unit [179,280].

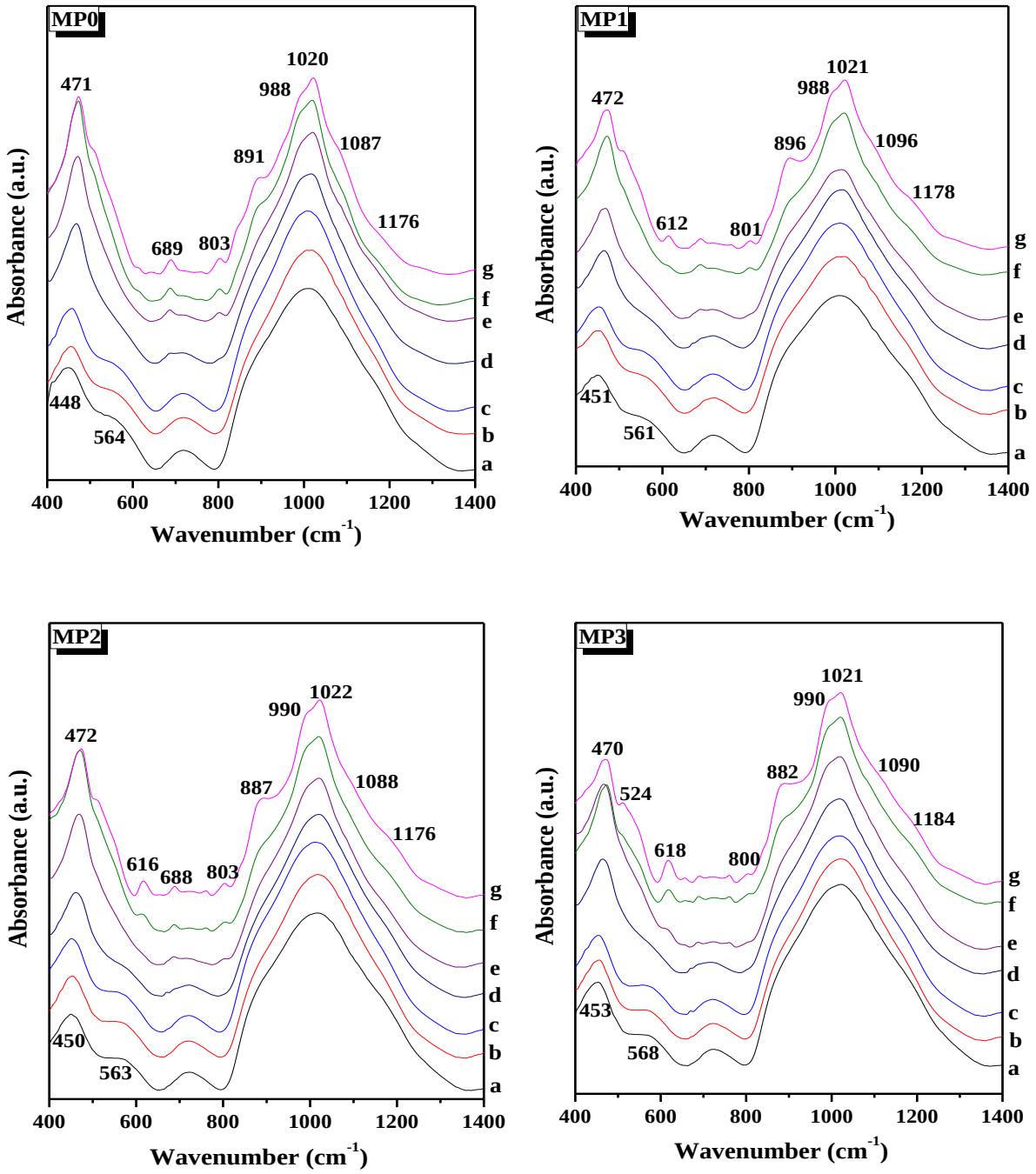

Figure III-53 *FT-IR spectra of different MAS specimens treated for 1 h at: (a) BG, (b) 700, (c) 750, (d) 800, (e) 850, (f) 900 and (g) 950 °C*

Figure III-53 shows only three clearly visible absorbance bands in the sample MP0 when heat is treated at 850 °C for 1 h. It means that at 850 °C, all the glass specimens are not well crystallized. The IR spectra of glasses heated at 950 °C are clearly different from that of BGs. The multi-component bands appeared in the region 1400–800 cm^{-1} indicate the mineralogical complexity of these GCs. With the increase of crystallization temperature, the intensity of the main absorption bands increases, which indicates the improvement of crystallinity. The band at

725 cm^{-1} decreased in intensity, and then disappeared with the increase of heating temperature. This may indicates the transformation of a glass structure to a glass ceramic material. In addition, the intensity of the band at about 600–400 cm^{-1} is lower than the band at about 1300–800 cm^{-1} in the free-P_2O_5 specimen (MP0). By increasing heating temperature, the intensity of the 600–400 cm^{-1} band increases and becomes approximately as high as the 1300–800 cm^{-1} band. It can be found also that some new absorption bands are appear, the main band locates at 470 cm^{-1} could be attributed to bending vibrations of O–Si–O and O–Al–O [277] and the weak bands near 688, 760 and 802 cm^{-1} could be attributed to vibrations of 4 and/or 6-membered silico- and alumino-silico-oxygen rings present in the glass structure [277], bending vibration of Al–O–Al in [AlO_4] tetrahedron [284] and symmetric stretching vibration of Si–O–Al bond [283], respectively. The band at 880–887 cm^{-1} is associated with asymmetric stretching vibrations of Si–O^- and Al–O^- [277,285], the shoulder near 990 cm^{-1} with stretching vibrations of Si–O (Si) [277], the most intense band with the maximum at 1020–1030 cm^{-1} with the presence of the combination of the asymmetric stretching vibration of two types of bridging bonds Si–O(Si), Si–O(Al) and broken bridges Si–O^- and Al–O^- [286], the shoulder at ~1090 cm^{-1} with asymmetric stretching vibration of Si–O–Si bond in [SiO_4] tetrahedron [283] or asymmetric stretching of P–O–P groups [122], the shoulder at 1180 cm^{-1} with stretching vibrations of Si=O [277] and the shoulder near 1270 cm^{-1} with asymmetric stretching vibration of [BO_3] units [280].

Mg^{2+} can induce the non-uniform arrangement of anionic charge [278]. Mg^{2+} and K^+ ions help to the balance of $[AlO_4]^-$ tetrahedron, contributing to the formation of $[AlO_4]_2Mg$ and $[AlO_4]K$ complexes in glass networks [280]. The excellent compatibility between the complexes and [SiO_4] tetrahedron facilitates the formation of mica units [$AlSiO_3$] [287]. The bands near 1176 and 470 cm^{-1} and the shoulder at about 840 cm^{-1} can be interpreted as vibration modes in fluor-phlogopite [288,289].

Forsterite crystals containing Mg^{2+} ions are also precipitated when crystallization temperature increased. The bands at about 890 and 612 cm^{-1} and the shoulders at about 838 and 515 cm^{-1} corresponding to forsterite are found (Figure III.53) [239,290,291]. With the increase of crystallization temperature, the contents of forsterite increase, while fluor-phlogopite decreases. It is possibly due to the increasing of Mg^{2+} ions mobility from the decomposition of fluor-phlogopite, resulting the formation of forsterite [269].

III.3.7 Mechanical properties

III.3.7.1 Hardness

The Vickers microhardness and the Young's modulus of our MAS glass ceramics were compared to the data for the BGs, as presented in Table III-24. The microhardness values of the investigated BGs are ranging from 9.12 to 9.54 GPa. MP0 base glass exhibit the largest H_v value; of 9.54 GPa. In addition, crystallized samples show a lower microhardness compared to the base glasses. The mechanical properties are related to the microstructure. After crystallization, the mechanical properties decrease with the increase of the crystal size and the volume fraction of fluor-ophlogopite or forsterite phases [292]. The H_v of the MAS glass ceramics is in the range from 8.33 to 8.66 GPa. The H_v does not show a clear dependence on the P_2O_5 concentration. The determined H_v of the MAS glass ceramics is in the same range as those reported in the literature [284,293].

Table III-24 *Microhardness values of MAS BG and GC samples (the errors are standard deviation from mean)*

	(Gpa)	MP0	MP1	MP2	MP3
BG	H_v	09.54 ± 0.30	09.42 ± 0.35	09.12 ± 0.24	09.28 ± 0.54
	E	97.80 ± 3.14	99.71 ± 3.27	94.80 ± 1.15	95.62 ± 3.85
GC	H_v	08.56 ± 0.27	08.33 ± 0.66	08.66 ± 0.70	08.56 ± 0.73
	E	104.76 ± 3.25	93.77 ± 3.63	96.18 ± 2.86	94.20 ± 4.07

The observed changes in hardness after heat-treatment can be correlated with the type and content of the precipitated phase as well as the residual glassy phases. It is probably due to the size of tested samples. It is found that the microhardness of large size sample is considerably higher than the microhardness of small size sample [294]. Since the phlogopite crystals act as an insulator, the heat diffusion or absorption will be problematic in large samples, thus, some temperature gradients caused to new phases like forsterite. Hence, the value of microhardness will decreased.

The Young's moduli of BGs are in the range from 94.80 to 99.71 GPa. The *E* of GC samples containing P_2O_5 are slightly lower than those of BG samples, while it is higher in the

free-P_2O_5 sample after heat-treatment. The highest Young's modulus; of 104.76 GPa, was observed for the GC sample MP0.

III.3.7.2 Machinability

Table III-25 shows cutting energy and machinability parameter of the respective glass ceramics specimens, which were calculated from equation (III.1) and equation (III.2), respectively. According to Tables III-24 and Table III-25, MP2 base glass specimen has the lowest H_v value (9.12 GPa) and it has the highest machinability parameter (m) of (-0.470) with lower cutting energy (μ_1) of 145 J.mm^{-3}, indicating that it has a better machinability than the other studied MAS samples. The machinability increases in the GC materials compared to the base glasses, which due to the presence of crystal phases such as, phlogopite and fosterite in the GC materials. Phlogophite is known in "mica-glass" for its good machining property [295].

Table III-25 *The machining parameters of the investigated MAS specimens*

		MP0	**MP1**	**MP2**	**MP3**
BG	***m***	-0,521	-0,506	-0,470	-0,489
	μ_1 (J.mm^{-3})	160,079	155,454	144,655	150,482
GC	***m***	-0,401	-0,397	-0,403	-0,401
	μ_1 (J.mm^{-3})	125,290	124,384	125,896	125,287

It is also observed from Table III-25, that m increases with the increase of P_2O_5 concentration for base glasses, while it remains constant for the corresponding glass ceramics. It is also observed an increase of machinability, from -0.5 for BGs to -0.4 for GCs, and this indicates that the machinability would be improved by the presence of the crystal phase. The machinability is correlated with microstructure and crystal formation (as found in FE-SEM results). In addition, the crystals formed after heat treating may present similar machinability.

By the heat-treatment, glass ceramic specimen MP1 shows a lowest hardness value 8.33 GPa and a highest machinability parameter, m = -0.397. The above results clearly indicated that, as the P_2O_5 content increased (2.0–3.0 mol%) the machinability of the specimens decreased. The P_2O_5 lead to a decrease in the machinability of MAS BGs and GCs.

III.3.7.3 Flexural strength

Figure III-54 shows the flexural strength of the MAS glass ceramics as a function of P_2O_5 concentration. The values of σ are between 95 and 131 MPa, and in the same range of MAS glass ceramics [102,106]. When P_2O_5 concentration changed from 1.0 to 2.0 mol%, the flexural strength decreased from 106 to 95 MPa, respectively. The maximum flexural strength is 131 MPa in MP3, affected by amount of crystalline phases. The strength values of the studied MAS glass ceramic are quite similar and the effect of P_2O_5 is not clear as shown in the graph.

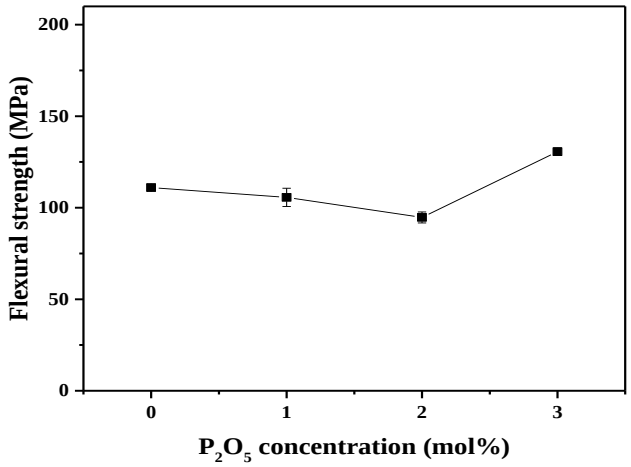

Figure III-54 *Flexural strength as a function of P_2O_5 concentration*

III.3.8 Optical properties

III.3.8.1 Transparence

Photographs of the BG samples are shown in Figure III-55. Obviously, the variations in transparency with decrease of P_2O_5 concentration can be clearly distinguished by the naked eyes. In addition, adding a low concentration of P_2O_5 (1.0 mol%) leads to a higher transparent specimen (MP1) than the free-P_2O_5 specimen (MP0). It suggested that using 1.0 mol% P_2O_5 as nucleating agent in MAS glass ceramic was favorable to obtain almost colorless transparent glass ceramic.

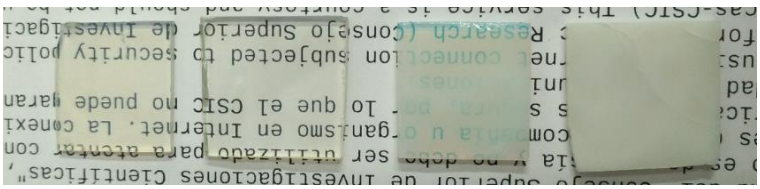

Figure III-55 *Visual appearance of BGs: MP0, MP1, MP2 and MP3 from left to right, respectively*

III.3.8.2 UV-Vis transmission spectra

Figure III-56 shows the optical transmittance spectra recorded for the BGs and GCs. It can be seen from Figure III-56 that the transmittance in the ultraviolet range falls at the low wavelength range, and the corresponding absorption phenomena are associated with the number of BOs [241]. The optical cutoff of MP0 and MP2 is 320 nm, while it increased to 355 nm for MP2 and MP3. The transmittance (MP0 & MP1 BGs) increases continuously and reaches approximate 85% in the visible range then remains an approximately flat line in the NIR range with high transmittance (85 %). Incorporation of P_2O_5 (1.0 mol%) changes the transmittance degree in the visible region which becomes slightly stronger.

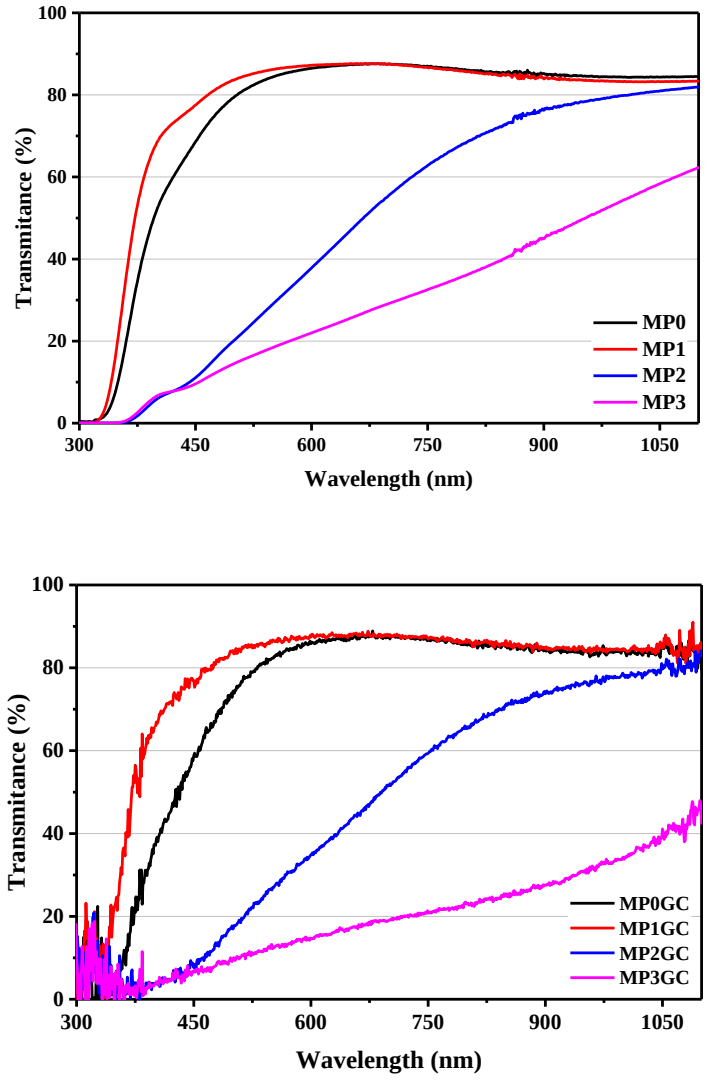

Figure III-56 *UV visible spectra of MAS samples*

Addition of P_2O_5 allowed for the production of highly homogeneous initial glasses and for the increase in the transmittance of glass ceramics, as compared with glass ceramics without

P_2O_5 [191]. With further increasing of P_2O_5 content, the light transmittance of MP2 and MP3 specimens decrease gradually. The crystal size increased as P_2O_5 content increased, which increased scattering intensity but reduced light transmittance. Samples with P_2O_5 (MP1, MP2 & MP3) exhibit little absorption in the range λ~420–430 nm, which explains the color observed.

Comparing MAS samples obtained by the heat-treatment process in Figure III-56, it can be found that MP1GC and MP3GC maintain the highest and lowest transmittances, respectively. Light transmittance of samples MP0GC and MP1GC reaches ~85 % within NIR range. It is clear that the transparency of MP3GC is reduced by the heat-treatment. That is, micro-crystals precipitated in the glass ceramic samples can scatter the visible ray, particularly, a light of lower wavelengths. The transmittance of glass ceramic depends on the degree of crystallinity and crystal size. The samples heat-treated at higher temperatures have relatively larger crystallites with higher volume fraction crystallized, resulting in semi-transparency or opacity.

III.3.8.3 Optical band gap energy

The optical band gap, E_v, of the studied samples have been estimated by drawing Tauc plots of $(\alpha h\nu)^2$ *vs.* energy as shown in Figure III-57. The values obtained for E_v are shown in Table III-26 for the studied MAS samples.

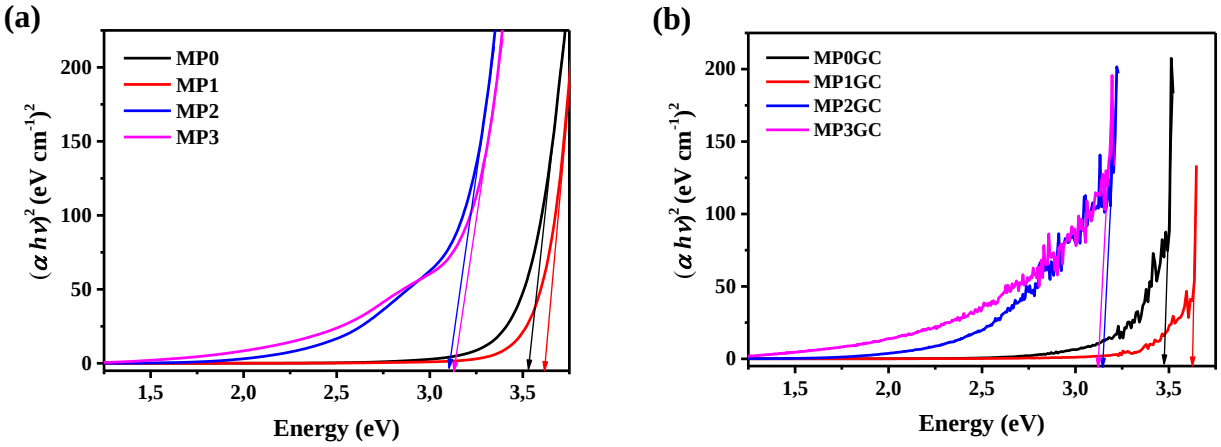

Figure III-57 *Schematic of band gap calculation using the Tauc plot for the MAS samples: (a) BGs and (b) GCs*

It can be seen from Figure III-57 and Table III-26 that the energy gap increases in the base glass MP1 to 3.61 eV then decreases strongly with increasing P_2O_5 content reaching 3.10 and 3.13 eV in the MP2 and MP3 samples, respectively. The shift of the band gap towards higher energies was observed with increasing P_2O_5 concentration.

Table III-26 *Optical band gap E_v of MAS samples*

		MP0	MP1	MP2	MP3
E_v (eV)	***BG***	3.52	3.61	3.10	3.13
	GC	3.47	3.62	3.11	3.12

After heat-treatment process, the optical energy gap slightly decreases for the free-P_2O_5, however, it is nearly constant in (MP1GC, MP2GC & MP3GC). The decrease of the band gap energy can be associated with the increase of the amount of the NBOs then the system has made it easier for the electrons to move through the materials [245].

III.3.8.4 Color parameters

The color factors (*L**, *a** and *b**) have been determined from the transmittance spectra of BGs and GCs. The corresponding chromatic coordinate values are given in the Table III-27.

Table III-27 *Chromatic coordinates of different BG and GC samples*

	L*	***a****	***b****
MP0	93.26	-02.17	11.54
MP1	94.20	-01.28	05.93
MP2	61.43	06.86	34.40
MP3	50.22	02.84	20.76
MP0GC	92.17	-02.83	18.60
MP1GC	94.24	-01.41	06.38
MP2GC	58.98	06.43	39.06
MP3GC	42.01	02.32	18.59

In accordance with Table III-27, the free-P_2O_5 base glass (MP0) presents a high brightness (*L**=93.26). However, the addition of (1.0 mol%) P_2O_5 increase slightly the brightness to 94.20 then further increase of P_2O_5 content decreases the brightness reaching a minimum value of (*L** = 50.22) for the MP3 sample, which presented a light beige color. In addition, with the increase of P_2O_5 content (2.0–3.0 mol%) it has been noted a slight shift from

green to red for *a** parameter (negative and positive values indicate the predominance of the green and red color, respectively) and a more marked shift to higher positive value for *b** parameter (positive values indicate the predominance of the yellow color).

After heat-treatment process, the observed variation for the color factors corresponds to the variation of color intensity according to CIELAB classification. The MP0GC and MP1GC samples are also characterized by lower values of *a** and *b** indicating a tendency to achromatism.

III.3.8.5 Refractive index

It is clear from Table III-28 that the prepared BGs show low refractive index (in the range 1.5368–1.5431). The refractive index decreases gradually with the increase of P_2O_5 content. After heat-treatment, the refractive index in MAS specimens increases after the formation of crystals. As a larger amount of forsterite (n_D = 1.69–1.70) is precipitated in MP1 specimen, it may result in a larger refractive index difference than the precipitation of fluor-phlogopite crystals (n_D = 1.55–1.63) in the MP3 specimen.

Table III-28 *Values of refractive index, n_D, of MAS specimens*

		MP0	MP1	MP2	MP3
n_D	**BG**	1.5420	1.5417	1.5396	1.5365
	GC	1.5422	1.5441	1.5408	1.5391

III.3.9 Characterization of silver stained glass ceramics

III.3.9.1 FTIR-ATR results

The room temperature FTIR-ATR absorbance spectra of different painted MAS samples are presented in Figure III-58. The spectra are shown in the range of 600–1300 cm^{-1}, which is characteristic of the studied materials.

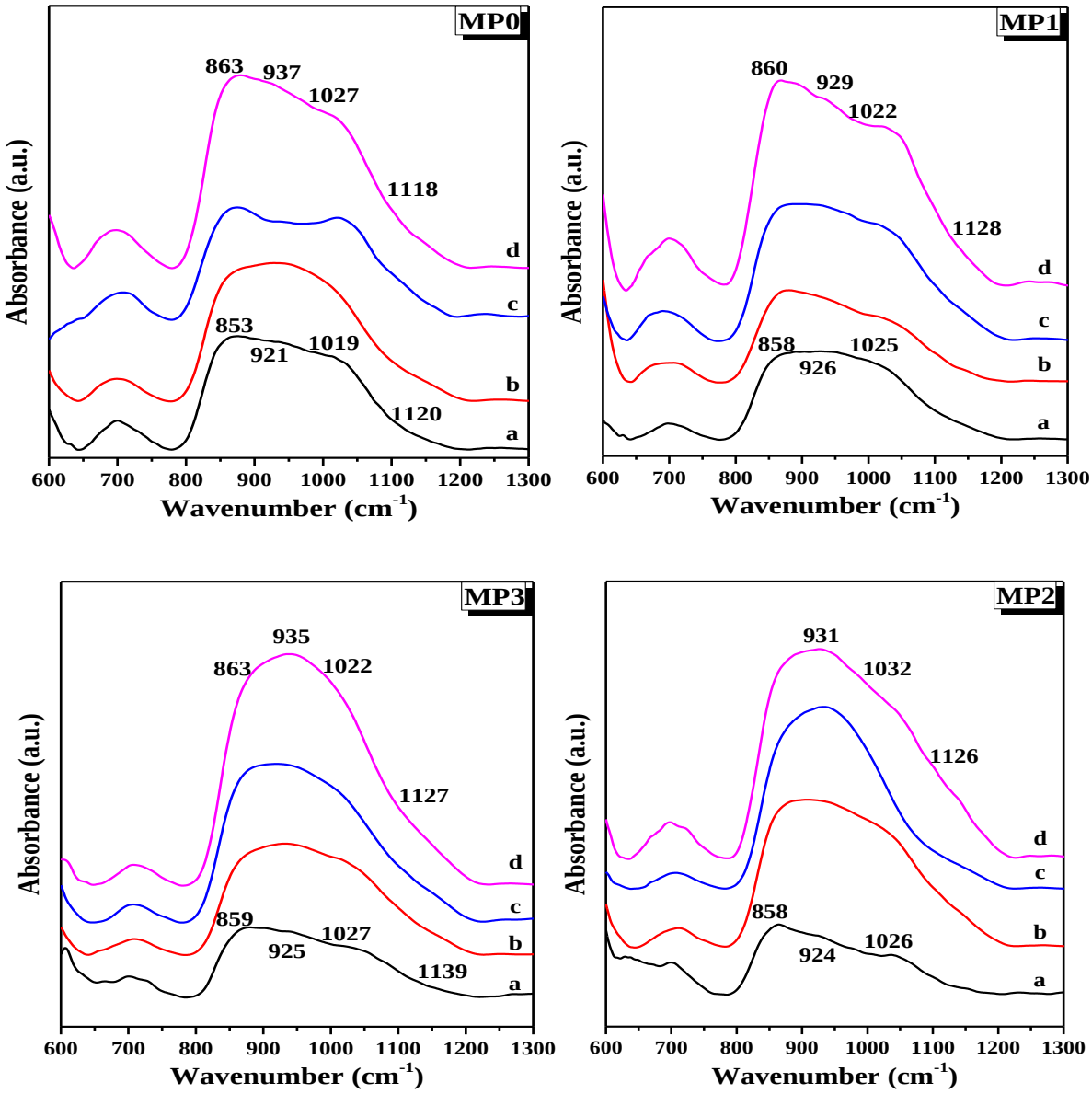

Figure III-58 *FTIR-ATR spectra of painted MAS specimens: (a) GC 'reference', (b) 2h, (c) 4h and (d) 8h*

As observed from Figure III-58, there are nearly two broad bands present in all the painted MAS samples located in the ranges of about 1250–800 cm^{-1} and 800–650 cm^{-1}. The band ranging from 1250–800 cm^{-1} corresponds to the asymmetric stretching mode Si−O [296]. Spectrum 800–650 cm^{-1} is assigned to the symmetric bending vibrations Si–O-(Si,Al) between the tetrahedrons [239]. After heated samples for 8 h, the width of the strong band 1250–800 cm^{-1} decreases, hence, the bands in the region 1000–800 cm^{-1} shift to high wavenumbers while the bands at 1200–1000 cm^{-1} shift to lower frequencies. In addition, the intensity of the absorption band near 860 cm^{-1} increases gradually with increase in crystallization holding time for the samples MP0 and MP1. However, for MP2 and MP3 samples; it is clearly seen that the intensity

of the bands at ~931 cm^{-1} is higher with increasing holding time. It is found that the bands at about 920 and 865 cm^{-1} correspond to the Si–O (NB) [296]. The shift of the bands toward higher wavenumber may indicates a strengthening of the chemical bonds in the network when Ag^{+} is added in the network, due to a network polymerization [246]. The increase in intensity for the Ag-treated glass ceramics could be due to an effect of enhancement of the IR signal of Si–O bonds due to the presence of silver nanoparticles around such bonds.

III.3.9.2 UV-Vis transmission spectra

Figure III-59 shows UV-Vis transmission spectra of silver painted glass ceramics as well as the spectrum for the unpainted glass ceramic substrate.

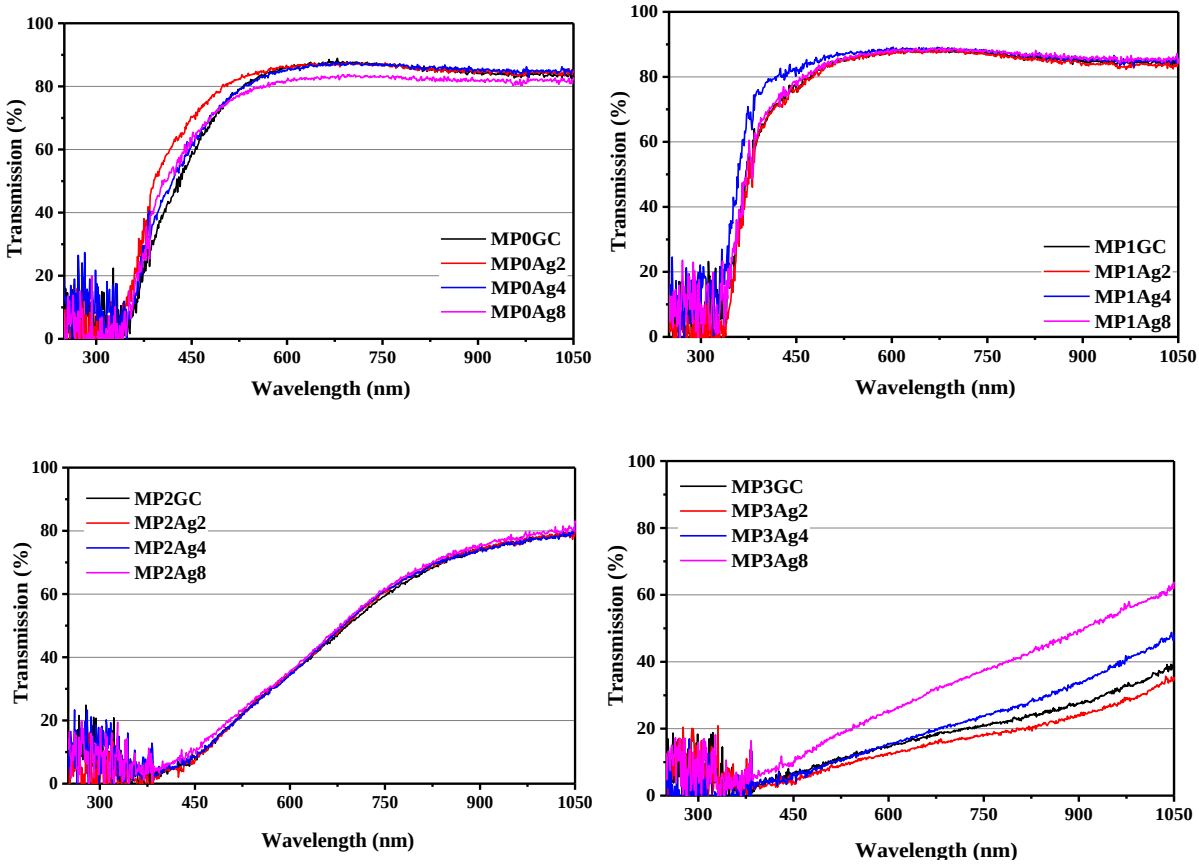

Figure III-59 *UV-Vis spectra of painted MAS glass ceramics*

The behavior of painted GC materials spectral curves is similar to that of the unpainted GC. The optical cutoff of (MP0Ag2–MP0Ag8 and MP1Ag2–MP1Ag8) is in the region between 340–350 nm, while it increase to the region between 380–390 nm for MP2Ag2–MP2Ag8 and MP3Ag2–MP3Ag8. The transmittance of the painted samples increased after silver stain for the sample MP3Ag.

III.3.9.3 Optical band gap energy

The optical band gap, E_v, of the painted samples have been estimated by drawing Tauc plots of $(\alpha h\nu)^2$ *vs.* energy as shown in Figure III-60. The values obtained for E_v are shown in Table III-29 for the studied samples.

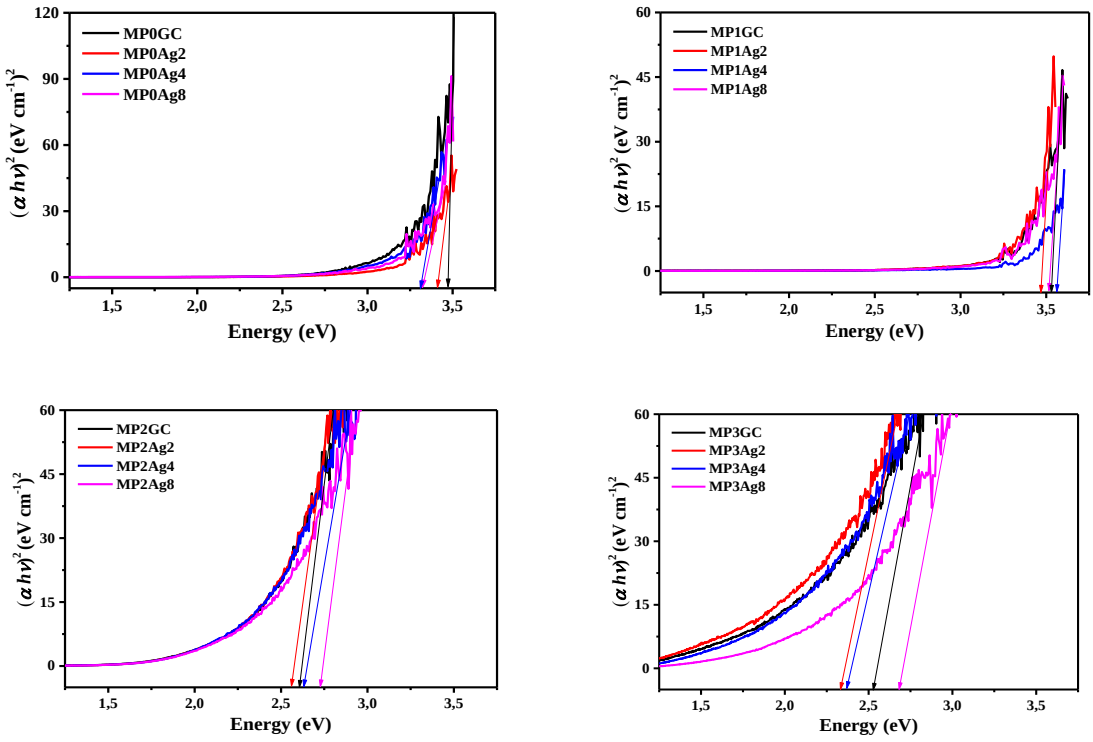

Figure III-60 *Schematic of band gap calculation using the Tauc plot for the studied MAS samples*

It is clear from the Table III-29 that the optical band gap of MP0Ag sample decreased gradually when the heating time increased. However, it showed a decrease on heating up to a period of 2 h for the other specimens. For further increase in heating time, these values started increasing.

Table III-29 *Optical band gap E_v of the studied MAS samples*

		GC	*Ag2h*	*Ag4h*	*Ag8h*
E_v (eV)	**MP0**	3.47	3.41	3.31	3.32
	MP1	3.53	3.46	3.56	3.51
	MP2	2.60	2.56	2.63	2.73
	MP3	2.52	2.32	2.37	2.68

III.3.10 Bacterial analysis

The antibacterial properties of the MAS GC samples were all determined after 90 min incubation with the bacterial cell suspension. Figure III-61a shows the logarithm reduction (CFU/specimen) observed in the painted MAS glass ceramic respect to the reference glass ceramic sample. A significant logarithm reduction (>3 log) against *E. coli* for all samples was obtained. A logarithm reduction higher than 3 means a safe disinfection and a high antimicrobial activity [297]. By increasing P_2O_5 concentration, the logarithm reduction values against *E. coli* are nearly equal to 7 log, indicating that the bactericidal properties of Ag-dopped MAS glass ceramics are P_2O_5 concentration independent.

As observed in Figure III-61b, bacterial adhesion generally decreased gradually in all the painted MAS samples, reaching the lowest values for the samples treated for 8 h after Ag-doping. At the 90 min incubation time the release of silver from nanoparticles of the different compositions can be considered the same. The release of silver ions for almost all painted samples (Figure III-61c) was of, ~3 µg in solution, which is enough to have biocide activity in agreement with the results obtained in a previous work [249]. Silver nanoparticles act in two ways against *E. coli* : (i) they are able to penetrate inside the bacteria and cause further damage or; (ii) they release silver ions, which will have an additional contribution to the bactericidal effect of the silver nanoparticles such as reported in previous works [298,299].

The coating of MAS glass ceramic containing 16 wt% of $AgNO_3$ showed a CFU reduction of 99.9999 % for all studied samples (>6 log reduction) against *E. coli*. The obtained antibacterial results clearly show that this glass ceramic is effective to diminish the growth of bacteria and also to inhibit adhesion and biofilm formation against *E. coli*. This means that the presence of silver nanoparticles distributed on the glass ceramic surfaces confers it a very high biocide property against *E. coli* ATCC 25922.

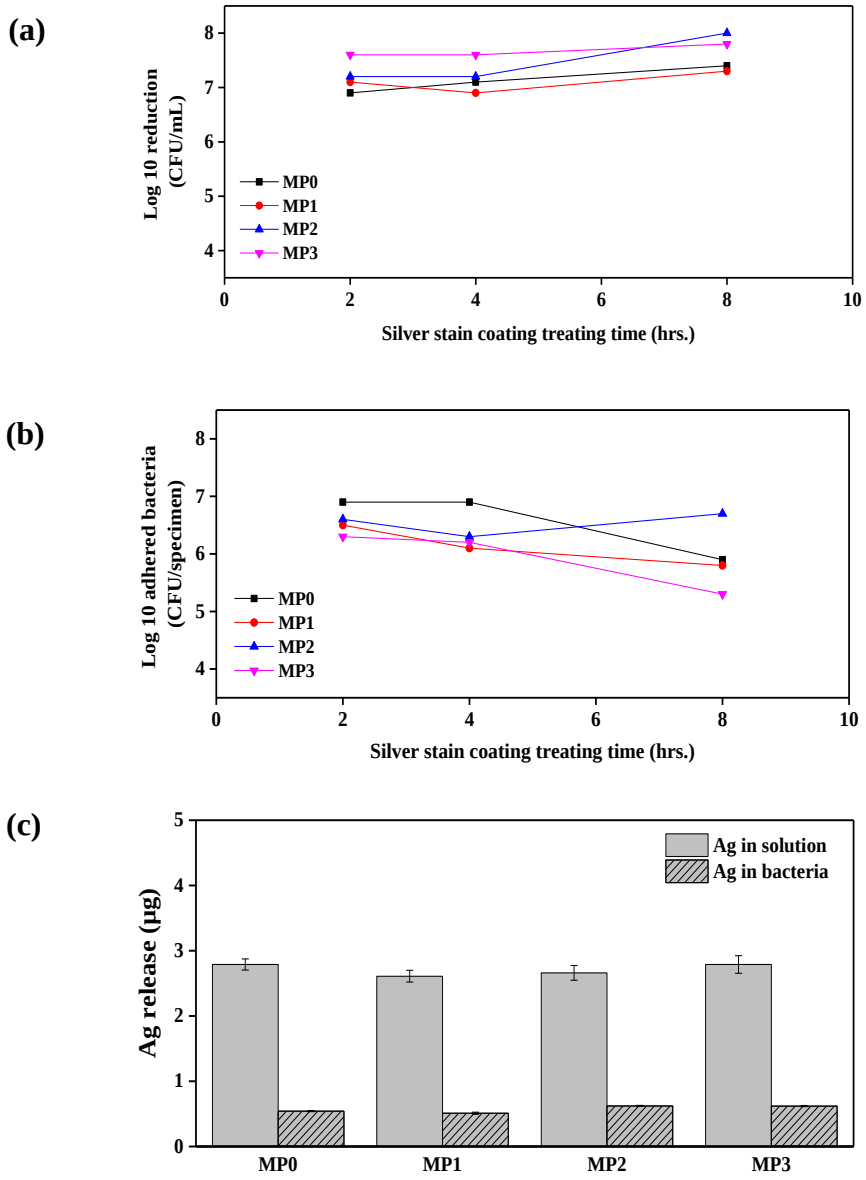

Figure III-61 *Antibacterial efficacy corresponding to different painted MAS GCs: (a) logarithm of reductions of E. coli after 90 min, (b) logarithm of adhered bacteria and (c) means of Ag release*

General conclusion

General conclusion

In order to achieve the main objectives of this study, glass ceramic in the LMAS and MAS systems have been investigated. Several base glasses have been prepared by melting at high temperatures. Crystallization behavior of both glasses in the presence of F and P_2O_5 as nucleation agents was studied. There is a correlation between the different properties and crystallization behavior of LMAS and MAS glass ceramic systems.

In these systems, the addition of P_2O_5 reduces both the viscosity at high-temperature and the melting temperature of the both glass ceramic systems, while increases the glass transition temperature.

In this work, thermal stability and glass forming ability of LMAS and MAS systems were calculated by taking different approaches into account and it was found that both systems are good glass formers with high glass forming tendency. In addition, the increase of P_2O_5 content yields to an increase in the LMAS base glass transformation, crystallization temperatures, GFA and GS. The incorporation of P_2O_5 or the high Al_2O_3 concentration increases the glass stability in LMAS system. However, the most stable glass composition in MAS system was found as MP3 (3.0 mol%).

The activation energies for crystallization are in the range of 200–500 $kJ.mol^{-1}$ for both systems and as correspond to LAS and MAS glass ceramic materials. The addition of P_2O_5 lead to an increase in E_c for LMAS system. In contrast, the activation energy of MAS system increases with addition of 1.0 mol% P_2O_5, then decreases with the respective increasing of P_2O_5. Multiple nucleating agents in MAS system (both F and P_2O_5) may effectively lower the crystallization activation energy (more than 1.0 mol% of P_2O_5) compared with single one (F in MP0), which also could promote crystallization at lower temperatures. In addition, the crystallization mechanism is mainly of bulk type with a constant number of nuclei in both systems and it depends on the amount of P_2O_5, however, when the amount of P_2O_5 increases it tends to be surface type for LMAS system. For the LMAS glass without F and high Al_2O_3 concentration the crystallization presents a one- and two-dimensional growth of crystals, however for those samples containing F, the growth is two- and three-dimensional. In the other hand, for the MAS sample with single nucleating agent (F), the crystallization mechanism is of

surface type. The addition of trace amounts of P_2O_5 suppresses the surface crystallization and promoted bulk crystallization with one- and two-dimensional growth of crystals.

LMAS glass ceramic crystallize in lithium aluminum silicate ($Li_xAl_xSi_{1-x}O_2$), enstatite ($MgSiO_3$) and β-spodumene ($LiAlSi_2O_6$) when F is in their composition, whereas β-spodumene does not appear if F is not present in the glass composition. Furthermore, the binodal phase separation appeared in the LMAS samples having higher *Al*/*Li* value and free of F, while the spinodal phase separation appeared in the sample having F in the composition. Otherwise, MAS glass ceramic crystallize in forsterite (Mg_2SiO_4) and fluor-phlogopite (1M, $KMg_3(Si_3AlO_{10})F_2$). By the increase of P_2O_5, lithium aluminum silicate and forsterite become gradually the major crystalline phase in LMAS and MAS systems, respectively, which indicates the influence of this nucleating agent in the crystallization reactions.

There is a significant variation in the morphology of the crystalline phases with the changes in the nucleating agent content and the heat-treatment temperatures in MAS and LMAS systems. The difference in these morphologies lies in the respective crystallization mechanisms. The coexistence of P_2O_5 and F induce crystals formation in both glass ceramic systems by P_2O_5-inducing the phase separation and F-modifying the glass structure. In addition, with the increase of P_2O_5 content, the average size of crystals increases.

From the comparative study of variation of P_2O_5 in both glass ceramics, it is revealed that TEC of the LMAS glass ceramic decreases by increasing P_2O_5 due to the formation of crystal phases formed after heat-treatment. MAS samples have higher TEC values (7.98–10.21 MPa) than LMAS samples (8.38–9.16 MPa). The TEC of MAS system decreased with formation of forsterite and increased under the dominance of the fluor-phlogopite.

The LMAS base glasses possess lower H_v than the corresponding glass ceramics, inversely to the MAS system. The H_v in MAS system does not show a clear dependence on the P_2O_5 concentration, however, the addition of 1.0 mol% of P_2O_5 can contribute to the improvement of microhardness of the LMAS samples with H_v of 11.45 GPa and E of 118.02 GPa. In contrast, free-P_2O_5 MAS sample exhibit almost the largest H_v value; of 8.56 GPa and the highest Young's modulus; of 104.76 GPa. Indeed, it is revealed that the LMAS glass ceramic shows higher H_v and E compared to the MAS one. In addition, either Al_2O_3 or P_2O_5 does not lead to an important change in the machinability of LMAS and MAS base glasses and glass ceramics. For the LMAS system, the crystallization decreases the machinability, while it

leads to a high tendency to obtain machinable materials in the MAS system. Moreover, fluorine-containing LMAS glass ceramics are much stronger than glass ceramics of similar compositions but contain no fluorine and high aluminium content. The maximum flexural strength is 131 MPa (MP3) in MAS system, however, LMAS system achieves 190 MPa (GP3). The flexural strength is sensitive to a small addition of P_2O_5 in LMAS system, while it is nearly constant in MAS glass ceramic whatever the P_2O_5 concentration.

Si/*Al* molar ratio has a significant impact on the structural properties of LMAS glass ceramic. The higher content of silica, dominating bands are associated with bonds characteristic of Si–O tetrahedral and crystallization of β-spodumene. In turn, at higher content of alumina, dominating bands are associated with the vibrations of Si–O–Al and Si–O–Si due to the crystallization of $Li_xAl_xSi_{1-x}O_2$. Moreover, in MAS system, with the increase of crystallization temperature, the contents of forsterite increase due to the increasing of Mg^{2+} ions mobility from the decomposition of fluor-phlogopite, resulting the formation of more forsterite.

The high transparency of both system was found mainly resulted from the lower amount of P_2O_5 (1.0 mol%) added in both systems. The transparency of the glass ceramic samples is diminished with the increase of P_2O_5 concentration. Inversely to MAS BGs, the LMAS BGs possess higher refractive index than the corresponding BGs, and it decreases as the P_2O_5 content increase, however, MAS GCs show lower refractive index (1.5368–1.5431) than LMAS GCs (1.5724–1.5878).

LMAS and MAS glass ceramics doped with Silver were found to exhibit a very high biocide activity (6–8 log of reduction) against *E. coli*. The coating containing 16 wt% of $AgNO_3$ nanoparticles has an excellent biocidal activity. These painted glass ceramics not only are effective to decrease the growth of bacteria but also to inhibit adhesion and biofilm formation. Therefore, the LMAS and MAS glass ceramics are particularly promising for mechanical and biocide application (utensils of hospitals, worktops, surface of implants, touch screens, bathroom and kitchen surfaces, etc.), however, it needs a future analysis on their bactericidal effect against common Gram-positive and Gram-negative bacteria, as well as antifungal activity against yeast. In addition, optical properties such as the color relevant for their application will be determined.

Bibliographies

[1] Y. Xu, J. Cheng, W. Zheng, D. Gao, Study on the preparation and properties of silver-doped borosilicate antibacterial glass, J. Non. Cryst. Solids. 354 (2008) 1342-1346.

[2] M.A. Fiori, M.M. da S. Paula, A.M. Bernardin, H.G. Riella, E. Angioletto, Bactericide glasses developed by Na^+/Ag^+ ionic exchange, Mater. Sci. Eng. C. 29 (2009) 1569-1573.

[3] D. Guldiren, S. Aydin, Characterization and antimicrobial properties of soda lime glass prepared by silver/sodium ion exchange, Mater. Sci. Eng. C. 67 (2016) 144-150.

[4] L. Xia, G.W. Wen, C.L. Qin, X.Y. Wang, L. Song, Mechanical and thermal expansion properties of β-eucryptite prepared by sol–gel methods and hot pressing, Mater. Des. 32 (2011) 2526-2531.

[5] A. Hu, M. Li, D. Mao, Controlled crystallization of glass-ceramics with two nucleating agents, Mater. Charact. 60 (2009) 1529-1533.

[6] G.H. Beall, Design and Properties of Glass-Ceramics, Annu. Rev. Mater. Sci. 22 (1992) 91-119.

[7] M. Dressler, B. Rüdinger, J. Deubener, An in situ high-temperature X-ray diffraction study of early-stage crystallization in lithium alumosilicate glass-ceramics, J. Am. Ceram. Soc. 94 (2011) 1421-1426.

[8] L. Han, J. Song, C. Lin, J. Liu, T. Liu, Q. Zhang, Z. Luo, A. Lu, Crystallization, structure and properties of MgO-Al_2O_3-SiO_2 highly crystalline transparent glass-ceramics nucleated by multiple nucleating agents, J. Eur. Ceram. Soc. 38 (2018) 4533-4542.

[9] L.R. Pinckney, G.H. Beall, Microstructural evolution in some silicate glass-ceramics: A review, J. Am. Ceram. Soc. 91 (2008) 773-779.

[10] O.A. Al-Harbi, Effect of different nucleation catalysts on the crystallization of Li_2O–ZnO–MgO–Al_2O_3–SiO_2 glasses, Ceram. Int. 35 (2009) 1121-1128.

[11] G.H. Beall, D.A. Duke, Transparent Glass-Ceramics, J. Mater. Sci. 4 (1969) 340-352.

[12] Z.H. Bao, L.F. Miao, W.H. Jiang, J.M. Liu, J. Liang, T. Chen, Effect of B_2O_3 and P_2O_5 Addition on the Phase Separation and Crystallization of Li_2O-MgO-Al_2O_3-SiO_2 Glass-Ceramics, Mater. Sci. Forum. 848 (2016) 243-248.

[13] Y. Iqbal, W.E. Lee, D. Holland, P.F. James, Crystal nucleation in P_2O_5-doped lithium disilicate glasses, J. Mater. Sci. 34 (1999) 4399-4411.

[14] L. Radonjić, L. Nikolić, The effect of fluorine source and concentration on the crystallization of machinable glass-ceramics, J. Eur. Ceram. Soc. 7 (1991) 11-16.

[15] X. Guo, H. Yang, Effects of fluorine on crystallization, structure and performances of lithium aluminosilcate glass ceramic, Mater. Res. Bull. 41 (2006) 396-405.

[16] A.R. Molla, B. Basu, Microstructure, mechanical, and in vitro properties of mica glass-ceramics with varying fluorine content, J. Mater. Sci. Mater. Med. 20 (2009) 869-882.

[17] P.W. McMillan, Glass-ceramics, 2nd editio, Academic Press, 1964.

[18] J.S. Kim, E. Kuk, K.N. Yu, J.H. Kim, S.J. Park, H.J. Lee, S.H. Kim, Y.K. Park, Y.H. Park, C.Y. Hwang, Y.K. Kim, Y.S. Lee, D.H. Jeong, M.H. Cho, Antimicrobial effects of silver nanoparticles, Nanomedicine Nanotechnology, Biol. Med. 3 (2007) 95-101.

[19] L. Esteban-Tejeda, F. Malpartida, A. Esteban-Cubillo, C. Pecharromn, J.S. Moya, Antibacterial and antifungal activity of a soda-lime glass containing copper nanoparticles, Nanotechnology. 20 (2009).

[20] R.-A.F. De Réaumur, Mémoire sur l'art de faire une nouvelle espèce de porcelaine par des moyens extrêmement simples et faciles ou de transformer le verre en porcelaine, Mémoire de l'Académie Royale des Sciences, 1739.

[21] S.D. Stookey, Catalyzed Crystallization of Glass in Theory and Practice, Ind. Eng. Chem. 51 (1959) 805-808.

[22] E.D. Zanotto, A bright future for glass-ceramics, Am. Ceram. Soc. Bull. 89 (2010) 19-27.

[23] S. Lehmann, A Second Edition and a Second Look at Community Psychology, Contemp. Psychol. A J. Rev. 30 (1985) 627-628.

[24] H. Bach, Low Thermal Expansion Glass Ceramics, Springer-V, Springer-Verlag Berlin Heidelberg, 1995.

[25] S.D. Stookey, Methode of making ceramics and product thereof, US Patent 2,920,970, 1960.

[26] P.F. James, Glass ceramics: new compositions and uses, J. Non. Cryst. Solids. 181 (1995) 1-15.

[27] A. Sakamoto, S. Yamamoto, Glass-Ceramics: Engineering Principles and Applications, Int. J. Appl. Glas. Sci. 1 (2010) 237-247.

[28] G.H. Beall, L.R. Pinckney, Nanophase Glass-Ceramics, J. Am. Ceram. Soc. 82 (1999) 5-16.

[29] N.F. Borrelli, Electro-optic Effect in Transparent Niobate Glass-Ceramic Systems, J. Appl. Phys. 38 (1967) 4243-4247.

[30] H. Jain, Transparent Ferroelectric Glass-Ceramics, Ferroelectrics. 306 (2004) 111-127.

[31] T. Komatsu, T. Honma, Optical Active Nano-Glass-Ceramics, Int. J. Appl. Glas. Sci. 4 (2013) 125-135.

[32] T. Komatsu, T. Honma, Laser patterning and characterization of optical active crystals in glasses, J. Asian Ceram. Soc. 1 (2013) 9-16.

[33] G.P. Kothiyal, A. Ananthanarayanan, G.K. Dey, Glass and glass-ceramics, in: Funct. Mater., 2012: p. 323-386.

[34] D. Krause, B. Hans, Low Thermal Expansion Glass Ceramics, 2005.

[35] W. Höland, G.H. Beall, Glass-ceramic technology, 2nd edi., Wiley-Blackwell, 2012.

[36] L.R. Pinckney, G.H. Beall, Microstructural Evolution in Some Silicate Glass–Ceramics: A Review, J. Am. Ceram. Soc. 91 (2008) 773-779.

[37] D.R. Neuville, L. Cormier, D. Caurant, L. Montagne, E.D. Zanotto, From Glass to Crystal: Nucleation, Growth and Phase Separation: from Research to Applications, EDP sciences, 2017.

[38] J.E. Shelby, Introduction to Glass Science and Technology, 2nd edi., The Royal Society of Chemistry, 2005.

[39] J.M. Rincon, Principles of Nucleation and Controlled Crystallization of Glasses, Polym. Plast. Technol. Eng. 31 (1992) 309-357.

[40] J.Q. and A. Makishima, Rare-Earth Containing Nanocrystal Precipitation and Up-conversion Luminescence in Oxyfluoride Glasses, J. Nanosci. Nanotechnol. 5 (2005) 1-5.

[41] M. Nogami, A. Ohno, Laser precipitation of SnO_2 nanocrystals in glass and energy transferred-fluorescence of Eu^{3+}ions, J. Non. Cryst. Solids. 330 (2003) 264-267.

[42] A. Stone, M. Sakakura, Y. Shimotsuma, G. Stone, P. Gupta, K. Miura, K. Hirao, V. Dierolf, Directionally controlled 3D ferroelectric single crystal growth in $LaBGeO_4$ in glass by femtosecond laser irradiation, 17 (2009) 23284-23289.

[43] F. Goutaland, M. Mortier, B. Capoen, S. Turrell, M. Bouazaoui, A. Boukenter, Y. Ouerdane, UV-assisted crystallisation of tellurite and germanate-based glasses, Opt. Mater. (Amst). 28 (2006) 1276-1279.

[44] I.S. Gutzow, J.W.P. Schmelzer, The Vitreous State, Springer Berlin Heidelberg, Berlin, Heidelberg, 2013.

[45] T. Komatsu, Design and control of crystallization in oxide glasses, J. Non. Cryst. Solids. 428 (2015) 156-175.

[46] G. Tammann, W. Hesse., The dependence of viscosity upon the temperature of supercooled liquids, Z. Anorg. Allg. Chem. 156 (1926) 245-257.

[47] S.D. Stookey, History of the Development of Pyroceram, Res. Manage. 1 (1958) 155-163.

[48] J. Gibbs, On the Equilibrium of Heterogeneous Substances, Trans. Connect. Acad. Arts Sci. 3 (1879) 1874-1878.

[49] M. Volmer, A. Weber, Nucleation in supersaturated formations, Keimbildung in übersättigten Gebilden, Zeitschrift für Phys. Chemie. 119U (1926) 277-301.

[50] R. Becker, W. Döring, Kinetic treatment of germ formation in supersaturated vapour, Kinetische Behandlung der Keimbildung in übersättigten Dämpfen, Ann. Phys. 416 (1935) 719-752.

[51] W. Vogel, Structure and Crystallization of Glasses, Elsevier. 4 (1971) 21-127.

[52] M. H. Lewis, Glasses and Glass-Ceramics, Springer Netherlands, Dordrecht, 1989.

[53] E. Apel, C. van't Hoen, V. Rheinberger, W. Höland, Influence of ZrO2 on the crystallization and properties of lithium disilicate glass-ceramics derived from a multi-component system, J. Eur. Ceram. Soc. 27 (2007) 1571-1577.

[54] T. Uno, T. Kasuga, S. Nakayama, A.J. Ikushiina, Microstructure of Mica-Based Nanocomposite Glass-Ceramics, J. Am. Ceram. Soc. 76 (1993) 539-541.

[55] M. Mortier, A. Monteville, G. Patriarche, Devitrification of fluorozirconate glasses: From nucleation to spinodal decomposition, J. Non. Cryst. Solids. 284 (2001) 85-90.

[56] D.R. Uhlmann, A.G. Kolbeck, Phase separation and revolution in concepts of glass structure, Phys. Chem. Glas. 17 (1976) 146-158.

[57] W. Höland, E. Apel, C. van 't Hoen, V. Rheinberger, Studies of crystal phase formations in high-strength lithium disilicate glass–ceramics, J. Non. Cryst. Solids. 352 (2006) 4041-4050.

[58] M.J. Dejneka, The luminescence and structure of novel transparent oxyfluoride glass-ceramics, J. Non. Cryst. Solids. 239 (1998) 149-155.

[59] M.J. Dejneka, Transparent oxyfluoride glass ceramics, MRS Bull. 23 (1998) 57-62.

[60] C.A. Angell, Spectroscopy simulation and scattering, and the medium range order problem in glass, J. Non. Cryst. Solids. 73 (1985) 1-17.

[61] R. Böhmer, K.L. Ngai, C.A. Angell, D.J. Plazek, Nonexponential relaxations in strong and fragile glass formers, J. Chem. Phys. 99 (1993) 4201-4209.

[62] Q. Zheng, J.C. Mauro, Y. Yue, Reconciling calorimetric and kinetic fragilities of glass-forming liquids, J. Non. Cryst. Solids. 456 (2017) 95-100.

[63] C.T. Moynihan, S.K. Lee, M. Tatsumisago, T. Minami, Estimation of activation energies for structural relaxation and viscous flow from DTA and DSC experiments, Thermochim. Acta. 280-281 (1996) 153-162.

[64] H.E. Kissinger, Reaction Kinetics in Differential Thermal Analysis, Anal. Chem. 29 (1957) 1702-1706.

[65] L.M. Wang, V. Velikov, C.A. Angell, Direct determination of kinetic fragility indices of glassforming liquids by differential scanning calorimetry: Kinetic versus thermodynamic fragilities, J. Chem. Phys. 117 (2002) 10184-10192.

[66] K. Chebli, J.M. Saiter, J. Grenet, A. Hamou, G. Saffarini, Strong-fragile glass forming liquid concept applied to GeTe chalcogenide glasses, Phys. B Condens. Matter. 304 (2001) 228-236.

[67] M.M. Wakkad, E.K. Shokr, S.H. Mohamed, Optical and calorimetric studies of Ge-Sb-Se glasses, J. Non. Cryst. Solids. 265 (2000) 157-166.

[68] A. Goel, E.R. Shaaban, F.C.L. Melo, M.J. Ribeiro, J.M.F. Ferreira, Non-isothermal crystallization kinetic studies on MgO-Al2O3-SiO2-TiO2 glass, J. Non. Cryst. Solids. 353 (2007) 2383-2391.

[69] Q. Zheng, M. Potuzak, J.C. Mauro, M.M. Smedskjaer, R.E. Youngman, Y. Yue, Composition–structure–property relationships in boroaluminosilicate glasses, J. Non. Cryst. Solids. 358 (2012) 993-1002.

[70] D. Turnbull, Under What Conditions Can A Glass Be Formed?, Contemp. Phys. 10 (1969) 473-488.

[71] M.C. Weinberg, Glass-forming ability and glass stability in simple systems, J. Non. Cryst. Solids. 167 (1994) 81-88.

[72] A.A. Cabral, A.A.D. Cardoso, E.D. Zanotto, Glass-forming ability versus stability of silicate glasses. I. Experimental test, J. Non. Cryst. Solids. 320 (2003) 1-8.

[73] C. Suryanarayana, A. Inoue, Bulk Metallic Glasses, second, CRC Press, 2017.

[74] A. Inoue, T. Zhang, T. Masumoto, Reductilization of embrittled LaAlNi amorphous alloys by viscous flow deformation in a supercooled liquid region, J. Non. Cryst. Solids. 156-158 (1993) 598-602.

[75] K. Mondal, B.S. Murty, On the parameters to assess the glass forming ability of liquids, J. Non. Cryst. Solids. 351 (2005) 1366-1371.

[76] Z.Z. Yuan, S.L. Bao, Y. Lu, D.P. Zhang, L. Yao, A new criterion for evaluating the glass-forming ability of bulk glass forming alloys, J. Alloys Compd. 459 (2008) 251-260.

[77] Z.P. Lu, C.T. Liu, A new glass-forming ability criterion for bulk metallic glasses, Acta Mater. 50 (2002) 3501-3512.

[78] X.H. Du, J.C. Huang, C.T. Liu, Z.P. Lu, New criterion of glass forming ability for bulk metallic glasses, J. Appl. Phys. 101 (2007) 1-4.

[79] P. Zhang, H. Wei, X. Wei, Z. Long, X. Su, Evaluation of glass-forming ability for bulk metallic glasses based on characteristic temperatures, J. Non. Cryst. Solids. 355 (2009) 2183-2189.

[80] Q. Chen, J. Shen, D. Zhang, H. Fan, J. Sun, D.G. McCartney, A new criterion for evaluating the glass-forming ability of bulk metallic glasses, Mater. Sci. Eng. A. 433 (2006) 155-160.

[81] X.H. Du, J.C. Huang, New criterion in predicting glass forming ability of various glass-forming systems, Chinese Phys. B. 17 (2008) 249-254.

[82] G.J. Fan, H. Choo, P.K. Liaw, A new criterion for the glass-forming ability of liquids, J. Non. Cryst. Solids. 353 (2007) 102-107.

[83] A. Hrubý, Evaluation of glass-forming tendency by means of DTA, Czechoslov. J. Phys. 22 (1972) 1187-1193.

[84] M. Saad, M. Poulain, Glass Forming Ability Criterion, Mater. Sci. Forum. 19-20 (1987) 11-18.

[85] Y. Bai, L. Peng, Q. Zhu, Z. Hao, Non-isothermal crystallization kinetics of stoichiometric lithium disilicate-based glasses with Al_2O_3 additives, J. Non. Cryst. Solids. 445-446 (2016) 116-122.

[86] W.A. Johnson, R.F. Mehl, Reaction kinetics in processes of nucleation and growth, Trans. AIME. 135 (1939) 396-415.

[87] M. Avrami, Interfacial electrochemistry: theory: experiment, and applications, J. chem. Phys. 7 (1939) 103.

[88] A.N. Kolmogorov, On the statistical theory of the crystallization of metals, Bull. Acad. Sci. USSR, Math. Ser. 1 (1937) 355-359.

[89] H.E. Kissinger, Variation of peak temperature with heating rate in differential thermal analysis, J. Res. Natl. Bur. Stand. (1934). 57 (1956) 217.

[90] T. Ozawa, Kinetics of non-isothermal crystallization, Polymer (Guildf). 12 (1971) 150-158.

[91] T. Ozawa, A New Method of Analyzing Thermogravimetric Data, Bull. Chem. Soc. Jpn. 38 (1965) 1881-1886.

[92] J.A. Augis, J.E. Bennett, Calculation of the Avrami parameters for heterogeneous solid state reactions using a modification of the Kissinger method, J. Therm. Anal. 13 (1978) 283-292.

[93] C.S. Ray, D.E. Day, An Analysis of Nucleation-Rate Type of Curves in Glass as Determined by Differential Thermal Analysis, J. Am. Ceram. Soc. 80 (1997) 3100-3018.

[94] T.S. Rao, T.L.S. Rao, A.M.Shaker, K.Venkatraman, Crystallization kinetics of amorphous $Fe_{77}B_{16}Si_5Cr_2$ metallic glass, Int. J. Innov. Res. Sci. Eng. Technol. 5 (2016) 18072-18079.

[95] K. Matusita, S. Sakka, Kinetic study of crystallization of glass by differential thermal analysis-criterion on application of Kissinger plot, J. Non. Cryst. Solids. 38-39 (1980) 741-746.

[96] X.J. Xu, C.S. Ray, D.E. Day, Nucleation and Crystallization of Na_2O-2CaO-3SiO_2 Glass by Differential Thermal Analysis, J. Am. Ceram. Soc. 74 (1991) 909-914.

[97] K. Matusita, S. Sakka, Y. Matsui, Determination of the activation energy for crystal growth by differential thermal analysis, J. Mater. Sci. 10 (1975) 961-966.

[98] K. Matusita, S. Sakka, Kinetic Study on Non-Isothermal Crystallization of Glass by Thermal Analysis, Bull. Inst. Chem. Res. Kyoto Univ. 59 (1981) 159-171.

[99] H.-J. Wang, B.-T. Li, H.-X. Lin, W. Chen, L. Luo, Effects of MgO on Crystallization and Microwave Dielectric Properties of MgO-Al_2O_3-SiO_2-TiO_2-La_2O_3 Glass-Ceramics, Int. J. Appl. Glas. Sci. 5 (2014) 436-442.

[100] G.H. Chen, Effect of ZnO addition on properties of cordierite-based glass-ceramics, J. Mater. Sci. Mater. Electron. 18 (2007) 1253-1257.

[101] A. Hunger, G. Carl, C. Rüssel, Formation of nano-crystalline quartz crystals from ZnO/MgO/Al_2O_3/TiO_2/ZrO_2/SiO_2 glasses, Solid State Sci. 12 (2010) 1570-1574.

[102] M. Dittmer, C. Rüssel, Colorless and high strength MgO/Al_2O_3/SiO_2 glass-ceramic dental material using zirconia as nucleating agent, J. Biomed. Mater. Res. Part B Appl. Biomater. 100B (2012) 463-470.

[103] A. Gawronski, C. Patzig, T. Höche, C. Rüssel, Effect of Y_2O_3 and CeO_2 on the crystallisation behaviour and mechanical properties of glass–ceramics in the system MgO/Al_2O_3/SiO_2/ZrO_2, J. Mater. Sci. 50 (2015) 1986-1995.

[104] S. Seidel, M. Dittmer, W. Wisniewski, W. Höland, C. Rüssel, Effect of the ZrO_2 concentration on the crystallization behavior and the mechanical properties of high-strength MgO–Al_2O_3–SiO_2 glass–ceramics, J. Mater. Sci. 52 (2017) 1955-1968.

[105] W. Tang, Q. Zhang, Z. Luo, J. Yu, X. Gao, Y. Li, A. Lu, CoO-doped MgO–Al_2O_3–SiO_2-colored transparent glass–ceramics with high crystallinity, Appl. Phys. A. 124 (2018) 191.

[106] M. Dittmer, C.F. Yamamoto, C. Bocker, C. Rüssel, Crystallization and mechanical properties of $MgO/Al_2O_3/SiO_2/ZrO_2$glass-ceramics with and without the addition of yttria, Solid State Sci. 13 (2011) 2146-2153.

[107] A. Gawronski, C. Patzig, T. Höche, C. Rüssel, High-strength glass-ceramics in the system $MgO/Al_2O_3/SiO_2/ZrO_2/Y_2O_3$ – microstructure and properties, CrystEngComm. 15 (2013) 6165.

[108] R. Casasola, J.M. Pérez, M. Romero, Effect of fluorine content on glass stability and the crystallisation mechanism for glasses in the SiO_2-CaO-K_2O-F system, J. Non. Cryst. Solids. 378 (2013) 25-33.

[109] J. Wang, C. Liu, G. Zhang, J. Xie, J. Han, X. Zhao, Crystallization properties of magnesium aluminosilicate glass-ceramics with and without rare-earth oxides, J. Non. Cryst. Solids. 419 (2015) 1-5.

[110] J. Wang, J.S. Cheng, Z.L. Deng, Effect of alkali metal Oxides on viscosity and crystallization of the MgO-Al_2O_3-SiO_2 glasses, Phys. B Condens. Matter. 415 (2013) 34-37.

[111] L.. Pinckney, Transparent, high strain point spinel glass-ceramics, J. Non. Cryst. Solids. 255 (1999) 171-177.

[112] G. Chen, X. Liu, Sintering, crystallization and properties of $MgO–Al_2O_3–SiO_2$ system glass-ceramics containing ZnO, J. Alloys Compd. 431 (2007) 282-286.

[113] H. Ohsato, J.S. Kim, C. Il Cheon, I. Kagomiya, Crystallization of indialite/cordierite glass ceramics for millimeter-wave dielectrics, in: Ceram. Int., Elsevier, 2015: p. S588-S593.

[114] H.-J. Wang, B.-T. Li, H.-X. Lin, W. Chen, L. Luo, Effects of La2O3 on Crystallization, Microstructure, and Properties of MgO-Al_2O_3-SiO_2-TiO_2-La_2O_3 Glass-ceramics, Int. J. Appl. Glas. Sci. 7 (2016) 80-87.

[115] S.B. Sohn, S.Y. Choi, Y.K. Lee, Controlled crystallization and characterization of cordierite glass-ceramics for magnetic memory disk substrate, J. Mater. Sci. 35 (2000) 4815-4821.

[116] T. Benitez, S. Y. Gómez, A.P.N. de Oliveira, N. Travitzky, D. Hotza, Transparent ceramic and glass-ceramic materials for armor applications, Ceram. Int. 43 (2017) 13031-13046.

[117] D.G. Grossman, J.L.M. Johnson, Glass-ceramic composition for dental constructs, 4,652,321, 1987.

[118] D.S. Baik, K.S. No, J.S. Chun, Y.J. Yoon, H.Y. Cho, A comparative evaluation method of machinability for mica-based glass-ceramics, J. Mater. Sci. 30 (1995) 1801-1806.

[119] M. Tiegel, A. Herrmann, C. Rüssel, J. Körner, D. Klöpfel, J. Hein, M.C. Kaluza, Magnesium aluminosilicate glasses as potential laser host material for ultrahigh power laser systems, J. Mater. Chem. C. 1 (2013) 5031-5039.

[120] S.-P. Hwang, J.-M. Wu, Effect of Composition on Microstructural Development in, Am. Ceram. Soc. 84 (2001) 1108-1112.

[121] S.Z. Hussain, S.K. Durrani, K. Saeed, A. Hussain, N. Hussain, M. Ahmad, Phase and Thermal Analysis of Magnesium Aluminum Silicate Glass Ceramic, J Pak Mater Soc. 4 (2010) 1-7.

[122] L. Han, J. Song, C. Lin, J. Liu, T. Liu, Q. Zhang, Z. Luo, A. Lu, Crystallization, structure and properties of MgO-Al_2O_3-SiO_2 highly crystalline transparent glass-ceramics nucleated by multiple nucleating agents, J. Eur. Ceram. Soc. 38 (2018) 4533-4542.

[123] J.W. Cao, Y.H. Li, K.M. Liang, Effect of P2O5 on evolution of microstructure of $MgO–Al_2O_3–SiO_2$ glass ceramics, Adv. Appl. Ceram. 108 (2009) 352-357.

[124] S. Seidel, C. Patzig, M. Krause, T. Höche, A. Gawronski, Y. Hu, C. Rüssel, The effect of CeO_2 on the crystallization of MgO-Al_2O_3-SiO_2-ZrO_2 glass, Mater. Chem. Phys. 212 (2018) 60-68.

[125] L. Barbieri, A. Bonamartini Corradi, C. Leonelli, C. Siligardi, T. Manfredini, G.C. Pellacani, Effect of TiO_2 addition on the properties of complex aluminosilicate glasses and glass-ceramics, Mater. Res. Bull. 32 (1997) 637-648.

[126] F.H. Margha, S.A.H.M. Abdel-Hameed, N.A.E.S. Ghonim, S.A. Ali, S. Kato, S. Satokawa, T. Kojima, Crystallization behaviour and hardness of glass ceramics rich in nanocrystals of ZrO_2, Ceram. Int. 35 (2009) 1133-1137.

[127] O. Dargaud, L. Cormier, N. Menguy, L. Galoisy, G. Calas, S. Papin, G. Querel, L. Olivi, Structural role of Zr^{4+}as a nucleating agent in a MgO-Al2O3-SiO2 glass-ceramics: A combined XAS and HRTEM approach, J. Non. Cryst. Solids. 356 (2010) 2928-2934.

[128] J. Wang, J. Cheng, L. Tang, P. Tian, Effect of nucleating agents and heat treatments on the crystallization of magnesium aluminosilicate transparent glass-ceramics, J. Wuhan Univ. Technol. Mater. Sci. Ed. 28 (2013) 69-72.

[129] Z. Strnad, Glass Ceramic Materials: Liquid Phase Separation, Nucleation, and Crystallization in Glasses, Glass science and technology, vol.8, 1986.

[130] G. hua Chen, Sintering, crystallization, and properties of CaO doped cordierite-based glass-ceramics, J. Alloys Compd. 455 (2008) 298-302.

[131] P. Amista, M. Cesari, A. Montenero, G. Gnappi, L. Lan, Crystallization behaviour in the system MgO-Al_2O_3-SiO_2, J. Non. Cryst. Solids. 192-193 (1995) 529-533.

[132] H. Shao, K. Liang, F. Zhou, G. Wang, A. Hu, Microstructure and mechanical properties of MgO–Al_2O_3–SiO_2–TiO_2 glass–ceramics, Mater. Res. Bull. 40 (2005) 499-506.

[133] G.H. Beall, Chain silicate glass-ceramics, J. Non. Cryst. Solids. 129 (1991) 163-173.

[134] G.H. Beall, J.E. Pierson, L.R. Pinckney, Forsterite glass-ceramics of high crystallinity and chrome content, 6,660,669 B2, 2003.

[135] P. Wange, T. Höche, C. Rüssel, J. Dieter Schnapp, Microstructure-property relationship in high-strength MgO-Al2O3-SiO2-TiO2 glass-ceramics, J. Non. Cryst. Solids. 298 (2002) 137-145.

[136] P. Lu, Y. Zheng, J. Cheng, D. Guo, Effect of La2O3addition on crystallization and properties of Li_2O-Al_2O_3-SiO_2 glass-ceramics, Ceram. Int. 39 (2013) 8207-8212.

[137] A. Ananthanarayanan, G.P. Kothiyal, L. Montagne, B. Revel, MAS-NMR studies of lithium aluminum silicate (LAS) glasses and glass-ceramics having different Li_2O/Al_2O_3 ratio, J. Solid State Chem. 183 (2010) 120-127.

[138] M.D. Karkhanavala, F.A. Hummel, The Polymorphism of Cordierite, J. Am. Ceram. Soc. 36 (1953) 389-392.

[139] A.W.A. El-Shennawi, A.A. Omar, A.R. El-Ghannam, Expansion characteristics of some Li_2O-MgO-Al_2O_3-SiO_2 glasses and glass-ceramics, Ceram. Int. 17 (1991) 25-29.

[140] A.W.A. El-Shennawi, A.A. Omar, A.M. Morsy, The role of titania and titania mixtures in the nucleation and crystallization of spodumene-willemite-diopside glasses, Thermochim. Acta. 58 (1982) 125-153.

[141] A.W.A. El-Shennawi, A.A. Omar, A.R. El-Ghannam, Crystallization of spodumene-lithium magnesium orthosilicate glasses, Ceram. Int. 16 (1990) 47-52.

[142] Z.H. Bao, L.F. Miao, W.H. Jiang, J.M. Liu, J. Liang, T. Chen, Effect of B_2O_3 and P_2O_5 Addition on the Phase-separation and Crystallization of Li_2O-MgO-Al_2O_3-SiO_2 Glass-ceramics, Mater. Sci. Forum. 848 (2016) 243-248.

[143] Q. Fu, F. Zhao, H. Li, H. Peng, X. Nan, A Multi-interlayer LMAS Joint of C/C-SiC Composites and LAS Glass Ceramics, J. Mater. Sci. Technol. 31 (2015) 467-472.

[144] Q.G. Fu, H. Peng, X.Y. Nan, H.J. Li, Y.H. Chu, Effect of SiC nanowires on the thermal shock resistance of joint between carbon/carbon composites and Li_2O-Al_2O_3-SiO_2 glass ceramics, J. Eur. Ceram. Soc. 34 (2014) 2535-2541.

[145] Q.G. Fu, H. Peng, H.J. Li, J. Wang, Q. Zhu, A gradient LMAS interlayer joint of SiC coated C/C composites to LAS glass ceramics, Ceram. Int. 40 (2014) 2461-2466.

[146] X. Guo, H. Yang, C. Han, F. Song, Crystallization and microstructure of Li_2O-Al_2O_3-SiO_2 glass containing complex nucleating agent, Thermochim. Acta. 444 (2006) 201-205.

[147] G. Xingzhong, Z. Lingjie, Y. Hui, Effects of Li replacement on the nucleation, crystallization and microstructure of Li_2O-Al_2O_3-SiO_2 glass, J. Non. Cryst. Solids. 354 (2008) 4031-4036.

[148] I. Alekseeva, O. Dymshits, M. Tsenter, A. Zhilin, Influence of various alkali and divalent metal oxides on phase transformations in NiO-doped glasses of the Li_2O-Al_2O_3-SiO_2-TiO_2 system, J. Non. Cryst. Solids. 357 (2011) 2209-2214.

[149] Y. Wang, J. Ohwaki, New transparent vitroceramics codoped with Er^{3+} and Yb^{3+} for efficient frequency upconversion, Appl. Phys. Lett. 63 (1993) 3268-3270.

[150] J. Méndez-Ramos, V. Lavín, I.R. Martín, U.R. Rodríguez-Mendoza, V.D. Rodríguez, A.D. Lozano-Gorrín, P. Núñez, Role of the Eu^{3+} ions in the formation of transparent oxyfluoride glass ceramics, J. Appl. Phys. 89 (2001) 5307-5310.

[151] N. Henry, P. Deniard, S. Jobic, R. Brec, C. Fillet, F. Bart, A. Grandjean, O. Pinet, Heat treatments versus microstructure in a molybdenum-rich borosilicate, J. Non. Cryst. Solids. 333 (2004) 199-205.

[152] J.D. Musgraves, J. Hu, L. Calvez, Springer Handbook of Glass, Springer International Publishing, Cham, 2019.

[153] I.M. Hamouda, Current perspectives of nanoparticles in medical and dental biomaterials, J. Biomed. Res. 26 (2012) 143-151.

[154] L. Esteban-Tejeda, F. Malpartida, A. Esteban-Cubillo, C. Pecharromán, J.S. Moya, Antibacterial and antifungal activity of a soda-lime glass containing copper nanoparticles, Nanotechnology. 20 (2009) 505701.

[155] T. Kasuga, H. Kume, Y. Abe, Porous glass-ceramics with bacteriostatic properties in silver-containing titanium phosphates: Control of release of silver ions from glass-ceramics into aqueous solution, J. Am. Ceram. Soc. 80 (1997) 777-780.

[156] B. Cabal, F. Malpartida, R. Torrecillas, A. Hoppe, A.R. Boccaccini, J.S. Moya, The development of bioactive glass-ceramic substrates with biocide activity, Adv. Eng. Mater. 13 (2011) 462-466.

[157] S. Taruta, K. Mukoyama, S. Suzuki, Crystallization process and some properties of calcium mica-apatite glass-ceramics, J. Non. Cryst. Solids. 296 (2001) 201-211.

[158] D.G. Grossman, Machinable Glass-Ceramics Based on Tetrasilicic Mica, J. Am. Ceram. Soc. 55 (1972) 446-449.

[159] E. Apel, J. Deubener, A. Bernard, M. Höland, R. Müller, H. Kappert, V. Rheinberger, W. Höland, Phenomena and mechanisms of crack propagation in glass-ceramics, J. Mech. Behav. Biomed. Mater. 1 (2008) 313-325.

[160] L. Wondraczek, P. Pradeau, Transparent hafnia-containing β-quartz glass ceramics: Nucleation and crystallization behavior, J. Am. Ceram. Soc. 91 (2008) 1945-1951.

[161] X.Z. Guo, H. Yang, M. Cao, C. Han, F.F. Song, Crystallinity and crystallization mechanism of lithium aluminosilicate glass by X-ray diffractometry, Trans. Nonferrous Met. Soc. China (English Ed. 16 (2006) 593-597.

[162] P. Loiseau, D. Caurant, N. Baffier, L. Mazerolles, C. Fillet, Glass–ceramic nuclear waste forms obtained from SiO_2–Al_2O_3–CaO–ZrO_2–TiO_2 glasses containing lanthanides (Ce, Nd, Eu, Gd, Yb) and actinides (Th): study of internal crystallization, J. Nucl. Mater. 335 (2004) 14-32.

[163] S. Pérez-Villar, J. Rubio, J.L. Oteo, Study of color and structural changes in silver painted medieval glasses, J. Non. Cryst. Solids. 354 (2008) 1833-1844.

[164] M.J. Pascual, A. Durán, M.O. Prado, A new method for determining fixed viscosity points of glasses, Phys. Chem. Glas. 46 (2005) 512-520.

[165] N. Cornejo, L. Pascual, A. Tamayo, F. Rubio, M.A. Rodríguez, J. Rubio, Crystallization mechanism of glass-ceramics prepared from Ni-Cu-Co mining wastes, J. Non. Cryst. Solids. 358 (2012) 3028-3035.

[166] W. Vogel, Glass Chemistry, Second edi, Springer Berlin Heidelberg, Berlin, Heidelberg, 1994.

[167] J.-J. Aguilera-Correa, A. Mediero, F.-M. Conesa-Buendía, A. Conde, M.-Á. Arenas, J.-J. De-Damborenea, J. Esteban, Microbiological and Cellular Evaluation of a Fluorine-Phosphorus-Doped Titanium Alloy, a Novel Antibacterial and Osteostimulatory Biomaterial with Potential Applications in Orthopedic Surgery, Appl. Environ. Microbiol. 85 (2019) 1-17.

[168] T.J. Kinnari, J. Esteban, E. Gomez-Barrena, N. Zamora, R. Fernandez-Roblas, A. Nieto, J.C. Doadrio, A. López-Noriega, E. Ruiz-Hernández, D. Arcos, M. Vallet-Regí, Bacterial adherence to SiO2-based multifunctional bioceramics, J. Biomed. Mater. Res. - Part A. 89 (2009) 215-223.

[169] C. Pérez-Jorge, A. Conde, M.A. Arenas, R. Pérez-Tanoira, E. Matykina, J.J. de Damborenea, E. Gómez-Barrena, J. Esteban, In vitro assessment of Staphylococcus epidermidis and Staphylococcus aureus adhesion on TiO2 nanotubes on Ti-6Al-4V alloy, J. Biomed. Mater. Res. Part A. 100A (2012) 1696-1705.

[170] D. Kumar, R.G. Ward, D.J. Williams, Effect of fluorides on silicates and phosphates, Discuss. Faraday Soc. 32 (1961) 147.

[171] J.C. Mauro, Effect of fragility on relaxation of density fluctuations in glass, J. Non. Cryst. Solids. 357 (2011) 3520-3523.

[172] P. Glatz, M. Comte, L. Cormier, L. Montagne, B. Doumert, G.G. Moore, Different roles of phosphorus in the nucleation of lithium aluminosilicate glasses, J. Non. Cryst. Solids. 493 (2018) 48-56.

[173] J. Wu, S. Hwang, Effects of (B_2O_3, P_2O_5) Additives on Microstructural Development and Phase- • Transformation Kinetics of Stoichiometric Cordierite Glasses, J. Am. Ceram. Soc. 83 (2000) 1259-1265.

[174] A. Arvind, A. Sarkar, V.K. Shrikhande, A.K. Tyagi, G.P. Kothiyal, The effect of TiO_2 addition on the crystallization and phase formation in lithium aluminum silicate (LAS) glasses nucleated by P_2O_5, J. Phys. Chem. Solids. 69 (2008) 2622-2627.

[175] W. Zheng, J. Cui, L. Sheng, H. Chao, Z. Peng, C. Shen, Effect of complex nucleation agents on preparation and crystallization of CaO-MgO-Al_2O_3-SiO_2 glass-ceramics for float process, J. Non. Cryst. Solids. 450 (2016) 6-11.

[176] P. Glatz, M. Comte, L. Cormier, L. Montagne, B. Doumert, G.G. Moore, Different roles of phosphorus in the nucleation of lithium aluminosilicate glasses, J. Non. Cryst. Solids. 493 (2018) 48-56.

[177] L. Lilensten, Q. Fu, B.R. Wheaton, A.J. Credle, R.L. Stewart, J.T. Kohli, Kinetic study on lithium-aluminosilicate (LAS) glass-ceramics containing MgO and ZnO, Ceram. Int. 40 (2014) 11657-11661.

[178] A. Gaddam, H.R. Fernandes, D.U. Tulyaganov, M.J. Ribeiro, J.M.F. Ferreira, The roles of $P_2O_5$and SiO_2/Li_2O ratio on the network structure and crystallization kinetics of non-stoichiometric lithium disilicate based glasses, J. Non. Cryst. Solids. 481 (2018) 512-521.

[179] L. Han, J. Song, Q. Zhang, Z. Luo, A. Lu, Crystallization, structure and characterization of MgO-Al_2O_3-SiO_2-P_2O_5 transparent glass-ceramics with high crystallinity, J. Non. Cryst. Solids. 481 (2018) 123-131.

[180] I.W. Donald, The crystallization kinetics of a glass based on the cordierite composition studied by DTA and DSC, J. Mater. Sci. 30 (1995) 904-915.

[181] C.S. Ray, D.E. Day, Identifying internal and surface crystallization by differential thermal analysis for the glass-to-crystal transformations, Thermochim. Acta. 280-281 (1996) 163-174.

[182] L.E. Marques, A.M.C. Costa, M.C. Crovace, A.C.M. Rodrigues, A.A. Cabral, Influence of particle size on nonisothermal crystallization in a lithium disilicate glass, J. Am. Ceram. Soc. 98 (2015) 774-780.

[183] Y.M. Sung, S.A. Dunn, J.A. Koutsky, The effect of boria and titania addition on the crystallization and sintering behavior of Li_2O-Al_2O_3-$4SiO_2$ glass, J. Eur. Ceram. Soc. 14 (1994) 455-462.

[184] J. Shyu, H. Lee, Sintering, Crystallization, and Properties of B_2O_3/P_2O_5-Doped Li_2O-Al_2O_3-$4SiO_2$ Class-Ceramics, J. Am. Ceram. Soc. 78 (1995) 2161-2167.

[185] A. Hu, M. Li, D. Mao, Preparation of whisker β-spodumene glass-ceramics, J. Am. Ceram. Soc. 89 (2006) 358-360.

[186] V.R. Mastelaro, E.D. Zanotto, Anisotropic residual stresses in partially crystallized Li_2O-$2SiO_2$ glass-ceramics, J. Non. Cryst. Solids. 247 (1999) 79-86.

[187] X. Guo, H. Yang, M. Cao, Nucleation and crystallization behavior of Li_2O-Al_2O_3-SiO_2 system glass-ceramic containing little fluorine and no-fluorine, J. Non. Cryst. Solids. 351 (2005) 2133-2137.

[188] X. Guo, X. Cai, J. Song, G. Yang, H. Yang, Crystallization and microstructure of CaO-MgO-Al_2O_3-SiO_2 glass-ceramics containing complex nucleation agents, J. Non. Cryst. Solids. 405 (2014) 63-67.

[189] A.L. Patterson, The scherrer formula for X-ray particle size determination, Phys. Rev. 56 (1939) 978-982.

[190] M. Chen, F. He, J. Shi, J. Xie, H. Yang, P. Wan, Low Li2O content study in Li_2O-Al_2O_3-SiO_2 glass-ceramics, J. Eur. Ceram. Soc. 39 (2019) 4988-4995.

[191] U. Kang, T.I. Chuvaeva, A.A. Onushchenko, A. V. Shashkin, A.A. Zhilin, H.J. Kim, Y.G. Chang, Radiative properties of Nd-doped transparent glass-ceramics in the lithium aluminosilicate system, J. Non. Cryst. Solids. 278 (2000) 75-84.

[192] W. Höland, V. Rheinberger, M. Frank, Mechanisms of nucleation and controlled crystallization of needle-like apatite in glass-ceramics of the SiO_2–Al_2O_3–K_2O–CaO–P_2O_5 system, J. Non. Cryst. Solids. 253 (1999) 170-177.

[193] S. Taruta, T. Ichinose, T. Yamaguchi, K. Kitajima, Preparation of transparent lithium-mica glass-ceramics, J. Non. Cryst. Solids. 352 (2006) 5556-5563.

[194] V. Khani, P. Alizadeh, Crystallization Kinetics and Characterization of Nanostructure Mica Glass-Ceramics With Optical Transparency, J. nanostructures. 4 (2014) 45-53.

[195] B.I. Sharma, M. Goswami, P. Sengupta, V.K. Shrikhande, G.B. Kale, G.P. Kothiyal, Study on some thermo-physical properties in Li2O–ZnO–SiO2 glass-ceramics, Mater. Lett. 58 (2004) 2423-2428.

[196] H. Grussaute, L. Montagne, G. Palavit, J.L. Bernard, Phosphate speciation in Na_2O-CaO-P_2O_5-SiO_2 and Na_2O-TiO_2-P_2O_5-SiO_2 glasses, J. Non. Cryst. Solids. 263 (2000) 312-317.

[197] M.D. O'Donnell, S.J. Watts, R. V. Law, R.G. Hill, Effect of P_2O_5 content in two series of soda lime phosphosilicate glasses on structure and properties - Part II: Physical properties, J. Non. Cryst. Solids. 354 (2008) 3561-3566.

[198] D.S. Brauer, M.N. Anjum, M. Mneimne, R.M. Wilson, H. Doweidar, R.G. Hill, Fluoride-containing bioactive glass-ceramics, J. Non. Cryst. Solids. 358 (2012) 1438-1442.

[199] I.W. Donald, B.L. Metcalfe, A.E.P. Morris, Influence of transition metal oxide additions on the crystallization kinetics, microstructures and thermal expansion characteristics of a lithium zinc silicate glass, J. Mater. Sci. 27 (1992) 2979-2999.

[200] H. Darwish, S.N. Salama, S.M. Salman, Contribution of germanium dioxide to the thermal expansion characteristics of some borosilicate glasses and their corresponding glass-ceramics, Thermochim. Acta. 374 (2001) 129-135.

[201] O. García-Moreno, A. Fernández, S. Khainakov, R. Torrecillas, Negative thermal expansion of lithium aluminosilicate ceramics at cryogenic temperatures, Scr. Mater. 63 (2010) 170-173.

[202] M. Bengisu, R.K. Brow, Effect of long-term heating and thermal cycling on thermal expansion, phase distribution, and microhardness of lithium aluminosilicate glass-ceramics, J. Non. Cryst. Solids. 331 (2003) 137-144.

[203] D.U. Tulyaganov, S. Agathopoulos, I. Kansal, P. Valério, M.J. Ribeiro, J.M.F. Ferreira, Synthesis and properties of lithium disilicate glass-ceramics in the system SiO_2-Al_2O_3-K_2O-Li_2O, Ceram. Int. 35 (2009) 3013-3019.

[204] B. Li, S. Wang, Y. Fang, Effect of Cr_2O_3 addition on crystallization , microstructure and properties of Li_2O-Al_2O_3-SiO_2 glass-ceramics, J. Alloys Compd. 693 (2017) 9-15.

[205] O. García-Moreno, A. Borrell, B. Bittmann, A. Fernández, R. Torrecillas, Alumina reinforced eucryptite ceramics: Very low thermal expansion material with improved mechanical properties, J. Eur. Ceram. Soc. 31 (2011) 1641-1648.

[206] Z. Xiao, J. Zhou, Y. Wang, M. Luo, Microstructure and Properties of Li_2O-Al_2O_3-SiO_2-P_2O_5 Glass-Ceramics, Open Mater. Sci. J. 5 (2011) 45-50.

[207] M.J. Toplis, D.B. Dingwell, The variable influence of P_2O_5 on the viscosity of melts of differing alkali/aluminium ratio: Implications for the structural role of phosphorus in silicate melts, Geochim. Cosmochim. Acta. 60 (1996) 4107-4121.

[208] C.A.M. Mulder, Defect structures in silica glass, J. Non-CrystaUine Solids. 95 & 96 (1987) 303-310.

[209] S. Perez-Villar, A. Tamayo, M.A. Mazo, F. Rubio, J. Rubio, Application of the Raman and IR/ATR spectroscopies to the study of the glasses upon grinding, Bol. la Soc. Española Cerámica y Vidr. 47 (2008) 89-94.

[210] Y. Li, K. Liang, J. Cao, B. Xu, Spectroscopy and structural state of V^{4+} ions in lithium aluminosilicate glass and glass-ceramics, J. Non. Cryst. Solids. 356 (2010) 502-508.

[211] S.K. Sharma, B. Simons, Raman study of crystalline polymorphs and glasses of spodumene composition quenched from various pressures, Am. J. Sci. 66 (1981) 118-126.

[212] P.F. McMillan, B.T. Poe, P.H. Gillet, B. Reynard, A study of SiO2 glass and supercooled liquid to 1950 K via high-temperature Raman spectroscopy, Geochim. Cosmochim. Acta. 58 (1994) 3653-3664.

[213] O.S. Dymshits, I.P. Alekseeva, A.A. Zhilin, M.Y. Tsenter, P.A. Loiko, N.A. Skoptsov, A.M. Malyarevich, K. V Yumashev, X. Mateos, A. V Baranov, Structural characteristics and spectral properties of novel transparent lithium aluminosilicate glass-ceramics containing (Er,Yb)NbO_4 nanocrystals, J. Lumin. 160 (2015) 337-345.

[214] C. Haiyan, H. Guosong, M. Hanfen, G. Fuxi, Structure and Raman spectra of glasses containing several glass-forming oxides and no glass-modifying oxide, J. Non. Cryst. Solids. 80 (1986) 152-159.

[215] H. Aguiar, J. Serra, P. González, B. León, Structural study of sol-gel silicate glasses by IR and Raman spectroscopies, J. Non. Cryst. Solids. 355 (2009) 475-480.

[216] A.K. Yadav, P. Singh, A review of the structures of oxide glasses by Raman spectroscopy, RSC Adv. 5 (2015) 67583-67609.

[217] Y. Hase, I.V.P. Yoshida, Li-O Raman bands of (Li_2CO_3)-Li-6 and (Li_2CO_3)-Li-7, Spectrochim. Acta - Part A Mol. Biomol. Spectrosc. 35 (1979) 377-378.

[218] P.F. McMillan, Structural Studies of Silicate Glasses and Melts-Applications and Limitations of Raman Spectroscopy, Am. Mineral. 69 (1984) 622-644.

[219] C. Nelson, D.R. Tallant, Raman studies of sodium silicate glasses with low phosphate contents, Phys. Chem. Glas. 25 (1984) 31-38.

[220] R. Dupree, D. Holland, M.G. Mortuza, The role of small amounts of P_2O_5 in the structure of alkali disilicate glasses, Phys. Chem. Glas. 29 (1988) 18-21.

[221] G.A.H. Mekhemer, Characterization of phosphated zirconia by XRD, Raman and IR spectroscopy, Colloids Surfaces A Physicochem. Eng. Asp. 141 (1998) 227-235.

[222] Hao Gan, P.C. Hess, Phosphate speciation in potassium aluminosilicate glasses, Am. Mineral. 77 (1992) 495-506.

[223] L. Popovic, B. Manoun, D. de Waal, M.K. Nieuwoudt, J.D. Comins, Raman spectroscopic study of phase transitions in Li3PO4, J. Raman Spectrosc. 34 (2003) 77-83.

[224] L. Xia, Y. Yang, X. Zhang, J. Zhang, B. Zhong, T. Zhang, H. Wang, G. Wen, Crystal structure and wave-transparent properties of lithium aluminum silicate glass-ceramics, Ceram. Int. 44 (2018) 14896-14900.

[225] M. Zhang, H. Xu, E.K.H. Salje, P.J. Heaney, Vibrational spectroscopy of beta-eucryptite ($LiAlSiO_4$): optical phonons and phase transition(s), Phys. Chem. Miner. 30 (2003) 457-462.

[226] Y. Sun, Z. Zhang, L. Liu, X. Wang, FTIR, Raman and NMR investigation of $CaO–SiO_2–P_2O_5$ and $CaO–SiO_2–TiO_2–P_2O_5$ glasses, J. Non. Cryst. Solids. 420 (2015) 26-33.

[227] F. Gan, G. Huang, S. Chen, Vibrational spectra of multicomponent inorganic glasses, J. Non. Cryst. Solids. 52 (1982) 203-210.

[228] J. Shi, F. He, C. Ye, L. Hu, J. Xie, H. Yang, X. Liu, Preparation and characterization of $CaO–Al_2O_3–SiO_2$ glass-ceramics from molybdenum tailings, Mater. Chem. Phys. 197 (2017) 57-64.

[229] M. Chatterjee, M.K. Naskar, Sol-gel synthesis of lithium aluminum silicate powders: The effect of silica source, Ceram. Int. 32 (2006) 623-632.

[230] M. Sitarz, The structure of simple silicate glasses in the light of Middle Infrared spectroscopy studies, J. Non. Cryst. Solids. 357 (2011) 1603-1608.

[231] B.N. Roy, Spectroscopic Analysis of the Structure of Silicate Glasses along the Joint $xMAlO_2$-$(1–x)SiO_2$ (M = Li, Na, K, Rb, Cs), J. Am. Ceram. Soc. 70 (1987) 183-192.

[232] D.S. Baik, kwang S. No, J.S.-S. Chun, Mechanical properties of mica glass-ceramics, J. Am. Ceram. Soc. 78 (1995) 1217-22.

[233] D.P. Mukherjee, A.R. Molla, S.K. Das, The influence of MgF_2 content on the characteristic improvement of machinable glass ceramics, J. Non. Cryst. Solids. 433 (2016) 51-59.

[234] D.L. Sidebottom, The fragility of alkali silicate glass melts: Part of a universal topological pattern, J. Non. Cryst. Solids. 516 (2019) 63-66.

[235] D.S. Baik, K.S. No, J.S. Chun, H.Y. Cho, Effect of the aspect ratio of mica crystals and crystallinity on the microhardness and machinability of mica glass-ceramics, J. Mater. Process. Technol. 67 (1997) 50-54.

[236] L. Xia, X. Wang, G. Wen, B. Zhong, L. Song, Nearly zero thermal expansion of β-spodumene glass ceramics prepared by sol-gel and hot pressing method, Ceram. Int. 38 (2012) 5315-5318.

[237] H.J. Holland, S.T. Gulati, A Mechanism for Strengthening Fluorine-Containing Lithium Aluminum Silicate Glass-Ceramics, J. Am. Ceram. Soc. 63 (1980) 686-690.

[238] M. Chavoutier, D. Caurant, O. Majérus, R. Boulesteix, P. Loiseau, C. Jousseaume, E. Brunet, E. Lecomte, Effect of TiO2 content on the crystallization and the color of (ZrO_2,TiO_2)-doped Li_2O-Al_2O_3-SiO_2 glasses, J. Non. Cryst. Solids. 384 (2014) 15-24.

[239] M. Leśniak, J. Partyka, K. Pasiut, M. Sitarz, Microstructure study of opaque glazes from SiO_2–Al_2O_3–MgO–K_2O–Na_2O system by variable molar ratio of SiO_2/Al_2O_3 by FTIR and Raman spectroscopy, J. Mol. Struct. 1126 (2016) 240-250.

[240] P.E. Doherty, D.W. Lee, R.S. Davis, Direct Observation of the Crystallization of Li_2O-Al_2O_3-SiO_2 Glasses Containing TiO2, J. Am. Ceram. Soc. 50 (1967) 77-81.

[241] C.F. Bohren, D.R. Huffman, Absorption and Scattering of Light by Small Particles, JOHN WILEY & SONS, 1983.

[242] N.F. Mott, E.A. Davis, Non-Crystalline semiconductors, in: Electron. Process Non-crystalline Mater., 2nd ed., Oxford University Press, 2012: p. 199-314.

[243] J. Tauc, Optical properties of amorphous semiconductors, in: Amorph. Liq. Semicond., 1st ed., Springer US, 1974: p. 159-214.

[244] Y.H. Elbashar, A.M. Ibrahim, H.A. Elshaikh, A.G. El-Din Mostafa, Influence of CuO and Al_2O_3 addition on the optical properties of sodium zinc phosphate glass absorption filters, Optik (Stuttg). 127 (2016) 7041-7053.

[245] H. Elhaes, M. Attallah, Y. Elbashar, A. Al-Alousi, M. El-Okr, M. Ibrahim, Modeling and optical properties of P_2O_5-ZnO-CaO-Na_2O glasses doped with copper oxide, J. Comput. Theor. Nanosci. 11 (2014) 2079-2084.

[246] A. Mishra, J. Rocherullé, J. Massera, Ag-doped phosphate bioactive glasses: thermal, structural and in-vitro dissolution properties, Biomed. Glas. 2 (2016) 38-48.

[247] S. Pérez-Villar, J. Rubio, J.L. Oteo, Study of color and structural changes in silver painted medieval glasses, J. Non. Cryst. Solids. 354 (2008) 1833-1844.

[248] C.U. Devi, A.K. Sharma, V.V.R.N. Rao, Electrical and optical properties of pure and silver nitrate-doped polyvinyl alcohol films, Mater. Lett. 56 (2002) 167-174.

[249] L. Esteban-Tejeda, F. Malpartida, L.A. Díaz, R. Torrecillas, F. Rojo, J.S. Moya, Glass-(nAg, nCu) biocide coatings on ceramic oxide substrates, PLoS One. 7 (2012) 3-8.

[250] J.L. Elechiguerra, J.L. Burt, J.R. Morones, A. Camacho-Bragado, X. Gao, H.H. Lara, M.J. Yacaman, Interaction of silver nanoparticles with HIV-1, J. Nanobiotechnology. 3 (2005) 1-10.

[251] V.S. Kumar, B.M. Nagaraja, V. Shashikala, A.H. Padmasri, S.S. Madhavendra, B.D. Raju, K.S.R. Rao, Highly efficient Ag/C catalyst prepared by electro-chemical deposition method in controlling microorganisms in water, J. Mol. Catal. A Chem. 223 (2004) 313-319.

[252] C.N. Lok, C.M. Ho, R. Chen, Q.Y. He, W.Y. Yu, H. Sun, P.K.H. Tam, J.F. Chiu, C.M. Che, Silver nanoparticles: Partial oxidation and antibacterial activities, J. Biol. Inorg. Chem. 12 (2007) 527-534.

[253] D.U. Tulyaganov, S. Agathopoulos, H.R. Fernandes, J.M.F. Ferreira, Processing of glass-ceramics in the SiO_2–Al_2O_3–B_2O_3–MgO–CaO–Na_2O–(P_2O_5)–F system via sintering and crystallization of glass powder compacts, Ceram. Int. 32 (2006) 195-200.

[254] V.M.F. Marques, D.U. Tulyaganov, G.P. Kothiyal, J.M.F. Ferreira, The effect of TiO_2 and P_2O_5 on densification behavior and properties of Anortite-Diopside glass-ceramic substrates, J. Electroceramics. 25 (2010) 38-44.

[255] H. Harper, P.F. James, P.W. McMillan, Crystal nucleation in lithium silicate glasses, Discuss. Faraday Soc. 50 (1970) 206-213.

[256] P.F. James, Kinetics of crystal nucleation in silicate glasses, J. Non. Cryst. Solids. 73 (1985) 517-540.

[257] E.D. Zanotto, Isothermal and adiabatic nucleation in glass, J. Non. Cryst. Solids. 89 (1987) 361-370.

[258] E.D. Zanotto, M.C. Weinberg, Trends in homogeneous crystal nucleation in oxide glasses, Phys. Chem. Glas. 30 (1989) 186-192.

[259] H.A. Davies, The formation of metallic glasses, Phys. Chem. Glas. 17 (1976) 159-173.

[260] M.L.F. Nascimento, L.A. Souza, E.B. Ferreira, E.D. Zanotto, Can glass stability parameters infer glass forming ability?, J. Non. Cryst. Solids. 351 (2005) 3296-3308.

[261] A.F. Kozmidis-Petrović, Theoretical analysis of relative changes of the Hruby, Weinberg, and Lu-Liu glass stability parameters with application on some oxide and chalcogenide glasses, Thermochim. Acta. 499 (2010) 54-60.

[262] H. Shao, K. Liang, F. Peng, Crystallization kinetics of MgO-Al_2O_3-SiO_2 glass-ceramics, Ceram. Int. 30 (2004) 927-930.

[263] Y.M. Sung, The effect of additives on the crystallization and sintering of 2MgO-2Al_2O_3-5SiO_2 glass-ceramics, J. Mater. Sci. 31 (1996) 5421-5427.

[264] S.C. Von Clausbruch, M. Schweiger, W. Höland, V. Rheinberger, The effect of P_2O_5 on the crystallization and microstructure of glass-ceramics in the SiO_2–Li_2O–K_2O–ZnO–P_2O_5 system, J. Non. Cryst. Solids. 263-264 (2000) 388-394.

[265] D. Holland, Y. Iqbal, P. James, B. Lee, Early stages of crystallisation of lithium disilicate glasses containing P_2O_5 – An NMR study, J. Non. Cryst. Solids. 232-234 (1998) 140-146.

[266] K. Ariane, A. Tamayo, A. Chorfa, F. Rubio, J. Rubio, Kinetic study on the effect of adding P_2O_5 to the LMAS glass-ceramic, Boletín la Soc. Española Cerámica y Vidr. 5 (2019) 133-140.

[267] P.K. Jha, O.P. Pandey, K. Singh, Structural and thermal properties of Na_2S-P_2S_5 glass and glass ceramics, J. Non. Cryst. Solids. 379 (2013) 89-94.

[268] E. Hamzawy, Crystallization behaviour of fluorphlogopite glass ceramics, Ceram. Silikaty. 45 (2001).

[269] A. Faeghi-Nia, V.K. Marghussian, E. Taheri-Nassaj, Effect of B_2O_3 on crystallization behavior and microstructure of MgO-SiO_2-Al_2O_3-K_2O-F glass-ceramics, Ceram. Int. 33 (2007) 773-778.

[270] D. Hulsenberg, A. Harnisch, A. Bismarck, Microstructuring of Glasses, Springer Berlin Heidelberg New York, 2008.

[271] M. Goswami, A. Sarkar, T. Mirza, V.. Shrikhande, Sangeeta, K.. Gurumurthy, G.. Kothiyal, Study of some thermal and mechanical properties of magnesium aluminium silicate glass ceramic, Ceram. Int. 28 (2002) 585-592.

[272] S. Salman, S. Salama, E. Mahdy, Crystallization and thermo-mechanical properties of Li_2O-ZnO-CaO-SiO_2 glass-ceramics with In_2O_3 and Fe_2O_3 additives, Process. Appl. Ceram. 9 (2015) 215-223.

[273] D.A. McKeown, M.I. Bell, E.S. Etz, Raman spectra and vibrational analysis of the trioctahedral mica phlogopite, Am. Mineral. 84 (1999) 970-976.

[274] T. Mouri, M. Enami, Raman spectroscopic study of olivine-group minerals, J. Mineral. Petrol. Sci. 103 (2008) 100-104.

[275] C.C. Lin, High-pressure Raman spectroscopic study of Co- and Ni-olivines, Phys. Chem. Miner. 28 (2001) 249-257.

[276] A. Chopelas, Single crystal Raman spectra of forsterite, fayalite, and monticellite, Am. Mineral. 76 (1991) 1101-1109.

[277] J. Partyka, M. Leśniak, Raman and infrared spectroscopy study on structure and microstructure of glass-ceramic materials from SiO_2-Al_2O_3-Na_2O-K_2O-CaO system modified by variable molar ratio of SiO_2/Al_2O_3, Spectrochim. Acta - Part A Mol. Biomol. Spectrosc. 152 (2016) 82-91.

[278] C.I. Merzbacher, W.B. White, The structure of alkaline earth aluminosilicate glasses as determined by vibrational spectroscopy, J. Non. Cryst. Solids. 130 (1991) 18-34.

[279] C. Huang, E.C. Behrman, Structure and properties of calcium aluminosilicate glasses, J. Non. Cryst. Solids. 128 (1991) 310-321.

[280] L. Yu, H. Xiao, Y. Cheng, Influence of magnesia on the structure and properties of MgO-Al_2O_3-SiO_2-F-glass-ceramics, Ceram. Int. 34 (2008) 63-68.

[281] J. Partyka, M. Leśniak, Preparation of glass-ceramic glazes in the SiO_2-Al_2O_3-CaO-MgO-K_2O-Na_2O-ZnO system by variable content of ZnO, Ceram. Int. 42 (2016) 8513-8524.

[282] D. Pal, A.K. Chakraborty, S. Sen, S.K. Sen, The synthesis, characterization and sintering of sol-gel derived cordierite ceramics for electronic applications, J. Mater. Sci. 31 (1996) 3995-4005.

[283] H. Gui, C. Li, C. Lin, Q. Zhang, Z. Luo, L. Han, J. Liu, T. Liu, A. Lu, Glass forming, crystallization, and physical properties of MgO-Al_2O_3-SiO_2-B_2O_3 glass-ceramics modified by ZnO replacing MgO, J. Eur. Ceram. Soc. 39 (2019) 1397-1410.

[284] L. Han, J. Song, Q. Zhang, Z. Luo, A. Lu, Crystallization, structure and characterization of MgO-Al_2O_3-SiO_2-P_2O_5 transparent glass-ceramics with high crystallinity, J. Non. Cryst. Solids. 481 (2018) 123-131.

[285] A.R. Molla, A.M. Rodrigues, S.P. Singh, R.F. Lancelotti, E.D. Zanotto, A.C.M. Rodrigues, M. Reza Dousti, A.S.S. de Camargo, C.J. Magon, I.D.A. Silva, Crystallization, mechanical, and optical properties of transparent, nanocrystalline gahnite glass-ceramics, J. Am. Ceram. Soc. 100 (2017) 1963-1975.

[286] M. Leśniak, J. Partyka, M. Sitarz, Impact of ZnO on the structure of aluminosilicate glazes, J. Mol. Struct. 1126 (2016) 251-258.

[287] E.A. Poraĭ-Koshit͡s, Phase-separation phenomena in glasses, 1973.

[288] A. Gianfagna, F. Scordari, S. Mazziotti-Tagliani, G. Ventruti, L. Ottolini, Fluorophlogopite from Biancavilla (Mt. Etna, Sicily, Italy): Crystal structure and crystal chemistry of a new F-dominant analog of phlogopite, Am. Mineral. 92 (2007) 1601-1609.

[289] D.A. McKeown, M.I. Bell, E.S. Etz, Raman spectra and vibrational analysis of the trioctahedral mica phlogopite, Am. Mineral. 84 (1999) 970-976.

[290] A. Goel, D.U. Tulyaganov, E.R. Shaaban, C.S. Knee, S. Eriksson, J.M.F. Ferreira, Structure and crystallization behaviour of some $MgSiO_3$-based glasses, Ceram. Int. 35 (2009) 1529-1538.

[291] N. V. Chukanov, A.D. Chervonnyi, Infrared Spectroscopy of Minerals and Related Compounds, 2016.

[292] B. Yu, K. Liang, S. Gu, Effect of the microstructure on the mechanical properties of CaO-P_2O_5-SiO_2-MgO-F- glass ceramics, Ceram. Int. 29 (2003) 695-698.

[293] Z. Shamsudin, A. Hodzic, C. Soutis, R.J. Hand, S.A. Hayes, I.P. Bond, Characterisation of thermo-mechanical properties of MgO-Al_2O_3-SiO_2 glass ceramic with different heat treatment temperatures, J. Mater. Sci. 46 (2011) 5822-5829.

[294] A. Faeghinia, M. Razavi, Microstructural design of phlogopite glass-ceramics, Glas. Phys. Chem. 42 (2016) 182-187.

[295] S. Taruta, T. Hayashi, K. Kitajima, Preparation of machinable cordierite/mica composite by low-temperature sintering, J. Eur. Ceram. Soc. 24 (2004) 3149-3154.

[296] S. Kapoor, A. Goel, A.F. Correia, M.J. Pascual, H.Y. Lee, H.W. Kim, J.M.F. Ferreira, Influence of ZnO/MgO substitution on sintering, crystallisation, and bio-activity of alkali-free glass-ceramics, Mater. Sci. Eng. C. 53 (2015) 252-261.

[297] U.S. EPA, National primary drinking water regulations, Arsen. Clarifications to. (2009).

[298] J.R. Morones, J.L. Elechiguerra, A. Camacho, K. Holt, J.B. Kouri, J.T. Ramírez, M.J. Yacaman, The bactericidal effect of silver nanoparticles, Nanotechnology. 16 (2005) 2346-2353.

[299] Q.L. Feng, J. Wu, G.Q. Chen, F.Z. Cui, T.N. Kim, J.O. Kim, A mechanistic study of the antibacterial effect of silver ions on Escherichia coli and Staphylococcus aureus, J. Biomed. Mater. Res. 52 (2000) 662-668.

Appendices

Appendix A: LMAS crystallization kinetics

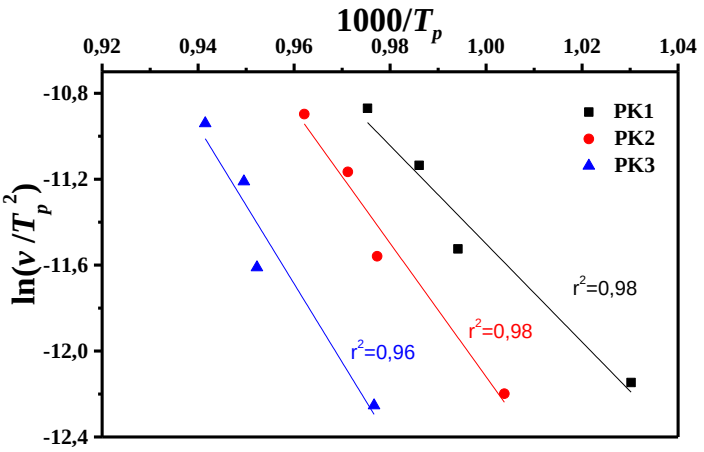

Figure 1A *Kissinger Plot of GP0 specimen*

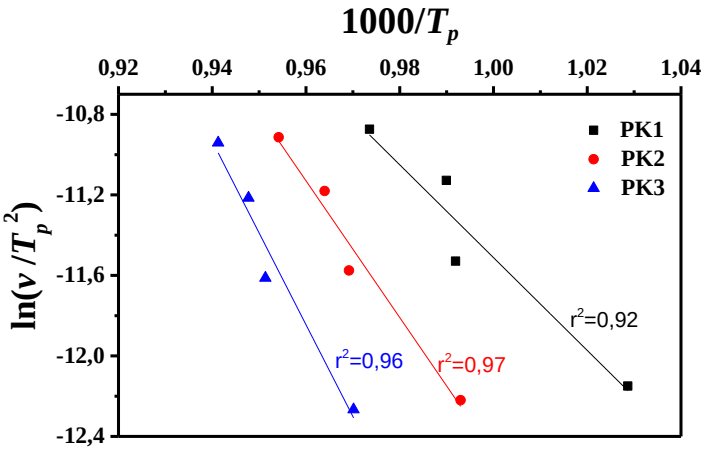

Figure 2A *Kissinger Plot of GP1 specimen*

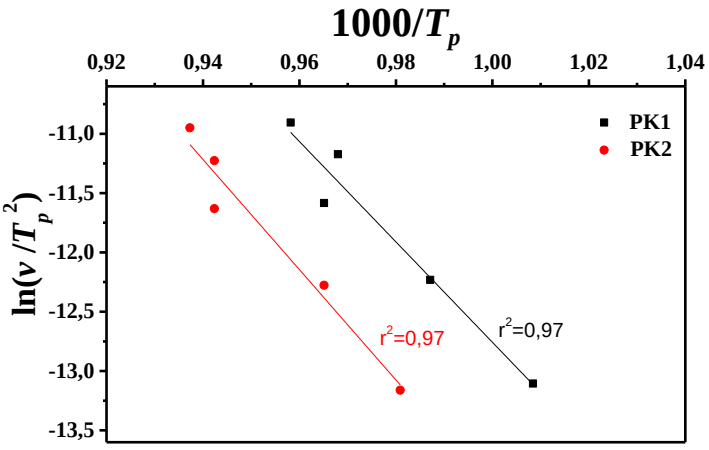

Figure 3A *Kissinger Plot of GP2 specimen*

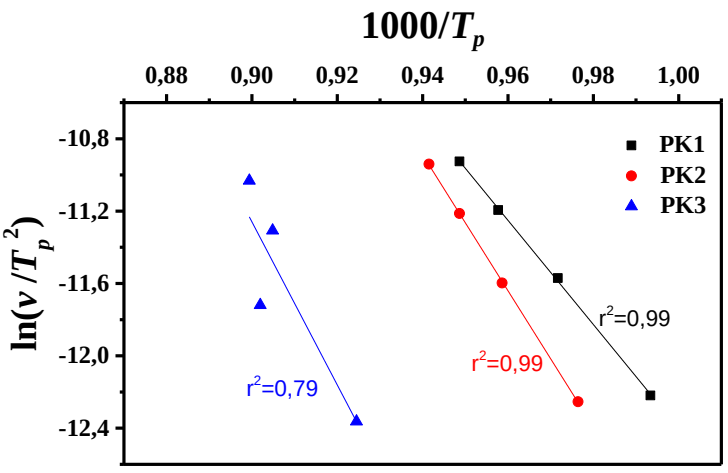

Figure 4A *Kissinger Plot of GP3 specimen*

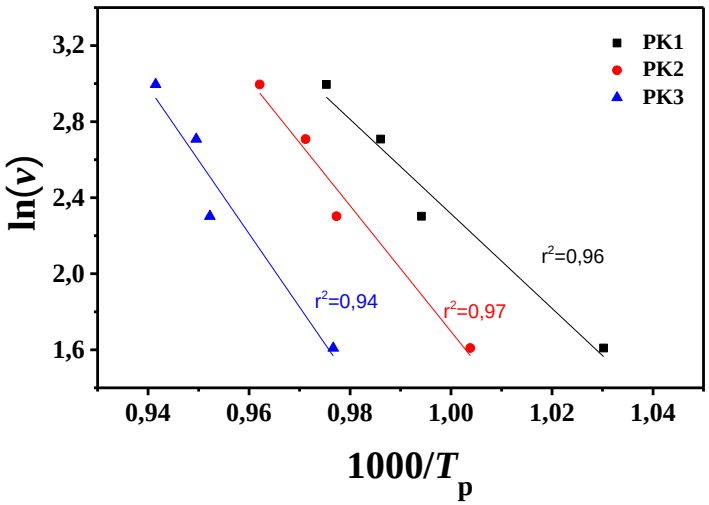

Figure 5A *Ozawa plot of GP0 specimen*

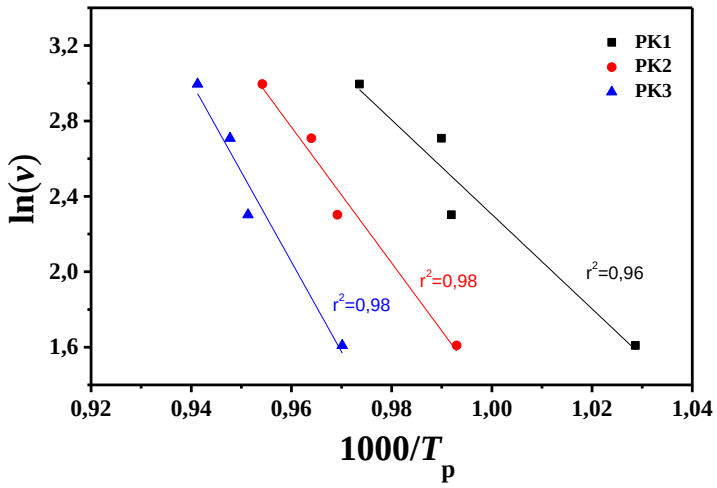

Figure 6A *Ozawa plot of GP1 specimen*

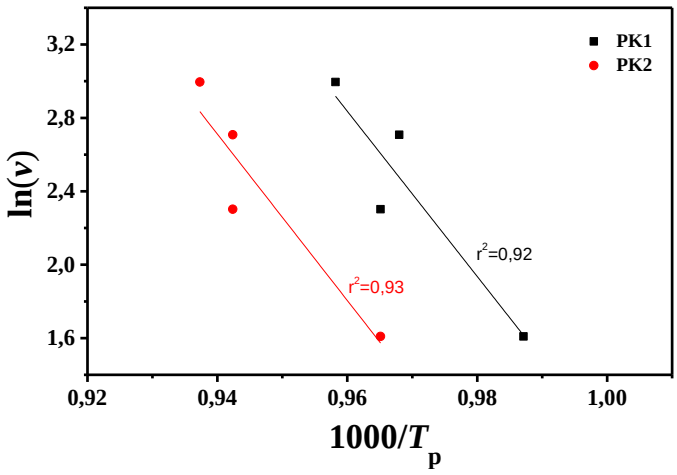

Figure 7A *Ozawa plot of GP2 specimen*

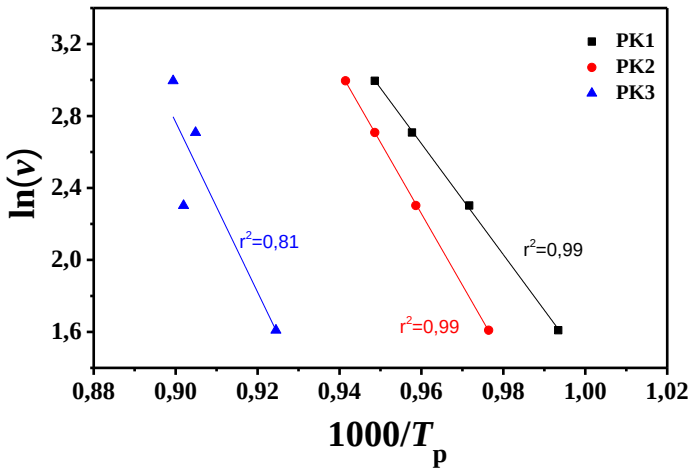

Figure 8A *Ozawa plot of GP3 specimen*

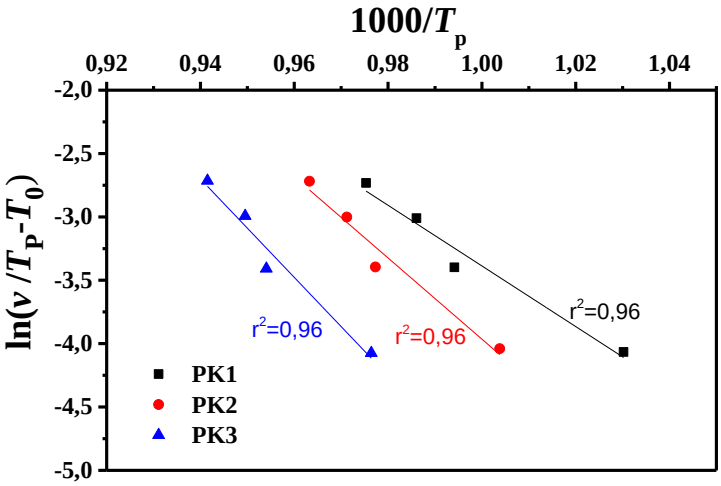

Figure 9A *Augis & Bennett plot of GP0 specimen*

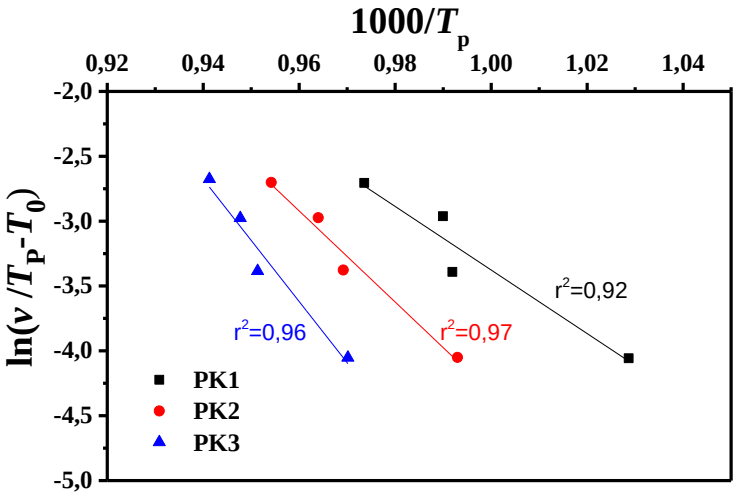

Figure 10A *Augis & Bennett plot of GP1 specimen*

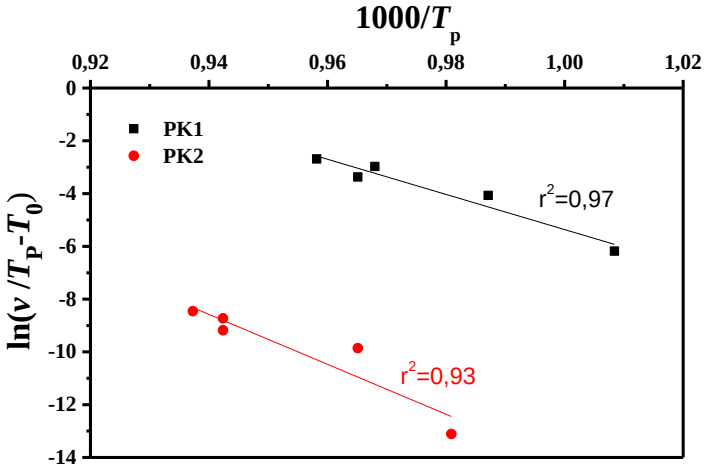

Figure 11A *Augis & Bennett plot of GP2 specimen*

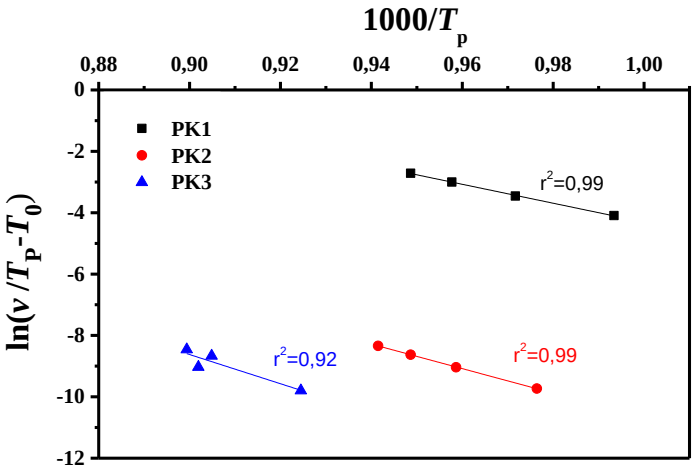

Figure 12A *Augis & Bennett plot of GP3 specimen*

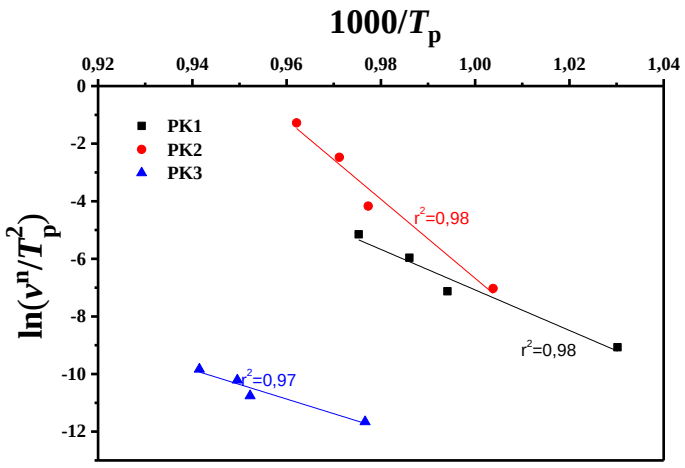

Figure 13A *Matusita & Sakka plot of GP0 specimen*

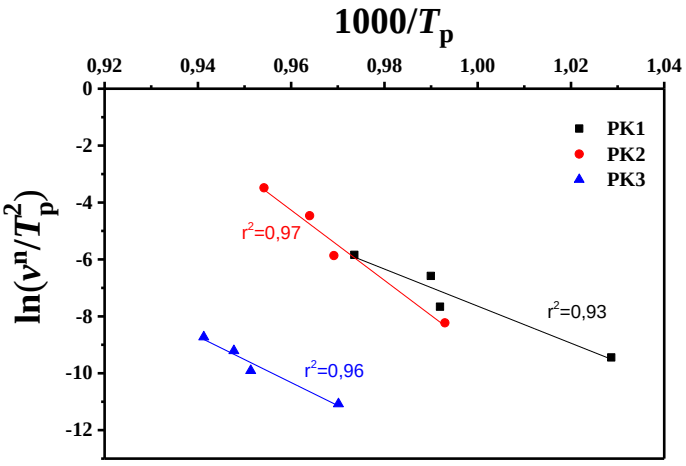

Figure 14A *Matusita & Sakka plot of GP1 specimen*

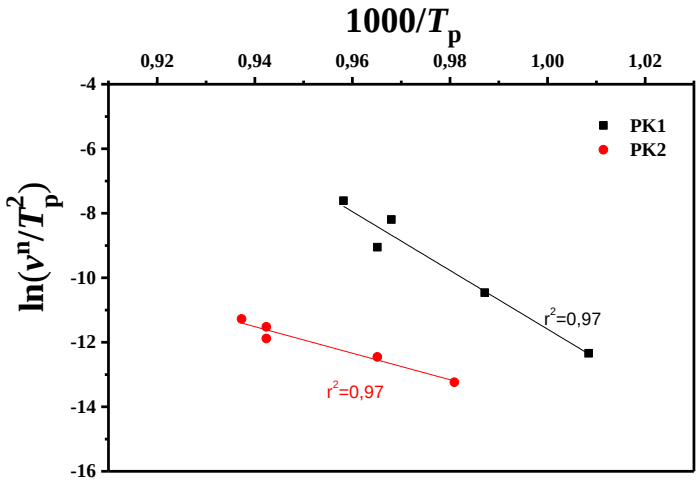

Figure 15A *Matusita & Sakka plot of GP2 specimen*

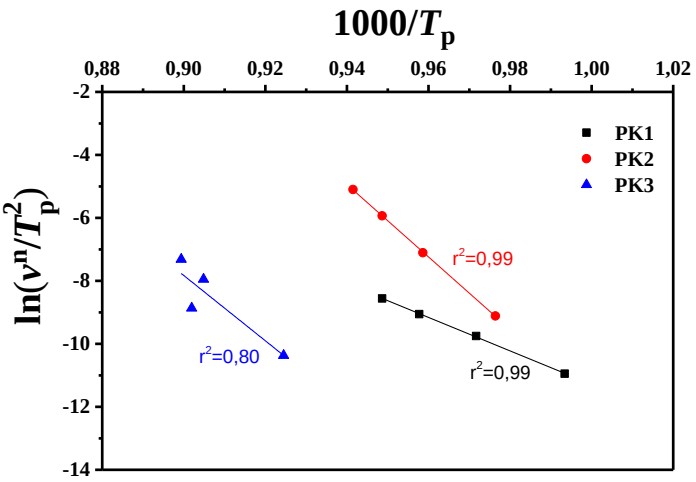

Figure 16A *Matusita & Sakka plot of GP3 specimen*

Appendix B: JCPDS cards of LMAS system

B1) Name and formula

Reference code: 00-040-0073

PDF index name: Lithium Aluminum Silicate

Zeolite name: Unnamed zeolite

Chemical formula: $Li_xAl_xSi_{1-x}O_2$

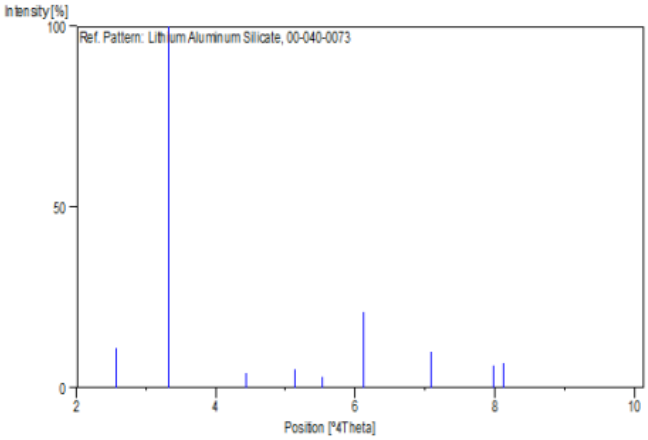

Figure 1B *Stick pattern of Lithium Aluminum Silicate*

B2) Name and formula

Reference code: 00-035-0797

Common name: β-spodumene

PDF index name: Lithium Aluminum Silicate

Empirical formula: $AlLiO_6Si_2$

Chemical formula: $LiAlSi_2O_6$

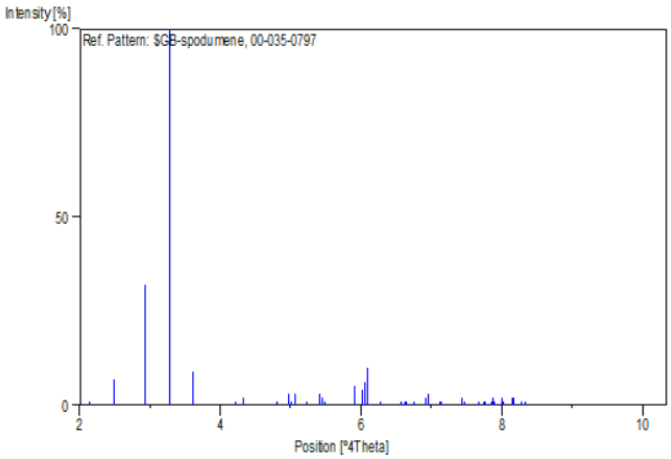

Figure 2B *Stick pattern of β-spodumene*

B3) Name and formula

Reference code: 00-022-0714

Mineral name: Enstatite, ordered

PDF index name: Magnesium Silicate

Empirical formula: MgO_3Si

Chemical formula: $MgSiO_3$

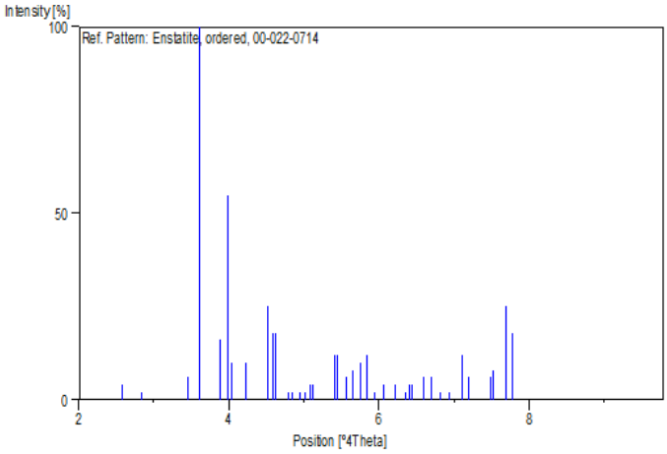

Figure 3B *Stick pattern of Enstatite*

B4) Name and formula

Reference code: 00-034-1495

PDF index name: Magnesium Aluminum Zirconium Oxide

Empirical formula: Al2.40Mg5O12Zr1.70

Chemical formula: Mg5Al2.4Zr1.7O12

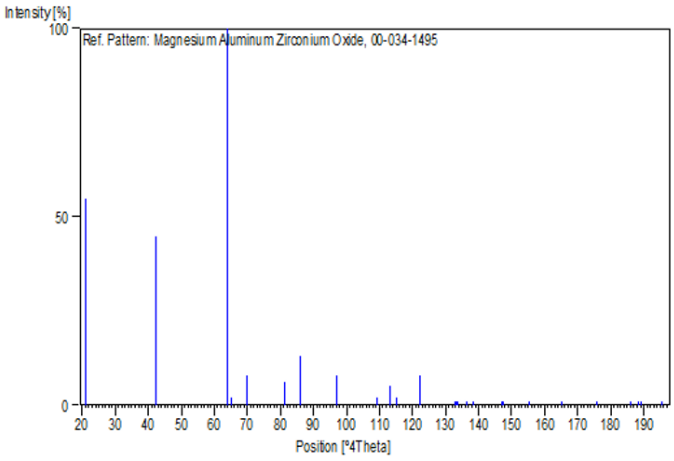

Figure 4B *Stick pattern of Magnesium Aluminum Zirconium Oxide*

B5) Name and formula

Reference code: 00-010-0063

PDF index name: Titanium Oxide

Empirical formula: O3Ti2

Chemical formula: Ti2O3

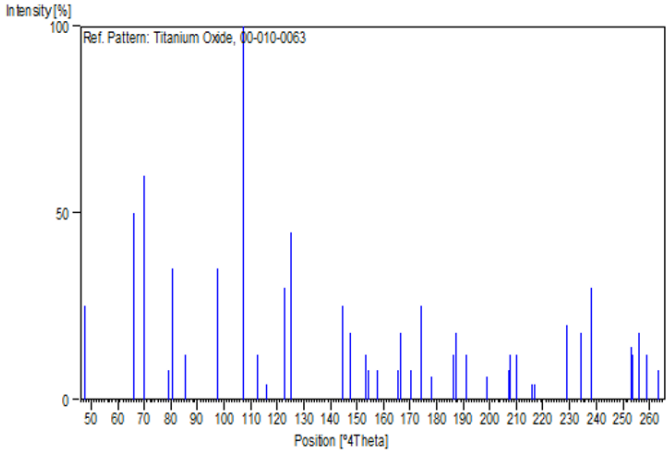

Figure 5B *Stick pattern of Titanium Oxide*

Appendix C: HSM photographs of LMAS system

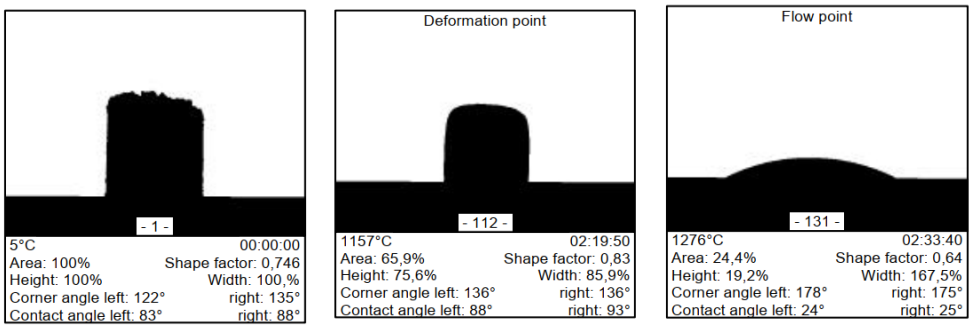

Figure 1C *HSM photographs of GP0 specimen*

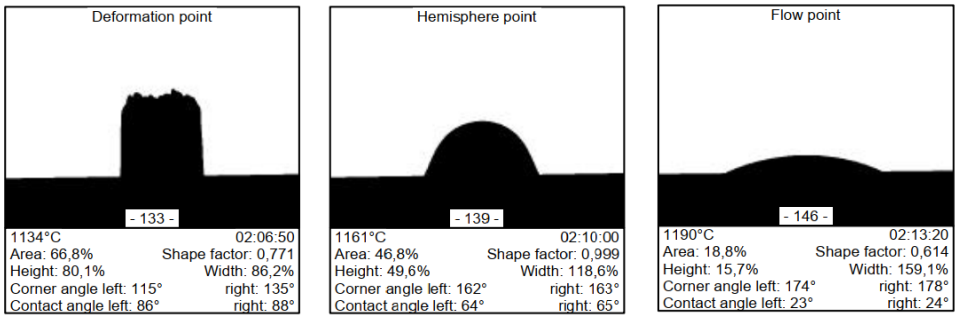

Figure 2C *HSM photographs of GP1 specimen*

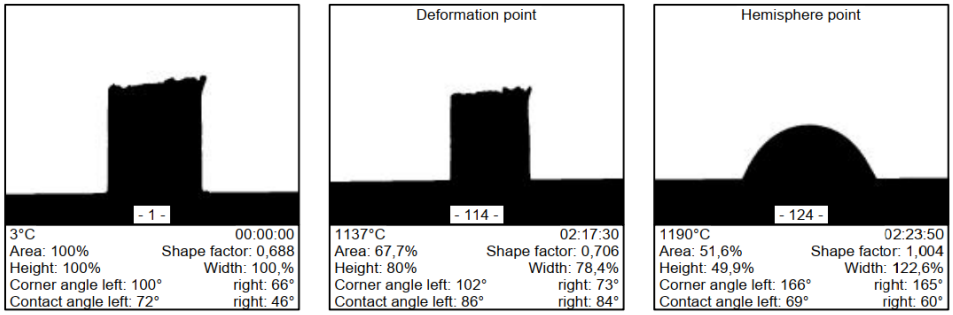

Figure 3C *HSM photographs of GP2 specimen*

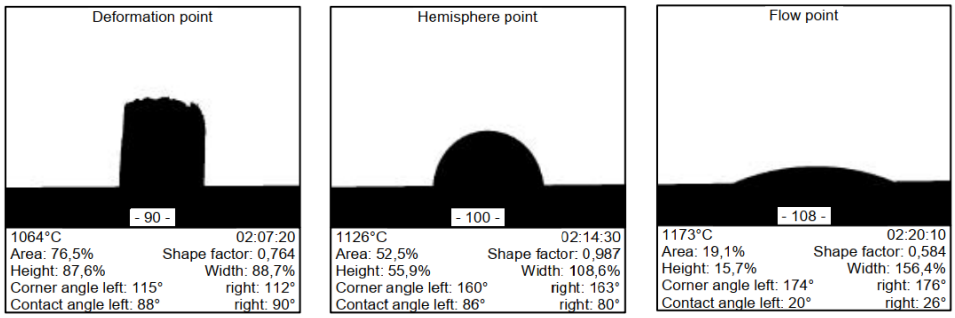

Figure 4C *HSM photographs of GP3 specimen*

Appendix D: MAS crystallization kinetics

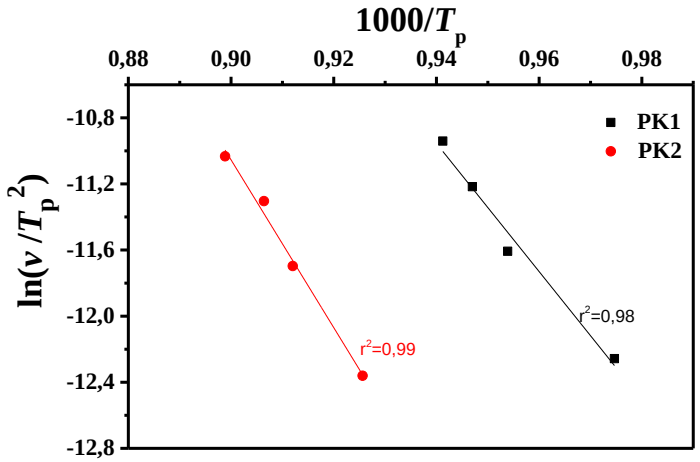

Figure 1D *Kissinger plot of MP0 specimen*

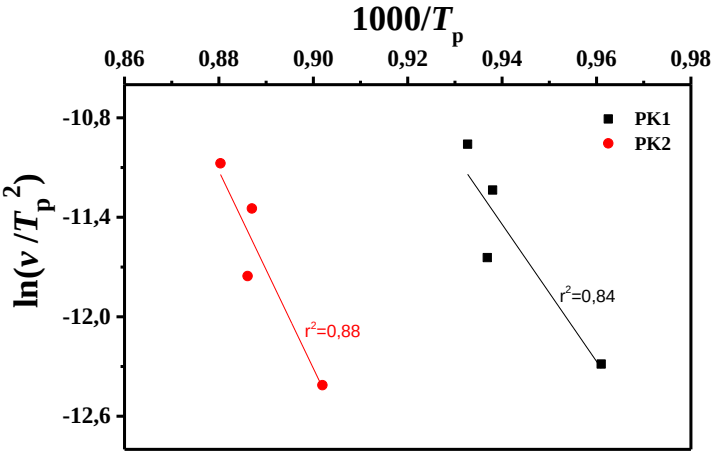

Figure 2D *Kissinger plot of MP1 specimen*

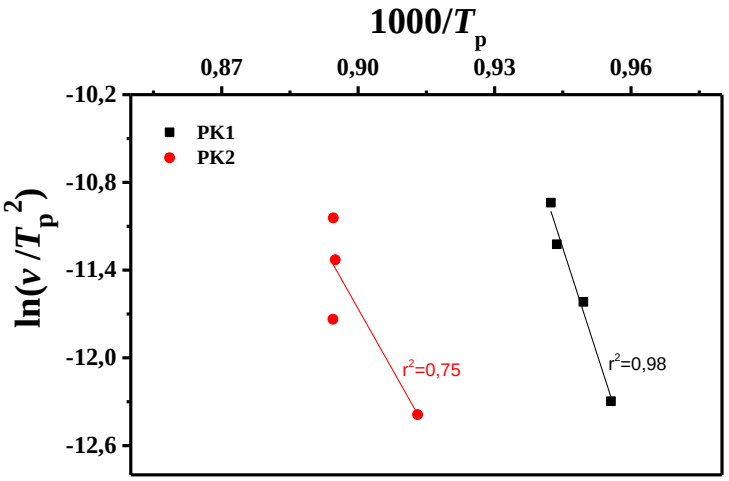

Figure 3D *Kissinger plot of MP2 specimen*

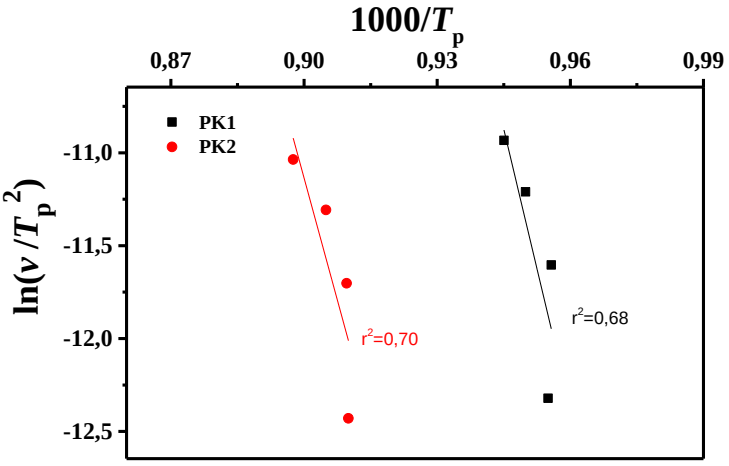

Figure 4D *Kissinger plot of MP3 specimen*

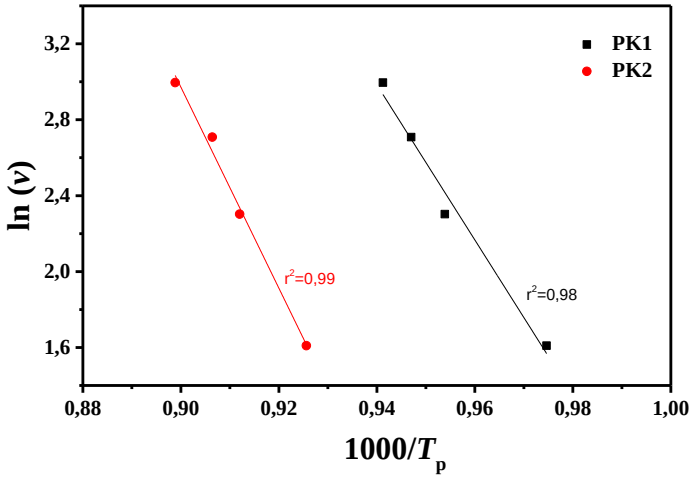

Figure 5D *Ozawa plot of MP0 specimen*

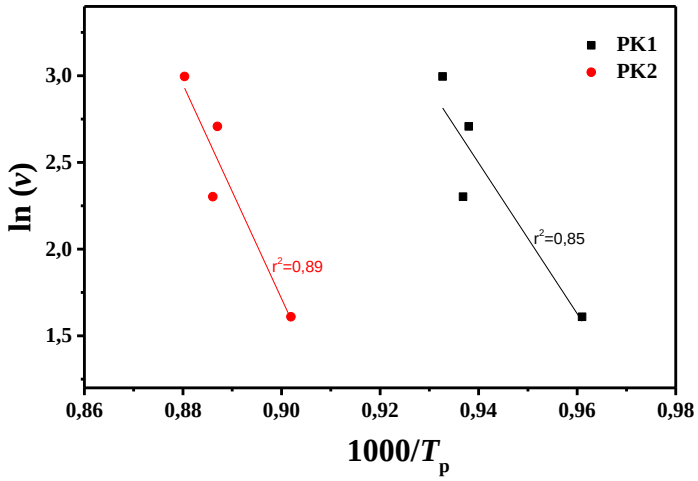

Figure 6D *Ozawa plot of MP1 specimen*

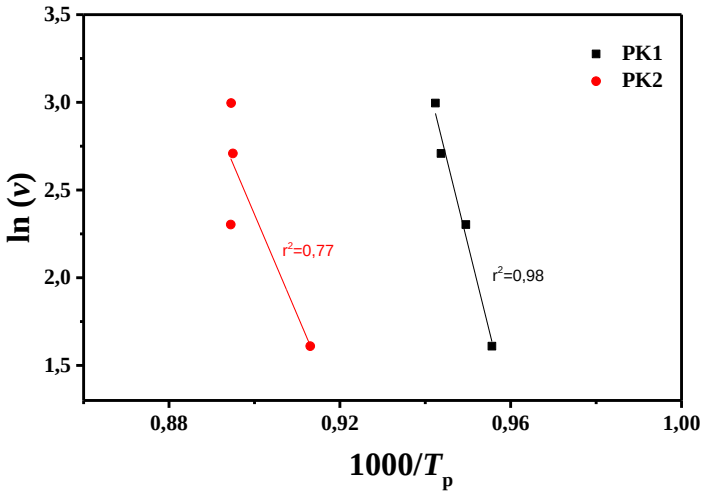

Figure 7D *Ozawa plot of MP2 specimen*

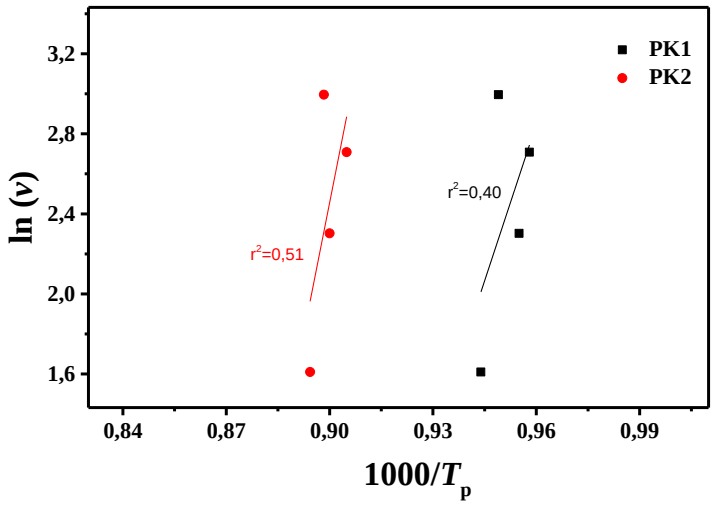

Figure 8D *Ozawa plot of MP3 specimen*

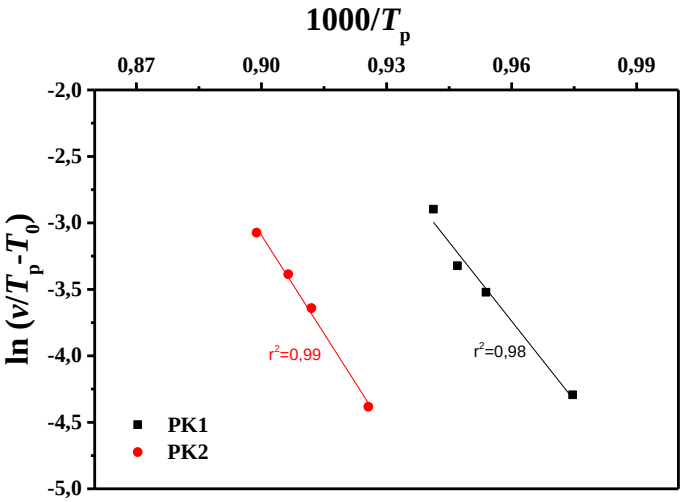

Figure 9D *Augis & Bennett plot of MP0 specimen*

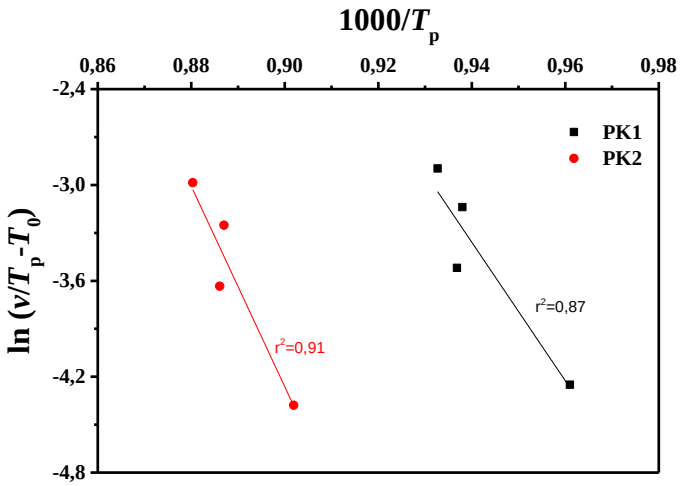

Figure 10D *Augis & Bennett plot of MP1 specimen*

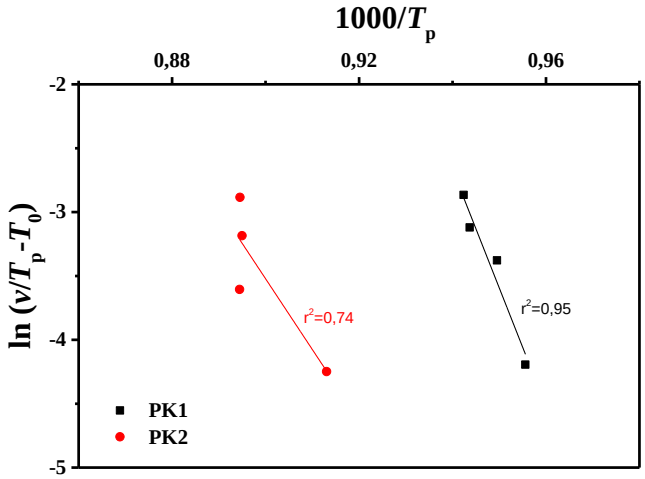

Figure 11D *Augis & Bennett plot of MP2 specimen*

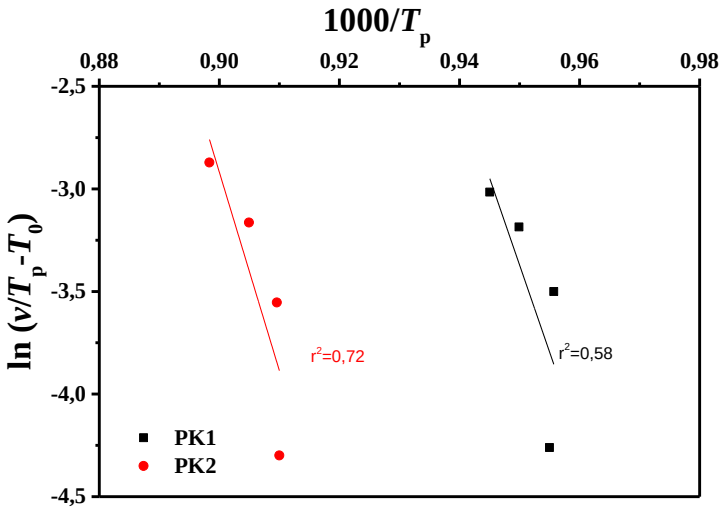

Figure 12D *Augis & Bennett plot of MP3 specimen*

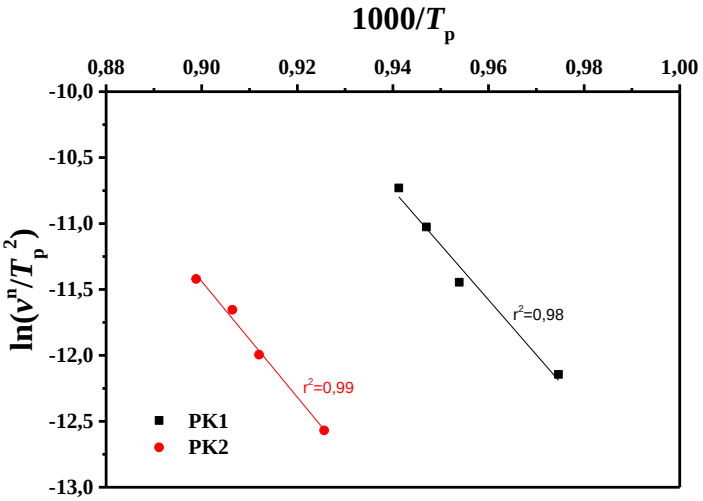

Figure 13D *Matusita & Sakka plot of MP0 specimen*

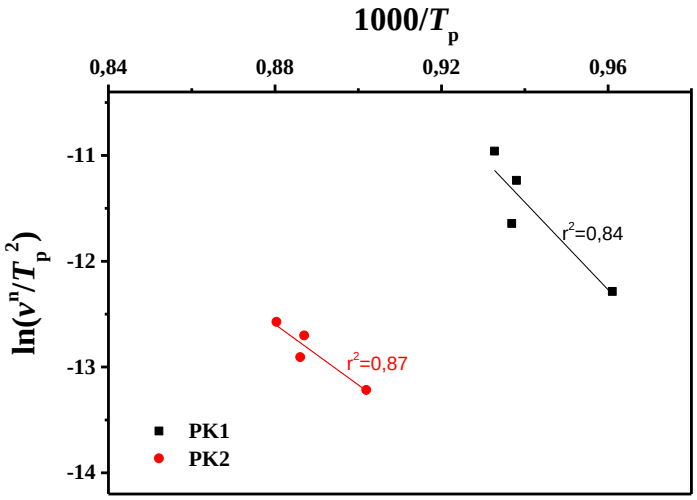

Figure 14D *Matusita & Sakka plot of MP1 specimen*

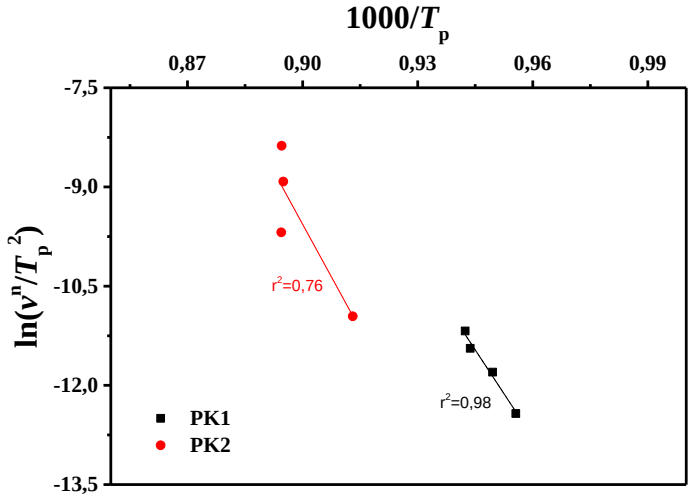

Figure 15D *Matusita & Sakka plot of MP2 specimen*

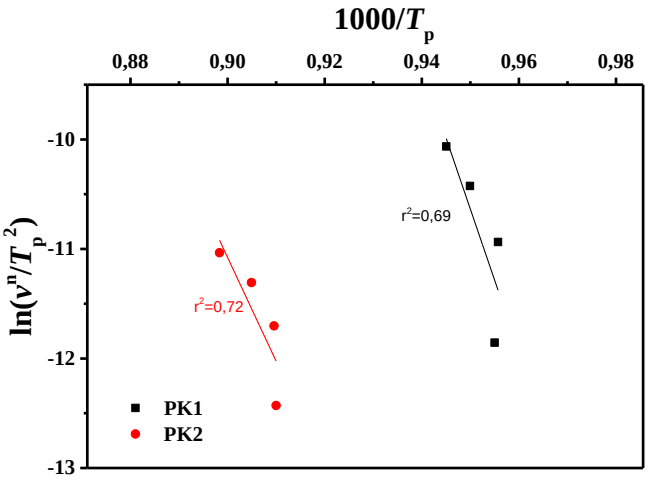

Figure 16D *Matusita & Sakka plot of MP3 specimen*

Appendix E: JCPD crystalline phases of MAS system

E1) Name and formula

Reference code: 00-004-0769

Mineral name: Forsterite, syn

PDF index name: Magnesium Silicate

Empirical formula: Mg_2O_4Si

Chemical formula: Mg_2SiO_4

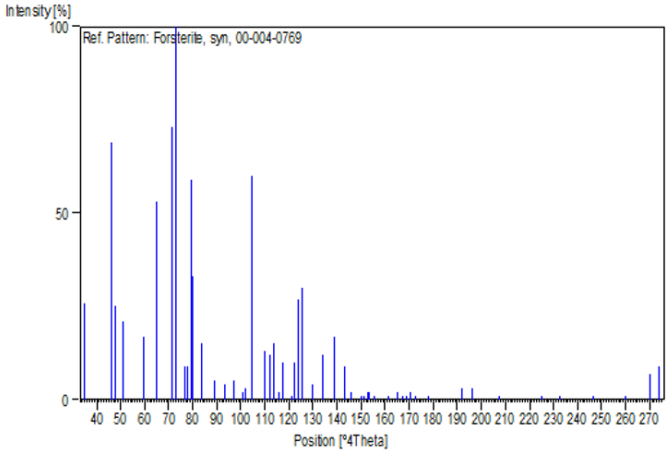

Figure 1E *Stick pattern of Forsterite*

E2) Name and formula

Reference code: 00-010-0494

Mineral name: Fluor-phlogopite, 1M

PDF index name: Potassium Magnesium Aluminum Fluoride Silicate

Empirical formula: $AlF_2KMg_3O_{10}Si_3$

Chemical formula: $KMg_3(Si_3AlO_{10})F_2$

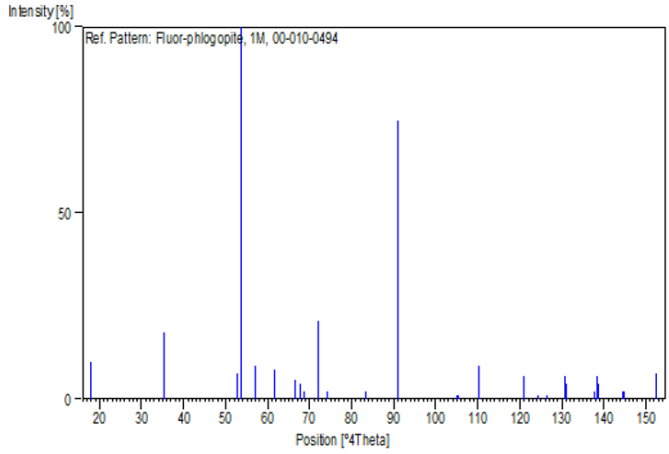

Figure 2E *Stick pattern of Fluor-phlogopite*

Appendix F: HSM photographs of MAS system

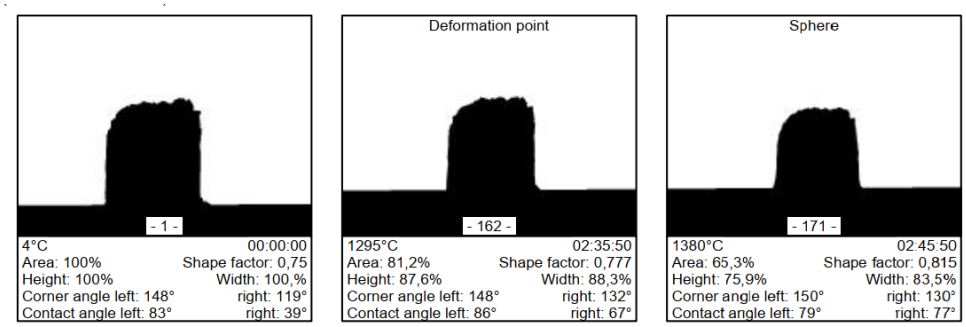

Figure 1F *HSM photographs of MP1 specimen*

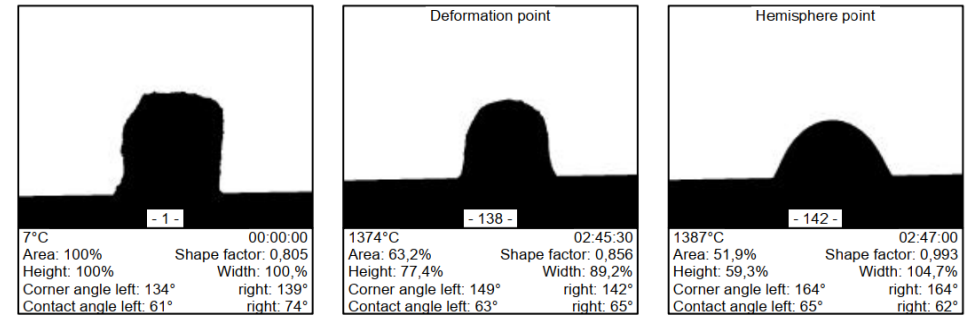

Figure 2F *HSM photographs of MP2 specimen*

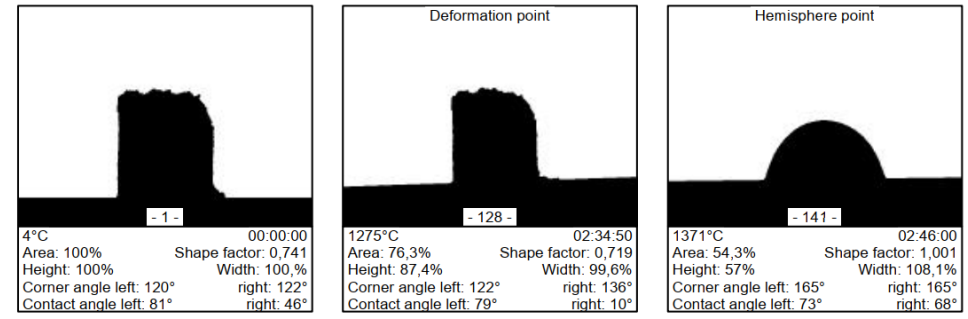

Figure 3F *HSM photographs of MP3 specimen*

Abstract

Contribution to the development of glass ceramics with excellent mechanical and biocide properties

This study was carried out on the kinetics and crystallization behavior of $LiO_2–MgO–Al_2O_3–SiO_2$ (LMAS) and $MgO–Al_2O_3–SiO_2$ (MAS) glass ceramic systems. In addition, a comparative study of the effect of variation of P_2O_5 concentration (from 0.0–3.0 mol%) on the properties of both glass ceramics was carried out. The biocide activity of the Silver-coated samples was studied against the bacteria *Escherichia coli*. The results obtained show that LMAS and MAS glass ceramics exhibit excellent mechanical and optical properties and a high *anti-E. coli* biocide activity.

Keywords: Glass ceramic, MAS, LAS, LMAS, P_2O_5, mechanical properties, optical properties, biocide.

Résumé

Contribution au développement des vitrocéramiques à propriétés mécaniques et biocide élevées

Cette étude a été effectuée sur la cinétique et le comportement à la cristallisation des vitrocéramiques de types $LiO_2–MgO–Al_2O_3–SiO_2$ (LMAS) et $MgO–Al_2O_3–SiO_2$ (MAS). En outre, une étude comparative de l'effet de la concentration de P_2O_5 (du 0.0–3.0 mol%) sur les propriétés des deux types de vitrocéramiques a été réalisée. L'activité biocide après un revêtement à base d'Argent des échantillons vitrocéramiques a été étudiée contre la bactérie *Escherichia coli*. Les résultats obtenus montrent que les vitrocéramiques étudiées LMAS et MAS présentent d'excellentes propriétés mécaniques et optiques et une activité biocide *anti-E. coli* élevée.

Mots clés : Vitrocéramique, MAS, LAS, LMAS, P_2O_5, propriétés mécaniques, propriétés optiques, biocide.

الملخص

المساهمة في تطوير خزف زجاجي بخصائص ميكانيكية ممتازة و إبادة حيوية عالية

أجريت هذه الدراسة على حركية وسلوك التبلور لنوعين من الخزف الزجاجي $LiO_2–MgO–Al_2O_3–SiO_2$ (LMAS) و $MgO–Al_2O_3–SiO_2$ (MAS). كما تم إجراء دراسة مقارنة لتأثير تغير تركيز P_2O_5 (من 0.0–3.0 مول٪) على خصائص كلا نوعي الخزف الزجاجي. تمت دراسة نشاط بكتيريا *Escherichia coli* على سطح الخزف الزجاجي المطلي بالفضة. أظهرت النتائج المتحصل عليها أن الخزف الزجاجي LMAS و MAS يتميز بخصائص ميكانيكية وبصرية ممتازة بالإضافة الى نشاط إبادة حيوية عالي ضد *E. coli*.

كلمات مفتاحية: خزف زجاجي ، MAS ، LAS ، LMAS ، P_2O_5 ، خصائص ميكانيكية ، خصائص بصرية ، مبيد حيوي.